Physik-Department

Institut für Experimentalphysik E12

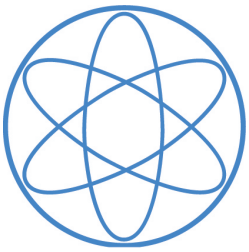

Search for ^{60}Fe of Supernova Origin in Earth's Microfossil Record

Dissertation

von

Peter Ludwig

Technische Universität

München

Technische Universität München
Fakultät für Physik
Lehrstuhl für Experimentalphysik E12

Search for ^{60}Fe of Supernova Origin in Earth's Microfossil Record

Peter Ludwig

Vollständiger Abdruck der von der Fakultät für Physik der Technischen Universität München zur Erlangung des akademischen Grades eines

Doktors der Naturwissenschaften (Dr. rer. nat.)

genehmigten Dissertation.

Vorsitzender:		Univ.-Prof. Dr. Björn Garbrecht
Prüfer der Dissertation:	1.	Univ.-Prof. Shawn Bishop, Ph.D.
	2.	Univ.-Prof. Dr. Stefan Schönert
	3.	Prof. Michael Wiescher, Ph.D., University of Notre Dame, USA (nur schriftliche Beurteilung)

Die Dissertation wurde am 14.07.2015 bei der Technischen Universität München eingereicht und durch die Fakultät für Physik am 21.09.2015 angenommen.

Abstract

The main objective of this thesis was the search for a supernova-produced ^{60}Fe signature in fine-grained magnetic particles, primarily magnetofossils, in marine sediment.

When a massive star explodes as a supernova, it ejects part of its mass, including freshly synthesized elements, into the interstellar medium. Should this happen close to the solar system, supernova ejecta can be deposited on Earth. ^{60}Fe presents us with an excellent target to search for such a signature in geological reservoirs. Firstly, because of its long half-life ($\sim$ 2.6 Ma), and secondly, because there is no expected terrestrial background, making an identification of a supernova ^{60}Fe signature easier. Specifically, this project focused on a ^{60}Fe search in so-called magnetofossils, which are the remains of magnetite chains built up by magnetotactic bacteria in marine sediment. These bacteria build up intracellular chains of small crystals of magnetite for movement in the Earth's magnetic field and are expected to incorporate ^{60}Fe if it is present in the ocean. To this end, two sediment cores from the Eastern Equatorial Pacific, ODP leg 138 sites 848 and 851, were analyzed.

In order to identify the signature of small-grained magnetic particles in the sediment, magnetic measurements were performed, including hysteresis curves, remanence magnetization measurements, and First-Order Reversal Curve measurements. These analyses revealed that the concentration of magnetofossils is $15 - 60$ μg/g of dry sediment weight. Additionally, it was possible to characterize the primary extraction method for iron, the citrate-bicarbonate-dithionite technique, a very mild leaching that dissolves primarily small-grained iron-oxides. After iron extraction, the samples were purified in a specifically designed chemical procedure, yielding highly pure Fe_2O_3. Magnetic measurements on a representative sample showed that the the iron in the Fe_2O_3 sample contains $\geq$24% iron from magnetofossils. This assures that the extraction procedure minimizes dilution of a possible ^{60}Fe/Fe signal by avoiding the dissolution of large, primary grains which do not contain ^{60}Fe, while magnetofossils are completely dissolved.

The ratio of ^{60}Fe to stable Fe was then measured with ultra-sensitive accelerator mass spectrometry using the GAMS setup at the Maier-Leibnitz-Laboratory in Garching, Germany. The setup features a 14 MV Tandem accelerator and a gas-filled magnet for isobar separation of stable ^{60}Ni. The sensitivity reached was $^{60}\text{Fe/Fe} \approx 2 \times 10^{-17}$. An increased ^{60}Fe/Fe concentration was observed in both sediment cores, in layers spanning an age of $1.7 - 2.7$ Ma with a peak concentration concentration of $^{60}\text{Fe/Fe} \approx (3 - 8) \times 10^{-16}$. The signal cannot be explained by cosmic-ray production of ^{60}Fe due to the lack of an

increased ^{53}Mn/Mn concentration and was thus interpreted as the deposition of material from of one or more supernovae.

Zusammenfassung

Das Hauptthema dieser Arbeit war die Suche nach einer supernova-produzierten ^{60}Fe Signatur in feinkörnigen magnetischen Partikeln, hauptsächlich Magnetofossilien, in Ozeansediment.

Wenn ein schwerer Stern als Supernova explodiert, schleudert er einen Teil seiner Bestandteile, inklusive frisch erzeugter Elemente, in das interstellare Medium hinaus. Sollte dies in der Nähe unseres Sonnensystems passieren, können Supernovaauswürfe auf der Erde landen. ^{60}Fe stellt ein ausgezeichnetes Ziel für einen Suche nach solch einer Signatur in geologischen Reservoirs da. Erstens wegen seiner langen Halbwertszeit (~ 2.6 Ma), und zweitens weil es keinen terrestrischen Untergrund gibt. Insbesondere lag der Fokus bei diesem Projekt auf einer ^{60}Fe Suche in sogenannten Magnetofossilien, welche die Überreste von Magnetitketten darstellen, die von magnetotaktischen Bakterien in Ozeansedimenten erzeugt wurden. Diese Bakterien bauen intrazellulare Ketten aus kleinen Magnetitkristallen auf, um sich damit im Magnetfeld der Erde fort zu bewegen. Zu diesem Zweck wurden zwei Bohrkerne aus dem Östlichen Äquatorialen Pazifik, ODP leg 138, Bohrstellen 848 und 851, analysiert.

Um die Signatur von magnetischen Partikeln im Sediment zu identifizieren wurden magnetische Messungen durchgeführt, darunter Hystereseschleifen, magnetische Remanenzmessungen und First-Order Reversal Curve Messungen. Diese Analysen haben gezeigt, dass die Konzentration von Magnetofossilien etwa $15 - 60$ μg/g Anteil an der Masse des trockenen Sedimentes hat. Zusätzlich war es möglich die primäre Extraktionsmethode für Eisen, die Citrat-Bicarbonat-Dithionit Technik, zu charakterisieren. Diese stellt die eine sehr milde Leaching dar, die primär feinkörnige Eisenoxide auflöst. Nach der Eisenextraktion wurden die Extrakte aufbereitet um hochreine Fe_2O_3 Proben herzustellen. Magnetische Messungen an einer repräsentativen Sedimentprobe haben gezeigt, dass das Eisen in der extrahierten Fe_2O_3 Probe zu mindestens 24% aus Magnetofossilien kommt. Dies zeigt, dass die Extraktionsprozedur eine mögliche Verdünnung des ^{60}Fe/Fe Signals minimiert, da das Auflösen von großen, primären Partikeln, die kein ^{60}Fe enthalten, verhindert wird.

Das Verhältnis von ^{60}Fe zu stabilem Fe wurde dann mit hochempfindlicher Beschleunigermassenspektrometrie am GAMS Aufbau am Maier-Leibnitz-Laboratorium in Garching, Deutschland, gemessen. Der Aufbau verfügt über einen 14 MV Tandem Beschleuniger und einen Gasgefüllten Magneten für Isobarentrennung von stabilem ^{60}Ni. Die erreichte Empfindlichkeit war $^{60}\text{Fe/Fe} \approx 2 \times 10^{-17}$. Eine erhöhte ^{60}Fe/Fe Konzentration wurde in

beiden Sedimentkernen beobachtet, und zwar in Sedimentschichten, die einem Alter von 1.7−2.7 Ma entsprechen, mit einer maximalen Konzentration von ^{60}Fe/Fe $\approx (3-8)\times10^{-16}$. Das Signal kann nicht durch Erzeugung von ^{60}Fe durch kosmische Strahlung erklärt werden, da eine entsprechend hohe Konzentration von ^{53}Mn/Mn nicht beobachtet wurde, und wurde daher als Eintrag von einer oder mehrerer Supernova Explosionen interprätiert.

Contents

1. Introduction

Supernova (SN) explosions are among the most violent and energetic events in the universe. They can occur either in binary star systems, when mass accretion onto a white dwarf (WD) star induces a thermonuclear disruption of the WD in a thermonuclear supernova (TNSN), or when a massive star ($M \gtrsim 10\ M_{\odot}$) comes towards the end of its lifetime and undergoes a core-collapse supernova (CCSN) explosion. SNe can eject a great amount material into the interstellar medium (ISM). SNe occur with a frequency of about 1-5 SNe per century in our galaxy (Cappellaro et al., 2005; Diehl et al., 2006a; Adams et al., 2013). It is thus possible that, over geologically significant timescales, SNe have occurred close to our solar system (< 100 pc). A nearby SN event can influence (mostly negatively) life on Earth (Ellis and Schramm, 1995, and references therein). One not particularly harmful, but curious effect, is the possible deposition of freshly synthesized SN material into solar system reservoirs. For stable isotopes, it is impossible to distinguish such SN-deposits from so-called primordial material. Primordial refers to isotopes whose half-life is so long ($\gtrsim 10^8$ a), that they could have been produced before the formation of the solar system.

It was first suggested by Korschinek et al. (1996) and later discussed in more detail by Ellis et al. (1996) that SN signatures might be preserved in the form of long-lived radioactive isotopes which are not primordial. One of the isotopes which can be formed in those stars and ejected into the ISM is ^{60}Fe. It is mostly synthesized in the helium and carbon shell burning phases of very massive stars (Limongi and Chieffi, 2006b) and thus ejected primarily in CCSN. Other examples of isotopes which can be introduced into the ISM by SNe include ^{26}Al, ^{53}Mn, and additionally, if the r-process actually occurs in CCSNe, ^{244}Pu.

Considering possible SN tracers in terrestrial samples, ^{60}Fe has proven to be the best-suited isotope. ^{60}Fe has practically no anthropogenic background (^{60}Fe/Fe $< 10^{-16}$) and is also rarely produced in cosmic ray spallation on Earth due to shielding by Earth's atmosphere and the low abundance of spallation targets in the atmosphere (mostly Ni). It should be mentioned here that for ^{60}Fe measurements in lunar or meteoritic samples, however, cosmogenic production of ^{60}Fe, mainly by galactic cosmic ray (GCR) spallation on nickel targets, cannot be neglected. Although the amount of ^{60}Fe in a single CCSN event can be very large ($10^{-5} - 10^{-3}\ M_{\odot}$) (Limongi and Chieffi, 2006b), the concentration of ^{60}Fe to stable Fe in samples showing a SN signature can be expected to be extremely low (^{60}Fe/Fe $\approx 10^{-16} - 10^{-15}$). An ultrasensitive detection method is thus required to detect such tiny concentrations.

The most sensitive experimental technique for the detection of trace amounts of long-lived radioisotopes is accelerator mass spectrometry (AMS). It is an ion counting technique in which the desired particles are extracted from a sample as negative ions and subsequently accelerated in a tandem accelerator. The high energy ($\sim$ 100 MeV beam energy for large accelerators) allows for complete suppression of molecular background and the use of nuclear physics particle identification techniques to individually identify and count atoms of the species of interest. All ^{60}Fe measurements in this work were carried out at the GAMS (Gas-filled Analyzing Magnet System) facility at the Maier-Leibnitz-Laboratory (MLL) in Garching, Germany, which is capable of complete isobaric suppression of stable ^{60}Ni.

The AMS facility at the MLL has already been used for several experiments in the greater context of achieving a better understanding of nucleosynthesis processes in the universe, including searches for ^{60}Fe in other terrestrial archives (Knie et al., 1999, 2004; Fitoussi et al., 2008), lunar archives (Fimiani et al., 2014), ^{244}Pu (Lachner et al., 2012), and superheavy elements in natural samples (Ludwig et al., 2012). Of those experiments, the most important finding has been the detection of an increased ^{60}Fe/Fe ratio in layers, corresponding to an age of approximately $1.9 - 2.6$ Ma, of a Pacific Ocean ferromanganese crust (Knie et al., 2004). The ferromanganese crust data in this age range shows an enhanced concentration of ^{60}Fe/Fe $\approx 2 \times 10^{-15}$. This ^{60}Fe signature was interpreted as deposited material from one or more SN explosions in the vicinity of the solar system at a distance $30 - 50$ pc. These results have subsequently spawned a very active, multi-disciplinary area of research, covering nuclear astrophysics, astronomical observation, geology, and experimental physics.

When a SN ejects ^{60}Fe, it can be incorporated into dust grains (Gomez, 2013; Cherchneff, 2014) and enter our solar system (Athanassiadou and Fields, 2011). These grains, with a typical size of $0.1 - 5$ μm, can then be deposited onto planets and satellites, such as the Earth and the Moon. When entering the Earth's atmosphere as dust particles, a fraction of the material will ablate, releasing ^{60}Fe into the atmosphere, allowing it to settle onto the surface slowly. Another fraction which is not completely ablated can reach the surface after some mass loss as a micro-meteorite (MM). Both of these mechanisms lead to the incorporation of ^{60}Fe into geological reservoirs on Earth.

The reservoirs chosen for this work are two sediment cores from the Eastern Equatorial Pacific. They were recovered by the Ocean Drilling Program (ODP) on expedition ODP 138 (drilling sites 848 and 851), which were among several cores drilled on a north-south transect along 110^0W. Within the context of SN searches for ^{60}Fe, the sedimentation rates of these cores ($\sim$ 6 m/Ma in 848, and $\sim$ 19 m/Ma in 851) allow for AMS sample production with good time resolution.

For ^{60}Fe sample production from natural samples, it is imperative that the ^{60}Fe/Fe atom concentration of the final AMS sample is as close to the original concentration in the targeted minerals as possible. This is critical, since dilution with stable Fe by an overly

aggressive extraction procedure could reduce ^{60}Fe/Fe down below the detection limit of AMS. Marine sediment contains a large variety of iron-bearing minerals. However, not all of those minerals can be expected to carry a ^{60}Fe signature. Assuming a large fraction of ^{60}Fe is dissolved in the oceans, the water becomes enriched with ^{60}Fe, which follows the complex iron-cycle and finally reaches the sediment surface. In the case of marine sediment, it can then only be expected for iron-bearing grains which have formed in-situ during that time (so-called secondary particles) to incorporate the full ratio of ^{60}Fe/Fe present in the ocean water without significant dilution. In contrast to secondary particles, primary particles have formed elsewhere and were transported to the sediment by wind and water. Primary particles can only contain ^{60}Fe on their surface, not in their interiors.

It is thus desirable to produce AMS samples which consist of iron that comes mostly from secondary iron-bearing minerals. The main target for extraction chosen for this work are iron oxides, predominantly magnetite (Fe_3O_4). One way to distinguish primary and secondary iron oxide grains is their grain size. While the size of primary grains is typically on the order of micrometers, secondary grains are normally smaller than 200 nm. In the case of magnetite, this implies another interesting possibility of distinction: for magnetite, typical primary particles represent multi-domain (MD) particles, while most secondary magnetite grains are single-domain (SD) and it is, in principle, possible to distinguish between them using magnetic analysis. A preliminary magnetic analysis of the sediment cores using ARM/IRM measurements (Bishop and Egli, 2011) revealed that small-grained magnetite particles are very abundant with an average concentration of about $15-60$ μg/g in the sediment, which hints to the presence of a very interesting type of mineral: magnetofossils.

Magnetofossils are chains of SD magnetite particles, which are built up by magnetotactic bacteria which use the chains for magnetotaxis (movement along Earth's magnetic field lines). Magnetotactic bacteria live just below the water-sediment interface and thus undergo sedimentation after their death. Amazingly, the chain structure of magnetofossils can not only survive sedimentation, but also be preserved over geologically significant timescales (Vali et al., 1987). Magnetofossils present an excellent target for extraction to produce AMS samples, since their unique magnetic signature (resembling non-interacting uniaxial SD particles) can be detected and thus used to characterize different extraction methods and determine their mass fraction in sediment.

Within the scope of this thesis, two different approaches for the extraction of iron for AMS sample production were considered: a weak chemical leaching known as Citrate-Bicarbonate-Dithionite (CBD) and a magnetic extraction technique. The magnetic extraction involves suspending sediment material in water and pumping it continuously past a magnetized iron finger. Any magnetic grains which are not embedded too deeply in the carbonate matrix can then stick to the magnetic finger and be physically removed. This technique was, however, not used for AMS sample production because of its low yield. However, it was shown to be well-suited for production of samples for electron microscopy,

which was performed at the Chemistry Department of TU München, confirming again the presence of biogenic magnetite.

The layout of this thesis is as follows. In chapter 2, a thorough discussion of the role of ^{60}Fe in astrophysics, leading finally to its incorporation into geological archives, especially via magnetotactic bacteria, will be given. A detailed description of the sediment material and the procedures used for AMS sample production can be found in chapter 3. Chapter 4 is aimed at a discussion of the results of all magnetic measurements that were used to characterize the sediment and the extraction techniques. The experimental AMS technique and the GAMS setup at the MLL in Garching will be presented in chapter 5. Afterward, the results of the ^{60}Fe AMS measurements and their interpretation will be shown in chapter 6, followed by a short conclusion in chapter 7.

The ^{60}Fe results in this work were supplemented by a limited multi-isotope study of 14 samples from core 851. The samples underwent a strong hydroxylamine-based leaching procedure and AMS samples for ^{10}Be, ^{26}Al, and ^{53}Mn were prepared at the Helmholtz-Zentrum Dresden-Rossendorf (HZDR). AMS measurements for ^{10}Be and ^{26}Al were performed at the DREAMS (DREsden AMS) setup at the HZDR, while ^{53}Mn was measured at the GAMS setup. The results of this study are presented in appendix B.

2. ^{60}Fe - from supernovae to magnetofossils

Every ^{60}Fe nucleus of SN origin which can be detected on Earth would have had a fascinating journey: from its formation in a massive star, its ejection in a SN event, its travel through space, to its deposition on Earth, and its incorporation into a geological reservoir, until finally being unearthed and examined by curious scientists. Understanding this journey requires some information from the fields of nuclear physics, nuclear astrophysics, astrophysics, geology, and biology, which will be discussed in this chapter.

2.1. The radioisotope ^{60}Fe

Iron is the 26th element in the periodic table. It is the 4th most abundant element on Earth by mass ($\sim 5-6\%$) and has 4 stable isotopes (^{54}Fe, ^{56}Fe, ^{57}Fe, and ^{58}Fe). The only long-lived radioisotope ($T_{1/2} > 10$ a) is ^{60}Fe. Until recently, the suggested half-life value was $T_{1/2} = (2.62 \pm 0.04)$ Ma (Rugel et al., 2009). In a recent re-measurement, the determined value was $T_{1/2} = (2.50 \pm 0.12)$ Ma (Wallner et al., 2015a). For this work, the error-weighted mean these two sources is used: $T_{1/2} = (2.61 \pm 0.04)$ Ma. This half-life puts ^{60}Fe in a unique position: on the one hand, it is long-lived enough for the isotope to survive over geophysical timescales and preserve the record of astrophysical events over millions of years. On the other hand, it is not primordial, which means that it is short-lived enough that any ^{60}Fe already present on Earth at the time of formation of the solar system would already have decayed.

^{60}Fe undergoes β^--decay to ^{60}Co, which in turn β^--decays ($T_{1/2} = 5.3$ a) to stable ^{60}Ni. A decay scheme is displayed in Fig. (2.1). In most cases, the decay of ^{60}Fe via ^{60}Co to ^{60}Ni is accompanied by the emission two γ-rays with energies $E_1 = 1173$ keV and $E_2 = 1333$ keV.

For the isotope ^{26}Al ($T_{1/2} = 0.717$ Ma (weighted mean over all available values, see Auer et al., 2009, and references therein)), which is also linked to active nucleosynthesis, gamma-ray observations of our galaxy have already been established (Diehl et al., 2006b; Bouchet et al., 2015). Similarly, ^{60}Fe induced gamma-ray lines could also provide observational astrophysics with the possibility to identify regions of active nucleosynthesis in our galaxy. However, due to its long half-life, the specific gamma-ray activity of ^{60}Fe originating from CCSNe is quite diffuse and difficult to detect. Combined with a challenging background

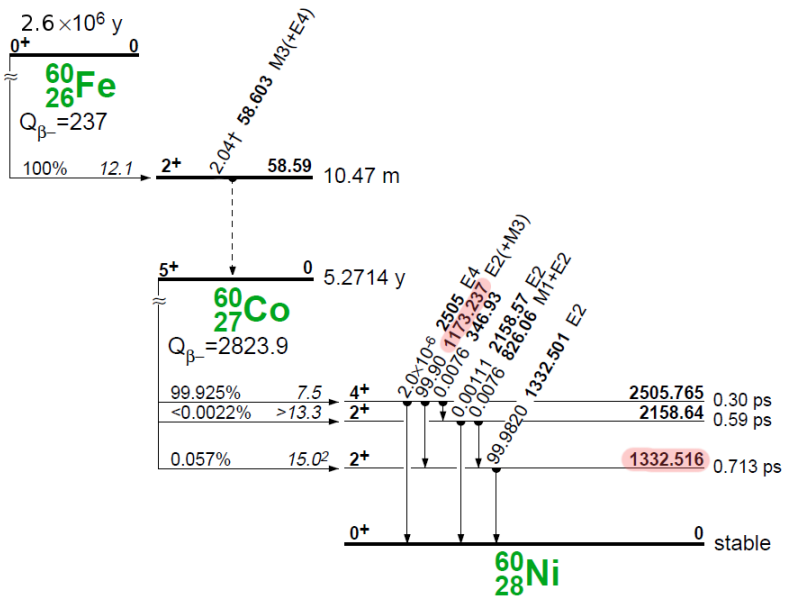

Figure 2.1: Decay scheme of ^{60}Fe. The two astrophysically important γ-decay lines at $E_1 = 1173$ keV and $E_2 = 1333$ keV are marked in pink. Dashed line indicates that energy-level-spacing is not to scale here. Figure adapted from Firestone (1996).

situation and a lower gamma-ray flux than for ^{26}Al, spatially resolved ^{60}Fe maps of our galaxy are still out of reach, but the gamma-ray lines themselves have been observed (Wang et al., 2007).

2.2. Nucleosynthesis

2.2.1. Overview

The astrophysical processes which create new elements are referred to as nucleosynthesis. An overview of the abundances of the elements observed in the solar photosphere, supplemented with some meteoritic abundances, using data from Asplund et al. (2009), can be seen in Fig. (2.2). The main challenge of nuclear astrophysics is explaining the rich variety of elements which we can observe in our solar system today by finding suitable nucleosynthesis processes and identifying them with associated astrophysical sites.

The most prominent features seen in Fig. (2.2) are as follows:

- The even-odd structure, favoring high abundances for elements with even Z. This can be explained by taking the pair-binding energy into account.
- A general decrease in abundance for heavier elements is obvious.
- High abundances of the elements Fe and Ni, corresponding to the maximum in binding energy per nucleon and the end of stellar fusion reactions.

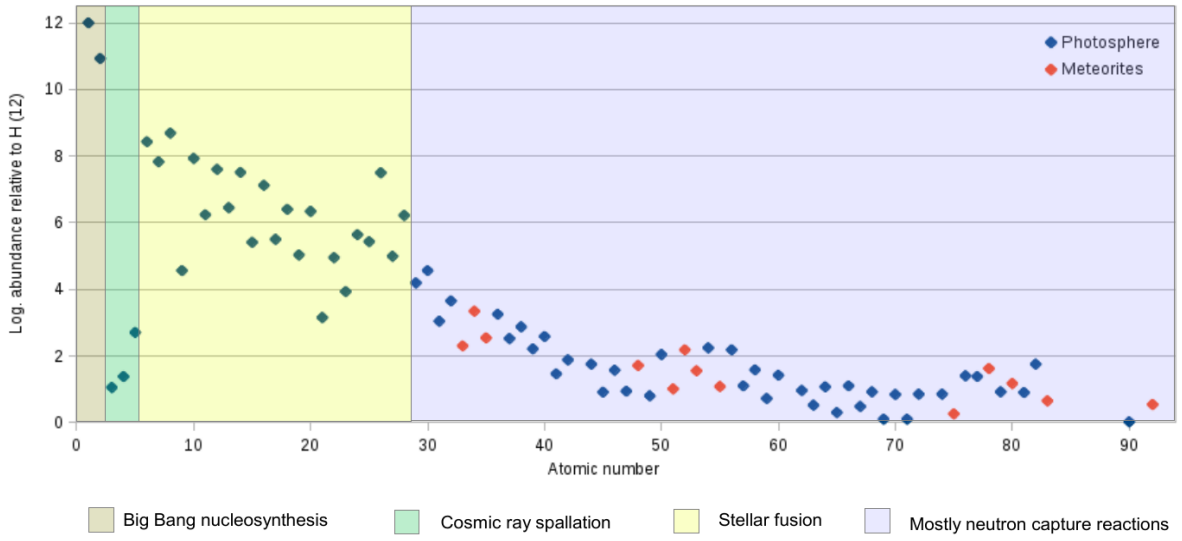

Figure 2.2: The figure shows a combination of photospheric solar abundances, supplemented with meteoritic ones, where no photospheric data was available. All values are taken from Asplund et al. (2009). The colored boxes show regions where synthesis of elements is mostly due to the indicated mechanisms.

- Slightly increased abundances can be observed near the neutron shell closures at $N = 50$, $N = 82$, and $N = 126$, corresponding to the regions $Z \approx 26$, $Z \approx 54$, and $Z \approx 80$.

In the early 20th century, it was generally believed that the isotopic composition of the universe is relatively static, with most elements having formed quickly after the Big Bang. However, rapid expansion and lack of stable nuclei with $A = 5$ and $A = 8$ after the Big Bang limited nucleosynthesis to only the lightest elements (H, He, some Li). This still left the production mechanism for all heavier elements unknown and represented one of the biggest mysteries in astrophysics during that time. It was not until 1957, when the groundbreaking, famous B2FH-paper was released (Burbridge et al., 1957), providing, for the first time, a coherent picture of ongoing nucleosynthesis in stars. These authors suggested that the synthesis of most elements can be split up into two basic scenarios: stellar nuclear fusion producing elements up to the iron peak and neutron capture processes forming heavier elements. Until today, the the general ideas of the B2FH paper are still valid, even though some details have changed due to new experimental and observational data becoming available.

2.2.2. Stellar burning phases

The nuclear astrophysics aspects of this section are based on information from Rolfs and Rodney (1988) and Illiadis (2007). Only specialized literature is cited separately.

The existence of life on Earth, made possible by the extremely continuous energy output of our sun, infers the existence of an efficient energy production mechanism, generating

power over billions of years while providing the sun with enough thermal energy to prevent its gravitational collapse. Stars can achieve this by nuclear fusion reactions. In this way, lighter elements (starting from H and He) can be transformed into heavier ones, in different stellar burning stages. The general idea of subsequent burning stages in stars implies that first, nuclear burning transforms seed nuclei into a heavier product. After the fuel is exhausted, the star's core contracts, increasing density and temperature, until the next burning stage can be ignited, using the ashes of the last stage as fuel. In many cases, the previous burning stage can continue in a shell around the core. This continues until the iron group elements (Fe, Ni, Co) are reached and the synthesis of heavier elements in fusion reactions is suppressed, since nuclear binding energy reaches its maximum in this region.

The evolution of a star depends mainly on its initial mass, but is also influenced by its metallicity (i.e. abundance of elements heavier than He), rotation, and possible companion stars. In the following, the typical evolutionary stages of stars of solar metallicity are introduced.

After the formation of a star from a gas cloud undergoing gravitational collapse, the proto-star contracts further until the temperature and density in its interior are high enough to ignite the first burning stage: hydrogen burning, which transforms hydrogen into helium via the net reaction $4\,^1\mathrm{H} \rightarrow\ ^4\mathrm{He} + 2\mathrm{e}^- + 2\overline{\nu}_\mathrm{e} + Q$, where Q is the energy released per reaction, with 16 MeV $\leq Q \leq$ 26 MeV. Depending on the conditions in the stellar interior (temperature, elemental composition), hydrogen burning proceeds through the p-p cycle ($M \lesssim 1.6\ M_\odot$), which involves the direct reaction between two protons as a starting point. In more massive stars (providing a certain metallicity), hydrogen burning is more efficient in the CNO-cycle, which essentially uses the available C,N, and O atoms as a catalyst. After the initial hydrogen fuel has been exhausted, the subsequent cessation of energy production causes the stellar core to contract, increasing both density and temperature, while hydrogen burning continues in a shell around the core.

Stars with $M \lesssim 0.4\ M_\odot$ cannot reach conditions necessary for He ignition and will thus end their evolution as He white dwarfs in the far future. More massive stars continue with H-shell burning, expanding to become red giant stars. When the conditions (temperature, density) are met, the star can proceed with the next core burning stage: He burning. Depending on whether the conditions in the core are electron degenerate ($M < 2\ M_\odot$) or not, He burning will start with a violent thermonuclear runaway, the He core flash, or quiescently commence burning. The main reaction involved is the so-called triple-α process. This is a two-step reaction, which first forms ^{8}Be by fusing two alpha particles ($^4\mathrm{He}(^4\mathrm{He},\gamma)^8\mathrm{Be}$, $Q = -92$ keV). Even though this reaction has a negative Q-value, a small equilibrium abundance of ^{8}Be can build up, and another alpha particle can be subsequently captured: $^8\mathrm{Be}(^4\mathrm{He},\gamma)^{12}\mathrm{C}$. Subsequent α-captures can form the nucleus ^{16}O. The primary ashes of He-burning are thus ^{12}C and ^{16}O.

For low- and intermediate-mass stars ($0.5\ M_\odot \lesssim M \lesssim 8\ M_\odot$), the evolution following

He exhaustion is quite complex. These stars are unable to ignite further burning stages in their cores, and are thus left with shell burning. In a complex interplay between H and He shell burning phases, these stars enter the so-called Asymptotic Giant Branch (AGB) phase (Iben and Renzini, 1983; Herwig, 2005). This phase is explained in more detail in Sec. (2.3.2). In the end, they run out of shell burning material and end their lives as C/O white dwarfs.

The evolution of stars with masses in the range $8\ M_\odot \lesssim M \lesssim 10\ M_\odot$ is not completely understood and subject of current research. They are able to ignite C burning, producing mainly Ne and some Mg in C + C reactions (lowest Coulomb barrier). Following fuel exhaustion, they are believed to undergo an extreme form of AGB phase, the so-called Super-AGB phase (Herwig, 2005), after which they leave behind a O/Ne/Mg white dwarf, representing the ashes of C burning. It is also not excluded that under certain conditions, stars in this mass range can explode in electron capture supernovae (ECSNe)(Wanajo et al., 2009).

Stars with $M \gtrsim 10\ M_\odot$ can produce the necessary conditions to ignite even heavier burning phases. After C burning, Ne burning occurs by way of a photodisintegration rearrangement producing mainly ^{16}O and ^{24}Mg. Afterward, O burning occurs, yielding mainly S and Si. With each burning stage, the center of the star gets hotter and more dense. The subsequent Si burning is then another photodisintegration rearrangement, but on a larger scale. All electromagnetic and strong reactions are in equilibrium, connecting all nuclei in what is referred to as the nuclear statistical equilibrium (NSE). The most abundant species in NSE are isotopes of Fe and Ni, but the exact composition depends strongly on the ratio of neutrons to protons. Since the maximum of nuclear binding energy is reached, the synthesis of elements heavier than Fe and Ni requires other mechanisms. At the end of their lifetime, such stars explode in CCSN, which will be explained in more detail in Sec. (2.4.2).

2.2.3. Nucleosynthesis beyond iron

The main reaction type able to produce heavy elements is neutron capture. Due to the absence of a Coulomb barrier for neutrons, neutron capture usually has large cross sections. Nucleosynthesis above iron can be divided roughly into two domains: the rapid neutron capture process (r-process) and the slow neutron capture process (s-process), which each contributing about 50% to the production of elements heavier than iron in the universe.

In the r-process, the required neutron density is so high (up to $n \approx 10^{27}$ cm^{-2}) that the nucleosynthesis path is quickly driven towards the most neutron-rich isotopes. This path involves isotopes so far off stability that their properties, such as mass, are largely unknown. After the neutron flux ceases (few seconds), the synthesized nuclei are allowed to beta-decay back towards the valley of stability, creating a large variety of stable iso-

topes, including the heaviest ones observed, such as actinides. The astrophysical site(s) of the r-process have not been confirmed yet, but likely scenarios include CCSNe and neutron-star mergers (Freiburghaus et al., 1999; Argast et al., 2004).

The s-process, on the other hand, is quite well understood. The main reason for this is that the relatively low neutron densities involved (10^7 cm$^{-2} \leq n \leq 10^{11}$ cm^{-2}) take the nucleosynthesis path along the valley of stability, where the isotopes' properties are well known. Over typical timescales of 10^3 to 10^5 years, the s-process can produce most stable isotopes and finally stops at ^{209}Bi from seed nuclei in the Fe-region. In order to reproduce the observed abundances of s-process isotopes (i.e. isotopes exclusively produced by the s-process), a superposition of two different neutron exposures is deduced. The weak s-process component, responsible for nucleosynthesis in the mass range $56 < A < 90$, can take place in the He and C shell burning phases of massive stars, making use of the ^{22}Ne$(\alpha, \mathrm{n})^{25}$Mg neutron source. Heavier isotopes are synthesized in the main s-process component, which occurs in the AGB phase of low and medium mass stars. In a dynamic interplay between H and He shell burning phases, the s-process makes use of the ^{22}Ne$(\alpha, \mathrm{n})^{25}$Mg source during a He burning episode, as well as ^{13}C$(\alpha, \mathrm{n})^{16}$O after the formation of a ^{13}C-pocket afterward (Lugaro et al., 2003).

2.3. Formation of ^{60}Fe

The radioisotope ^{60}Fe can be produced and destroyed in various ways. The main reactions involved are indicated in Fig. (2.3). Depending on the scenario under consideration the abundance evolution of ^{60}Fe is quite complex and involves all reactions with non-negligible contributions.

2.3.1. Massive stars

The following discussion is based on Limongi and Chieffi (2006a) and Limongi and Chieffi (2006b), who examined the ^{60}Fe production sites in models of massive stars. The main production mechanism of ^{60}Fe is the s-process in massive stars via successive neutron capture on ^{58}Fe, while it can be destroyed by radioactive decay or subsequent neutron capture. The resulting abundance evolution of the number density $N_{^{60}\mathrm{Fe}}$ of ^{60}Fe can be written as

$$\frac{\mathrm{d}N_{^{60}\mathrm{Fe}}}{\mathrm{d}t} = +N_n N_{^{59}\mathrm{Fe}} \langle \sigma v \rangle_{^{59}\mathrm{Fe}(n,\gamma)} - N_n N_{^{60}\mathrm{Fe}} \langle \sigma v \rangle_{^{60}\mathrm{Fe}(n,\gamma)} - N_{^{60}\mathrm{Fe}} \lambda_{^{60}\mathrm{Fe}(\beta^- \overline{\nu})} \tag{2.1}$$

where the first term denotes the production rate via neutron captures on ^{59}Fe (with the reaction rate per particle pair $\langle \sigma v \rangle$), the second the destruction rate via neutron captures on ^{60}Fe, and the third the destruction rate resulting from radioactive beta-decay to ^{60}Co.

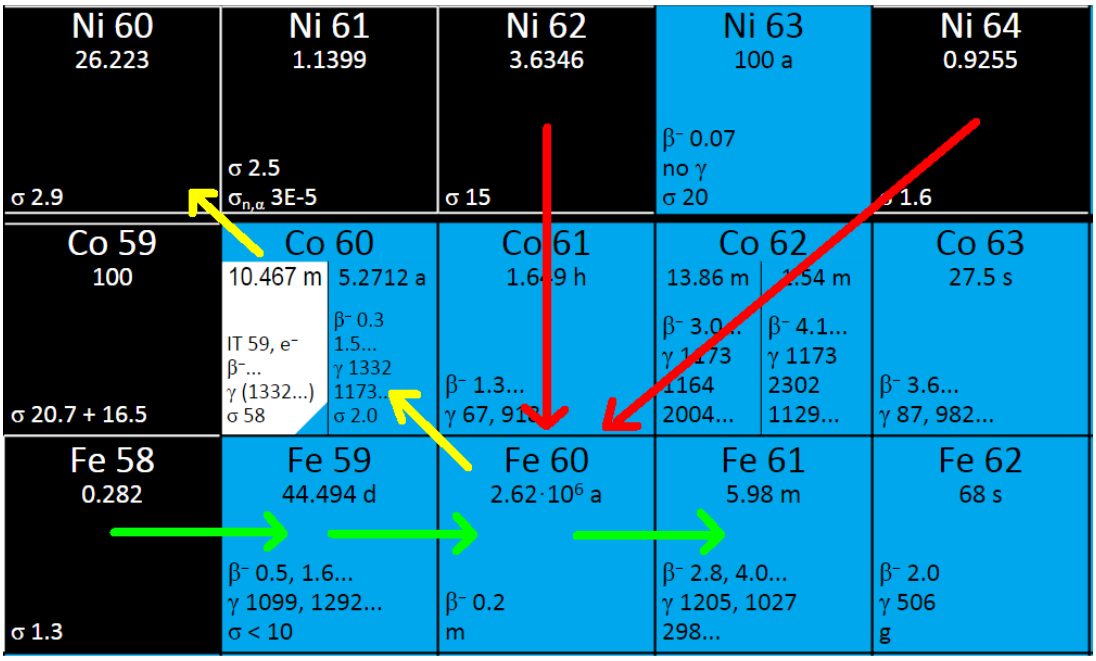

Figure 2.3: Excerpt of the chart of nuclides showing ^{60}Fe and all relevant production and destruction mechanisms for this nuclide; green: (n,γ) reactions; red: spallation reactions on Ni-targets; yellow: beta-decay chain to the stable ^{60}Ni. Image produced using Nucleonica (2014).

Because of the high neutron densities required to synthesize an appreciable amount of ^{60}Fe, partial destruction of ^{60}Fe will predominantly take place via neutron capture. There are also two factors limiting the temperature for ^{60}Fe synthesis: firstly, the half-life of ^{59}Fe, the mother nucleus, reduces significantly above 0.5 GK, owing to thermal activation of additional decay channels from excited states. This explicitly makes the decay-rate λ in Eq.(2.1) temperature dependent. Secondly, above 2.5 GK, photodisintegration of ^{60}Fe becomes efficient. Typical neutron densities required for ^{60}Fe production are around of 3×10^{10} cm^{-3} below 0.5 GK, rising to 3×10^{11} cm^{-3} at 1 GK and 6×10^{12} cm^{-3} at 2 GK.

Although the synthesis of ^{60}Fe is favored by low temperatures, a high temperature is required to overcome the Coulomb barrier for the activation of the ^{13}C(α,n)^{16}O and ^{22}Ne(α,n)^{25}Mg neutron sources. Additionally, a convective burning zone is preferred, since it prevents a local exhaustion of fuel (^{58}Fe and neutrons) and can transport freshly synthesized ^{60}Fe to cooler regions where its half-life is longer and the neutron density is lower, preventing its destruction. These factors limit the choice of stellar sites for ^{60}Fe production to few select burning scenarios.

In He burning phases, free neutrons are generated via the reaction ^{22}Ne(α,n)^{25}Mg. For core He burning, however, neutron densities never reach values required for significant ^{60}Fe production. In He shell burning, only very massive stars ($M > 40 M_{\odot}$) (with high mass loss in their Wolf-Rayet phase), reach a high enough neutron density for significant ^{60}Fe synthesis. Another important site for ^{60}Fe synthesis is C shell burning. While C core burning cannot provide enough neutrons, temperatures during C shell burning are high

enough ($>$ 1 GK) to produce ^{60}Fe with neutrons from ^{22}Ne(α,n)^{25}Mg.

The more advanced burning phases produce little to no ^{60}Fe, either because of the lack of convection (Ne burning) or too high temperatures, leading to photodisintegration (O, Si burning). A final episode of ^{60}Fe synthesis occurs during the SN explosion. When the SN shock wave passes through the stellar material, conditions for ^{60}Fe formation can be met once again when temperature reaches $T \approx 2.2$ GK. This ensures that a sufficient neutron supply is generated, while the temperature is still low enough for ^{60}Fe not to be photo-disintegrated. This temperature is reached in the C convective shell, and depending on the exact composition, significant ^{60}Fe production is possible. The individual contributions of the mentioned scenarios to the total ^{60}Fe mass synthesized vary with the initial stellar mass. Typically, explosive synthesis is a minor contribution. While in stars with $M < 40\ M_\odot$, the contribution from C shell burning dominates, in more massive stars ($M > 40\ M_\odot$), the He shell burning contribution can dominate. A summary of ^{60}Fe yields as a function of stellar mass from simulations by different groups can be seen in Fig. (2.4).

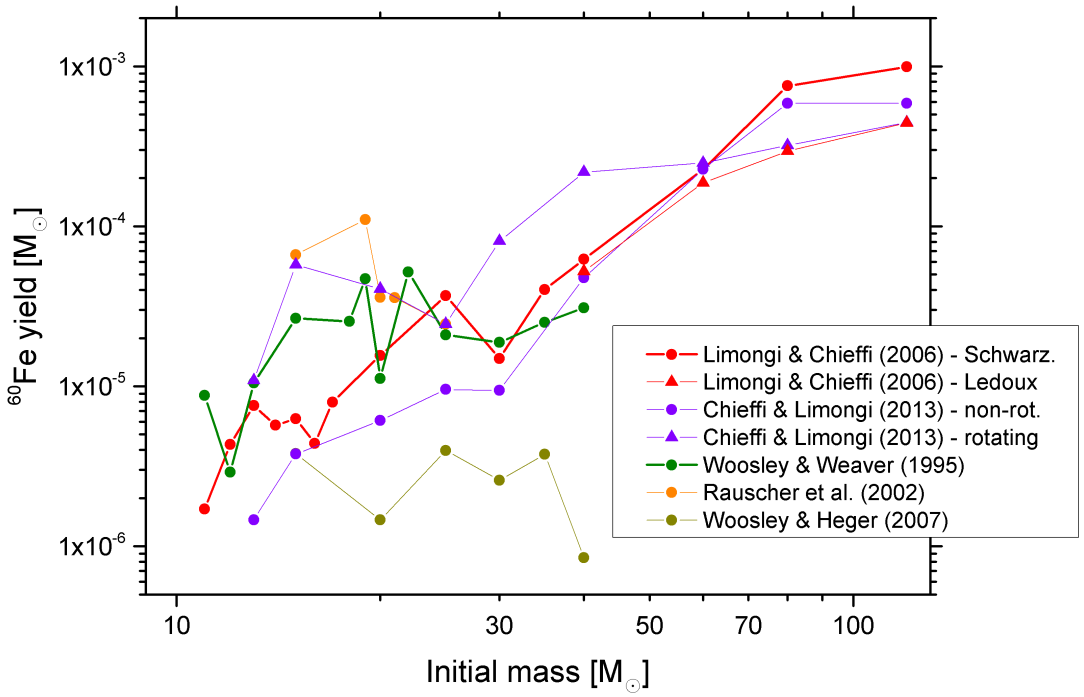

Figure 2.4: ^{60}Fe yields from SNe plotted over the initial stellar mass, including data from 5 different publications. The data from Chieffi and Limongi (2013) includes a rotating, and a non-rotating model, and the data from Limongi and Chieffi (2006b) features two different treatments of convection in He shell burning (Schwarzschild and Ledoux model).

The models agree that typical yields of ^{60}Fe are on the order of $10^{-6} - 10^{-4}\ M_\odot$ for initial stellar masses below 40 $M_\odot$, and can be up to a magnitude higher for very massive

stars.

2.3.2. AGB stars

The Asymptotic-Giant-Branch (AGB) is an evolutionary phase in the life of stars in the mass range $0.5M_\odot \lesssim M \lesssim 8M_\odot$. These stars have consumed their H and He fuel in core burning phases and are left with a C/O core surrounded by an initially inert He shell and a H shell with H shell burning ongoing on the bottom. This H shell burning adds He as its ashes to the inert He shell until the shell reaches conditions for He burning. Due to degeneracy, this results in violent He shell bursts known as thermal pulses (TP-AGB phase), which last only for $100 - 1000$ a. During this phase, the star's radius can extend even further than in the red giant phase. In the case of our sun, it might even engulf the inner planets during the AGB phase. Afterward, the He shell becomes inert again and H shell burning first has to refuel it again over $10^4 - 10^5$ a. Free neutrons are generated by the $^{13}C(\alpha,n)^{16}O$ and $^{22}Ne(\alpha,n)^{25}Mg$ reactions and serve to feed the s-process which can produce appreciable amounts of ^{60}Fe. When the star runs our of shell burning fuel after several pulses, it becomes a C/O white dwarf.

A set of simulations was performed by Karakas (2010) for different initial stellar masses in the range $1M_\odot - 6.5\ M_\odot$ and different metallicities. A summary of their findings can be seen in Fig. (2.5).

Interestingly, the yield of ^{60}Fe per solar mass of initial stellar material can even be higher than for some SN models. However, to obtain the total contribution of ^{60}Fe from AGB stars compared to SNe, one has to weight the data from Fig. (2.5) with an initial mass function (which takes into account the abundance of stars of different masses) and factor in the typical life-times of stars with different masses. This was done by Lugaro and Karakas (2008), who arrived at a ratio of AGB to SN type II production rate in our galaxy of $\sim 3\%$. This analysis was based on data from Limongi and Chieffi (2006b) for SNe and Karakas and Lattanzio (2007) for AGB stars. Using more current data from Karakas (2010), the AGB contribution to the ISM is more likely to be in the range of $1\% - 2\%$, thereby making AGB stars a very minor contributor to the galactic ^{60}Fe budget.

2.3.3. Spallation and extraterrestrial influx

^{60}Fe is formed by spallation reactions involving solar and galactic cosmic rays (SCR and GCR), mostly on Ni targets. This has been observed in samples from Ni-rich meteorites and also on the lunar surface, where trace amounts of ^{60}Fe can be found (Fimiani et al., 2014). Fortunately, Earth's atmosphere prevents the formation of ^{60}Fe on the surface, and the atmosphere itself contains no target for ^{60}Fe production.

Outside of Earth's atmosphere, however, formation of ^{60}Fe by spallation is an issue, e.g. in lunar samples. A high cosmogenic background could make the identification of a possible ^{60}Fe signal as SN input difficult. In terrestrial samples, a possible contamination

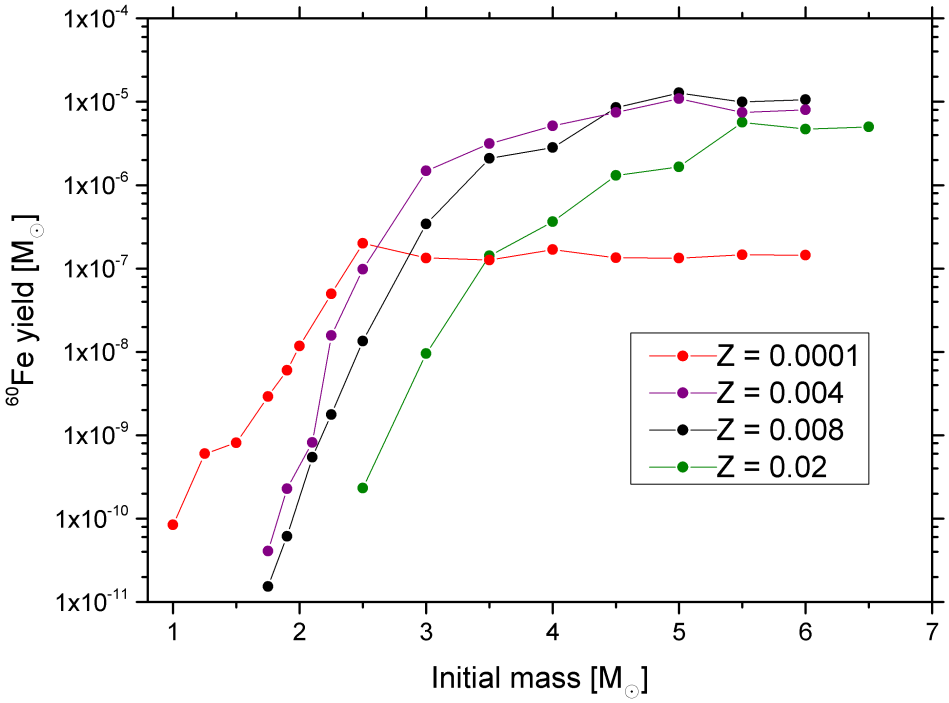

Figure 2.5: ^{60}Fe yield from simulations of AGB stars of different initial mass for four different metallicities $Z = 0.02$ corresponds to solar metallicity. Plot generated from additional data available from Karakas (2010).

could originate from MMs of non-SN origin. These are mainly interplanetary dust particles (IDPs), with grain size of typically 100 μm. On their path through the solar system, IDPs are irradiated by GCR and SCR, which can produce ^{60}Fe by spallation primarily on Ni nuclei (see e.g. Merchel et al., 2000).

It was even suggested by Basu et al. (2007) and Stuart and Lee (2012) that the ^{60}Fe anomaly in the Ferromanganese crust could have been caused by MMs and thus be of cosmogenic and not SN origin. The main differences between these two origins for the atmospheric transport are the grain size and the entrance velocity. While SN dust particles are expected to ablate mostly or completely, it is known that meteoritic remains of IDPs can be found on Earth, and also in marine sediments (Blanchard et al., 1980; Taylor and Brownlee, 1991), in the form of cosmic spherules of several μm size. This means that if a sample preparation technique is chosen which does not separate cosmic spherules out, a contamination of ^{60}Fe to stable Fe by cosmogenic ^{60}Fe can occur. This problem was avoided in this work by designing a very selective chemical extraction technique as will be discussed in the next chapter.

2.4. Supernovae

2.4.1. General information

SN explosions are the most violent way for stars to end their lives and have amazed human observers for thousands of years. Originally, the name SN was chosen because these objects appeared suddenly (from Latin *nova* meaning new) and were extremely bright, even able to outshine their entire host galaxies. They have also been observed in the Milky Way, but since they are relatively rare (1-5 SNe per century in our galaxy (Cappellaro et al., 2005; Diehl et al., 2006a; Adams et al., 2013)), and often obstructed by dust in the galactic disc, the last observed SN in the Milky Way was SN 1604, seen by Johannes Kepler as the brightest star in the night sky. By observing the light-curves of SNe, it is possible to distinguish different types. In general, there are two different basic astrophysical scenarios leading to SN explosions.

On the one hand, TNSN explosions of type Ia occur in binary star systems, where Roche-Lobe overflow from one star (typically a main sequence star) onto a white dwarf (WD) causes the mass of the WD to exceed the Chandrasekhar mass limit, causing a thermonuclear explosion, disrupting the entire star (Hillebrandt and Niemeyer, 2000). On the other hand, there are CCSN explosions. In this scenario, a massive star ($M \gtrsim 10 M_{\odot}$) evolves until the end of silicon burning and then undergoes gravitational collapse. Since only massive stars produce significant amounts of ^{60}Fe, the following discussion will focus on CCSNe. For a discussion of the contribution of TNSNe to the radioactivities observed in the solar system, the reader is referred to Huss et al. (2009), and references therein.

2.4.2. Core-collapse supernovae

Obtaining a deeper understanding of CCSN explosions requires a quantitative description of the hydrodynamical and nuclear processes in the stellar interior, which is fully compatible with observation. Even though much progress has been made over the past decades, fully physical 3-dimensional models of CCSNe are still limited by computational requirements (Burrows, 2013). This section introduces the key concepts of CCSN explosions, from the progenitor to the final remnant.

Progenitor

Summarizing the pre-SN evolution, the life of the core of a massive star can be thought of as one long compression process, periodically halted by the ignition of a new burning stage, making use of the ashes left behind by the previous one. Nonetheless, after each burning stage, the contraction continues, increasing density and temperature until the next burning stage can provide stability again. While the early stages last very long (order of Ma for H burning), the final stages consume their fuel very fast (only weeks for Si burning). During all this time, the star loses energy in the form of photons and

after the onset of carbon burning, also through the emission of thermal neutrinos. Before the subsequent gravitational collapse, the progenitor has evolved to a Chandrasekhar-mass iron-core, surrounded by shells of progressively lighter elements in an onion-like structure. The initial physical parameters in the core are typically $T \approx (6-10)$ GK and $\rho \approx (6-15) \times 10^9$ g/cm^3. (Burrows, 2013).

Collapse

At the onset of gravitational collapse, the pressure is mainly provided by electrons, but the increasing density ($\rho > 10^{10}$ g/cm^3) causes electron captures onto the nuclei, increasing their neutron number. The resulting loss of electrons (and thus pressure) increases the rate of collapse. The increasing temperature causes photodisintegration of nuclei, partially undoing the final stages of nucleosynthesis, since the NSE at such high temperature favors high abundances of α particles and free nucleons (Illiadis, 2007). At the same time, neutrino losses are very high. All these processes lead to the final collapse of the core, which proceeds almost at free-fall velocity, reducing a Fe sphere of roughly the size of the Earth, down to a proto-neutron star (PNS) of about 30 km radius in about 1 s (Woosley and Janka, 2005).

During collapse, the core material can be separated into two regions: a homologous core, where infall is subsonic with $v \propto r$, where r is the distance from the center, and an outer core, with supersonic infall. This is caused by the rapid decrease of the speed of sound towards with increasing r. While the homologous core can preserve some of its structural integrity, collapsing at up to 1/4 of the speed of light (Woosley and Janka, 2005), this infall cannot be communicated to the outer core. The pressure-gradient moves outward at the local speed of sound causing outer core material to be accelerated almost by free-fall acceleration with $v \propto r^{-1/2}$ (Arnett, 1996).

Bounce and Shock

The collapse proceeds until the density reaches nuclear density ($\rho \geq 2.7 \times 10^{14}$ g/cm^3) and the repulsive part of the strong nuclear force stops further contraction (Janka, 2012). The infalling homologous core is reflected and hits the outer core, which is still collapsing, creating a shock front. This initial bounce shock is, however, not able to produce a SN explosion, since neutrino losses and photo-dissociation at the shock front reduce the available kinetic energy and the shock front becomes an accretion shock within only few ms after the bounce (Burrows, 2013).

The main open question in CCSN research is how the SN shockwave is reignited. Among others (for a more detailed discussion, see. e.g. Janka, 2012), one possible solution could be the delayed emission of neutrinos, which were trapped in the PNS. At the high density in the PNS and due to sufficiently high neutrino energies, the mean free path of neutrinos is so short that they become effectively trapped in the core for several seconds

(Arnett, 1996).

The remnant of a CCSN explosion depends on several factors, like initial mass, metallicity, and rotation, and can be either a black hole or a neutron star, with typically 1.4 $M_\odot$ and a radius of 11.5 km (Lattimer, 2012).

Types of CCSNe

Depending on the intensity of spectral lines of H, He, and Si, CCSNe are divided into types II, Ib, and Ic. The absence of spectral lines of H, for type Ib (or H and He, for type Ic) can occur after a massive star loses its envelope in late stages of evolution (e.g. Wolf-Rayet stars).

A special type of CCSN is represented by so-called electron-capture SNe (ECSNs). These explosions originate from stars with a mass in the range $7M_\odot \lesssim M \lesssim 10M_\odot$. The main difference between this type of SN and regular core collapse is that the core of the star does not consist of iron. The progenitors are super-AGB stars with a core consisting mainly of O, Ne, and Mg. The SN is triggered by electron capture reactions on Ne and Mg, reducing the electron number and thus the effective Chandrasekhar mass, leading to further heating and contraction, igniting O and Ne burning, leading to a positive feedback between electron captures and nuclear burning. The resulting core collapse leads to the formation of a proto-neutron star, while the outward energy release becomes visible as a relatively weak type II SN explosion. (For more information, see Takahashi et al., 2013, and references therein.)

2.4.3. Supernovae and Earth

Supernova observations and danger

Hundreds of new SNe are found every year by scanning galaxies for newly occurring light sources. SN explosions emit enough light to be seen over billions of light-years for weeks. Even after several weeks, when light emission of the ejecta has declined, their light curves are still powered by radioactive decay of ^{56}Ni and ^{56}Co. The total energy released in a CCSN is on the order of 10^{53} erg, about 99% of which is released as neutrinos. Considering this high amount of energy, the question of the danger of a nearby SN to humanity often arises. A possible mechanism by which a nearby SN could harm life on Earth is by exerting damage to Earth's ozone layer. This was first suggested by Ruderman (1974) and taken up later by Ellis and Schramm (1995). Ellis and Schramm (1995) calculated that a 95% removal of the O_3 layer over 300 yr would be possible for a SN event at $d = 10$ pc, exposing life on Earth to deadly amounts of ultraviolet solar radiation. In a more recent study, Gehrels et al. (2003) estimate the maximum distance for mass extinctions due to ozone layer depletion to be $d \leq 8$ pc, and the SN rate within this radius to be one per 1.5 Ga. Although SN explosions are currently not believed to be the main cause for large extinction events on Earth, it cannot be excluded that at least some such events were

actually caused by SNe.

Recent SN activity and Local Bubble

Our solar system is located on the Orion Arm of the Milky Way Galaxy, within a cavity of hot, low-density gas at least 100 pc across, the local bubble (LB). Smith and Cox (2001) suggested that the LB was excavated by a series of SN explosions several Ma ago. By back-tracing stellar trajectories, Benítez et al. (2002) concluded that this could have been caused by stars from the association Scorpius-Centaurus (Sco-Cen), specifically its sub-groups Upper Centaurus Lupus (UCL), Lower Centaurus Crux (LCC), and Upper Scorpius (US) which could have come closer than 100 pc to out solar system in the past. Benítez et al. (2002) and Berghöfer and Breitschwedt (2002) already suspected that this might be the source of the ^{60}Fe signal observed by Knie et al. (1999). Later, Fuchs et al. (2006) estimated that the most likely scenario is an excavation of the local bubble by 14-20 SN which lead to the formation of the LB about 14.5 Ma ago (Breitschwerdt et al., 2009). In a recent study by Breitschwerdt et al. (2012) ISM simulations of the LB showed that SN in the UCL and LCC formations agree well with observations of the LB, with the last SN having exploded 2.2 Ma ago at a distance of ~ 85 pc to Earth.

In a different approach, Kachelriess et al. (2015) analyzed the composition and energy spectrum of cosmic rays, concluding that these are compatible with a single nearby SN explosion ~ 2 Ma ago. Unfortunately, the search for neutron stars left behind by the SN (or SNe) responsible for the signal observed by Knie et al. (2004) has been unsuccessful as of yet (Neuhäuser et al., 2011).

2.5. Supernova searches with ^{60}Fe

2.5.1. AMS isotope selection - why ^{60}Fe?

It was first considered by Korschinek et al. (1996) and later by Ellis et al. (1996) that it could be possible to detect SN ejecta on Earth in the form of isotopic anomalies. Searching for the signature of material deposited into solar system reservoirs by SNe is not an easy task. The only candidate isotopes are those which fulfill the following criteria:

1. Their half-life must be short enough not to be primordial ($T_{1/2} \lesssim 10^8$ a), i.e. the isotope must not still be present from the formation of the solar system.
2. Their half-life must be long enough to still be present in detectable amounts over a geological timescale ($T_{1/2} \gtrsim 10^5$ a).
3. It must be present in sufficient amounts in SN debris (i.e. sufficiently high production and ejection yield)
4. A detection technique must exist allowing for the detection at the required sensitivity.
5. Background sources must be either negligible, or low but very well known.

This limits the choice of candidate isotopes to a short list. With respect to requirement (5), two mass regions are of particular interest: firstly, the region around mass 60, since these isotopes are too heavy to be produced in copious amounts by cosmic rays, but still too light to be produced by nuclear fission. Secondly, very heavy isotopes ($A \gtrsim 240$) can also be expected to be practically background free, since only small anthropogenic contaminations by atomic bombs and nuclear fission and reprocessing plants is expected. Now taking requirement (3) into account, the lower mass region is favored for SN searches, since the abundance of very heavy isotopes is generally several orders of magnitude lower. Concerning requirements (1) and (2), the choice of isotopes with suitable half-lives is limited. An overview of all isotopes with 10^4 a $\leq T_{1/2} \leq 10^9$ a can be seen in Fig. (2.6).

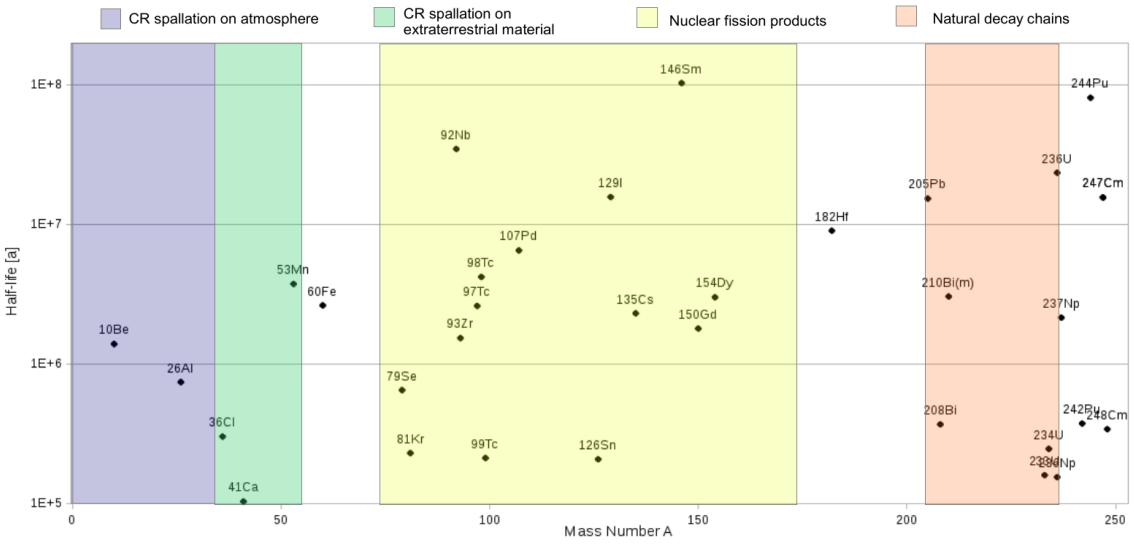

Figure 2.6: The figure shows all known isotopes with half-lives in the range 10^5 a $\leq T_{1/2} \leq 10^9$ a. The colored boxes indicate regions where significant background sources can be expected in AMS measurements of terrestrial samples. CR = Cosmic ray. (m) indicates a long-lived isomeric state.

The most favorable candidate isotopes are ^{60}Fe, ^{182}Hf, ^{244}Pu, and ^{247}Cm. Unfortunately, ^{182}Hf has proven to be very difficult to measure with AMS (Vockenhuber et al., 2007). In the case of ^{244}Pu, AMS measurements are less challenging due to the lack of a stable isobar. In a recent study by Wallner et al. (2015b), the amount of ^{244}Pu detected was 1-2 orders magnitude lower than predicted by nucleosynthesis models, which might hint to the rarity of actinide nucleosynthesis and perhaps to an origin from other scenarios such as neutron star mergers.

As can be seen in Fig. (2.6), other long-lived AMS isotopes like ^{26}Al and ^{53}Mn have the problem of cosmogenic background, i.e. significant production of these isotopes by cosmic rays. Whether or not the SN signal of one of these isotopes could be detectable on Earth depends on the signal strength relative to cosmogenic background.

Considering all of the above arguments, ^{60}Fe is the best suited isotopes for SN searches in terrestrial reservoirs, such as ice cores, sediments, and ocean crusts. Over the last

decades, there have been a number of efforts aiming at the detection of live ^{60}Fe atoms in solar system reservoirs, including a search in Pacific Ocean ferromanganese crusts, which will be discussed briefly in the following section.

2.5.2. Ferromanganese crusts

Ferromanganese crusts are geological formations of mainly Fe and Mn oxides. These crusts form over a substrate rock in ocean depths of several thousand meters, at places where normal sedimentation is prevented by strong bottom currents. Especially hydrogenetic crusts, whose composition is dictated by the above water, represent an interesting geological reservoir for radioisotope analysis. These slow growing (< 10 mm/Ma) crusts are typically several cm thick and thus cover several Ma of geological history.

The first ^{60}Fe analysis of a ferromanganese crust from Mona Pihoa in the South Pacific (Knie et al., 1999) revealed an unexpectedly high concentration of ^{60}Fe/Fe in the top layer ($0 - 2.8$ Ma), which hinted to the deposition of extraterrestrial material, despite poor time resolution. Measurements with better time resolution of another ferromanganese crust from the Pacific Ocean followed (Knie et al., 2004) and confirmed the ^{60}Fe signature. Originally, the layers containing the signal were thought to correspond to an age of approximately 2.8 Ma. However, after advanced ^{10}Be dating, the signal has later been re-evaluated to lie in the range $1.7 - 2.6$ Ma (Fitoussi et al., 2008). This signal was later confirmed by using a chemical leaching technique instead of complete dissolution (Fitoussi et al., 2008). A summary of both measurements can be seen in Fig. (2.7). This finding was attributed to the deposition of SN ejecta.

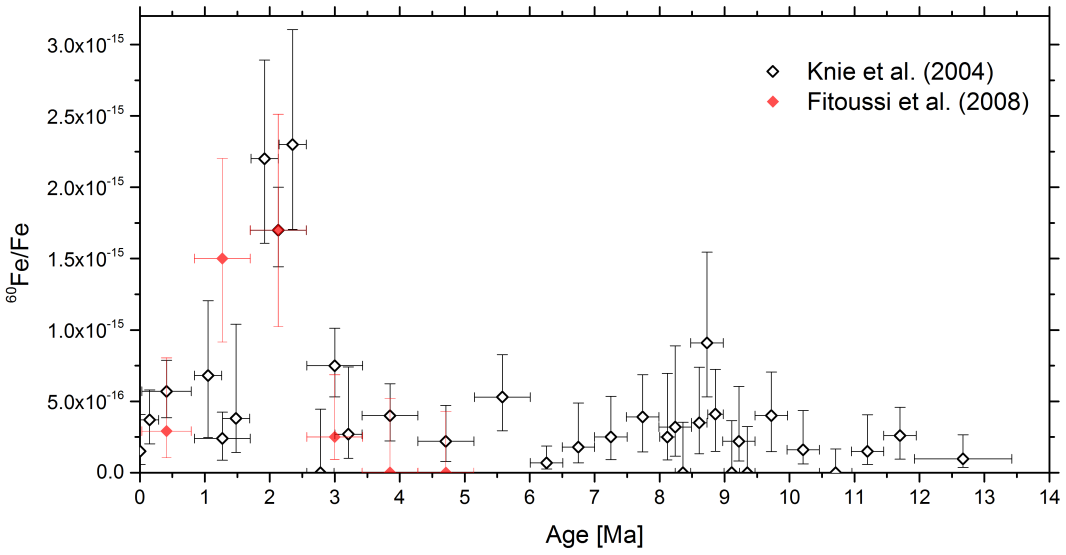

Figure 2.7: ^{60}Fe/Fe ratio plotted over sample age in the ferromanganese crust 237KD. Data from both Knie et al. (2004) and Fitoussi et al. (2008) are displayed.

Two key questions about the ^{60}Fe signal remained. The first question concerns the exact

time structure of the signal, which could not be analyzed in the ferromanganese crust due to the difficulty in sampling very thin layers (< 1 mm). The second question concerns the local interstellar fluence Φ_{LIF}, which is the number of ^{60}Fe atoms originally traveling through the interstellar medium at the time of deposition per cm^2. Crust measurements provide only indirect estimates of Φ_{LIF}, because an uptake factor, defined as the fraction of atmospheric ^{60}Fe flux that is actually incorporated into the crust, needs to be taken into account.

Both questions can be addressed by extending the search to other reservoirs. While the local interstellar fluence is best determined in lunar samples, where the uptake factor can be expected to be 100%, the time structure of the ^{60}Fe signal requires a reservoir of sufficiently large accumulation rate, such as marine sediments on Earth.

2.5.3. Earlier sediment measurements

After the discovery of the ^{60}Fe signal in the ferromanganese crust, a search in North Atlantic sediments was performed by Fitoussi et al. (2008). Fe was extracted from the sediment using a strong chemical leaching technique (hydroxylamine). This technique was also applied to the same ferromanganese crust analyzed by Knie et al. (2004) where similar concentrations of ^{60}Fe as in the original measurements were found. ^{60}Fe/Fe concentrations measured in the leached Atlantic sediment are shown in Fig. (2.8a).

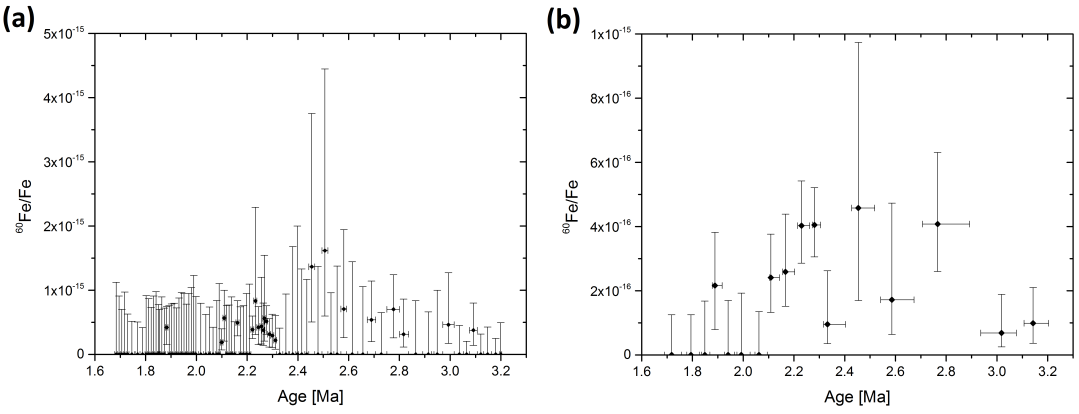

Figure 2.8: ^{60}Fe/Fe concentrations measured by Fitoussi et al. (2008) in a North Atlantic sediment core. (a) individual samples. (b) 5 adjacent samples grouped together and weighed by collected statistics.

Fitoussi et al. (2008) concluded that their measurements did not match the ^{60}Fe signature which in the ferromanganese crust. Possible reasons for this discrepancy are: (1) a lower initial deposition of ^{60}Fe in the North Atlantic, (2) signal dilution by detrital inputs, and (3) excessive chemical leaching of minerals containing only terrestrial Fe. Their result does, however, show a slight ^{60}Fe enhancement in the range $1.9 - 3.0$ Ma, which becomes more obvious when grouping 5 samples each to one data point as shown in Fig. (2.8b).

This was a first hint that if this was actually the same signature as observed by Knie et al. (2004), it could be a long exposure (∼1 Ma) rather than a sharp peak.

2.6. Transport of SN material to Earth

After the discovery of the ^{60}Fe anomaly in a ferromanganese crust by Knie et al. (1999) and later in another crust (Knie et al., 2004), there was a great need for a theoretical basis for transport and deposition of SN material into geological reservoirs here on Earth. Still today, the path of SN ejecta containing ^{60}Fe from ejection to final deposition on Earth is a field of active research and not completely understood. A promising candidate for successful transport of SN material containing ^{60}Fe are dust grains formed after the SN explosion.

2.6.1. Dust formation

Cosmic dust consists of solid grains of various chemical composition, such as carbon, metal oxides, silicates, metals, and other compounds, with grain sizes (diameters) from few nm to 100 μm. Cosmic dust can be sub-divided into several components, including IDPs, originating from inside our solar system (mostly from the asteroid belt between Mars and Jupiter), interstellar dust (ISD) from stellar sources within our galaxy, and intergalactic dust.

Focusing on nearby, recent SN events, the ISD component has to be examined. Sources of ISD include AGB stars, supergiants, Wolf-Rayet stars, Novae, and SNe. Dust production in SN explosions was already suggested by Hoyle and Wickramasinghe (1970) and was confirmed later by observations of SN remnants (SNRs) (for an overview on the topic, see Gomez, 2013, and references therein). Dust can be observed, for example by examining infrared (IR) emissions using telescopes such as Spitzer (Rho et al., 2008). Additionally, dust particles can be analyzed by space probes such as Ulysses and Galileo (see e.g. Landgraf et al., 1999).

The formation of dust grains in SN ejecta is not completely understood and is being approached by a combination of theoretical modeling, observation (observing SNRs over time), and laboratory experiments (simulating conditions of synthesis). In general, dust synthesis is a two step process, which first forms molecular clusters in chemical reactions which then condense to larger particles by surface deposition and coagulation (see e.g. Woolridge, 1998). Typical grain sizes after formation depend on the initial conditions (density, temperature, initial abundances), but are typically in the grain size range of few nm to few μm.

During the initial expansion phase of the remnant (several 100 a), it sweeps up the ISM until the mass is large enough to form a reverse shock wave. It may slow down, reduce in size, or even destroy dust particles. Nozawa et al. (2007) calculate that only dust particles

initially larger than ~ 0.2 μm survive practically unaltered, while smaller particles suffer erosion or destruction. Recent observations of the SNR SN 2010jl by Gall et al. (2014) even reveal that a typical grain size of 2 μm in the ejecta of this SN is realistic, with a maximum of 8.4 μm (Gomez, 2014). Furthermore, Gall et al. (2014) state that about 80% of the dust mass fraction is in grains > 0.2 μm, most of which will finally be deposited in the ISM.

This sounds very promising, since only little mass would be lost by grain destruction in the reverse shock. The question remains, however, what fraction of the SN ejecta finally escapes into the ISM as dust. The total amount of dust ejected in a single SN event is only poorly constrained by observation and modeling, and depends on the initial mass of the star. Typical dust ejection masses are likely in the range of $0.1 M_\odot - 1\ M_\odot$ (Gomez, 2013). Although this seems little compared to the total mass ejected in a SN explosion, especially for very massive stars, it has to be taken into account that most observations were made of fairly young (< 100 a) SN remnants, in which dust formation is not yet complete. Additionally, dust formation efficiency is different for various elements. Gomez (2013) come to the conclusion that most mass in the form of metals (including Fe) is in fact ejected in the form of dust by comparing the observed dust masses for different SNe with predicted metal ejecta masses.

2.6.2. SN material entering the solar system

The ability of a SNR to penetrate into the solar system had hardly been discussed before Korschinek et al. (1996) and Ellis et al. (1996) suggested the possibility of deposition of SN material on Earth. However, they only performed a rough estimation and no consistent picture of a penetration mechanism was available. After the ^{60}Fe anomaly was discovered by Knie et al. (1999), more research was sparked.

Fields et al. (2008) performed numerical hydrodynamical simulations of SNRs colliding with the solar wind. They found that, in order to push the Heliopause back to a distance of 1 AU from the sun, a SN explosion would have to occur within 10 pc of Earth, which is very close to a 'kill-radius' of roughly 8 pc (Gehrels et al., 2003). This result lead to the conclusion that the SN shockwave, in the form of a uniform plasma, pushing back the heliosphere is unlikely to explain the signature observed by Knie et al. (2004) and Fitoussi et al. (2008), due to the lack of severe extinction events in the time range $1.7 - 2.6$ Ma.

Another way for SN ejecta to enter the solar system is in the form of dust particles. This was already suggested along with the initial ^{60}Fe signal observation in the first ferromanganese crust by Knie et al. (1999). Athanassiadou and Fields (2011) examined the decoupling of dust grains from the bulk SN plasma when encountering the solar wind. In order to do this, they assumed dust grains with sizes between 0.1 μm and 0.7 μm with a density of 2.5 g/cm^3. They varied incident velocities and surface charges of the particles to calculate possible trajectories inside the solar system. They find that dust

grains can enter the solar system with typical deflection angles few degrees, mainly due to their charge. This leads to the conclusion that SN dust can indeed reach the Earth's orbit and be deposited onto the atmosphere if the grain size is > 0.1 μm.

2.7. From atmosphere to sediment

This section will give an overview of the highly complex system of transport mechanisms responsible for cycling of elements on Earth, with a focus on Fe, omitting fractionation effects. The iron cycle is responsible for the transport of iron (also ^{60}Fe) between reservoirs. Beginning with the input of extraterrestrial material into the atmosphere and the formation of radioisotopes by cosmic ray spallation (which can be neglected for ^{60}Fe), the journey of dust particles takes them through the atmosphere and its wind circulation patterns. After deposition onto the ocean through the complex mechanisms of iron chemistry in ocean water. Stable iron is added to the water through dust transport, rivers, and glaciers. After transport to the deep ocean, Fe can be incorporated into sediments. These processes are illustrated in Fig. (2.9).

2.7.1. Atmosphere

The Earth's atmosphere is continuously being bombarded by meteorites from space, mostly small dust grains but also larger objects. Most mass influx originates from IDPs with a typical size of 100 μm (Murad and Williams, 2002). When meteorites (or in our case, SN-produced dust particles) enter the atmosphere, critical parameters, controlling their trajectory, are the particles' the size, composition, incident angle, and velocity. Friction in the atmosphere causes the particles to heat up and thus also radiate heat. Mass loss can occur due to surface sputtering. If the particle gets hot enough to melt, thermal ablation has to be taken into account. Calculating whether or not a particle of a certain size and composition reaches the surface, and how much mass it loses is difficult since it involves many parameters. In simulations, most authors focus on atmospheric entry scenarios for IDPs, resulting in low initial velocities of $20 - 70$ km/s, which are typically considered (Vondrak et al., 2008; Briani et al., 2013). In the case of SN dust particles, velocities can be different. If the remnant has slowed down considerably, velocities might be comparable to IDP, if not, it is sensible to consider velocities of up to one order of magnitude higher, as e.g. in Athanassiadou and Fields (2011).

The deceleration of a meteorite in the atmosphere (neglecting gravity) is given by

$$\frac{\mathrm{d}v}{\mathrm{d}t} = -\frac{\Gamma \rho_\mathrm{a} \pi R^2 v^2}{m} \tag{2.2}$$

where Γ is the drag parameter (typically between 0.5 and 1), ρ_a is the atmospheric density, and R, v, and m are radius, velocity, and mass of the particle, respectively (Plane, 2012). Since all variables on the right hand side of Eq.(2.2) are time dependent, calculation of the

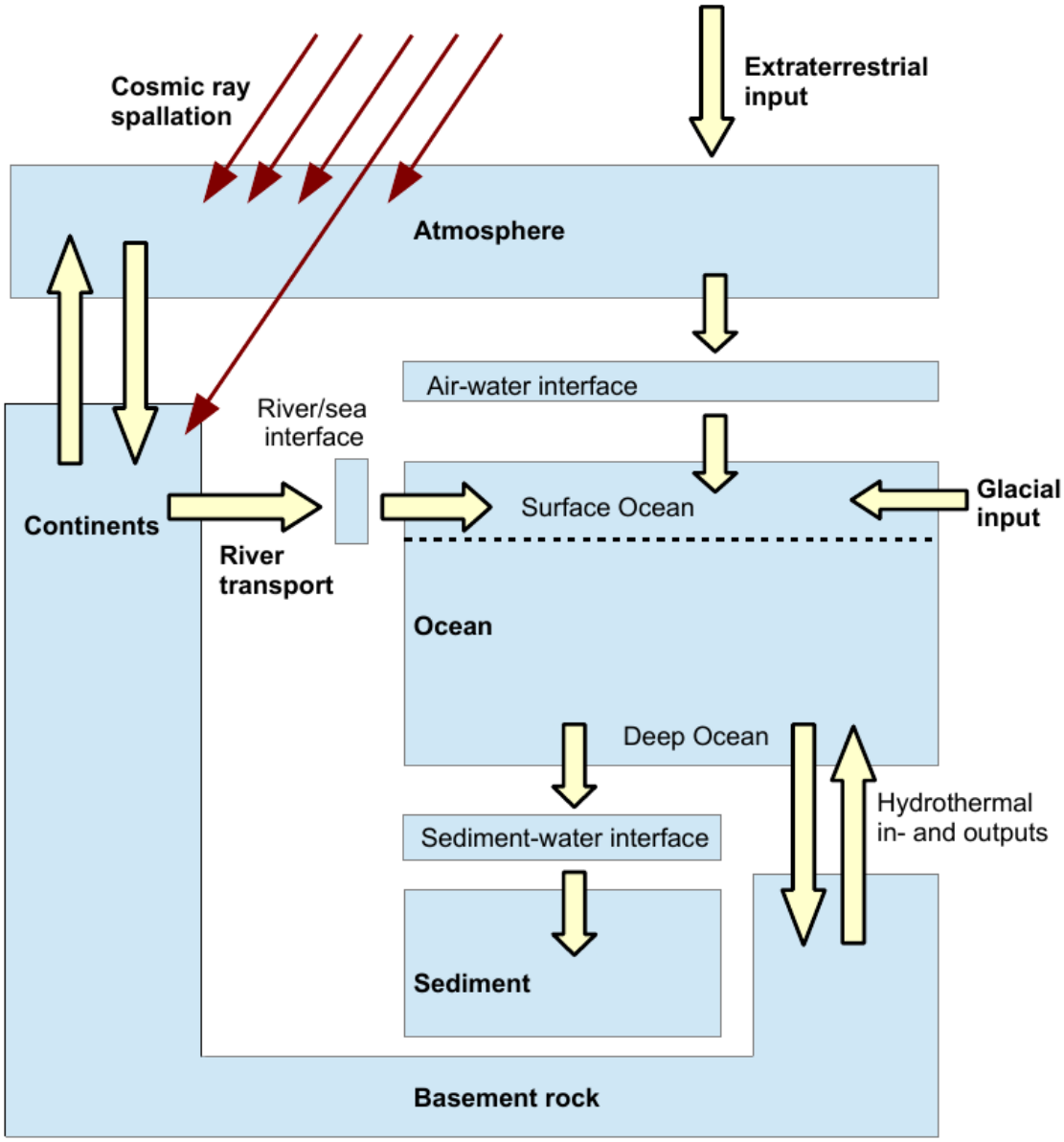

Figure 2.9: Schematic representation of transport processes and reservoirs involved in transport of material on Earth. Formation of isotopes by cosmic ray spallation is indicated by red arrows (less important on continents due to atmospheric shielding). Yellow arrows indicate transport processes, lengths are arbitrary.

particle trajectory is complex and requires numerical treatment. For a very rough estimate of the deceleration process, numerical integration of Eq. (2.2) for typical parameters of $\Gamma = 0.7$, density $\rho_m = 2.5$ g/cm^3, $2R = 0.1 - 10$ μm, and $v = 50 - 200$ km/s, and ignoring mass loss, the particles decelerate to $v < 5$ km/s after reaching a height of $80 - 120$ km above sea level and gravitational attraction takes over. However, in reality, the picture is a lot more complicated when taking into account a realistic atmospheric density profile, chemical composition of both atmosphere and meteoroid, shape of the meteoroid, and incident angle.

Another critical issue is the mass loss of the particle. Friction with the atmosphere will cause the particle to heat up and radiate. For the 0.1 μm$-$10 μm particles considered here, radiation according to Stefan-Boltzmann's law (proportional to R^2) prevents the particle from heating up quickly (proportional to R^3). This implies that very small particles might not be able to reach a temperature high enough to melt (depends on composition, typically 2000 K). This is a critical point, since both mass loss by non-thermal sputtering below the melting temperature and mass loss by thermal ablation above the melting temperature can occur. Vondrak et al. (2008) used a numerical code to calculate that mass loss by sputtering can reduce masses of light, fast meteoroids significantly (e.g. 40% for $v = 70$ km/s and $R < 4$ μm). Even though calculations by Rogers et al. (2005) were limited to larger particles, they predict complete mass loss for their smallest, fastest particles ($v = 71$ km/s and $R \approx 4$ μm), mostly by sputtering.

In order to obtain data for fast, small dust particles, a series of calculations were performed using the CAMOD (Chemical Ablation Model) code (Vondrak et al., 2008) specifically for this work (Plane and Sánchez, 2015, private communication). A representative chondritic dust composition similar to olivine (Fe_2SiO_4) and an incident zenith angle of 35° were chosen. The incident velocity was varied between 100 and 190 km/s, and the diameter of dust particles was between 0.15 and 0.40 μm, yielding a total of 60 calculations. The percentage of Fe lost during atmospheric entry was then calculated. A linear interpolation between data points allows for drawing a contour plot, which is shown in Fig. (2.10). The data show that a significant fraction of Fe can only be preserved in the grain for very small grain sizes and low entry velocities. For this work, it follows that it is a good assumption that most ^{60}Fe of SN origin is emitted into the atmosphere and can participate in the iron-cycle.

Loss of Fe is a superposition of non-thermal sputtering, evaporation, and thermal ablation. In the case of iron, mass loss will release mostly neutral Fe atoms, and Fe^+ ions (Plane, 2012). The chemistry of Fe in the mesosphere and upper thermosphere is highly complex and not completely understood due to lack of laboratory measurements of some key reaction rates (Plane, 2012). Woodcock et al. (2006) calculate a typical residence time for Fe of days before sinking below 100 km to only minutes to get below 90 km. Once below 85 km, Fe can be oxidized, typically forming FeO_3, $Fe(OH)_2$, FeOH, and FeOOH. Over several days, small, nm sized particles, referred to as meteoritic smoke particles are formed (Plane, 2012).

If the incident dust grain is not completely destroyed by the atmospheric entry, it will be slowed down until gravitational attraction takes over the equation of motion, transporting the particle downwards over minutes to be picked up by wind patterns.

In summary, it is possible that ^{60}Fe is deposited onto the oceans in the form of fine-grained, nm sized dust grains, as well as larger, μm sized meteoritic remains. They are likely to follow terrestrial aerosols for typical timescales of weeks, allowing for transport over thousands of km (Jickells et al., 2005) before reaching Earth's surface by dry or wet

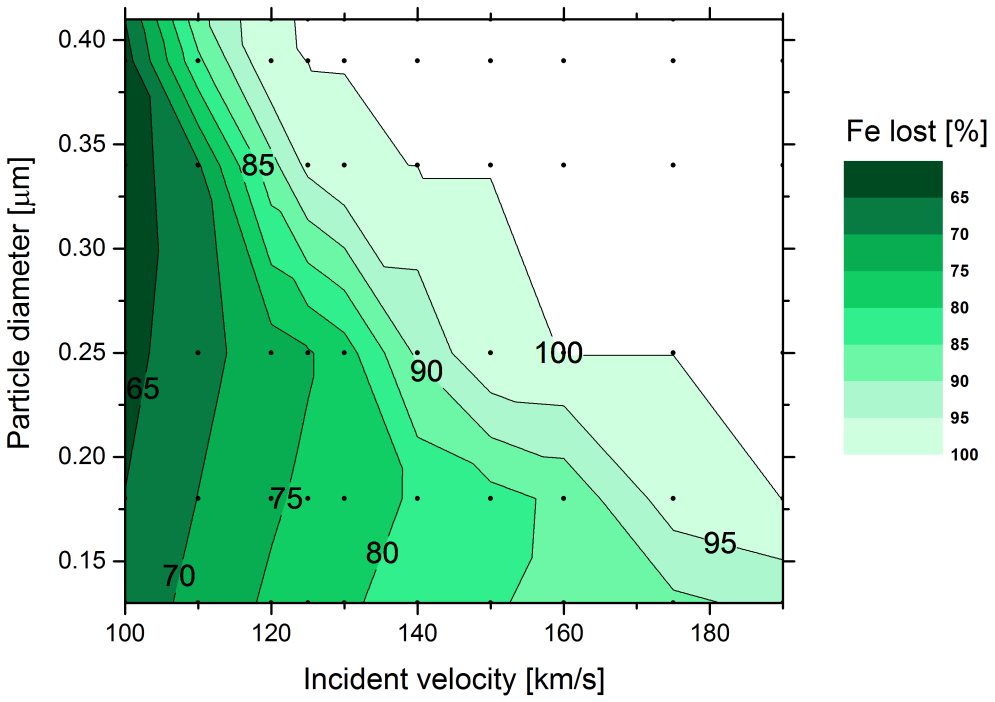

Figure 2.10: Contour plot depicting the fraction of Fe lost during atmospheric entry of dust grains of olivine with a density of 2.5 g/cm^3 and an incident zenith angle of 35^o. Contours obtained by linear interpolation between data points for 10 different velocities and 6 different particle masses. Data points are indicated by black dots.

deposition mechanisms.

2.7.2. Transport to sediment

When the small Fe-bearing grains fall into the ocean, Fe can be released, becoming part of the Fe cycle driven by redox chemistry. Fe has an active redox chemistry in the ocean. Fe typically occurs in the oxidation states +II and +III. Fe(II+) is soluble in water; however, it is rapidly oxidized to Fe(III+) in presence of dissolved oxygen. Fe(III+), on the other hand, precipitates as nanocrystalline oxyhydroxides (FeOOH). Depending on the active surface of the incoming Fe bearing particles (nm to μm), and their composition, Fe can be processed in different ways. Since Fe is one of the key nutrients in the oceans, along with other elements like N, P, and S: therefore living organisms actively participate and even drive the Fe cycle in the water and the underlying sediment (Zachara et al., 2002; Sarmineto and Gruber, 2006). If readily available, Fe is quickly consumed by photyplankton, thereby entering the nutrient chain, from which it is finally released within organic waste. In general, Fe, has a short residence time in the ocean of about 200 years before reaching the ocean floor. The main reason for this is the rapid Fe scavenging, which

ensures that only a negligible Fe fraction remains freely suspended in the water column (Chester and Jickells, 2012).

2.7.3. Sediment and Fe cycle

The ocean floor accumulates any material with sufficient density to sink and which does not dissolve easily. These deposits contain inorganic materials from dust, detrital inputs, and chemical precipitates, such as from detrital inputs of nearby land masses or inorganic precipitates, as well as organic products, such as waste material and skeletal remains. In a sediment with high detrital input and lack of nutrients, such as in the North Atlantic site analyzed by Fitoussi et al. (2008), the sediment will mostly preserve incoming particles, which will simply be buried under the next layer of sediment. On the other hand, organic processing in the top layers of sediments with low detrital input and a moderate nutrient content, such as at the Equatorial Pacific site examined in this work (see next chapter), is a very important factor for Fe mobilization. In this case, nutrients are sufficiently concentrated to sustain a variety of microorganisms (bacteria) and higher organisms to survive even at these extreme depths and without sunlight.

Microorganisms in the sediment gain energy by processing organic matter. In the surface layers (oxic zone), this is done efficiently by aerobic bacteria, which oxidize organic matter with O_2. In regions of high bioactivity, oxygen can be depleted below a certain depth in the sediment, since diffusion from the sediment-water interface is the only source of oxygen. Under anoxic conditions, anaerobic bacteria oxidize organic matter with other electron acceptors instead of oxygen, such as nitrates (nitrate reduction) and sulphate (sulphate reduction) (Fig. (2.11)). Between the nitrate and the sulphate reduction zones, so-called metal-reducing bacteria use Fe(III)-bearing minerals as electron acceptors, thereby reducing Fe(III) to Fe(II) and forming new Fe minerals (Zachara et al., 2002). Preferential Fe(III) sources are Fe oxyhydroxide nanoparticles, such as ferrihydrite and goethite, due to the large surface area and poor crystallinity (Zachara et al., 1998). Reduction products include the magnetic iron oxide magnetite (Fe_3O_4), which contains Fe(III) and Fe(II) cations (Lovley et al., 1987; Fortin and Langley, 2005). Fe reaction products can accumulate outside the cell, such as with most dissimilatory reducing bacteria, or intracellularly, as in magnetotactic bacteria.

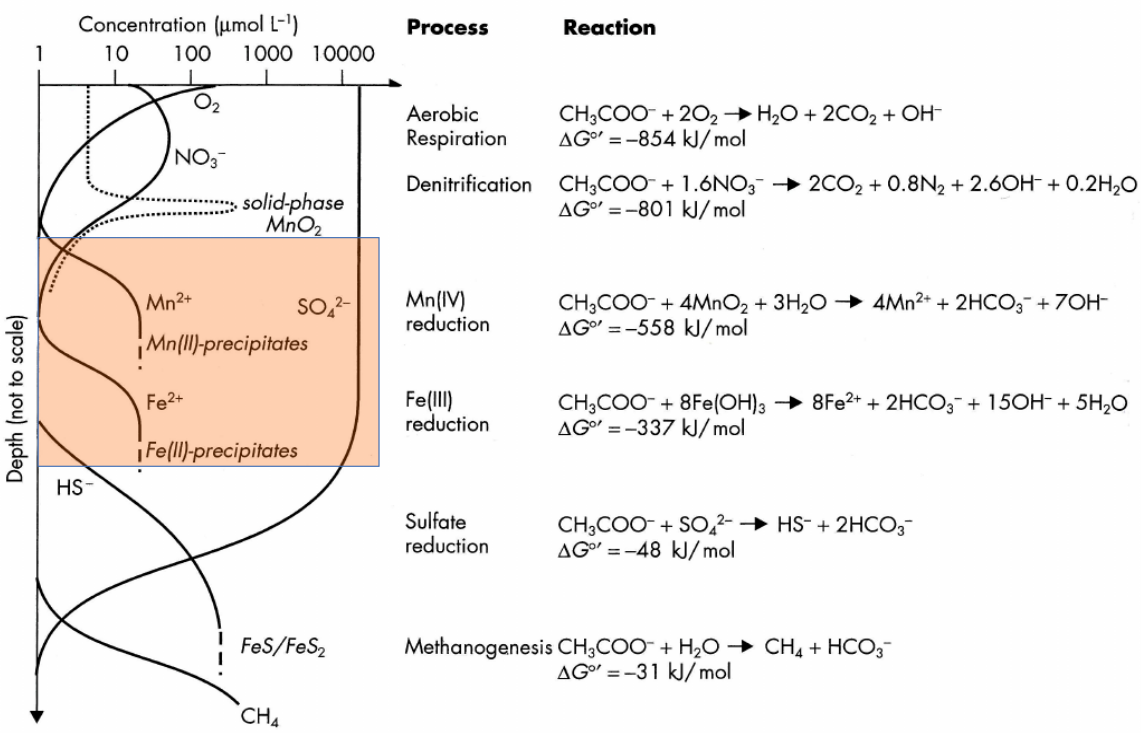

Figure 2.11: Typical reactions in different layers of marine sediments formed by biostratification. Orange area indicates the regime of magnetite-producing magnetotactic bacteria. Figure adapted from Konhauser (2007).

2.8. Magnetotactic bacteria

A special focus of this work is dedicated to ^{60}Fe incorporation into magnetite crystals produced by magnetotactic bacteria (MTB). MTB were accidentally discovered in the 1960s by S. Bellini, who noticed some bacteria swimming out of a mud sample along a direction determined by the magnetic field of a permanent magnet (Bellini, 2009b,a) and suspected that these bacteria had some sort if internal magnetic compass. Blakermore (1975) discovered MTB independently and showed that this compass consisted of a chain of magnetite crystals he called *magnetosomes*. The MTB's unique ability to move along magnetic field lines was called *magnetotaxis*, in analogy with *chemotaxis*, i.e. the ability to move along chemical gradients. MTB usually live inside the uppermost 10 cm of freshwater and marine sediment, at or below the so-called oxic-anoxic transition zone (OATZ), where dissolved oxygen drops to $< 1\%$ (Petermann and Bleil, 1993; Blakermore, 1982; Pan et al., 2005).

2.8.1. Magnetosomes

MTB can produce magnetosomes made of magnetite (Fe_3O_4) (Frankel et al., 1979) or greigite (Fe_3S_4) (Heywood et al., 1990). Usually, greigite-producing species are found in deeper layers where sulfide concentrations are higher. In this work, the focus is on

magnetite-producing species.

Magnetosomes are stoichiometric, defect-free nanocrystals with a length of $20-200$ nm and a width to length ratio between 0.2 and 1. The crystal shape is species-dependent; common morphologies include cubo-octahedra, prisms, and tooth-, arrowhead-, and bullet-shapes. (e.g. Spring and Bazylinski, 2006). In most species of MTB, magnetosomes are arranged in one or more parallel chains (Lefevre et al., 2011) or chain bundles (Hanzlik et al., 2002). Examples of different magnetosome chain types are shown in Fig. (2.12). In most cases, magnetosomes are surrounded by the so-called magnetosome membrane, which is thought to control the size and shape of the crystals (Tanaka et al., 2006; Schumann et al., 2008).

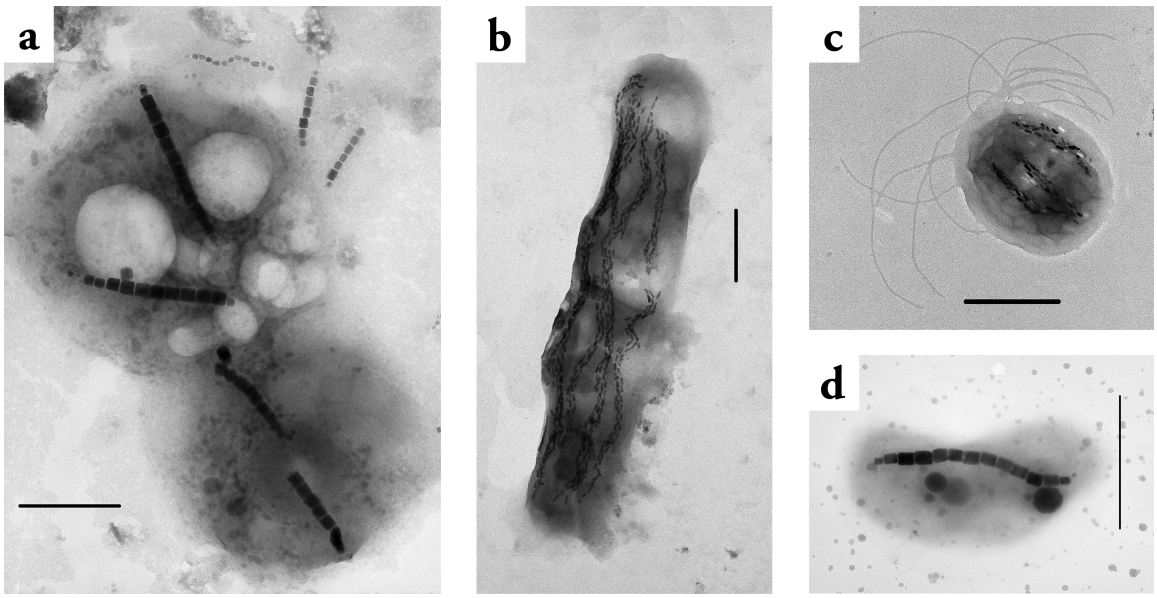

Figure 2.12: TEM images of wild-type MTB found in sediment from lake Chiemsee and a small pond. Scale bars are 1 μm. (a) Two coi containing two chains of prismatic magnetosomes each. (b) *M. bavaricum*, containing five chain bundles of tooth-shaped magnetosomes. Chain bundles are heavily distorted by drying artifacts. (c) 'Ovoid' coccus containing three chain bundles of tooth-shaped magnetosomes. (d) Vibrio containing a single chain of prismatic magnetosomes. Picture taken from Mao et al. (2014b).

2.8.2. Magnetotaxis

In order for magnetotaxis to work efficiently, magnetosome chains must maximize the total magnetic moment. This can be achieved when magnetosomes are small enough to contain a single magnetic domain, but large enough, so that their magnetization is not randomized by thermal activations. In case of magnetite and greigite, the range of sizes that satisfy this condition is much smaller than the usual range of inorganically precipitated particles, and, in case of magnetite, is comprised between $\sim$20 nm and $\sim$100 nm (Fig. (2.13a)).

With individual magnetosome crystals being ferrimagnetic single domain (SD) particles, the magnetic moment of the entire chain is given as the sum of its constituents, and acts as a microscopic compass needle (Fig. (2.13b)). MTB become passively aligned with Earth's magnetic field through the force exerted by the chain's magnetic moment and can propel themselves in water by flagellar rotation (Yan et al., 2012). Due to the inclination of Earth's magnetic field, the movement along its field lines can be used by MTB for searching for optimal living conditions. In nature, the movement of MTB should not be imagined as a straight line, but rather as a slightly biased random walk (Mao et al., 2014a,b). Mao et al. (2014b) showed that even an average 1% alignment (where 100% would correspond to a permanent parallel alignment) with Earth's magnetic field is sufficient for the species *M. Bavaricum* to migrate between different sediment layers, depending on redox conditions and nutrient requirements, or just to return to the OATZ after sediment disturbance by bioturbation.

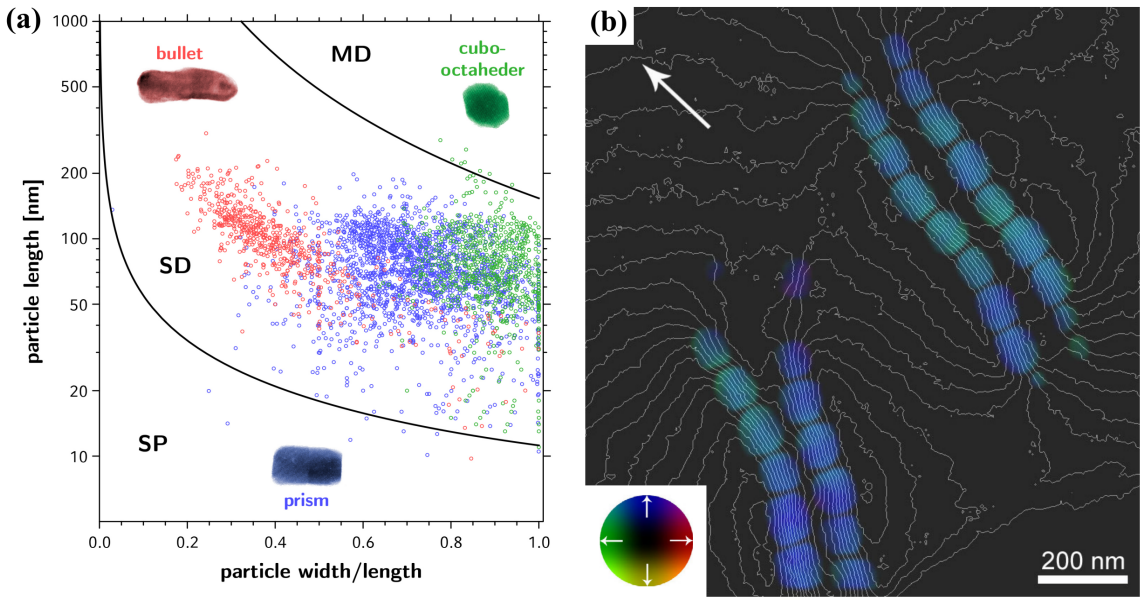

Figure 2.13: (a) Domain state diagram for different particle shapes and sizes. SD: Single Domain, MD: Multi Domain, SP: Superparamagnetic. SP-SD separation line corresponds to chains of 6 crystals with a spacing of 0.6 times their length between crystals. SD-MD line corresponds to a chain of 3 crystals. Data from about 1000 observations of bacterial magnetosomes. Courtesy of R. Egli, see also: Newell (2009, and references therein). (b) Magnetic phase contours measured using electron holography from two pairs of bacterial magnetite chains at 293 K, after magnetizing the sample parallel and antiparallel to the direction of the white arrow. Colours indicate show the direction of the magnetic induction (see color wheel on bottom left). The contour spacing is 0.25 radians. Figure taken from Simpson et al. (2005).

2.8.3. Magnetofossils and ^{60}Fe

As discussed in the previous section, MTB maintain themselves at a optimal depth below the sediment-water interface, so that the whole population slowly moves up as new sediment is deposited. Dead MTB cells, on the other hand, are left behind and are dissolved, leaving the magnetosome chain as the only fossil reminder. Such reminders, in form of intact or collapsed magnetosome chains, are called *magnetofossils*(Kopp and Kirschvink, 2008). Magnetofossils, along with any type of magnetite particles with similar size, can be preserved indefinitely in sediment, provided that the initial organic matter concentration is not large enough to support sulphate reduction (Fig. (2.11)), in which case sulphide ions promote the dissolution of small magnetite crystals and precipitation of greigite (Fe_3S_4) or pyrite (FeS). This process, known as reductive diagenesis (Canfield and Berner, 1987; Canfield et al., 1992), involves the reduction of a wide range of Fe minerals with a massive iron mobilization through up to several meters down the sedimentary column (Fu et al., 2008; Rowan et al., 2009). Early studies on reductive diagenesis of ultrafine ($\lesssim 100$ nm) magnetite particles (Leslie et al., 1990) suggested that magnetofossils would generally not be preserved over geological times. The development of adequate techniques for magnetofossil detection (Egli, 2004a; Egli et al., 2010), however, led to the discovery that magnetofossils occur in a wide range of sediment types and ages, and are therefore commonly preserved over geological times (Roberts et al., 2012).

Since MTB represent a source of secondary magnetite particles, any biologically available ^{60}Fe present at the time of magnetosome formation would also have been processed to form magnetosomes, thus preserving a possible SN signature $2-3$ Ma ago (Bishop and Egli, 2011) in the microfossil record of our planet. Although magnetofossils are not the only source of secondary Fe in sediment, they represent a well defined ^{60}Fe source that can be selectively retrieved by magnetic or chemical extraction. Furthermore, searching for ^{60}Fe in a magnetofossil bearing sediment ensures two essential conditions for positive results, namely that (1) sediment composition is not dominated by primary minerals from detrital inputs, which excessively dilute ^{60}Fe, and (2) reductive diagenesis with related iron mobilization did not occur, so that the temporal sequence of a possible event is correctly maintained. For this reason, the magnetofossil signature has been used to identify an appropriate sediment core location. In this framework magnetic detection methods have been refined in order to obtain quantitative estimates to be compared with the whole secondary Fe pool.

3. Sediment and AMS sample production

The primary sample material for this work comes from two marine sediment cores from the Eastern Equatorial Pacific. In this chapter, the path from the original sample material to AMS samples is outlined. This requires first a description of the sediment, followed by a discussion of Fe extraction techniques yielding Fe_2O_3 samples for AMS measurements of ^{60}Fe.

3.1. Sediment samples

3.1.1. ODP Leg 138

The sample materials chosen for this study are sediments from two drilling sites (848 and 851) from the Eastern Equatorial Pacific, sampled by the Ocean Drilling Program (ODP) during Leg 138 (Mayer et al., 1992). The expedition of ODP Leg 138 set out on the drill ship *JOIDES Resolution* from Balboa, Panama on May 5th, 1991, to drill several sites along two north-south transects centered at 95°W and 110°W. The goal of Leg 138 was to study the paleoceanography of the equatorial Pacific of the late Neogene. This required continuous, high-resolution sampling. Since it was not possible to drill a single core per site, which includes the entire depth of interest, all 11 sites of Leg 138 were cored multiply, with overlapping core segments. A map of the drill sites, including ocean current patterns, is displayed in Fig. (3.1).

Sediment samples from both drilling sites, 848 and 851, were used for the ^{60}Fe search in this work. In order to avoid confusion, the following simplified terminology will be used: although the samples from each site are actually composed of different drill cores, for simplicity reasons, all samples from site 848 will be referred to as *core 848*, while all samples from site 851 will be referred to as *core 851*.

3.1.2. Cores 848 and 851

The following summary is based on the detailed reports on drilling cores 848 and 851 by the Shipboard Scientific Party (1992a,b).

The material at both sites can generally be classified as being dominated by foraminifer

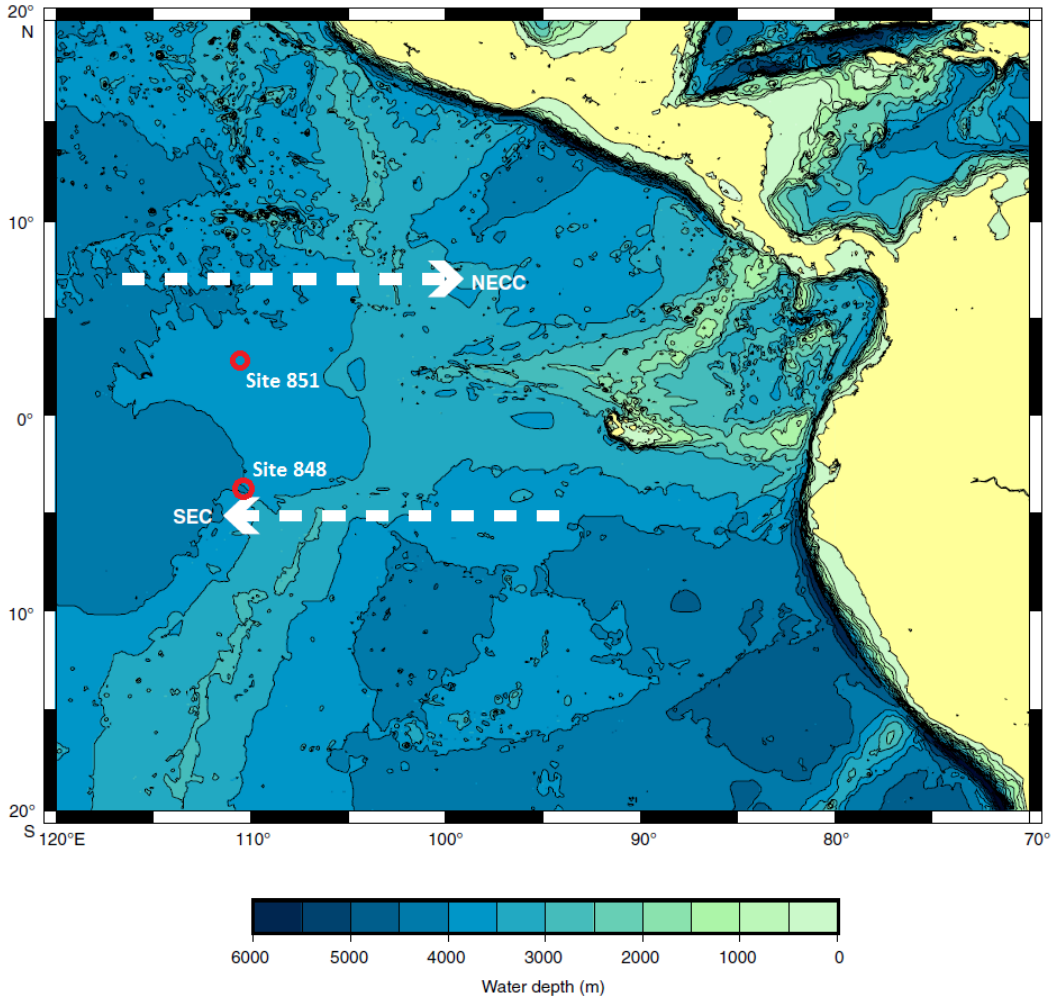

Figure 3.1: The map shows the position of the drilling sites of sites 848 and 851 of ODP Leg 138 and the dominant water flow patterns: NECC=North Equatorial Counter-current, SEC=South Equatorial Current. Map taken from Niitsuma et al. (2006).

nannofossil ooze with a carbonate content typically above 60%. The key difference between the two cores is the higher sedimentation rate of core 851. Both cores are very homogeneous and were sampled continuously (without gaps). Sampling of both cores and preliminary on-board analyses yielded excellent record fidelity. Core 851 even represents one of the best sources for depth-resolved studies ever recovered. An overview of sampling and composition details of both cores is shown in Tab. (3.1.2).

	Core 848	Core 851
Sampling date	June 4-6, 1991	June 16-21, 1991
Number of cores	4	5
Water depth	3850 m	3770 m
General description	nannofossil ooze	nannofossil ooze
Core height recovered	104 mbsf	320 mbsf
Oldest sediment layer	11.2 Ma	12.0 Ma
Avg. sedimentation rate	9.4 m/Ma	30.9 m/Ma

Table 3.1.: Details of sampling, sediment composition, and properties of Cores 848 and 851. mbsf = meters below surface.

3.1.3. Sediment dating

An age model for the cores in required to date the samples. Several tools can be employed to correlate the depth in the sediment (usually given as meters core depth (mcd)) with the age of sedimentation. The most important conditions for a reliable age model are an undisturbed sediment core with a relatively steady sedimentation rate and prominent age markers for magnetostratigraphy and biostratigraphy. Both conditions are met by cores form Leg 138, which represent an ideal reservoir for time-resolved studies. The age model employed in this study is based on Shackleton et al. (1995b).

Magnetostratigraphy

The Earth's magnetic field underwent several polarity reversals in the last 3.5 Ga. During a reversal, the existing dipolar component of the magnetic field disappears and a new dipole field with opposite poles forms withing $0.1-1$ ka. Each time interval with consistent magnetic polarity between two reversals is called a chron, which typically lasts for $1-100$ Ma. The last reversal occurred ~ 0.77 Ma ago (Merrill et al., 2012). The length of individual chrons is consistent with a homogeneous Poisson process (Shcherbakov and Fabian, 2012) and is therefore explainable by a random reversal process in the geodynamo.

The direction, and sometimes also the intensity, of the Earth's magnetic field are recorded in rocks and sediments, which represent the only source of information about its variations over geological times. The recording process in sediments relies on the mechanical alignment of magnetic particles during and shortly after deposition. Unlike volcanic

rocks, which provide snapshots of the Earth's magnetic field at the time of eruption, sediments provide a continuous, albeit smoothed record of field variations (Tauxe, 1993; Tenaby and Gubbins, 2000; Roberts et al., 2013).

Using these field reversals, a time scale for the geomagnetic polarity could be established already in the 1960s (Cox et al., 1963) and was improved over time (Berggren et al., 1985). By using this dating method, a crude time scale can already be established during shipboard analysis during the expedition. Combination of the 11 drill sites of Leg 138 yields a complete coverage of polarity transitions over the last 13 Ma.

Biostratigraphy

Another time scale can be established using biological markers. Over the course of natural evolution, different species of microscopic organisms become dominant and extinguished. Different species can be recognized in sediment layers of different depth as microfossils. The standard markers for biostratigraphy include calceous nannofossils (Okada and Bukry, 1980; Martini, 1971), planktonic foraminifers (Blow, 1967), radiolarians (Sanfilippo et al., 1985; Johnson et al., 1989), and diatoms (Barron, 1985a,b). The resulting age markers are known as biostratigraphic datum levels and can be used to supplement the data from magnetostratigraphy and are summarized in Fig. (3.2). A summary of biostratigraphy for Leg 138 can be found in Shackleton et al. (1995a).

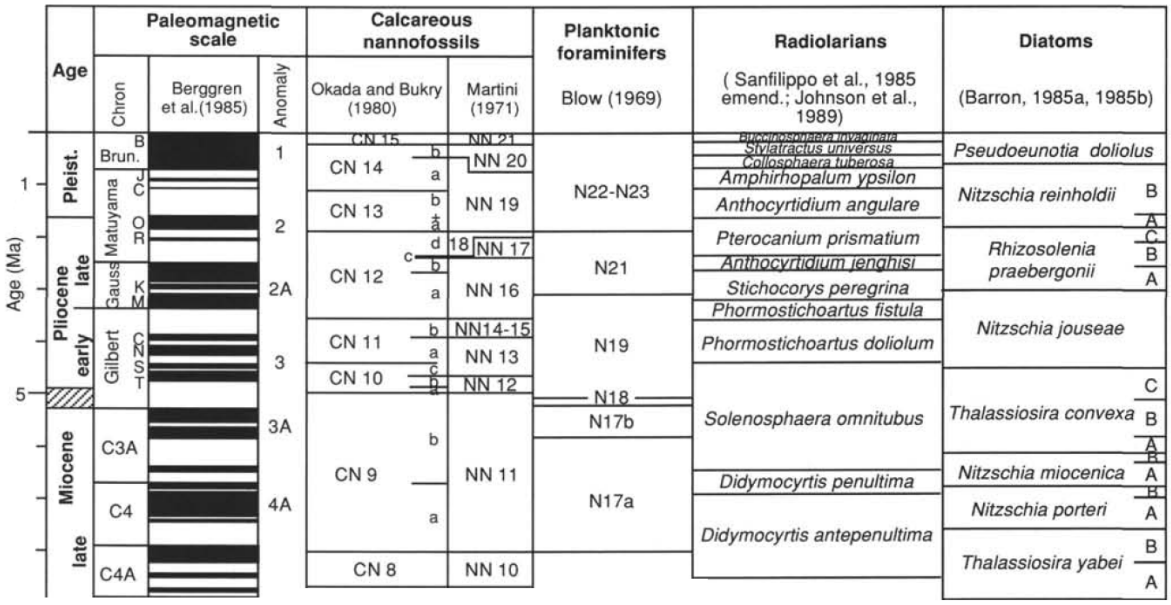

Figure 3.2: A combined time-scale for magneto- and biostratigraphy. The paleomagnetic regions on the left indicate epochs in Earth's history with normal (black), and reversed (white) magnetic polarity. On the right, a variety of biomarkers are shown. Figure was adopted from Mayer et al. (1992).

Orbital forcing

High frequency variations in key sediment parameters, such as density, color, and magnetic susceptibility provide valuable additional stratigraphic clues governed by astronomically driven climatic changes known as Milankovitch cycles. Milankovitch cycles describe periodic variations of the Earth-Sun system, in particular: (1) precession of the Earth's axis (21 ka period), (2) obliquity of the Earth's axis (41 ka period), (3) orbital inclination and shape (100 ka period). The application of Milankovitch forcing to the dating of Leg 138 is discussed in more detail in Shackleton et al. (1995b).

Age model

By combining all above mentioned techniques, Shackleton et al. (1995b) were able to calculate an age model for all sites of Leg 138. The age model was adopted for sample dating, whereby a linear interpolation was performed to obtain intermediate ages between data points (Fig. (3.3)).

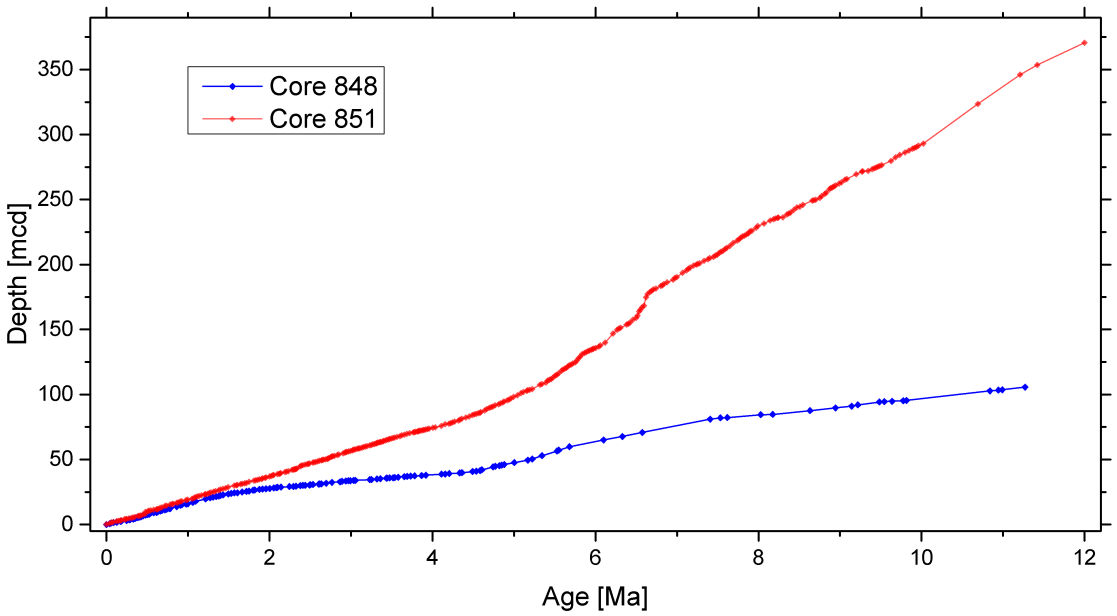

Figure 3.3: The age model obtained by Shackleton et al. (1995b) is displayed graphically here. The lines represent linear interpolations between data points.

The average sedimentation rates for both cores in the age interval of the expected SN signal ($1.7 - 2.7$ Ma) are conveniently determined by a linear fit (Fig. (3.4)). The resulting average sedimentation rates correspond to $r_{\text{sed}}(848) = (6.1 \pm 0.3)$ m/Ma for core 848 and $r_{\text{sed}}(851) = (19.3 \pm 1.0)$ m/Ma for core 851. Fitting residuals suggest that the sedimentation rates of both cores were constant within typical variations of 5% during the $1.7 - 2.7$ Ma time interval. This is an important feature, since the concentration of

any trace mineral with constant production or input rate is roughly constant over this time range.

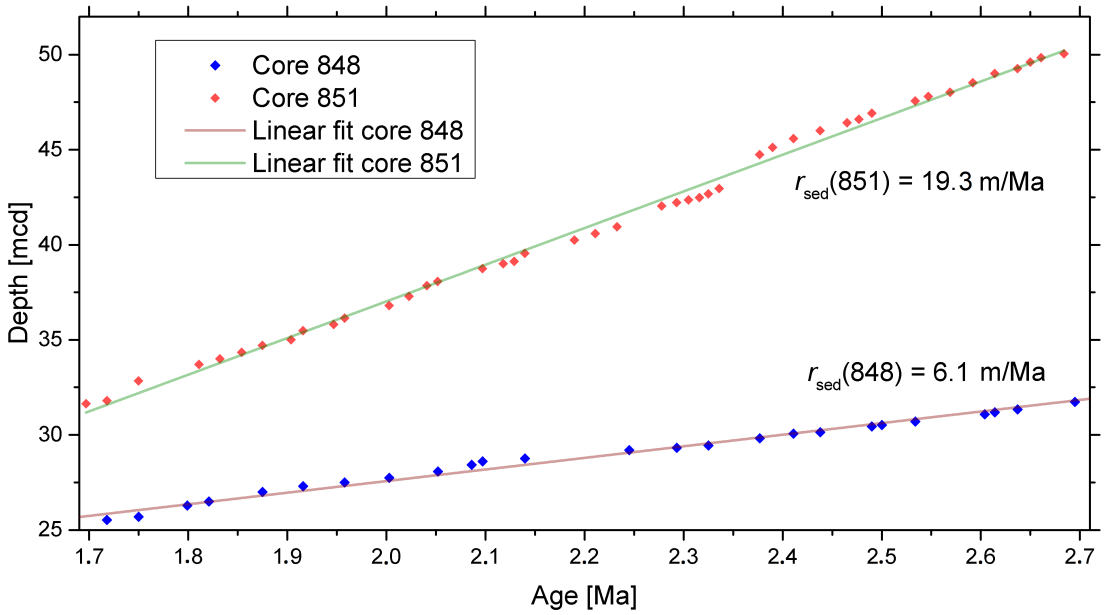

Figure 3.4: Age model zoomed to the region of the expected SN signal. Linear fits are included to extract the average sedimentation rate in this range.

3.2. Challenges of ^{60}Fe extraction

3.2.1. Signal dilution

After a suitable sediment has been selected, production of AMS samples requires proper extraction and purification procedures for isolating the isotopes to be examined. In the case of ^{60}Fe in sediment (especially targeting magnetofossils), Fe can be extracted either chemically or magnetically and then chemically purified, yielding an AMS sample of Fe_2O_3. Magnetic extraction is selective towards Fe contained in ferrimagnetic minerals, while chemical extraction affects only certain types of minerals and/or grain sizes. The ideal extraction procedure should only target Fe-bearing minerals that are expected to contain ^{60}Fe in order to maximize the ratio of ^{60}Fe/Fe measured in AMS. Dissolution of minerals that contain only terrestrial iron, such as those coming from rocks, can dilute the ratio of ^{60}Fe/Fe below the detection limit of AMS and render the experiment meaningless. Therefore, some knowledge about the origin of Fe-bearing minerals in sediment is required and is discussed in the following.

3.2.2. Primary and secondary iron minerals

Sedimentary minerals can be of primary origin, when they originate from eroded rocks, and secondary origin, when they are the product of chemical processes on Earth surface (e.g. soils) and in lakes or oceans. Among secondary minerals, a further distinction is made between authigenic minerals, which formed at the place where they are found (e.g. sediment) and non-authigenic, i.e. secondary minerals that have been transported from another place. As a general rule, primary minerals formed upon cooling from a melt or by transformation of existing rocks under high temperatures and pressures. Their grain size is mainly controlled by the cooling rate, with slowly cooling magma chambers forming up to mm-sized crystals (e.g. granite), and fast cooling lava forming glasses. On the other hand, secondary minerals are generally formed in aqueous solution and are more fine-grained or amorphous.

Primary iron oxides found in marine sediments have been discharged by rivers (detrital input) or transported as dust from arid regions of the continents. They generally consist of Ti-substituted magnetites ($Fe_{(3-x)}Ti_xO_4$) and hematites ($Fe_{(2-x)}Ti_xO_3$), and are usually > 1 μm in size (Franke et al., 2007). These particles and their weathering products are not expected to contain ^{60}Fe. Primary Fe oxides occurring in rapidly cooled rocks (glasses, tuff) can be considerably smaller (e.g. < 20 nm), and are usually included in a silicate matrix. As long as this matrix remains intact, such particles do not exchange Fe with the environment and therefore cannot contain ^{60}Fe either. In most cases, they retain some characteristics (e.g. shape, cation substitution) that makes them distinguishable from secondary minerals, even when being of similar sizes. These particles represent a problem for selective chemical extraction methods, because they can have the same dissolution characteristics as authigenic minerals. As shown later in this work, they represent a minor fraction of all magnetic oxides in cores 848 and 851.

Secondary Fe oxides and hydroxides (hematite, ferrihydrite, goethite, and magnetite) occur almost always as < 100 nm particles (Cornell and Schwertmann, 2003), which can easily exchange Fe with the environment through redox reactions, due to their large specific surface area (e.g. Zachara et al., 1998; Fortin and Langley, 2005; Taylor and Macquaker, 2011).

Only secondary particles containing Fe are expected to carry a possible SN ^{60}Fe signature, since they were formed at the time of enrichment of the ocean water with ^{60}Fe. Primary particles can incorporate some ^{60}Fe in their weathered surface, but not in their bulk volume, since they were not formed at the time of ^{60}Fe deposition.

There are two important characteristics of the secondary Fe-bearing particles targeted for extraction: firstly, they are small, and can therefore be targeted by selective chemical dissolution, therefore minimizing dilution by primary minerals. Secondly, magnetite particles possess unique magnetic signatures which enable inexpensive and fast characterization of sediments through magnetic measurements. In particular, sediments with strong primary Fe inputs can be distinguished from those containing mainly secondary

minerals. Furthermore, magnetic extraction can be used as an alternative to chemical extraction for selecting a specific Fe source.

3.3. Chemical Fe extraction

A Fe extraction technique with ideal selectivity towards secondary Fe does not exist. However, it is possible to choose one that minimizes the ratio between primary and secondary Fe in the extract. It was found that the Citrate-Bicarbonate-Dithionite (CBD) technique (Mehra and Jackson, 1958) is best suited for ^{60}Fe sample preparation.

3.3.1. CBD technique

Chemically targeting only small-grained Fe-bearing minerals of secondary origin is a challenging task, because primary mineral dissolution should be avoided (mild extraction) while maintaining a sufficient Fe yield (aggressive extraction). This lead to the consideration of an old technique, CBD, which was originally used for the removal of fine-grained Fe-bearing minerals from soils (Mehra and Jackson, 1958).

Extraction principle

In this procedure, the sample (e.g. soil or sediment) is digested in an aqueous solution of sodium citrate ($C_6H_5Na_3O_7$), sodium bicarbonate ($NaHCO_3$), and sodium dithionite ($Na_2S_2O_4$) at temperatures between $T = 20°$ C and $T = 90°$ C. It was later applied by Hunt et al. (1995) to dissolve small-grained magnetite and maghemite. Sodium dithionite is a strong reducing agent which can reduce and solubilize iron oxides. Its oxidation potential increases with pH because of hydroxyl consumption during oxidation of dithionite. At the same time, the solubility product of iron oxides increases under acidic conditions (low pH). This leads to a trade-off between high Fe solubility and high reducing capability of dithionite. After studying this behavior, Mehra and Jackson (1958) found that the optimal pH for reaction kinetics is 7.3. This means that a pH buffer is needed to supply additional hydroxyl to the system, which can be accomplished by adding NaOH or $NaHCO_3$. For this work, the chosen buffer was $NaHCO_3$, which also performed well in the original procedure by Mehra and Jackson (1958).

After Fe(III) on the surface of iron oxides is reduced to Fe(II), it is chelated by sodium citrate and the solution can be separated from the remaining soil/sediment. This procedure, if properly tuned, can be used to dissolve mainly small-grained iron oxides (Hunt et al., 1995).

Parameter optimization

In order to dissolve only particles of secondary origin and leave larger particles essentially intact, the CBD procedure has to be fine-tuned. Parameters that can influence the extraction strength are: extraction time t, extraction temperature T, concentration of C,B, and D, and the pre-treatment of the sample material.

After comparing various combinations of parameters on both, sediment samples, as well as artificial magnetite and hematite samples of different grain sizes, it was found that the most critical parameter is the extraction temperature T. Thus, all other parameters were fixed, using an extraction time of $t = 1$ h. The concentrations of the extraction chemicals C, B, and D suggested by Hunt et al. (1995) were used. The importance of temperature control became obvious when tests with artificial magnetite of $40 - 60$ nm grain size showed that complete dissolution is only possible at $T > 30°$C. A detailed study, showing that the ideal temperature for extraction of secondary Fe minerals is $T = 50°$C, based on magnetic measurements, was also performed and will be described in chapter 4.

Sediment preparation

Since AMS requires samples of at least 5 mg to reach sufficient sensitivity, and the concentration of small-grained Fe in the sediment is on the order of $10 - 100$ μg/g, the amount of sediment that had to be processed for a single AMS sample is very large. About 35 g of sediment (Fig. (3.6a)) are required for the production of a ~ 5 mg (Fe_2O_3) AMS sample, which is an adequate mass for production of a single AMS sample. This is a compromise between high yield and the maximum capacity of our extraction solution. Since some of the sediment samples were delivered wet, they had to be dried first (1 day at 60°C) and then ground in an achate mortar. After taking aliquots of at least 5 g, the fine sediment powder was weighed ($25 - 45$ g were used for each sample) and was then ready for CBD extraction. Aliquots from all samples have been stored and can be used for future studies, such as extended multi-radioisotope AMS measurements or further magnetic studies. A flowchart of the entire preparation procedure can be seen in Fig. (3.5).

CBD extraction procedure

200 ml of water were heated to $(50 \pm 2)°$C on a heating plate with a magnetic stirrer. While heating, 3.4 g of sodium-bicarbonate (B - $NaHCO_3$) and 12.6 g of sodium-citrate-dihydrate (C - $C_6H_9Na_3O_9$) were added and quickly dissolved. For sediment sample masses deviating from ~ 35 g, water volume and C,B, and D concentrations were scaled accordingly. Next, the sediment was added to the stirred solution. After confirming stable temperature and pH and that the sediment was well suspended and mixed into the solution, the reaction was started by adding 5.0 g of sodium-dithionite (D - $Na_2S_2O_4$). The extraction was allowed to continue for 1 h at 50°C under constant stirring. Over this time, the color of the sample changed from a light gray to blue-gray (Fig. (3.6b)).

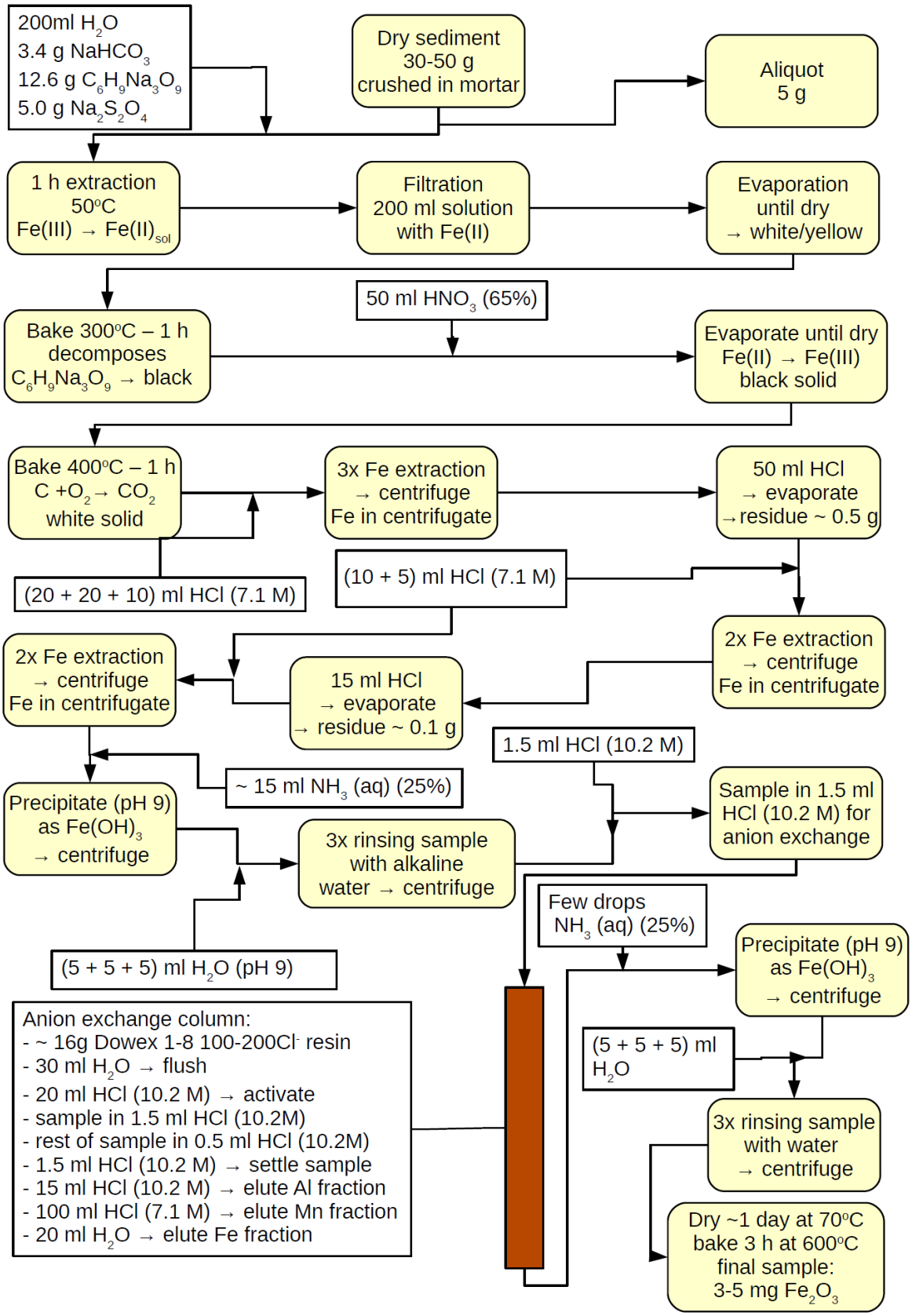

Figure 3.5: Flow chart of the entire chemical preparation procedure, including CBD extraction and ion exchange column.

The possible effect of stirring magnets on the extraction efficiency of magnetic minerals was tested by using artificial magnetite grains instead of sediment. Even though freely moving magnetic particles attach themselves to the magnet, they are completely dissolved, so that the stirring magnet did not represent a problem.

After the extraction, the sediment suspension was filtered in a vacuum filtration setup (filter diameter 90 mm) twice: first with a disc filter with pore size 1 μm, removing the bulk of the sediment, which could then be dried and used for other experiments, then with a disc filter with pore size 0.1 μm, removing the remaining sediment particles from the solution. The filtered solution then typically had a characteristic citrus-yellow color, indicating the presence of dissolved Fe(II) (Fig. (3.6c)).

3.3.2. Isolation of Fe

The extracted Fe solution was then transferred to a crystallization bowl (diameter 115 mm) and heated to 85°C under constant stirring. Water evaporated in $\sim$ 5 hours, leaving a white/yellow organic residue on the bottom of the bowl. This residue contained most of the initially added C, B, and D chemicals, as well as the targeted Fe(II). The yellow color is due to Fe-citrate complexes. In order to overcome Fe-chelation by sodium citrate, the sample was heated to 300°C in an oven for 1 h. Since sodium citrate quickly decomposed at this temperature, the sample was gray/black afterward (Fig. (3.6d)). The now freely accessible Fe(II) was the oxidized upon adding 50 ml HNO_3 (65%), which was subsequently evaporated at 70°C. The dried residual was again baked at 400°C for 1 hour. All freely available carbon was quickly oxidized and released as CO_2, leaving residue as a white liquid with some traces of red/orange coloring, indicating Fe(III). The sample became solid again (Fig. (3.6e)) upon cooling.

At this point, Fe(III) could be extracted with 7.1 M HCl. Three such extraction steps were performed by transferring the sample into a 50 ml centrifugation tube, where 20+10+10 ml of warm (40°C) HCl were added. After shaking and subsequent centrifuging, the HCl containing the Fe(III), could be poured off into a beaker. After the third extraction step, the 40 ml of HCl (clearly yellow from Fe(III)), were evaporated on a heating plate.

It was not possible to precipitate Fe(III) at this point. This had actually been the initial procedure, but it turned out that, contaminations in the HCl prevented the complete precipitation of iron hydroxide, making another evaporation step necessary.

After complete evaporation, the residue on the bottom of the beaker contained about 500 mg of white solids, and yellow/red traces from Fe(III). This residue was again dissolved in 7.1 M HCl in two extraction steps with 10+5 ml. Although the Fe(III) immediately dissolved, the rest of the sample was mostly unaffected. Thus, the sample could be centrifuged again, leaving most of the undesired residue on the bottom, while Fe(III) remained in the solution.

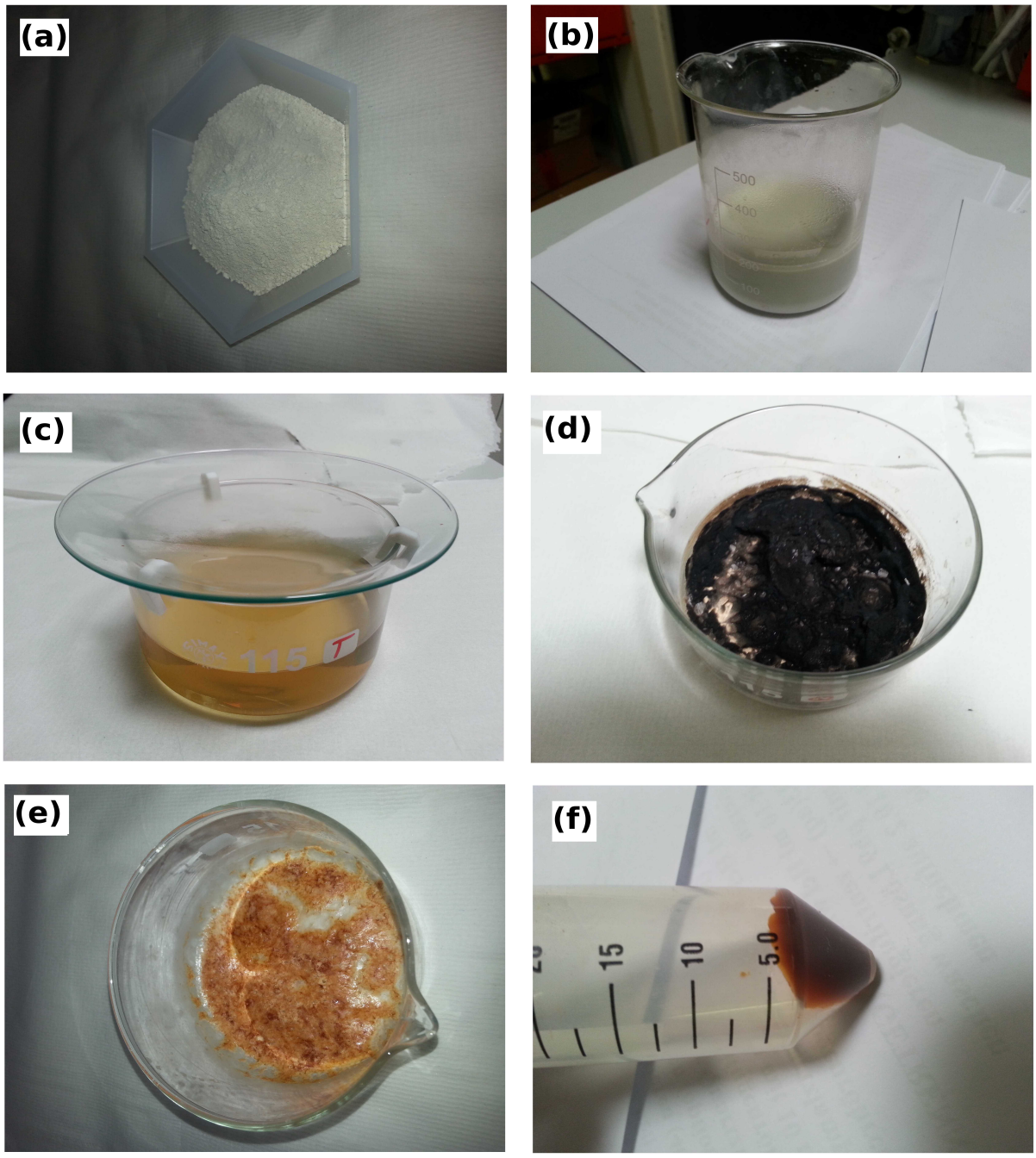

Figure 3.6: Photographs of the preparation procedure of a representative ^{60}Fe AMS sample from sediment core 848. (a) Crushed raw sediment (35 g). (b) Sediment suspended in water after CBD extraction, right before filtration. (c) Sample after filtration, ready for evaporation. (d) Same sample after citrate decomposition (oven). (e) After second baking step: white residue with orange Fe on top. (f) Iron hydroxide after precipitation.

This step was repeated one more time: the sample was again completely evaporated, taken up into fresh 7.1 M HCl with two extractions with 10+5 ml, and centrifuged. Finally, the centrifugate was neutralized by adding roughly the same volume of 25% ammonia solution (NH_3(aq)). The pH was increased to 8, where Fe(III) precipitated completely as iron hydroxide ($Fe(OH)_3$), which was separated by centrifugation. An important feature of this precipitation step was that Ni remained in solution, reducing possible AMS background from ^{60}Ni. The precipitated $Fe(OH)_3$ was washed three times with 5+5+5 ml of slightly alkaline water (pH 9), and then centrifuged, discarding the liquid each time (Fig. (3.6f)). Afterward, $Fe(OH)_3$ was taken up in 1.5 ml HCl 10.2 M (corresponds to commercially available 32% HCl).

3.3.3. Anion exchange and final sample

Additional purification of the sample was achieved using an anion exchange. This was necessary to separate Fe from other elements, which could possibly contaminate the final AMS sample if not removed, such as Mn, Ti, and Al. An exchange column (effective height 20 cm, diameter 10 mm) was filled with $\sim$ 16 g of ion exchange resin (Dowex 1-8 $100 - 200$ Cl^-). After flushing the column with 20 ml H_2O, the resin was activated with 20 ml HCl 10.2 M. The sample was then added onto the column dissolved in 1.5 ml HCl 10.2 M. The rest of the sample (residual after first transfer to the column) was added onto the column dissolved in another 0.5 ml HCl 10.2 M. Subsequently, another 16.5 ml of HCl 10.2 M were added, eluting the fraction containing e.g. Al and Ti from the sample. Then, 100 ml HCl 7.1 M were added, eluting the fraction containing Mn. In the end, Fe was eluted with 20 ml H_2O, precipitated again using ammonia solution and washed 3 times with H_2O. The sample was then dried in a quartz crucible at 70°C until dry, and then baked at 600°C for 3 hours, yielding typically 5 mg of pure Fe_2O_3 for AMS.

3.3.4. Possible sample contaminations

The goal of a successful sample preparation is the production of a pure sample of Fe_2O_3 with the same concentration of ^{60}Fe/Fe as in the targeted minerals. Problems can occur in several ways: firstly, the concentration of the radioisotope under investigation might be altered, either by dilution, or by contamination with radioactive material. Secondly, large amounts of the stable isobar can hinder AMS measurement efforts, and thirdly, large contaminations (in the percent range) with certain substances can prevent the extraction of a stable, high ion current from the ion source. Typical pitfalls in the case of ^{60}Fe will be discussed in the following.

Stable iron

Any contamination with stable Fe dilutes the original concentration of ^{60}Fe/Fe. In extreme cases, dilution can lower the ^{60}Fe/Fe ratio below the detection limit of the AMS setup. The two main dilution sources are the dissolution of unwanted Fe-bearing minerals (typically primary, large-grained), which will be discussed at a later point in this work, and Fe traces contained in the chemicals used in the preparation procedure. This contamination source can be quantified using blind samples with no sample material (i.e. sediment), which are subjected to the same extraction procedure used for real samples. Only an upper Fe contamination limit can be estimated in this manner, since the precipitation of small amounts of Fe (« 1 mg) is usually incomplete.

Therefore, aliquots (5 of 25 ml) of a representative blind sample were taken before both precipitations with ammonia solution, and the concentration of stable Fe was determined using inductively coupled plasma mass spectrometry (ICP-MS) at the Centro de Investigación, Tecnología e Innovación, Universidad de Sevilla, Spain. Preceeding the precipitation step before the anion exchange, the sample contained 0.03 mg Fe (in terms of the entire 25 ml sample). After the anion exchange (before the second precipitation step), another 0.02 mg Fe were detected. The blank level during this measurement was not determined, thus only an upper limit on the expected contamination can be obtained by summing the two contributions to 0.05 mg. Considering a typical sample weight of 3 mg Fe, the upper limit on contamination by stable Fe corresponds to $\lesssim 2\%$.

^{60}Fe

In contrast to dilution by stable Fe, it is also possible that the concentration of the radioisotope in the sample in increased unwillingly by contamination with other ^{60}Fe sources. This can occur, for example, when samples of very different concentrations are made using the sample preparation equipment withou sufficient cleaning. Fortunately, such cross-contaminations between samples could be ruled out in this work, since all sediment samples had very low concentrations of ^{60}Fe/Fe $<$ few 10^{-15}, and the standard samples (with ^{60}Fe/Fe$= 10^{-12} - 10^{-10}$) were always prepared in a different room and with dedicated equipment.

Nickel

A contamination with Nickel can potentially be harmful for the AMS measurement, since ^{60}Ni is the stable isobar for a measurement of ^{60}Fe. The sample preparation procedure used in this work eliminated Ni isobar problems, because most Ni could be suppressed during Fe hydroxide precipitation at pH 8. The remaining Ni in the final Fe_2O_3 samples could be easily suppressed with the GAMS setup, as will be described in chapter 5.

3.3.5. Chemical efficiency

The total efficiency of the chemical sample preparation procedure is defined here as the mass of Fe in the AMS sample, divided by the mass of CBD-extractable Fe in the sediment. This ratio was estimated by using $5-10$ mg of synthetic grains of magnetite (Alfa Aesar, Lot Nr. E08T027) in the grain size range $40-60$ nm instead of sediment. This was done periodically throughout the entire sample preparation. In total, the efficiency ϵ_{chem} was determined 17 times, resulting in an average of $\epsilon_{\text{chem}} = (85 \pm 5)\%$.

3.4. Description of produced AMS samples

A total of 109 ^{60}Fe sediment samples were prepared and measured with AMS. Some of them were split up into two chemistry samples if more than 50 g of sediment were available. At an average of 35 g per sample, this means that a total of 3.8 kg of sediment were processed. For core 851, sediment was only available in the range $1.6-3.7$ Ma and a total of 44 samples were prepared with an average Fe yield of 0.11 mg Fe per gram of sediment used for extraction. For core 848, samples between 0 and 3.2 Ma were prepared and additionally, 4 very old samples in the range $7-8$ Ma were included with an average Fe yield of 0.12 mg/g in a total of 65 samples. The Fe yield data is also plotted in Fig.(3.7) and shows that the yield for each sample can be quite different. This is mostly due to the changing amount of Fe available for CBD extraction, being closely related to the amount of small grained secondary iron oxide which will be investigated in the next chapter.

This also indicates that local dilution of a possible ^{60}Fe signal could be possible in samples with high yield. This is however not necessarily the case, since a higher yield of CBD extractable Fe could just indicate a higher abundance of ^{60}Fe-bearing minerals, but should be kept in mind for an interpretation of final ^{60}Fe data.

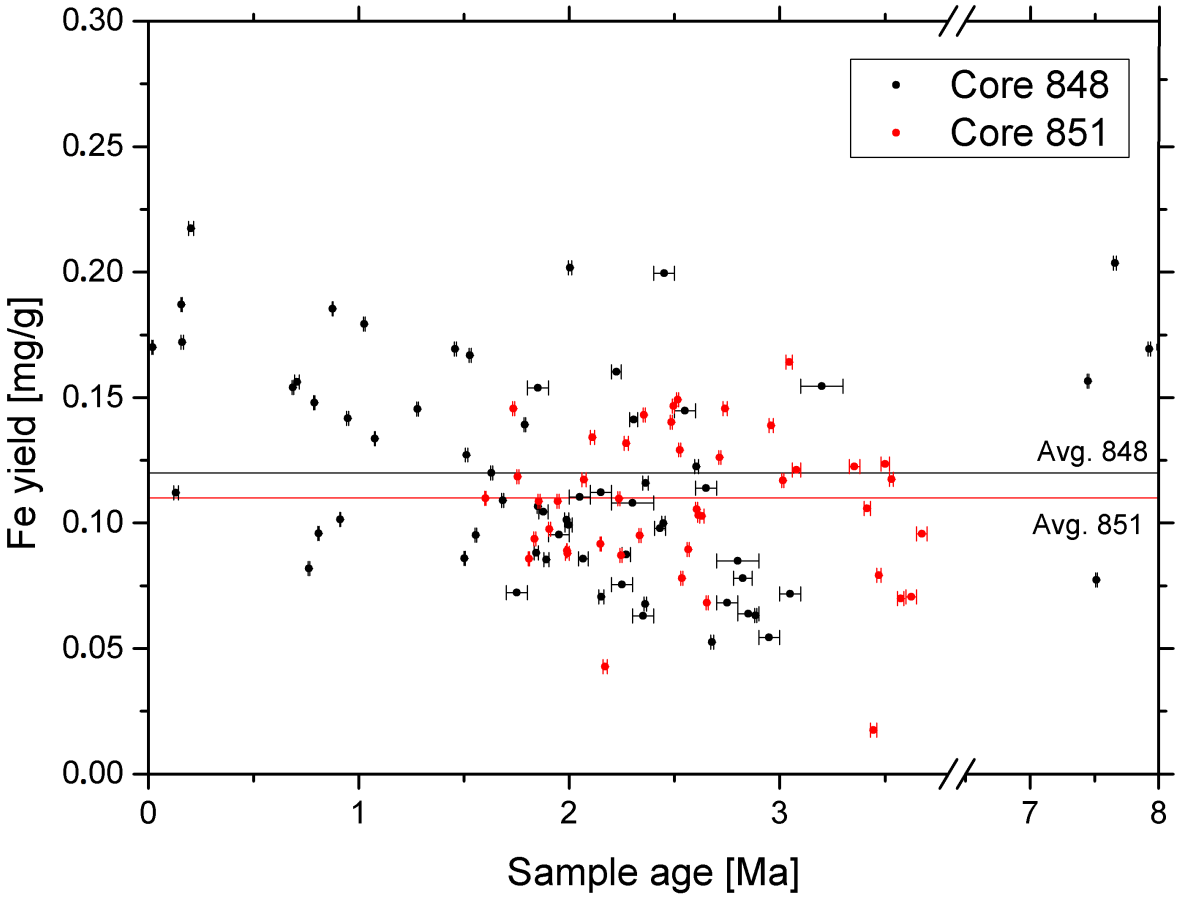

Figure 3.7: Fe yield of all ^{60}Fe AMS sediment samples prepared in this work. Y-axis gives yield as mg of Fe in final AMS sample divided by the amount of sediment used in the preparation of the sample in grams. X-error bars indicate age range from which sediment was combined to form the sample material.

4. Sample characterization using magnetic measurements

After a short introduction to general concepts of magnetism, the magnetic characterization of sediment samples chosen for ^{60}Fe extraction will be discussed. These samples bear a unique magnetic signature related to fossil magnetosome chains. The magnetic characterization of sediment is used, in combination with chemical extraction, to understand how secondary Fe oxides formed as part of the sedimentary iron cycle. For this purpose, new characterization techniques have been developed, which enabled, for the first time, a quantitative assessment of the important role of magnetotactic bacteria in the iron cycle.

4.1. Introduction and methods

4.1.1. Magnetism and magnetic ordering

The following introduction to the topic of magnetism is based on Coey (2012) and Tauxe et al. (2014).

The origin of the magnetization of iron and other magnetic materials lies in quantum mechanical effects. This connects the macroscopic physics of magnetism to a microscopic source of magnetization M, defined as the magnetic moment per unit volume. The magnetic moment is the vector sum of microscopic magnetic moments of atoms or molecules in a given substance. Depending on whether atoms/molecules possess a net magnetic moment, and on how these moments are coupled, three main classes of magnetic materials are defined: (1) diamagnetic materials, in which atoms/molecules do not possess an intrinsic magnetic moment unless an external magnetic field is applied, (2) paramagnetic materials, in which atoms/molecules possess an intrinsic magnetic moment, and (3) ferro-, ferri-, and antiferromagnetic materials, where atomic or molecular moments are strongly coupled and display a collective behavior. These three categories have distinct magnetic properties summarized by their hysteresis behavior (i.e. the magnetic moment M vs. applied field H). Para- and diamagnetic materials have a linear hysteresis described by

$$M = \chi \times H \tag{4.1}$$

where χ the so-called magnetic susceptibility, with $\chi < 0$ for diamagnetism, and $\chi > 0$ for paramagnetism. Paramagnetic hysteresis can be explained by the successive alignment of

microscopic magnetic moments in the applied field against thermal perturbations. The magnetization of ferromagnetic materials, on the other hand, depends on the previous history of H (magnetic memory). The hysteresis loop of such materials is open and depends on parameters such as temperature and the maximum applied field. A common characteristic of ferromagnetic hysteresis is the ability to retain a so-called remanent magnetization without an external field. This is possible because the material is characterized, within so-called magnetic domains, by a spontaneous magnetization M_s produced by the alignment of atomic or molecular magnetic moments. This spontaneous alignment is due to a strong coupling between electron spins. The Hamiltonian for the interaction of two neighboring spins S_i and S_j (in units of $\hbar$) due to the exchange interaction can be written as

$$H = -2JS_i \cdot S_j \tag{4.2}$$

with an exchange constant J which can be either positive or negative. These two cases generate a parallel alignment of spins ($J > 0$), resulting in ferromagnetism, or anti-parallel alignment ($J < 0$), resulting in anti-ferromagnetism. Another interesting phenomenon occurs if the atoms i and j belong to different sub-grids of a crystal. Since they do not necessarily need to have the same magnetic moment, even a negative interaction constant J can generate magnetic ordering with a net spontaneous magnetization in the case of different magnetic moments $m_i \neq m_j$. This type of ordering is referred to as ferrimagnetic because of its phenomenological similarity to ferromagnetism and its widespread occurrence in ferrites, of which magnetite is an important example. Magnetic ordering is counteracted by thermal perturbations and is completely removed above the so-called Curie temperature T_C. The Curie temperature is material-specific and separates the well-ordered ferromagnetic phase at $T < T_C$ ($M_s > 0$) from the disordered paramagnetic phase at $T > T_C$ ($M_s = 0$).

The bulk magnetization of ferromagnetic materials is often much smaller than M_s or even zero, because of the spontaneous formation of magnetic domains in which the M_s vector is oriented along different directions. Magnetic domains enable a reduction of the total energy associated with the magnetization, avoiding the generation of large internal and external fields.

4.1.2. Magnetic anisotropy

In chapter 3 it was shown that ferromagnetic particles in sediment can carry the ancient signature of geomagnetic field reversals. This leads to an important question: How is the magnetization of a particle fixed along a specific direction? When considering a uniformly magnetized (magnetization $\vec{M}$) ferromagnetic particle in an external field $\vec{H}_e$, its magnetostatic energy density (energy per volume) is given by

$$\epsilon_m = -\mu_0 \vec{M} \cdot \vec{H}_e. \tag{4.3}$$

This means that the lowest energy state is reached then the magnetization is aligned with the external field. However, free rotation of the particle magnetization is generally prevented by an energy barrier related to crystal structure and particle shape: the so-called magnetic anisotropy energy. This energy leads to preferred directions of the magnetization vector inside the crystal, so that the bulk magnetic moment coincides with one of these directions in the absence of an external field. Switching between such preferred directions is possible only by increasing the temperature, through thermal activation, or by application of a sufficiently strong external field. There are several sources of anisotropy energy, e.g. particle shape (shape anisotropy), crystal structure (magnetocrystalline anisotropy), and stress (magnetoelastic anisotropy).

One of the simplest models for particle magnetization (Stoner and Wolfarth, 1948) describes isolated magnetic particles that are small enough to contain a single magnetic domain: so-called single-domain (SD) particles. In this case, the particle's magnetization is homogeneous and coincides with M_s. The total magnetostatic energy density of SD particles with an ellipsoidal shape and negligible magnetocrystalline anisotropy can be written as

$$\epsilon_t = \epsilon_m + \epsilon_a = -\mu_0 M_\mathrm{s} H_e \cos(\phi - \theta) + K \sin^2(\theta) \tag{4.4}$$

where the first term represents the Zeeman energy from Eq. (4.3) and the second part describes the self-energy density caused by uniaxial magnetic anisotropy characterized by an anisotropy constant $K \propto M^2$, associated with particle elongation. This so-called shape anisotropy energy results from the so-called demagnetizing energy associated with the product of M_s with the internal field caused by M_s itself. ϕ is the angle between easy axis and $\vec{H}_e$ and θ is the angle between the easy axis and $\vec{M}$ as depicted in Fig. (4.1a). In absence of an external field ($H_e = 0$), the magnetization has two states of lowest energy, both along the easy axis, as seen in Fig. (4.1b). At non-zero H_e, one of the two directions along the long axis of the ellipsoid will be preferred. However, switching between the two requires overcoming an energy barrier which leads to hysteresis effects. This can be seen in Fig. (4.1c), where the external field is strong enough to alter the shape of the total energy density sufficiently to remove one of the energy minima. If the particle was originally in the magnetization state at $\theta = 180°$ of Fig. (4.1b), an increasing of the external field will cause the magnetization to rotate reversibly to slightly lower θ, until a situation as in Fig. (4.1c) is reached and an irreversible magnetization jump to the only remaining energy density minimum occurs. The Stoner-Wolfarth model provides a correct description of magnetite SD particles, because the magnetocrystalline anisotropy is negligible even for slightly elongated crystals.

As discussed above, the magnetic moment of a SD particle can be switched only by

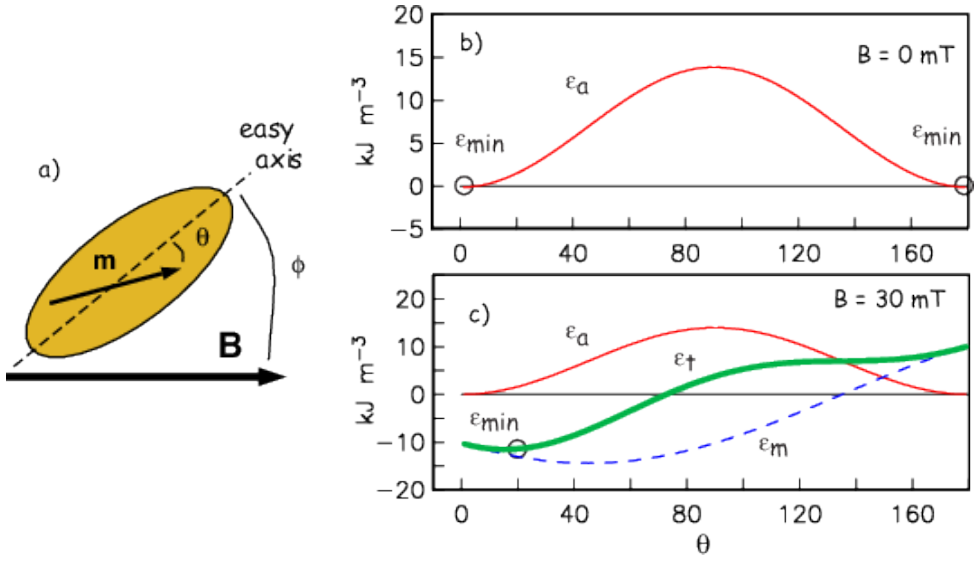

Figure 4.1: (a) Sketch of a uniaxial SD particle. B is an external magnetic field and m represents the magnetization. (b) Variation of the anisotropy energy $\epsilon_a$over different angles θ between magnetization and easy axis without external field. (c) Same as (b), but with external field of 30 mT. Also displayed are the magnetostatic energy density ϵ_m and the total energy density ϵ_t. Figure taken from Tauxe et al. (2014).

overcoming an energy barrier given by Eq. (4.4). Since this barrier is proportional to the particle volume, the barrier of small particles can be overcome by the thermal energy k_BT, in which case the magnetic moment of the particle is no longer stable, even in a null field. The threshold volume below which the SD magnetization becomes unstable depends on the anisotropy energy (i.e. shape), temperature, and the considered time interval. For magnetite, this threshold is generally located between $\sim$ 15 nm and $\sim$ 25 nm. SD particles affected by thermally activated switching of the magnetization are called superparamagnetic (SP). Like paramagnetic particles, they are characterized by a reversible magnetization curve in applied fields. However, SP particles exhibit a much larger susceptibility and a magnetic saturation in much smaller field.

4.1.3. Magnetic domains and grain sizes

A strong assumption of SD models is the uniform magnetization of the particles. This magnetic configuration minimizes the exchange energy between spins at the cost of higher demagnetizing energy. Above a certain critical size, non-homogeneous magnetization states become energetically favorable. In hard magnetic materials, i.e. materials with a strong magnetocrystalline anisotropy, the single-domain (SD) state is directly replaced by two or more domains separated by a thin zone where spin orientation switches from one preferred direction to another. This zone is called a domain wall, and particles containing several domains are referred to as multidomain (MD). In soft magnetic materials (weak magnetocrystalline anisotropy) such as magnetite, intermediate magnetic configurations

between SD and MD exist, where magnetization takes the form of one or more vortices. Particles with such configurations are called pseudo-single-domain (PSD) and their magnetic properties are intermediate between those of SD and MD particles. The upper size limit for magnetite SD particle depends on shape and lies in the range $40-100$ nm, while MD particles exist above ~ 300 nm.

Hysteresis properties are strongly influenced by the domain state of particles. SD hysteresis of randomly oriented particles is characterized by a large remanent magnetization ($M_{\rm rs} = 0.5M_{\rm s}$). On the other hand, the hysteresis of MD particles depends strongly on the freedom of domain walls to move inside the crystal. Defect-free particles contain easily movable domain walls, which, in zero field, tend to separate magnetic domains with opposed magnetizations, so that the net magnetic moment and therefore the demagnetizing energy is close to zero. Accordingly, the remanent magnetization of such particles is small. Strong domain wall pinning by defects, on the other hand, enable larger remanent magnetizations.

4.1.4. Magnetic signature of magnetofossils

Magnetotactic bacteria align themselves with the Earth's magnetic field through the magnetic moment of magnetosomes. In order to maximize the magnetic moment that can be attained with a given amount of Fe, magnetosomes need to be SD particles. For magnetite, the grain sizes for SD particles are defined by the so-called stable single-domain (SSD) range, which is comprised between ~ 15 nm and ~ 100 nm. Indeed, most magnetosomes are comprised within these limits (Fig. (2.13a)).

A single magnetosome would not possess a sufficiently large magnetic moment for aligning the whole bacterium. Therefore, magnetotactic bacteria contain chains of at least ~ 10 closely spaced magnetosomes. Magnetosome growth proceeds from the central part of the chain outwards, so that the correct magnetic moment direction of new magnetosomes is inherited from neighboring crystals and the whole chain acquires a total magnetic moment which is the sum of the magnetic moments of all individual crystals. Strong magnetic interactions between aligned crystals ensure that the whole chain behaves as a single SD particle, with the magnetic moments of individual crystals switching in unison if a sufficiently large magnetic field is applied. This property has been predicted theoretically (Jacobs and Bean, 1955), and verified experimentally on magnetotactic bacteria containing a single magnetosome chain (Penninga et al., 1995; Hanzlik et al., 2002). Because magnetosome chains are surrounded by the much larger cell body (Faivre and Schüler, 2008), magnetosome chains in a colony of living bacteria are always well separated from each other. Magnetostatic interactions between chains in different cells are thus negligible, and the magnetic properties are equivalent to those of randomly oriented, non-interacting SD particles (each chain is one of those particles). This situation is usually maintained in sediment containing magnetotactic bacteria after their death followed by cell dissolution,

as seen from their non-interacting SD properties (e.g. Egli, 2004a).

However, not all magnetofossils, and, more generally, not all secondary magnetite particles must necessarily display a SD signature. For example, many species of magnetotactic bacteria produce double or multiple chains of magnetosomes that do not behave as single SD particles. These cells have multiple magnetization states including one with zero net magnetic moment (Hanzlik et al., 2002). Furthermore, magnetosome chains can collapse after cell death (e.g. McNeill and Kirschvink, 1993). Experiments with aqueous suspensions of cultured bacteria produced clusters of strongly interacting magnetosomes after cell dissolution (Kobayashi et al., 2006); however, this result might not be applicable to natural samples, where the sediment matrix can prevent clustering of collapsed chains. Furthermore, a significant proportion of secondary SD magnetite might be produced by dissimilatory metal reducing bacteria. In this case, particles are free to form clusters, as observed in aqueous laboratory cultures (e.g. Lovley et al., 1987), although this may not necessarily occur in sediment, where bacteria and iron concentrations are much smaller. Finally, SD particles might also be of primary origin, for instance from windblown volcanic ashes (Straub and Schmincke, 1998; Jackson et al., 2006).

4.1.5. Hysteresis curves

Hysteresis loops provide fundamental information about bulk magnetic properties. A so-called major hysteresis loop is obtained by measuring the magnetization in a field that is swept from a large positive to a large negative value, whereby the minimum and maximum fields are sufficiently large to saturate the sample, i.e. $M(\pm H_{\max}) = \pm M_{\mathrm{s}}$. In the following, two simple hysteresis models are discussed for ideal SD and MD particles. For the case of SD hysteresis, consider first a single SD particle with its easy axis parallel to the external field $\phi = 0°$ (Fig. (4.2a)). Beginning with positive saturation, the external field is reduced. The magnetization stays at positive saturation until a spin-flip becomes energetically possible, in a so-called switching field $H = -H_{\mathrm{f}}$. When the field sweep is reversed, the magnetization only jumps back to its original orientation once the field again reaches $H = H_{\mathrm{f}}$. This rectangular hysteresis loop serves as fundamental element of the Preisach model of ferromagnetic hysteresis (Preisach, 1935), where a generic hysteresis loop is represented as a linear combination of elemental, rectangular loops called hysterons. In the case of other angles ϕ, the two branches of the hysteresis loop become curved, reflecting reversible rotation of the magnetization away from the magnetic easy axis and towards the applied field direction (Fig. (4.2b)). In the limit case of $\phi = 90°$, the loop becomes completely closed.

SD particles in natural samples are generally randomly oriented (Fig. (4.3)), so that the resulting hysteresis loop is the weighted average of loops shown in Fig. (4.2b) for $0° \leq \phi \leq 90°$. Unlike the case of single-particle loops (e.g. Fig. (4.2)), a collection of randomly oriented SD particles can exist in a demagnetized state (i.e. $H = 0$ and $M = 0$

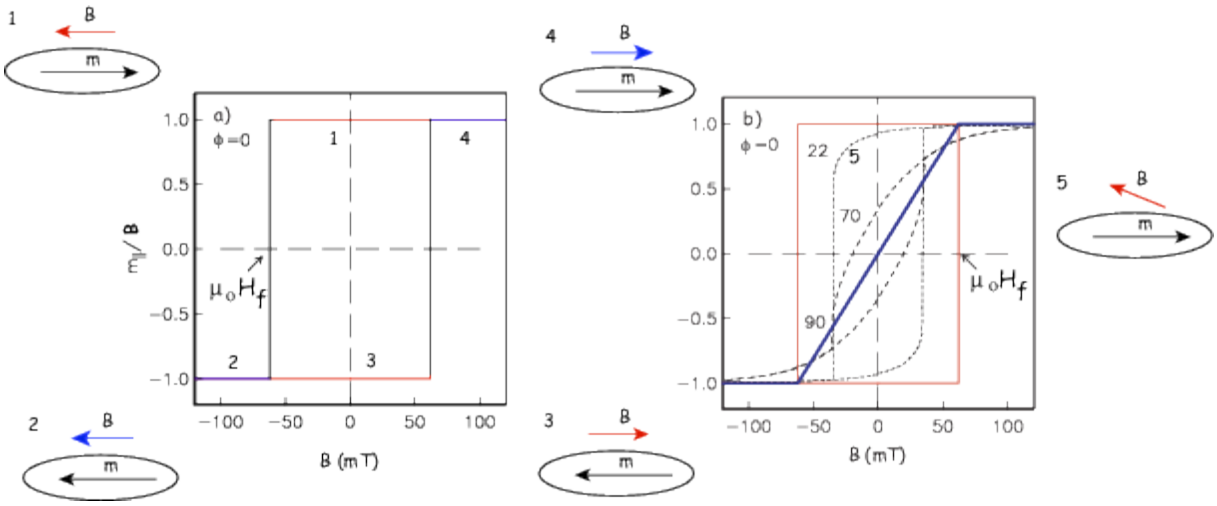

Figure 4.2: (a) Moment measured for a SD particle ($\phi = 0°$) with applied field starting at 0 mT and increasing in the opposite directions along track 1. When the flipping field $B = \mu_0 H_f$ is reached, the moment switches to the other direction along track 2. The field then switches sign and decreases along track 3 to zero, then increases again to the flipping field. The moment flips and the the field increases along track 4. b) Same as (a), for particles with different angle between easy axis and external field ϕ. Figure taken from Tauxe et al. (2014).

in Fig. (4.3)), which is obtained when the magnetization is parallel or anti-parallel to the easy axis at random. In practice, such demagnetized states are obtained by cooling from above the Curie temperature in zero field, or by subjecting the sample to a decaying alternating field (see Sec. (4.2)).

The magnetization curve obtained from a demagnetized state in increasingly strong field is called virgin curve, and its initial slope defines the so-called low field susceptibility χ_{lf}. The virgin curve merges with the major hysteresis loop when saturation is approached. Important hysteresis parameters in addition to the saturation magnetization M_s are (1) the saturation remanence M_{rs}, which is the magnetization remaining after decreasing the field amplitude from a value sufficient to saturate the sample to zero, (2) the coercive field H_c, which is the field where $M = 0$ on the lower branch of the major hysteresis loop, and (3) the coercivity of remanence H_{cr}, which is the positive field that must be applied to a negatively saturated sample in order to cancel its remanent magnetization.

Randomly oriented SD particles with uniaxial anisotropy are characterized by $M_{rs}/M_s = 0.5$ and $1 < H_{cr}/H_c < 2$ (Dunlop, 2002a). On the other hand, large, defect-free MD particles are characterized by drastically different hysteresis properties, governed by reversible domain wall displacements in the applied field. The ideal MD hysteresis loop is completely closed (i.e. $M_{rs}/M_s \to 0$ and $H_{cr}/H_c \to \infty$), due to the fact that the total particle energy is minimized when the vector sum of individual domain magnetizations is zero. Real MD hysteresis loops are characterized by small residual saturation remanence, due to domain wall pinning by crystal defects.

Hysteresis properties of sediments and rocks are usually represented in a plot of M_{rs}/M_s

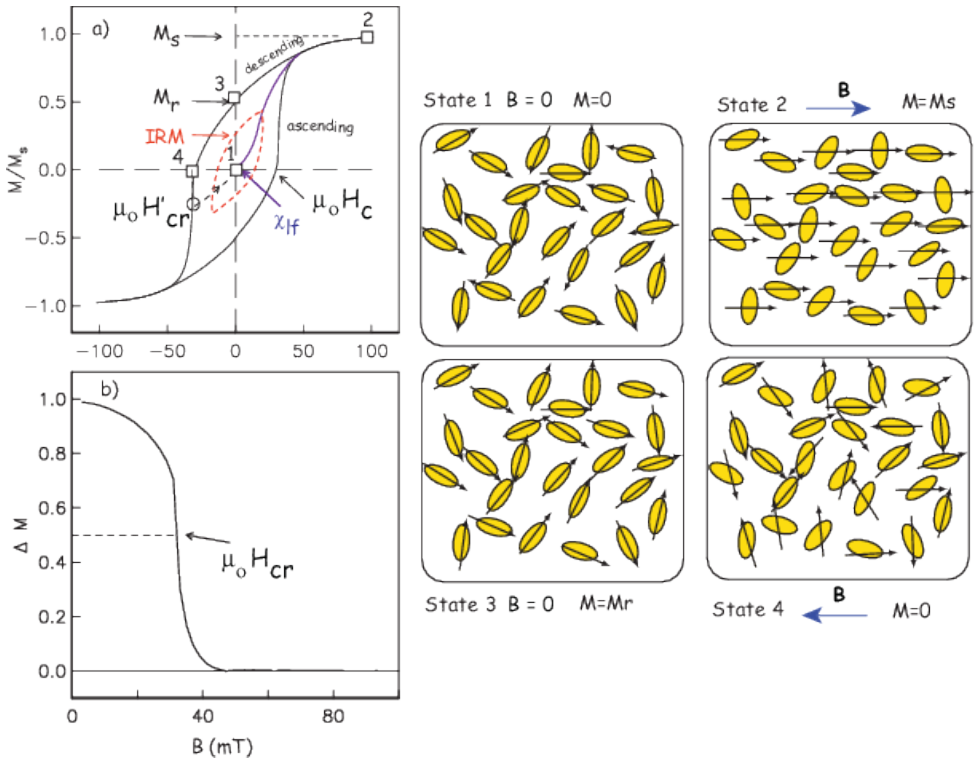

Figure 4.3: (a) Net response of a random assemblage of UNISD particles. Magnetization states (squares labeled 1 to 4) for representative particles are shown in the balloons labeled State 1- 4. The initial demagnetized state is 'State 1'. When all moments are parallel to the applied field (State 2), the magnetization is M_s. When the field is returned to zero, the magnetization is a saturation remanence (M_r; State 3). When the field is applied in the opposite direction and has remagnetized half the moments (State 4), the field is the bulk coercive field $\mu_0 H_{cr}$. When a field is reached that when reduced to zero leaves zero net remanence, that field is the coercivity of remanence (here labeled $\mu_0 H'_{cr}$). (b) Curve obtained by subtracting the ascending curve in (a) from the descending curve. The field at which half the moments have flipped, leaving a magnetization of one half of saturation is another measure of the coercivity of remanence, here labeled $\mu_0 H_{cr}$. Figure taken from Tauxe et al. (2014).

versus H_{cr}/H_c, which is called Day diagram (Day et al., 1977; Dunlop, 2002a,b). In this diagram, SD and MD hysteresis represent the end-members of mixing curves along which PSD particles and the bulk properties of most sediments usually occur (see Fig. (4.7)). Because of the intrinsic non-uniqueness of hysteresis parameters, other magnetic characterization techniques have been developed.

4.1.6. Anhysteretic remanent magnetization

Of particular interest for the characterization of magnetofossil-rich sediments is the anhysteretic remanent magnetization (ARM). This remanent magnetization results from the application of a strong alternating field (AF) with slowly decaying amplitude, superimposed to a small (i.e. < 0.1 mT) bias field H_{dc}. With $H_{dc} = 0$, this procedure produces a collectively demagnetized state (i.e. $M = 0$ and $H = 0$) for any assemblage of randomly oriented magnetic particles. Application of a small bias field results in a weak remanent magnetization $M_{ARM} << M$rs which is proportional to H_{dc}, i.e. $M_{ARM} = \chi_{ARM} \times H_{dc}$, where χ_{ARM} is the so-called ARM susceptibility.

Unlike other types of remanent magnetization, ARM is very sensitive to the domain state of particles and to the strength of magnetostatic interactions between particles. In particular, non-interacting SD particles, such as magnetofossils, acquire 1-3 orders of magnitude larger ARMs than interacting SD or non-SD particles (Egli and Lowrie, 2002). For the purpose of rock- and sediment magnetic characterization, χ_{ARM}, which is proportional to the concentration of magnetic minerals, is normalized by Mrs, so that the so-called ARM ratio $r_{ARM} = \chi_{ARM}/M_{rs}$ is a parameter that depends only on the magnetic properties of particles and not on their concentration. Non-interacting SD particles are characterized by $r_{ARM} = 1-5$ mm/A, as opposed to $r_{ARM} < 0.2$ mm/A for other magnetic systems (Egli and Lowrie, 2002; Egli, 2004a).

4.2. ARM/IRM analysis of sediment

Magnetofossil-bearing sediments and soils containing SD magnetite are characterized by unusually large ARM acquisition efficiencies, i.e. $r_{ARM} > 1$ mm/A compared to $r_{ARM} < 0.3$ mm/A values which are typical for detrital and dust inputs in sediment (Egli, 2004a). For this reason, r_{ARM} has been used to characterize the magnetic mineralogy of core 848 in a feasibility study of a supernova ^{60}Fe search in sediment (Bishop and Egli, 2011).

Here a similar analysis for sediment core 851 is discussed, using the data originally obtained in addition to 848 by Bishop and Egli (2011), along with a new set of measurements of core 851, spanning the age range $1.7 - 2.4$ Ma, in order to cover the entire range of the ^{60}Fe signal found by Knie et al. (2004), which was re-dated to lower age ($1.9-2.6$ Ma) (Fitoussi et al., 2008). The new dataset comprises 100 samples of about 3 g of sediment from

layers of roughly 10 ka thickness, which were measured at the paleomagnetic laboratory of the LMU Munich in 2013.

The measurement protocol used in this case was slightly different from the one used by Bishop and Egli (2011), which was chosen to measure the remanent magnetization acquired from a demagnetized state after applying a 0.1 T field (i.e., a so-called isothermal remanent magnetization IRM), instead of the saturation remanence M_{rs} that would be acquired in much larger fields, e.g. 1 T, as used here for core 851. A difference between the two magnetizations arises from the magnetic contributions of particles with a coercivity > 0.1 T, such as, for instance, hematite. Results from the two sets of measurements are shown in Fig. (4.4), whereby the systematic difference between mean r_{ARM} values depends on the difference between $\mathrm{IRM}_{0.1\ \mathrm{T}}$ and $\mathrm{IRM}_{1\ \mathrm{T}}$ due to a small amount of high-coercivity minerals.

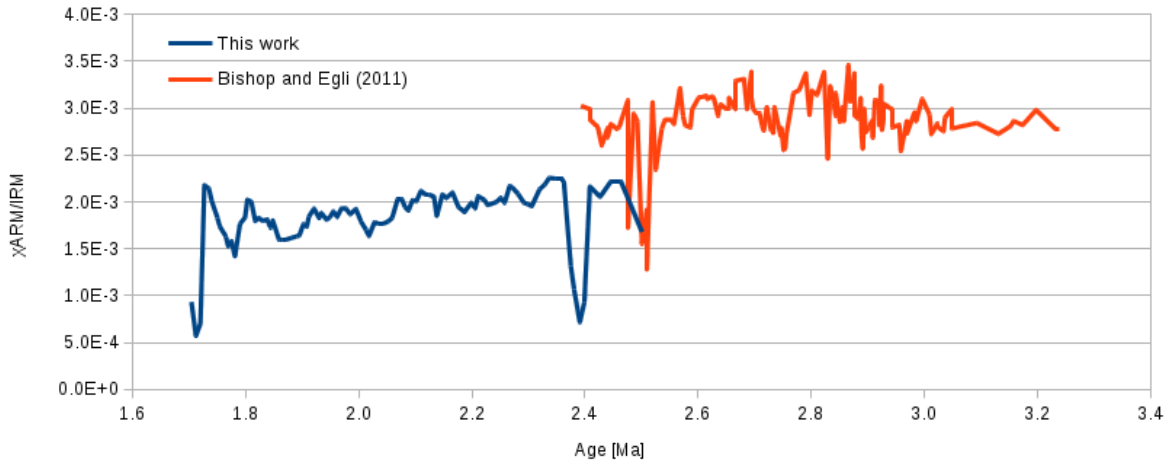

Figure 4.4: χ_{ARM}/IRM data for core 851 plotted over the age of sediment layers.

The most important conclusion that can be drawn from the χ_{ARM}/IRM measurement is that the average values of $\sim 2 \times 10^{-3}$ m/A for this work and $\sim 3 \times 10^{-3}$ m/A for Bishop and Egli (2011) are compatible with the characteristics of magnetofossil bearing sediments and, more generally, of sediment containing mainly SD magnetite particles that are well dispersed in the sediment matrix and therefore unaffected by magnetostatic interactions.

Although χ_{ARM}/IRM measurements do not enable the precise quantification of SD magnetite, due to unavoidable uncertainties of intrinsic values for primary and secondary magnetite particles, a rough upper limit estimate for secondary Fe contained in SD particles can be derived from IRM measurements assuming that the whole remanent magnetization is produced by SD magnetite particles with the ideal hysteresis properties described in Sec. (4.1), i.e. $M_{\mathrm{rs}}/M_{\mathrm{s}} = 0.5$. In this case, the expected concentration of SD Fe can be calculated using

$$c_{\text{SD-Fe}} = \frac{2m_{\mathrm{rs}}}{w\mu_{\mathrm{s}}} \frac{M_{\mathrm{Fe}}}{M_{\mathrm{Fe_3O_4}}} \tag{4.5}$$

where m_{rs} is the IRM, assumed to coincide with the saturation remanence and w is the sample mass, which was typically 4 ± 1 g. $\mu_{\mathrm{s}} = 92$ Am^2/kg is the spontaneous magnetization of magnetite, and M_{Fe} and $M_{\mathrm{Fe_3O_4}}$ are the molar masses of Fe and magnetite, respectively. A plot of the IRM magnetization is shown in Fig. (4.5).

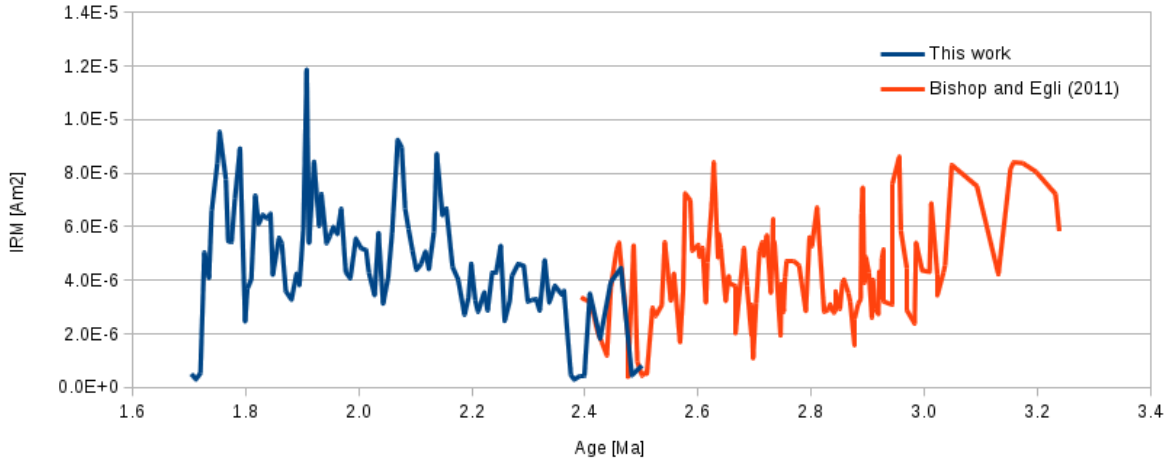

Figure 4.5: IRM data of core 851 plotted over the age of sediment layers.

Down-core fluctuations are partly due to the use of an average sample mass of 4 g, instead of the actual mass, which was not determined for all samples. The average IRM of both data sets is $m_{\mathrm{rs}} \approx 4.5 \times 10^{-6}$ Am^2. The resulting average concentration of SD Fe calculated with Eq. (4.5) is $c_{\text{SD-Fe}} = 1.7 \times 10^{-5}$, corresponding to 17 μg/g. This represents the minimum fraction of sediment expected to contain ^{60}Fe, since SD particles are usually of secondary nature, having been synthesized at the time of ^{60}Fe enrichment. This is also the minimum amount of Fe that a well-designed extraction procedure for AMS samples should remove from the sediment.

Re-evaluation of the data in Bishop and Egli (2011) showed that their estimation of the SD Fe concentration was rather pessimistic: a more careful estimation of the sample mass (averaging over all samples) yielded an average weight of (4 ± 1) g and thus an average of 4 g instead of 5 g as originally published. A summary of all ARM/IRM data containing original and re-evaluated data from Bishop and Egli (2011) and new data from this work can be seen in Tab. (4.2).

Core	Age [Ma]	Dataset	χ_{ARM}/IRM [m/A]	IRM [Am^2]	SD Fe [μg/g]
848	2.4 - 3.2	Bishop (2011) orig.	3.0×10^{-3}	6.0×10^{-6}	19
848	2.4 - 3.2	Bishop (2011) re-ev.	3.0×10^{-3}	7.0×10^{-6}	28
851	2.4 - 3.2	Bishop (2011) par.	2.9×10^{-3}	4.2×10^{-6}	17
851	1.7 - 2.4	this work	1.8×10^{-3}	4.7×10^{-6}	18
851	1.7 - 3.2	Avg. of last two lines	2.4×10^{-3}	4.5×10^{-6}	18

Table 4.1.: Summary of all ARM/IRM results, with all values averaged over the entire dataset each, including the expected fraction of single domain iron: SD Fe. The first line shows the result originally published by Bishop and Egli (2011). Line 2 shows a re-evaluation of that data using a more reliable average sample mass. Line 3 shows the result from the data obtained for core 851 in parallel to the 848 study in Bishop and Egli (2011). Line 4 shows the additional data obtained in this work. Line 5 is the average of the entire core 851 over both data sets of lines 3 and 4.

4.3. FORC measurements

As seen in previous sections, bulk magnetic properties of sediment do not support a rigorous quantitative discrimination between different magnetic mineral sources, providing only qualitative estimates of dominant components. A more precise characterization of ferrimagnetic minerals is obtained with complex measurements based on partial hysteresis loops, which scan the area included by the two branches of the major loop, thereby probing all magnetic states of a sample in a systematic way. Such measurements are time-consuming and therefore not applicable to whole sediment core sections. Here, a specially developed set of partial hysteresis curves in combination with selective chemical extraction were used, in order to obtain complete, quantitative information on primary and secondary Fe sources in a representative sediment sample from core 848.

4.3.1. FORC function and FORC diagrams

High-resolution First Order Reversal Curves (FORCs) are partial hysteresis measurements, which have been established as a valuable technique to probe the entire set of magnetization states contributing to the major hysteresis loop (Egli et al., 2010). Each FORC is prepared by sweeping the applied field from positive saturation to a so-called reversal field H_r ; measurements start at H_r by increasing the applied field H in small steps δH. A set of magnetization curves $M(H_r, H)$ is obtained with the systematic variation of H_r. A set of curves for a magnetofossil-bearing sediment is shown in Fig. (4.6a). Closer inspection (Fig. (4.6b)) shows a kink in each curve, in correspondence with $H = -H_r$. These kinks can be explained by the switching mechanism of isolated SD particles: field sweeping from positive saturation to $H_r < 0$ switches all particles with a coercive field $H_c < |H_r|$ to negative saturation. These particles are switched back in $H = H_c$ until $H = -H_r$ is reached and the original positive saturation is restored. Above this field,

magnetization changes are due only to reversible rotation of the magnetization, with no contribution from switching.

The measured curves define the *FORC function* :

$$\varrho(H_\mathrm{r}, H) = -\frac{1}{2}\frac{\partial^2 M}{\partial H_\mathrm{r} \partial H} = \frac{1}{8}\left[\frac{\partial^2 M}{\partial H_\mathrm{c}^2} - \frac{\partial^2 M}{\partial H_\mathrm{b}^2}\right] \tag{4.6}$$

over $H_\mathrm{r} > H$ (Mayergoyz, 1986), which is usually represented in transformed coordinates $H_\mathrm{c} = (H - H_\mathrm{r})/2$ and $H_\mathrm{b} = (H + H_\mathrm{r})/2$ in a so-called FORC diagram, as sketched in Fig. (4.6c). The coordinate transformation is motivated by the Preisach-Néel model of hysteresis (Preisach, 1935): In this case, the major hysteresis loop is represented as the superposition of infinitesimal elemental contributions consisting of rectangular loops called hysterons. Each hysteron is characterized by a coercive field H_c and is horizontally shifted by a bias field H_b, so that the FORC function coincides with the probability density of H_c- and H_b-values. In general, the hysterons of the Preisach model are mathematical constructs with no physical interpretation, which are used to provide a two-dimensional representation of hysteresis processes. An exception is represented by SD particles, in which case the hysterons represent a convenient approximation of the hysteresis loops of individual particles subjected to a local interaction field H_b (Néel, 1958). A modified version of the Preisach-Néel model (Egli, 2006) accounts for the curved loops of individual SD particles and the dependence of the interaction field on the collective magnetization of all particles. Qualitative FORC models have been developed for MD (Pike et al., 2001a; Church et al., 2011) and PSD hysteresis (Carvallo et al., 2003).

In order to calculate values of the FORC function, a polynomial fit in a square grid with $(2SF + 1) \times (2SF + 1)$ measurement points around the desired value of ϱ is performed, where SF is the so-called smoothing factor (Pike and Fernandez, 1999). For example, a small smoothing factor of 1 will lead to polynomial fits using 9 data points. In general, small smoothing factors preserve high-resolution features of the FORC diagram at cost of a higher measurement noise content and vice-versa. FORC measurements of sediments are particularly critical because of their weak magnetization and the presence of non-regular features requiring a high resolution representation of the FORC diagram.

SD, MD, and PSD domain states are characterized by distinct FORC signatures that enable at least a qualitative discrimination, even in the case of complex magnetic mixtures (Roberts et al., 2000; Pike et al., 2001b). This is particularly important for the case of PSD signatures, because the upper grain size limit for magnetite dissolution by CBD might include small (∼200 nm) PSD particles. (Fig. (4.6d)) also shows the expected FORC function of non-interacting UNISD particles.

The FORC function of linear chains of SD particles, as produced by magnetotactic bacteria, contains particular features that deserve further discussion. The FORC function ϱ_sd non-interacting SD particles (Fig. (4.6d)) is a superposition of an infinitely sharp ridge ϱ_cr along $H_\mathrm{b} = 0$, called the *central ridge* , and a continuous function $\varrho_\mathrm{ur}$that

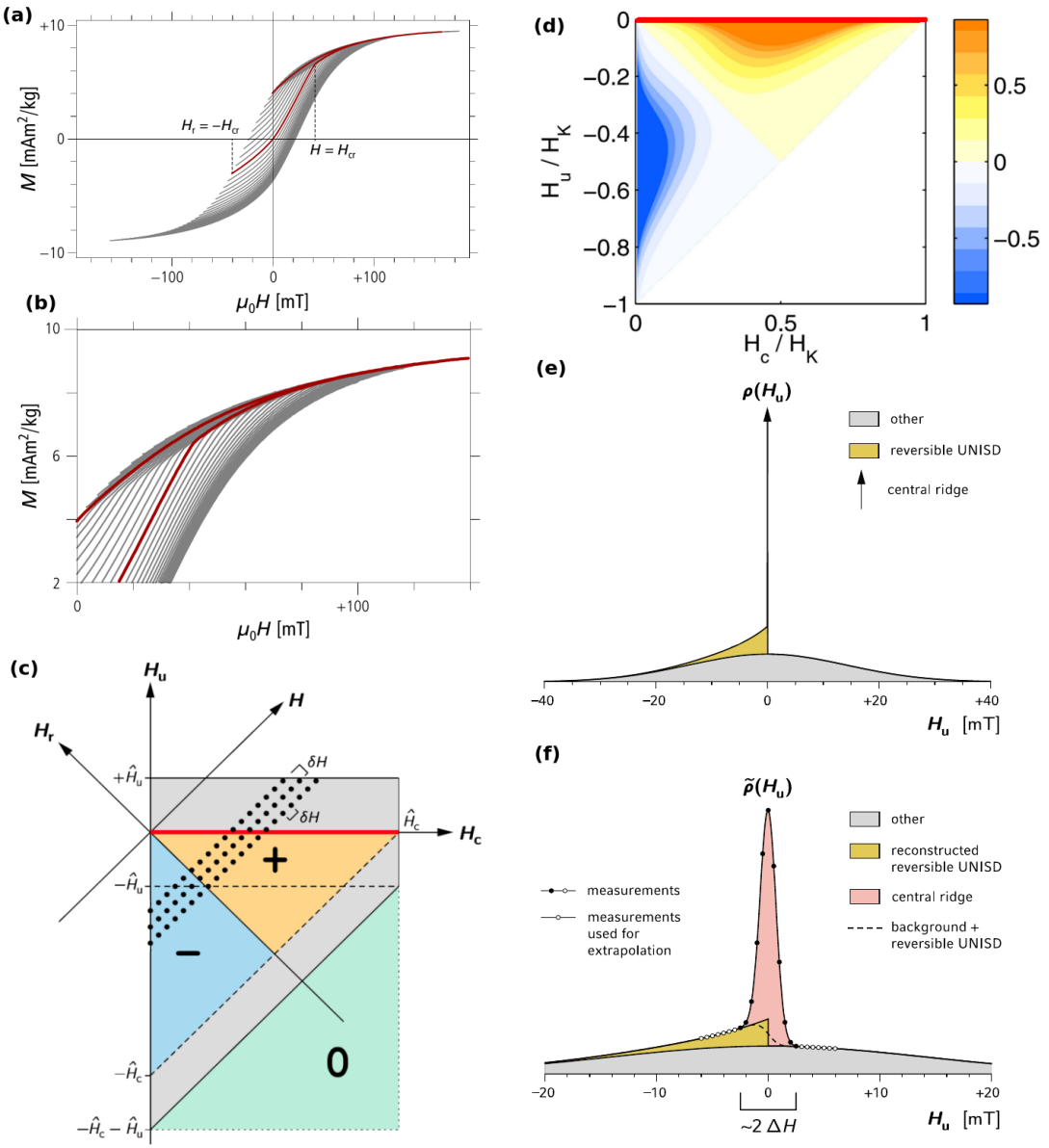

Figure 4.6: (a) FORCs in an untreated sediment sample, every 8th curve is shown. (b) Same as (a), zoomed in to the upper right quadrant. Curves with $H_r = -H_{cr}$ and $H_r = 0$ are highlighted in red. (c) Depiction of FORC space. Dots indicate measurement points for three consecutive FORCs, spaced by δH. Blue and yellow regions are the reversible contribution of non-interacting SD particles. Red line indicates the central ridge. For interacting particles or PSD/MD components, the FORC function extends further (gray area). (d) Theoretical FORC signature of an assemblage of non-interacting UNISD particles. Red line indicates central ridge. Figure adapted from Newell (2005). (e) Vertical cross-section through a FORC function of infinite resolution. Black arrow represents central ridge. Contributions of interacting UNISD particles or PSD/MD particles are shown in gray. (f) Same as (e) for a FORC function with finite resolution ΔH. Sum of the background (gray) and the reversible component (yellow) can be reconstructed by extrapolating measurements shown as open circles (dashed line). Pictures (c), (e), and (f) adopted from Egli et al. (2010).

covers the lower half-plane of the FORC space defined by $H_b < 0$ (Newell, 2005). The central ridge is produced by magnetization jumps in the symmetric hysteresis loops of individual particles (or chains) not biased by interaction fields, while ϱ_{ur} is produced by the reversible rotation of magnetic moments in the external field. The reversible contribution ϱ_{ur} is antisymmetric with respect to the $H_b = -H_c$ diagonal and negative below it. This negative contribution in the lower quadrant shows that the interpretation of the FORC diagram as a probability function of hysteron parameters, while intuitive, can be misleading (negative probabilities).

All contributions to the FORC function in the upper quadrant are associated with interacting SD particles and non-SD particles (Egli et al., 2010). This signature is approximately symmetrical about $H_b = 0$ (Pike and Fernandez, 1999; Carvallo et al., 2005; Muxworthy and Dunlop, 2002). This is illustrated in Fig. (4.6e), as a vertical cross-section through a FORC function of infinite resolution, and in Fig. (4.6f) for finite resolution (Egli et al., 2010).

The central ridge is a characteristic feature of non-interacting SD particles. Its infinite sharpness and amplitude makes it ideally suited for the detection of fossil magnetosome chains, even when mixed with other magnetic contributions in any proportion. Furthermore, it provides a straightforward interpretation of SD particle assemblage in terms of a probability density function $f(H_c)$ of coercivities (Egli et al., 2010):

$$\varrho_{cr}(H_c, H_b) \approx \frac{M_s}{2}\overline{S} f(H_c)\delta(2H_b) \tag{4.7}$$

where M_s is the saturation magnetization, δ the Dirac delta function, and $\overline{S}$ the mean amplitude of magnetization jumps in hysteresis loops of individual particles normalized to unit saturation ($\overline{S} = 1$ for rectangular loops, and $\overline{S} = 0.54$ for randomly oriented, uniaxial SD particles). Eq. (4.7) has immediate practical applications, since the integral over H_b gives the function:

$$\mu_{cr}(H_c) \approx \frac{M_s}{2}\overline{S} f(H_c) \tag{4.8}$$

which is directly proportional to the coercivity distribution. Furthermore, the integral of Eq. (4.8) over H_c defines a magnetization $I_{cr} = M_s\overline{S}/2$ that is proportional to the saturation magnetization of all non-interacting SD particles, regardless of the abundance of other magnetic components (Egli et al., 2010).

In real FORC diagrams of magnetofossil-bearing sediments, the SD signature described above overlaps with continuous contributions arising from other magnetic components. Procedures for separating the central ridge and calculate the corresponding coercivity distribution μ_{cr} are described in Egli et al. (2010) and Egli (2013).

4.3.2. AGFM setup at Bremen University

All FORC measurements in this work were performed at the Alternate Gradient Field Magnetometer (AGFM) setup of the department of Geosciences, Bremen University, Germany. It features a Princeton Measurements MicroMag 2900 AGFM with a fully automated data acquisition system. In an AGFM, the sample is placed at the end of a thin fiber, between a set of 8 copper coils (4 on each side), which generates a small alternating gradient field which exerts an oscillating force on the specimen. This force, which is proportional to the specimen's magnetic moment, is measured by a transducer connected to the thin fiber holding the sample. The DC magnetic field required for hysteresis and other types of measurement protocols is provided by an electromagnet. The main advantage of the AGFM setup over other designs, such as a vibrating sample magnetometer, is the high sensitivity, related to the fact that the AC gradient field is driven at the resonance frequency of the suspended sample mass. Measurement times for regular hysteresis loops are on the order of few minutes. The disadvantages of AGFM systems are the limited sample mass, as well as the application of a gradient field that can interfere with the DC field used for the measurements.

Samples of $\sim 20-30$ mg of sediment were pressed firmly into cylindrical plastic sample holders and sealed with cyanoacrylate glue. The resulting 3×5 mm cylinder was attached to the sample holder of the force-meter with vacuum grease. The AGFM is then calibrated using a sample of known magnetic moment.

4.3.3. FORC parameters and measurement procedure

A field increment of $\delta H = 0.5$ mT and a measurement time of 0.1 s have been used for all measurements. The remaining parameters of the FORC protocol have been chosen so that the measurements extend over 0 mT $\leq H_c \leq$ 120 mT and -120 mT $\leq H_b \leq +63$ mT with 450 partial hysteresis curves (i.e. Hc1= 0 mT, Hc2= 120 mT, Hb1= -40 mT, Hb2= +60 mT, Hcal= 186 mT, Hsat= 300 mT, pause at Hsat= 0.2 s, pause at Hcal= 0.5 s, pause at reversal = 0.5 s, smoothing = 5, see Egli (2013) for an explanation of these parameters). In order to obtain a better signal-to-noise ratio for our rather weak samples ($M_s \approx 10$ mAm^2/kg for the untreated sediment), 4 identical FORC measurements have been performed, each requiring 6 hours, and averaged to produce a single FORC diagram for each sample.

4.3.4. FORC analysis procedure VARIFORC

In the analysis of FORC data, the choice of SF is critical since it determines the number of data points used for polynomial regression. A high SF has the advantage of filtering out high-frequency background (good smoothing) but might not be able to resolve fine structures such as the central ridge. Using a low SF can preserve those structures and is

thus favorable for recognition of the central ridge. In conventional FORC data processing, a single SF is chosen for the entire FORC space and a polynomial regression is performed for each data point over fixed squared grids of $(2SF + 1) \times (2SF + 1)$ points (Pike and Fernandez, 1999) or over the first N nearest neighbors of a given point (Harrison and Feinberg, 2008).

For this work, the FORC processing software VARIFORC, described in Egli (2013), has been used. The main advantage of this protocol over conventional analysis methods is the use of a variable smoothing factor for optimization of the signal-to-noise ratio of the FORC diagram. VARIFORC employs two smoothing factors (s_c horizontal, and s_b vertical), resulting in rectangular grids for weighted regression. Additionally, both s_c and s_b are functions of the FORC coordinates. This results in high-resolution and less smoothing in critical regions (most importantly the central ridge) and less resolution and high smoothing where the amplitude of the FORC function is small. In this way, the low-amplitude part of the FORC function is calculated with a similar signal-to-noise ratio as the high-amplitude central ridge, which is optimally resolved by using the smallest possible vertical smoothing s_b allowed by the noise level. VARIFORC also calculates μ_{cr}, and other integrals of the FORC function.

4.3.5. Sample description

Since FORC measurements and the corresponding analyses are very time-consuming, this study could only be performed on one representative set of sediment samples. The master sample chosen for this purpose consisted of 100 g of dry sediment from core 848, time range 3.2-3.3 Ma, which were homogenized in an agate mortar. The two additional samples of volcanic ash in the original publication (Ludwig et al., 2013) are omitted in this discussion.

Specimen S0 was taken directly from the master sample material without additional treatment. Samples S1-30, S1-40, S1, and S1-60 were subjected to one CBD treatment at 30°C, 40°C, 50°C, and 60°C, respectively. Sample S5 underwent five very strong CBD treatments: two times for 12 hours at 50°C and three times for 24 hours at 80°C. An overview of sample details is shown in Tab. (4.2).

The amount of Fe extracted per gram of sediment ϵ was not determined for all samples, due to the fact that down-scaled versions of the CBD treatment (1/6 of chemicals, same concentrations) versions of the CBD procedure were used for treating smaller sample masses used for magnetic analysis instead of AMS sample production. Accordingly, only 5 g of the master sample were used to produce each CBD treated sample, resulting in extracted Fe masses which were too small to quantify correctly. Only in the case of sample S5, the total Fe_2O_3 mass (4.0 mg) was sufficiently large for an estimation of ϵ. An estimate of ϵ for sample S1 was obtained by treating 30 g of the master sample with a full scale CBD procedure. Using $\sim$ 3 mg of artificial magnetite (40-60 nm), the efficiency of this down-scaled CBD procedure was determined to be $\sim$ 90%.

Sample	Original material	Chemical treatment	ϵ [mg/g]	FORC data?
S0	Sediment	untreated	-	√
S1-30	Sediment	1× CBD, 1 h, 30 °C	n.d.	
S1-40	Sediment	1× CBD, 1 h, 40 °C	n.d.	
S1	Sediment	1× CBD, 1 h, 50 °C	n.d.	√
S1-2h	Sediment	1× CBD, 2 h, 50 °C	n.d.	
S1-12h	Sediment	1× CBD, 12 h, 50 °C	0.10	
S1-60	Sediment	1× CBD, 1 h, 60 °C	n.d.	
S5	Sediment	2× CBD, 12 h, 50 °C +3× CBD, 24 h, 80 °C	0.56	√

Table 4.2.: Overview of all samples prepared for the hysteresis and FORC study. ϵ is defined as the mass of extracted Fe per gram of sample material. ϵ was not determined for all samples (n.d.).

4.4. Sediment analysis

The main goals of this study were the optimization and characterization of the CBD extraction procedure, as well as an examination of the magnetic signature of the sediment samples. The focus of this characterization is on the quantitative analysis of secondary magnetic minerals, such as magnetofossils, which can carry a ^{60}Fe signature.

4.4.1. Bulk magnetic properties

Hysteresis properties have been determined for samples S0, S1, and S5 (Tab. (4.3)). A plot of the hysteresis properties on the Day diagram (Fig. (4.7)) provides a first qualitative evaluation of the dominant domain state of magnetic particles in the untreated sediment (S0) as well as the chemical extraction residue (S1) and the extracted particles (S0-S1). The Day diagram (Day et al., 1977) shown in (Fig. (4.7)) contains theoretical mixing lines between SD and MD particles and between SD and SP particles, as well as empirical end-member and trends defined by non-interacting and interacting SD particles (Dunlop, 2002a,b).

Sample	χ_{hf}	M_s	M_{rs}	$\mu_0 H_c$	$\mu_0 H_{cr}$	M_{rs}/M_s	H_{cr}/H_c
S0	33.2	10.52	4.213	23.41	34.86	0.401	1.489
S1	37.3	2.21	0.649	18.01	42.89	0.239	2.381
S5	31.7	1.30	0.389	21.71	66.53	0.298	3.064
S0–S1	-4.1	8.31	3.564	24.51	32.99	0.429	1.346

Table 4.3.: Magnetic properties of selected samples (susceptibility in mm^3/kg, magnetizations in mAm^2/kg, coercivities in mT). From hysteresis measurements: χ_{hf}-high-field susceptibility, M_s-saturation magnetization, M_{rs}-saturation remanence, $\mu_0 H_c$-coercivity, $\mu_0 H_{cr}$-coercivity of remanence. S0-S1 is the difference between identical measurements performed with S0 and S1.

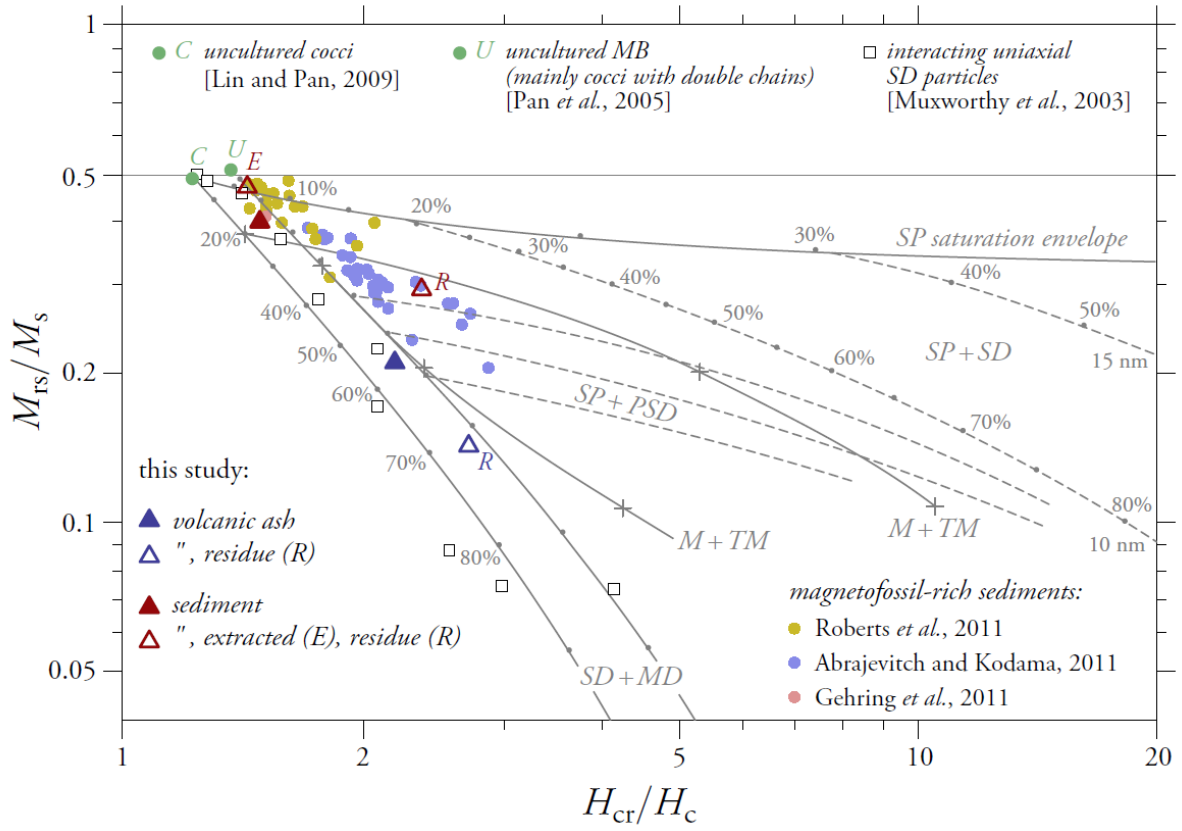

Figure 4.7: Day plot with mixing curves between domain states (lines redrawn from Fig. 12 in Dunlop (2002a), and Fig 9 in Dunlop (2002b), reference data for interacting SD magnetite particles (squares), magnetotactic bacteria (large dots), and samples in this study (blue triangles). Also includes samples from volcanic ash samples V0 and V1 from Ludwig et al. (2013).

The untreated sediment sample S0 plots close the the SD end-member of the diagram, with properties typical for magnetofossil-bearing sediments reported in literature (Abrajevitch and Kodama, 2011; Gehring et al., 2011; Roberts et al., 2011). The CBD-treated sediment sample S1 plots between the mixing curves for SD + MD and SD + SP particles, near the other limit of the data cluster corresponding to magnetofossil-bearing sediments. On the other hand, hysteresis properties of the extracted particles, calculated as difference S0–S1 between the measurements of S0 and S1, match closely those of uncultured magnetotactic bacteria extracted from sediment. This match is a hint that the extraction is targeting the correct particles. However, due to the non-uniqueness of Day diagram interpretations, further investigation based on high-resolution FORC diagrams is required for a precise assessment of CBD-extractable and non-extractable magnetic minerals.

4.4.2. Calibration of CBD extraction strength

As mentioned in the previous chapter, CBD extraction was performed at a temperature of $T = 50°\mathrm{C}$ for $t = 1$ h. This choice resulted from a systematic analysis of the extraction efficiency as a function of T, t, and the concentration of chemicals, whereby T has been found to have the strongest influence.

The optimal T should ideally allow the CBD procedure to dissolve all desired Fe-bearing particles (in our case secondary particles containing ^{60}Fe), and leave other particles intact in order to prevent signal dilution. This is however a very simplified scenario. The following five points, taken from Ludwig et al. (2013) give a more realistic account of the situation:

(1) all exposed iron oxides (e.g. magnetofossils, authigenic magnetite) smaller than a mineral-specific critical size D_1 are dissolved,

(2) all exposed iron oxides larger than a mineral-specific critical size $D_2 > D_1$ are preserved without significant alteration,

(3) all forms of iron oxides embedded in CBD-resistant minerals, regardless of their size, are preserved without alteration,

(4) exposed iron oxides of sizes comprised between D_1 and D_2 are only partially dissolved with consequent alteration of their magnetic properties,

(5) iron oxides embedded in CBD-soluble minerals are partially or entirely dissolved, depending on size and preservation state (e.g. cracks, weathering) of the host mineral.

For an optimal CBD protocol, all ^{60}Fe-bearing, secondary iron-oxides should have a grain size smaller than D_1 to be completely dissolved. Non-^{60}Fe-bearing, primary iron-oxides would need a grain size larger than D_2 to be essentially preserved. In reality, the grain size distributions of those species extend over wide and probably overlapping ranges. This means that a compromise between dissolving a high fraction of secondary minerals (high T), and preventing dissolution of primary minerals (low T) has to be found. Preliminary CBD extraction experiments have been performed with synthetic

magnetite ($40 - 60$ nm) in order to obtain a first hint towards the optimal T. These experiments showed that SD magnetite is completely dissolved by a 1 h CBD treatment only if $T > 30$°C.

The next step consisted in determining the optimal extraction temperature of sediment, according to the amount and nature of the extracted magnetic minerals. For this purpose, hysteresis measurements have been performed after CBD treatments at different temperatures. Hysteresis loops were compared on the basis of the single-valued function obtained from the difference between the upper and the lower branches. This function represents the irreversible component of hysteresis and contains information about the coercivity distribution of magnetic minerals (Fabian and Dobeneck, 1997).

Fig. (4.8a) shows the irreversible component of hysteresis after different CBD treatment protocols. All curves coincide above 0.1 T, which implies that minerals with high coercivity (e.g. hematite) are not affected by the extraction. Additionally, the difference between a 1 h and a 12 h extraction at 50°C is smaller than the difference between 1h extractions at 50°C and 60°C. This underlines that the temperature sensitivity of the procedure is the most critical parameter. The relative contribution of different coercivities at different T can be better seen in Fig. (4.8b), where the curves are normalized by M_{rs}. In general, the relative contribution of the low-coercivity component (i.e. between ± 0.1 T) decreases with increasing extraction strength. In general, the effects of increasing extraction temperatures are more pronounced between 30°C and 40°C, and between 60°C and the maximum treatment strength of sample S5, while similar results are obtained at $40° - 60°$. This extraction efficiency pattern can be explained by a bimodal magnetite grain size distribution with a relatively small overlap between the grain sizes of primary and secondary particles: at low temperatures, secondary minerals are incompletely extracted, yielding a temperature sensitive extraction efficiency, while primary minerals start to be dissolved at high temperatures. Variation of the extraction temperature over $40° - 60°$, on the other hand, affects only the largest secondary and smallest primary particles, whose contribution in terms of magnetization and Fe mass is relatively small. Therefore, $T = 50$°C is the best suited temperature for targeting secondary magnetite particles. The magnetic properties of extracted particles are determined by the difference between the irreversible hysteresis component, corresponding to a given extraction temperature (e.g. 50°C), and the most aggressive extraction, respectively (Fig. (4.8c)). The differences are similar - but not identical - to the irreversible hysteresis component of the untreated sediment. Overall, the measurements shown in Fig. (4.8c) support to the conclusion that most magnetic minerals in the sediment meet conditions (1)-(3) rather than (4) and (5), which means that CBD is an adequate extraction procedure for targeting secondary magnetite particles.

An upper limit for the total saturation remanence of CBD-extracted primary minerals can be estimated assuming that all minerals dissolved between 40°C and 60°C are of primary nature. The difference between M_{rs} values after CBD extraction at 50°C and 60°C

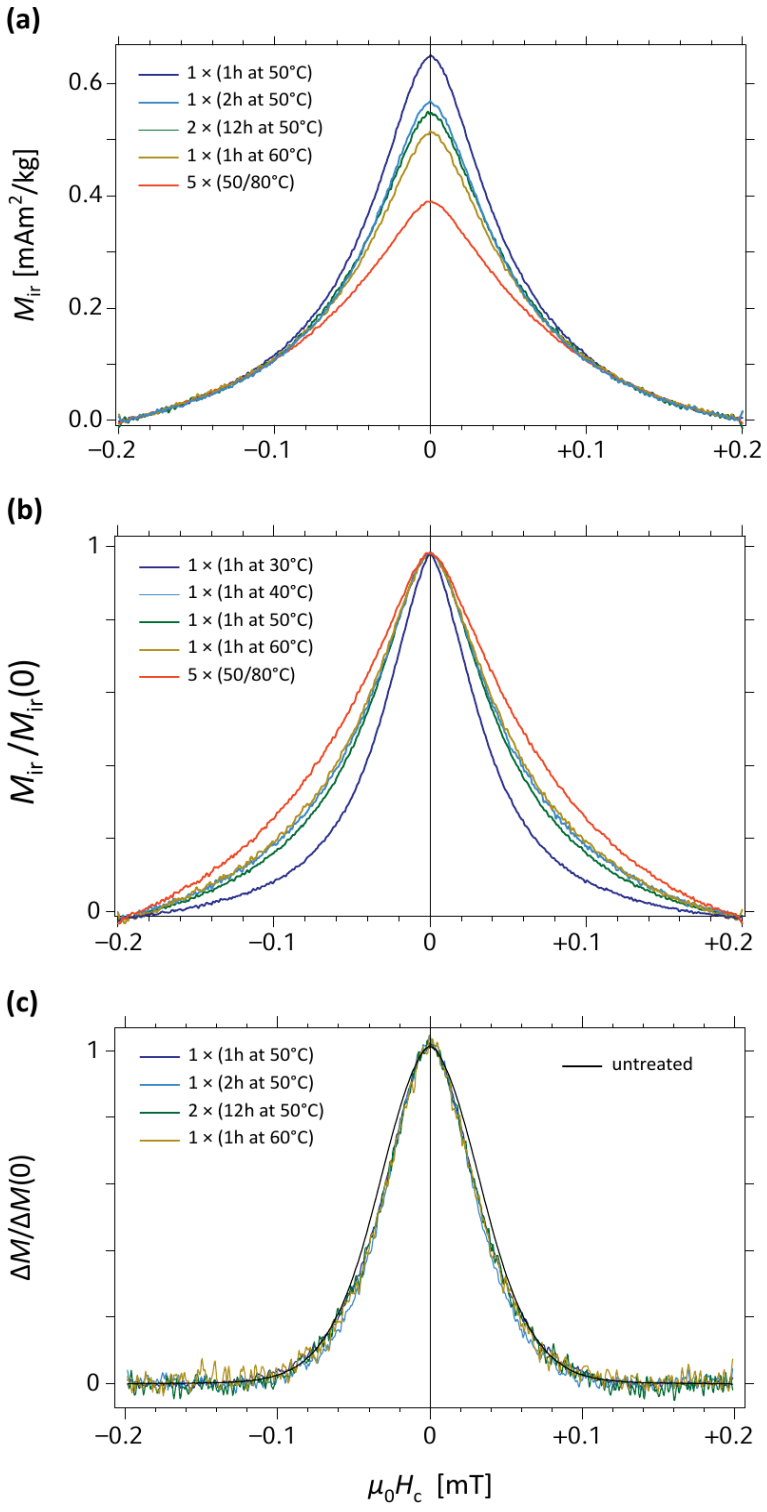

Figure 4.8: (a) Remanent hysteresis components of sediment subjected to CBD treatments with different extraction temperatures. (b) Same as (a), normalized to M_{rs}. (c) Same remanent component as in (a), normalized by their maximum magnetization at $H_c = 0$, after subtraction of the curve corresponding to the most aggressive treatment (S5: five extractions at temperatures up to 80°C). Adapted from Ludwig et al. (2013, Fig. 6).

is about 0.1 mAm^2/kg, while the difference between 40°C and 50°C is only about half. Assuming the amount of primary minerals dissolved drops by 50% every 10°C, a total amount of $1 + 1/2 + 1/4 + ... = 2$ times 0.1 mAm^2/kg, i.e. 0.2 mAm^2/kg is dissolved. Assuming $M_{rs}/M_s = 0.2$ for primary minerals (see S1 in Tab. (4.3)), this corresponds to $\leq$ 8% of the extracted M_s (see S0–S1 in Tab. (4.3)). We thus expect a maximum contribution of unwanted primary magnetic particles of 8% of the total secondary magnetic particles. This is a very good result for the goal of producing ^{60}Fe AMS samples with good extraction efficiency and minimum signal dilution.

4.4.3. FORC results

Hysteresis curves and FORC diagrams of pre- and post-CBD sediment are displayed in Fig. (4.9). Relevant FORC parameters are summarized in Tab. (4.4). As seen in Sec. (4.4.1), hysteresis properties of untreated sediment resemble those of non-interacting SD particles with minor, unknown contributions from particles with other domain states. On the other hand, the hysteresis properties of the CBD-residue suggest important non-SD contributions that cannot be interpreted in more detail.

The FORC diagram of untreated sediment bears the typical SD signatures seen in magnetofossil-bearing sediments, as observed in a variety of ocean and lake sediments (Egli et al., 2010; Itambi et al., 2010; Kind et al., 2011; Roberts et al., 2011; Yamazaki, 2012). This SD signature comprises a prominent central ridge as well as positive and negative contributions in the lower quadrant, which are symmetric about the $H_b = -H_c$ diagonal. Because of its sharpness, the central ridge can be isolated from other FORC contributions (see Fig. (4.10)) for further analysis (Egli et al., 2010; Ludwig et al., 2013). Finally, contributions over the upper quadrant are caused by interacting SD and non-SD particles. Such contributions are approximately symmetrical about $H_b = 0$ (Pike and Fernandez, 1999; Roberts et al., 2000). The total FORC magnetization associated with non-interacting SD particles on one hand, and interacting SD or non-SD particles on the other hand, is obtained by integrating the corresponding FORC signatures - i.e. the isolated central ridge and the upper quadrant - over H_c and H_b (Tab. (4.4)). Accordingly, the fraction of magnetization processes caused by interacting SD particles and non-SD particles can be estimated as $\frac{2I_{uq}}{I_{tot}} \approx 50\%$, where I_{tot} is the integral over the entire FORC space and I_{uq} is the integral of the FORC function over the upper quadrant, extrapolated with a factor 2 for an identical contribution over the lower quadrant.

The effect of the CBD extraction hysteresis properties (Fig. (4.9a)) and FORC signature (Fig. (4.9d)) is very prominent. CBD extraction reduces M_s, M_{rs}, I_{tot}, and I_{cr} to 21%, 15%, 19%, and 4.5% of their original values, respectively. The central ridge signature is significantly reduced, but still visible (Fig. (4.10e)). However, the coercivity distribution Fig. (4.10f) of S1 is (1) very different from the pre-CBD one Fig. (4.10c) (high-coercivity contributions), (2) similar to a volcanic ash sample examined in Ludwig et al. (2013), and

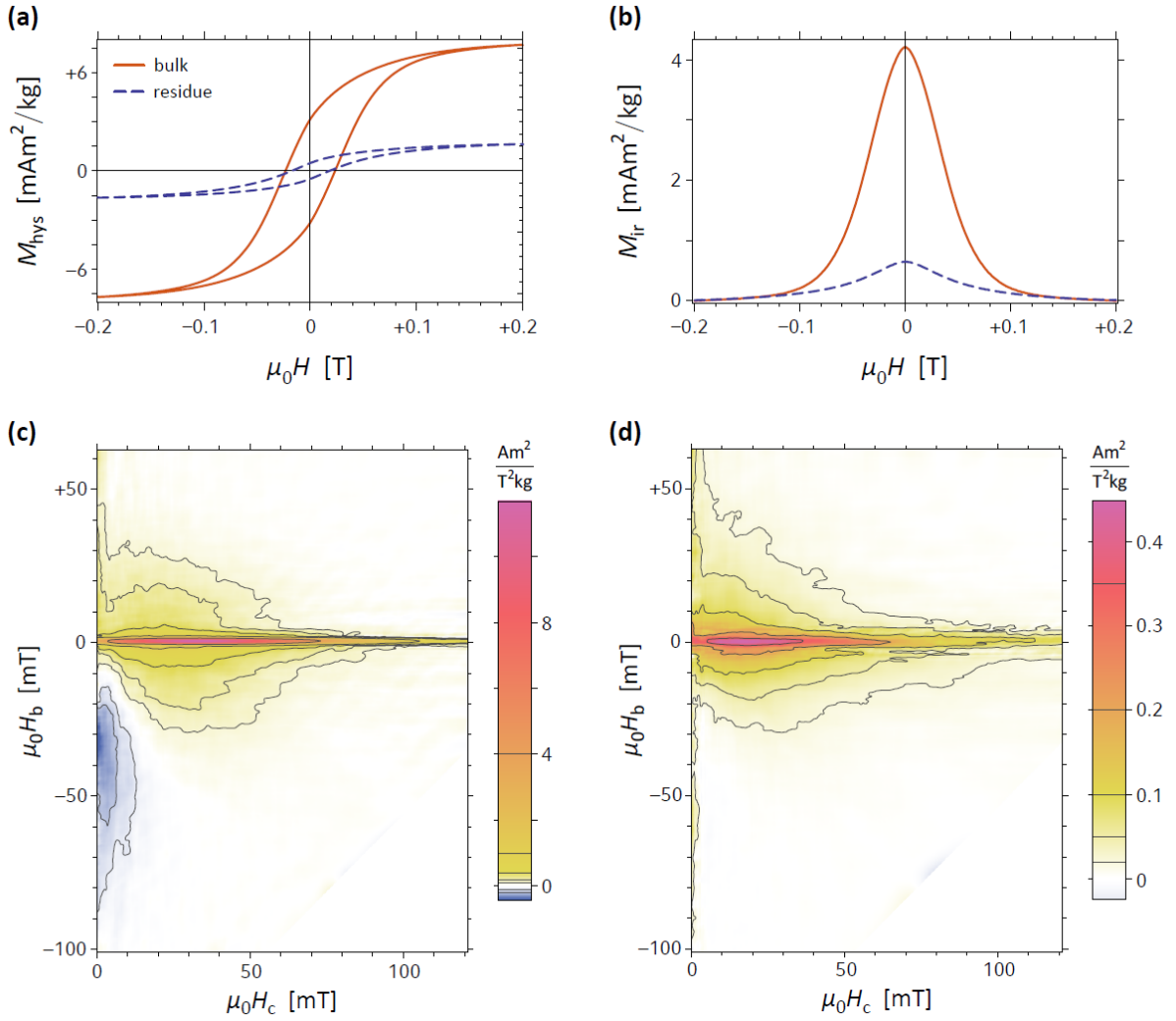

Figure 4.9: Hysteresis and FORC properties of sediment before (bulk, sample S0) and after (residue, sample S1) CBD extraction. (a) Hysteresis loops after paramagnetic correction with the approach-to-saturation law described in Fabian (2006). (b) Remanent components of the loops in (a). (c) FORC diagram of S0 (field increment: 0.5 mT, VARIFORC processing parameters: $s_{c,0} = 7$, $s_{b,0} = 3$, $s_{c,1} = s_{b,1} = 7$, $\lambda_c = \lambda_b = 0.07$). (d) FORC diagram of S1 (field increment: 0.5 mT, VARIFORC processing parameters: $s_{c,0} = 7$, $s_{b,0} = 5$, $s_{c,1} = s_{b,1} = 11$, $\lambda_c = \lambda_b = 0.1$).

(3) similar to the post-CBD coercivity distribution obtained from DC demagnetization. After subtraction of the central ridge, the FORC signature of S1 Fig. (4.10d) is characterized by triangular contour lines, which are typical for PSD magnetite particles (e.g. Roberts et al., 2000). This allows to conclude that the CBD extraction, by removing 95% of the central ridge signature, dissolves SD particles (such as magnetofossils and other secondary iron oxides), which are dispersed in the sediment matrix and not embedded in host-minerals. The residual FORC signature after CBD extraction is compatible with PSD magnetite particles which are too large to be completely dissolved by CBD, and a small amount of unextractable SD particles, probably protected from dissolution by embedding in a silicate matrix. This signature is compatible with volcanic ash inputs from the Andes (Ludwig et al., 2013).

	S0	S1	S0-S1	S5	Ely6
I_{tot}	3.965	0.743	3.214	0.408	
I_{cr}	2.241	0.120	2.121	0.062	
I_{uq}	0.930	0.301	0.629	0.162	
I_{neg}	0.343	0.013	0.330	0.016	
I_{ur}	0.450	0.075	0.451	0.051	0.106
M^*_{rs}	4.169	0.622	3.245	0.374	0.508
$\overline{S}$	0.83-0.90	0.67 ± 0.04	0.83-0.86	0.59 ± 0.06	0.70-0.80
$I_{\mathrm{tot}}/M_{\mathrm{s}}$	0.374	0.336	0.439	0.313	0.454
$I_{\mathrm{cr}}/M^*_{\mathrm{rs}}$	0.579	0.192	0.666	0.164	0.478
$I_{\mathrm{cr}}/I_{\mathrm{tot}}$	0.553	0.161	0.627	0.151	0.495
$I_{\mathrm{uq}}/M^*_{\mathrm{rs}}$	0.240	0.483	0.188	0.432	0.244
$I_{\mathrm{neg}}/M^*_{\mathrm{rs}}$	0.089	0.021	0.110	0.042	0.120
$M_{\mathrm{rscr}}/M^*_{\mathrm{rs}}$	0.60-1.00	–	0.77-1.00	–	0.60-1.00

Table 4.4.: All FORC related properties obtained for samples S0, S1, S5, S0-S1 (difference between identical measurements for S0 and S1), and for comparison, lake sample Ely6 from Egli et al. (2010). Magnetizations are given in $\mathrm{mAm^2/kg}$, except for Ely6, where the unit is $\mu\mathrm{Am^2/kg}$. The quantities calculated from the FORC function are: I_{tot}–total integral, I_{cr}–central ridge contribution, I_{uq}–integral over the upper quadrant after central ridge subtraction, I_{neg}–integral over negative contributions, I_{ur}–reversible non-interacting SD contribution, M^*_{rs}–saturation remanence deduced directly from FORC measurements, $\overline{S}$–the mean jump amplitude, and M_{rscr}–saturation remanence of particles contributing to the central ridge.

4.4.4. FORC analysis of CBD-extract

Since the CBD extraction at 50°C for 1 hour has been shown remove the desired SD component from the sediment without significant dissolution of unwanted magnetic minerals, the difference of identical measurements of samples S0 and S1 can be interpreted as the magnetic signature of CBD-extractable minerals. This provides the possibility of interpreting the origin of the magnetic Fe fraction in AMS samples prepared with the CBD

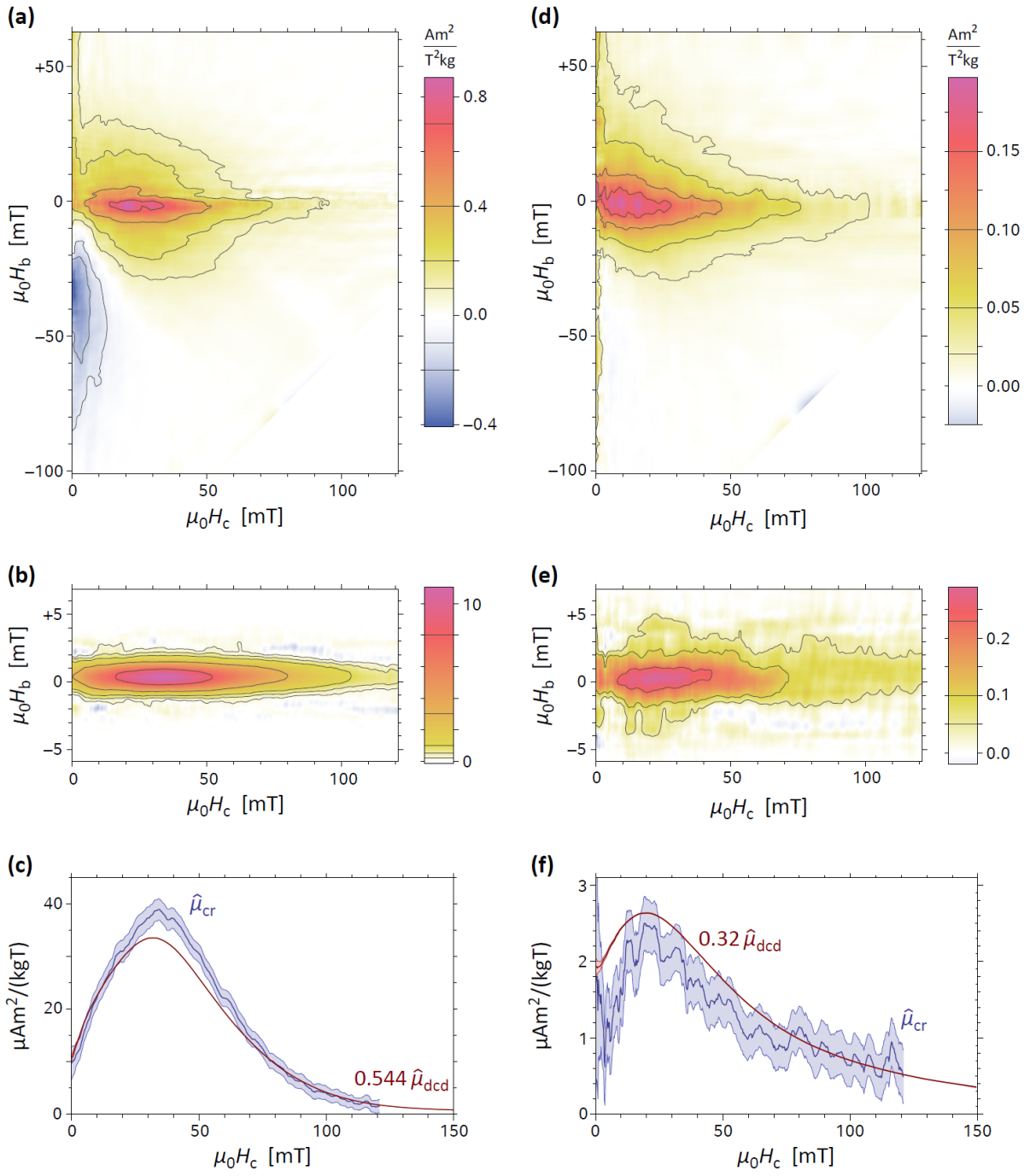

Figure 4.10: Detailed FORC analysis of sediment before (left plots) and after (right plots) CBD extraction. (a,d) FORC diagrams after central ridge subtraction, (b,e) central ridges, represented with 20x vertical exaggeration, (c,f) central ridge coercivity distributions $\hat{\mu}_{cr}$ (blue line) and coercivity distributions $\hat{\mu}_{dcd}$ from DC demagnetization (red line), scaled to fit the high-coercivity range of the central ridge. Confidence intervals (shaded) are given as ± 2 standard errors.

method. For this purpose, the FORC function of S0-S1 was calculated (see Fig. (4.11a)) and all corresponding parameters are listed in Tab. (4.4).

FORC function of S0-S1

The FORC function of S0-S1 (Fig. (4.11a)) is similar to that of S0, confirming that magnetite in this sediment occurs predominantly in form of extractable SD particles. Non-interacting SD particles associated with the central ridge (Fig. (4.11d)) are responsible for $\sim 67\%$ of all magnetization processes, recorded by FORC measurements. Remaining magnetization processes contribute to the upper quadrant of the FORC diagram (Fig. (4.11b)), which is characterized by elliptical contour lines typical for interacting SD particles.

The interpretation of FORC contributions unrelated to the central ridge is facilitated by the possibility to exclude large (> 1 μm) PSD and MD particles, which are not CBD extractable. Therefore, FORC contributions in the upper quadrant must be associated with < 1 μm PSD or interacting SD particles. Similar FORC signatures have been reported in magnetofossil-bearing lake sediments (Egli et al., 2010; Kind et al., 2011), marine sediments (Roberts et al., 2011, 2012; Yamazaki, 2012), and a concentrate of wild-type magnetotactic bacteria (Roberts et al., 2012). FORC measurements of the magnetotactic bacteria concentrate are particularly interesting, because non-SD contributions can be excluded in this case. Therefore, FORC contributions over the upper quadrant have been tentatively attributed to collapsed magnetosome chains.

The FORC signature extending over the upper quadrant is expected to be symmetric, or quasi-symmetric, about $H_\mathrm{b} = 0$, as seen in samples of interacting SD particles (Pike and Fernandez, 1999; Carvallo et al., 2005; Chen et al., 2007) and < 1 μm magnetites (Muxworthy and Dunlop, 2002). Consequently, it extends over the lower quadrant as well, where it overlaps with the reversible contributions of non-interacting SD particles. The lower quadrant is therefore not perfectly antisymmetric with respect to the $H_\mathrm{b} = -H_\mathrm{c}$ diagonal (Fig. (4.11b)) The total positive and negative contributions are $+0.802$ and -0.358 mAm^2/kg, respectively). The reversible contribution $\hat{\varrho}_\mathrm{ur}$ of SD particles can be estimated by subtracting the upper quadrant signature, extrapolated to the lower quadrant on the basis of the assumed symmetry about $H_\mathrm{b} = 0$:

$$\hat{\varrho}_\mathrm{ur}(H_\mathrm{c}, H_\mathrm{b} \leq 0) = \hat{\varrho}_0(H_\mathrm{c}, H_\mathrm{b}) - \hat{\varrho}_0(H_\mathrm{c}, -H_\mathrm{b}) \tag{4.9}$$

where $\hat{\varrho}_0$ is the measured FORC function from which the central ridge has been removed (Fig. (4.11b)) (hats over symbols are used to distinguish estimates gained from measurements, e.g. $\hat{\varrho}_0$). The reversible contribution reconstructed with Eq. (4.9) (Fig. (4.11c)) is close to the ideal case with identical positive and negative contributions (± 0.454 mAm^2/kg) that are symmetric about the $H_\mathrm{b} = -H_\mathrm{c}$ diagonal.

The central ridge distribution

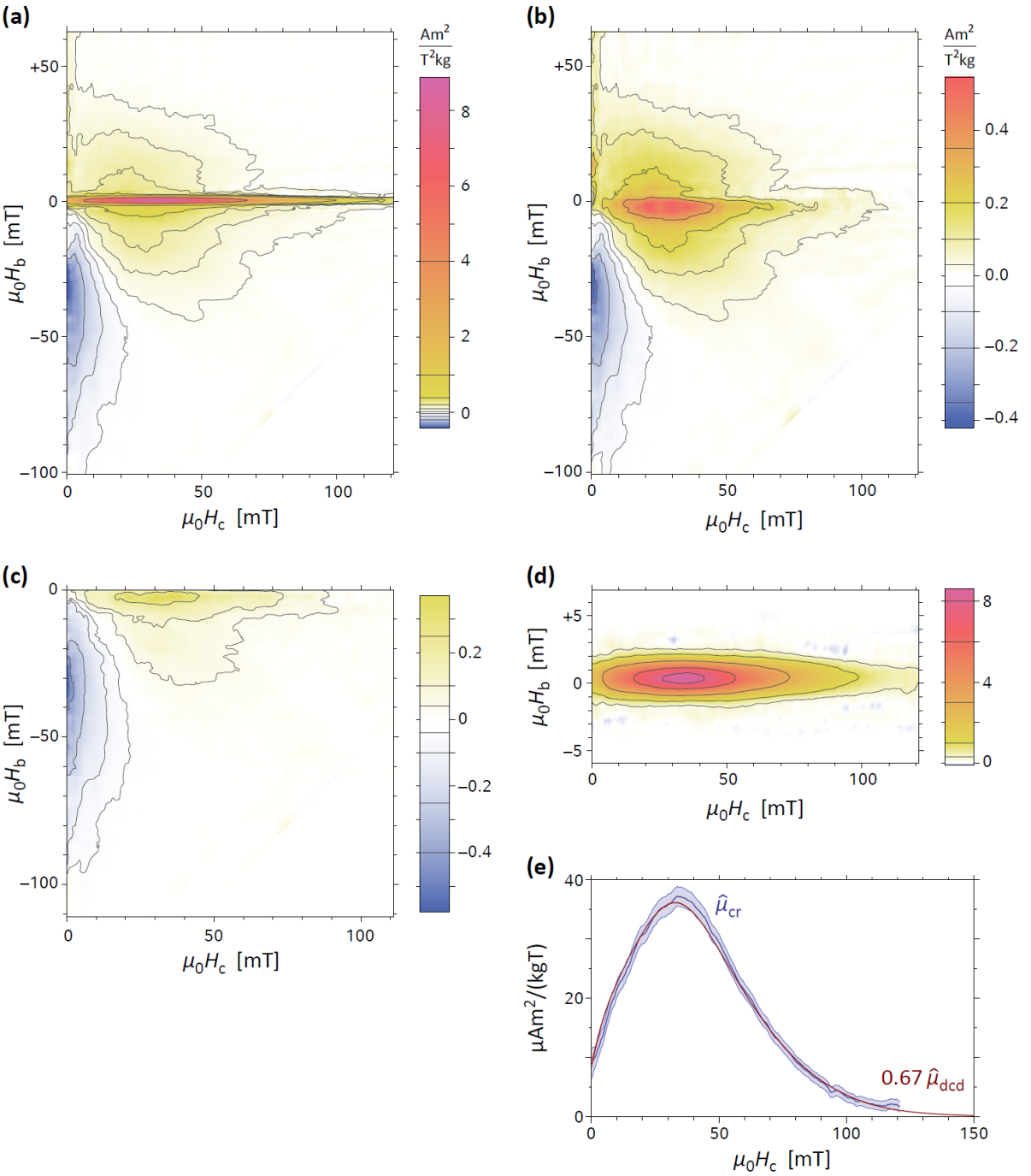

Figure 4.11: FORC properties of ferrimagnetic minerals extracted from sediment with a single CBD treatment at 50°C, calculated as differences between identical measurements of samples S0 (bulk) and S1 (residue). (a) FORC diagram, (b) FORC diagram after central ridge subtraction, (c) Reconstructed reversible SD contribution $\hat{\varrho}_{\mathrm{ur}}$, (d) central ridge, represented with 20x vertical exaggeration, (e) central ridge coercivity distribution $\hat{\mu}_{\mathrm{cr}}$ (blue line) and coercivity distribution $\hat{\mu}_{\mathrm{dcd}}$ from backfield demagnetization (red line), scaled to fit the high-coercivity part of the central ridge. Confidence intervals (shaded) are given as ±2 standard errors.

$$\hat{\mu}_{\mathrm{cr}}(H_{\mathrm{c}}) = 2 \int_{-\infty}^{+\infty} \hat{\varrho}_{\mathrm{cr}}(H_{\mathrm{c}}, H_{\mathrm{b}}) \mathrm{d}H_{\mathrm{b}} \tag{4.10}$$

(Fig. (4.11e)), obtained by integrating the central ridge contribution $\hat{\varrho}_{\mathrm{cr}}$ over H_{b} (Fig. (4.11d)), is equal to the coercivity distribution of non-interacting SD particles, multiplied by the mean amplitude $\overline{S}$ of the magnetization jumps in normalized single-particle hysteresis loops (Egli et al., 2010; Egli, 2013).

4.4.5. Central ridge magnetization

The integral of the central ridge coercivity distribution over H_{c} can be written as $I_{\mathrm{cr}} = 0.5\, M_{\mathrm{s}} \cdot \overline{S}$, where M_{s} is the saturation magnetization of all SD particles contributing to the central ridge, and $\overline{S}$ is the mean jump amplitude of normalized single-particle hysteresis loops. Because M_{s} is directly related to the concentration of of SD particles, I_{cr} can be used to estimate the total Fe mass contained in such particles, provided that an estimate of $\overline{S}$ is available.

$\overline{S}$ depends on the shape of single-particle hysteresis loops. For example, rectangular loops are characterized by $\overline{S} = 2$ (i.e. the difference between the saturated states ± 1). Randomly oriented SD particles with uniaxial magnetic anisotropy, on the other hand, are characterized by $\overline{S} = 0.54$ if thermal activation effects are negligible. Thermal activations tend to produce more squared loops and increase $\overline{S}$, up to the limit case of $\overline{S} = 1$ for small SD particles that are almost superparamagnetic. The switching mechanism of chains of SD particles, such as magnetosomes, is different from that of isolated SD particles, and tends to produce rectangular hysteresis loops with values of $\overline{S}$ more close to 1. An estimate of $\overline{S}$ can be derived from the FORC diagram, as detailed in Ludwig et al. (2013). This estimate is based on the following equations:

$$\begin{aligned} \overline{S} &= 1 - \frac{I_{\mathrm{ur}}}{M^*_{\mathrm{rs}}} \\ \frac{M_{\mathrm{rscr}}}{M^*_{\mathrm{rs}}} &= \frac{I_{\mathrm{cr}}}{M^*_{\mathrm{rs}} - I_{\mathrm{ur}}}, \end{aligned} \tag{4.11}$$

where M_{rs} is the saturation remanence deduced from FORC measurements, M_{rscr} is the (unknown) saturation remanence of SD particles contributing to the central ridge, I_{cr} is the integral of the isolated central ridge, and I_{ur} is the integral of reversible SD contributions to the lower quadrant of the FORC diagram. Estimates of $\overline{S}$, obtained from Eq. (4.11), as well as from a different method described in Ludwig et al. (2013), are listed in Tab. (4.4). Estimates obtained for the extracted particles (S0-S1) range from $\overline{S} = 0.83$ to $\overline{S} = 0.86$. These estimates are compatible with SD particles subjected to thermal activations and enable a relatively precise calculation of the associated Fe concentration, as shown later

in this section.

Origin of secondary magnetite particles

Secondary magnetite particles almost coincide with the CBD-extractable fraction analyzed in the previous sections, i.e. a mixture of non-interacting and interacting SD particles. The origin of such particles is further investigated with a coercivity analysis of the central ridge. This analysis is based on the representation of a coercivity distribution as linear combination of elemental distributions associated to so-called magnetic components, i.e. magnetic particle ensembles that share similar properties (e.g. shape and volume) associated with a common origin (Robertson and France, 1994; Kruiver et al., 2001; Egli, 2003; Heslop and Dillon, 2007). It was this kind of analysis that enabled the first identification of magnetofossils through similarities of the corresponding coercivity components with the coercivity distributions of cultured magnetotactic bacteria (Egli, 2004a). Details of such analysis for S0-S1 are discussed in Ludwig et al. (2013) and summarized in the following.

The central ridge coercivity distribution has been modeled with three components whose properties agree with those commonly found in magnetofossil-bearing sediments, i.e. a low-coercivity component (EX) with median $H_c \approx 19$ mT, and two components with median $H_c \approx 43$ mT (BS) and $H_c \approx 72$ mT (BH). These components are commonly found in freshwater and marine sediments (e.g. Abrajevitch and Kodama, 2009, 2011; Yamazaki and Ikehara, 2012). Components BS and BH with their narrow coercivity distributions have been attributed to chains of equidimensional and elongated magnetosomes, respectively (Egli, 2004a,b; Egli et al., 2010; Heslop et al., 2014).

The narrow BS and BH coercivity distributions can be explained by the uniform magnetic anisotropy of magnetosome chains resulting from tightly controlled magnetosome shape, size, and distances. The interpretation of the low-coercivity component EX is more difficult. Low coercivity and large distribution width, along with its occurrence in the central ridge, point to SD particles with poorly constrained, small intrinsic magnetic anisotropy, such as those formed by chemical precipitation in aqueous solution, either inorganically (Maher, 1988; Fairve et al., 2004), or by mediation of dissimilatory metal-reducing bacteria (Lovley et al., 1987; Moskowitz et al., 1989; Sparks et al., 1990).

The coercivity range of the interacting SD signature over the upper quadrant of the FORC range is similar to that of components EX and BS, and with the coercivity distribution of artificially collapsed magnetosome chains (Kobayashi et al., 2006), so that these two components could, at least in part, also be associated with fossil chain collapse.

Both interpretations of the coercivity components lead to similar origins of secondary particles produced during Fe redox cycling in sediment. As such, they are expected to incorporate ^{60}Fe in a similar manner.

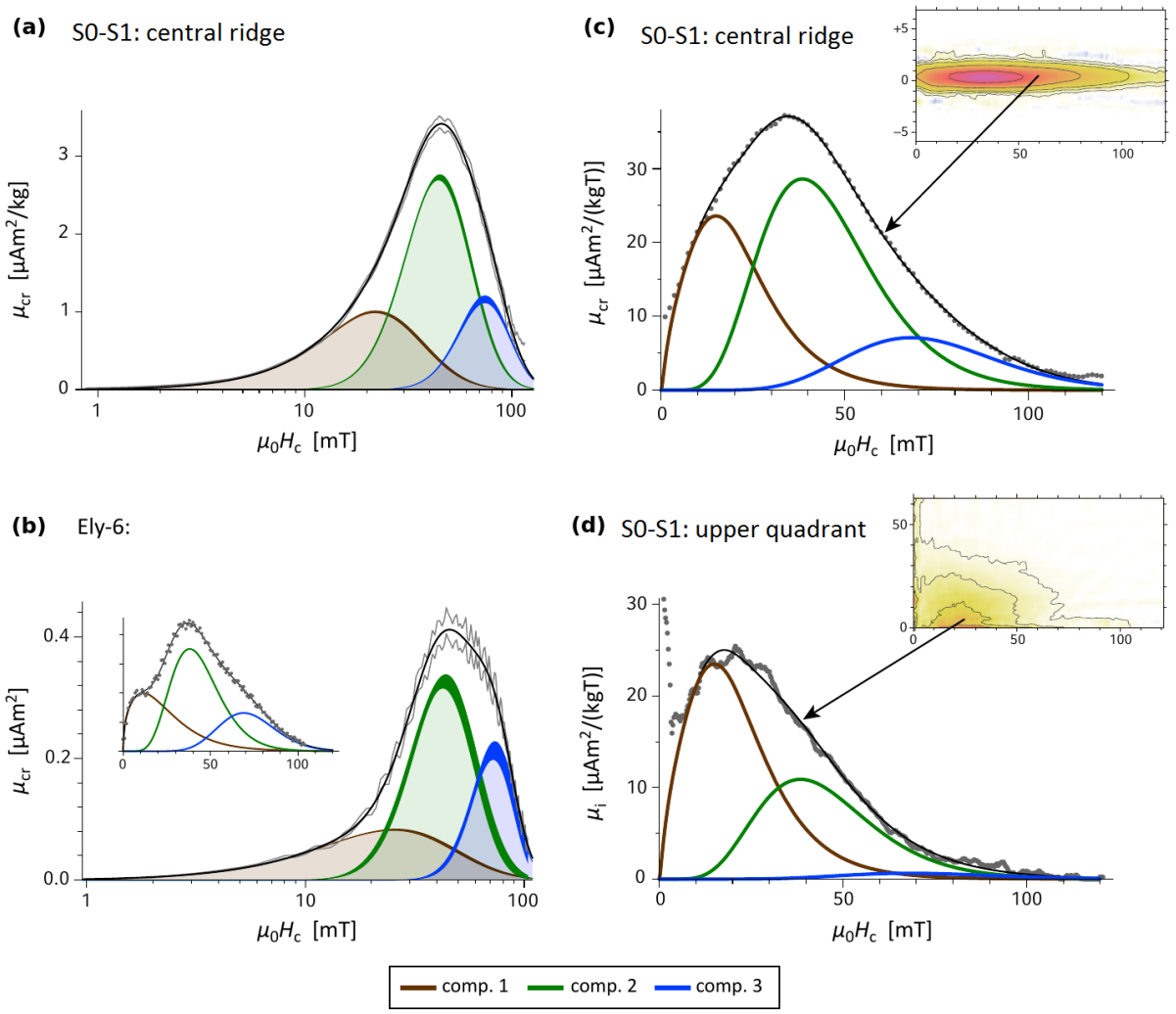

Figure 4.12: Analysis of central ridge coercivity distributions derived from FORC measurements of (a) CBD-extractable sediment particles (S0–S1), and (b) untreated lake sediment (Ely-6, Egli et al., 2010) on a logarithmic field scale as pair of gray lines delimiting the confidence interval given by ±2 standard errors. Insert of (b) shows the same distributions on a linear field scale. The distributions are fitted with three coercivity components (colored lines). The magnetization of each component is given by the shaded area under the corresponding curve. Thickness of colored lines represents the confidence interval of the fitting model (Egli, 2003). The sum of the three components is shown as thin black line. (c) Same as (a) on a linear scale. (d) Same as (c), but for the upper quadrant contribution. Inserts of (c) and (d) show the part of the FORC function used to calculate the distributions. Figure adapted from Fig. 10 and Fig. 11 from Ludwig et al. (2013).

Component	I_{cr}	I_{cr} (%)	$\mu_0 H_{1/2}$	σ	q	p
S0–S1	2.143	100	-	-	-	-
Comp. 1	0.67 ± 0.03	31	19 ± 0.6	0.32 ± 0.01	0.57 ± 0.1	(2)
Comp. 2	1.11 ± 0.03	52	43 ± 0.5	0.17 ± 0.03	(0.73)	(2)
Comp. 3	0.36 ± 0.01	17	72 ± 2	0.13 ± 0.05	(0.71)	(2)
Ely-6	0.244	100	-	-	-	-
Comp. 1	0.069 ± 0.01	28	20 ± 3	0.42 ± 0.1	0.54 ± 0.2	(2)
Comp. 2	0.122 ± 0.01	50	42 ± 1	0.16 ± 0.1	(0.73)	(2)
Comp. 3	0.053 ± 0.02	22	71 ± 2	0.11 ± 0.2	(0.71)	(2)
Egli (2004)	-	-	-	-	-	-
Comp. EX	-	-	18.2 ± 2.5	0.346 ± 0.013	0.607 ± 0.051	-
Comp. BS	-	-	43.1 ± 3.0	0.184 ± 0.017	0.728 ± 0.069	-
Comp. BH	-	-	72.0 ± 3.5	0.106 ± 0.009	0.710 ± 0.010	-

Table 4.5.: Results of central ridge coercivity analysis for S0–S1 and a magnetofossil-rich lake sediment (Ely-6, (Egli et al., 2010)). I_{cr} is the magnetization carried by the corresponding coercivity component and by the whole central ridge (in mAm^2/kg for S0–S1 and μAm^2 for Ely-6), $H_{1/2}$ is the median field, and σ, q, and p are parameters controlling the shape of the coercivity distribution on a $\log_{10}$ field (σ for the width, q for the skewness, and p for the squareness), see Egli (2003) for details. Parameters in parentheses have been kept fixed. Mean parameters for components EX, BS, and BH identified from the coercivity analysis of ARM and IRM demagnetization curves of several marine and freshwater sediment samples (Egli, 2004a) are shown for comparison.

4.4.6. Quantification of secondary minerals

The saturation magnetization M_s obtained for the extract S0-S1 (Tab. (4.3)) can be used to estimate the mass concentration of low-coercivity secondary minerals. Assuming pure magnetite composition, the mass concentration of iron in SD particles in S0-S1 can be calculated as

$$c_{\text{Fe-SD}} = (1 - \epsilon_p)\epsilon_{Fe} M_s/\mu_s = 6.0 \times 10^{-5} \text{ [grams Fe per gram sediment]} \quad (4.12)$$

where ϵ_s is the mass concentration of iron in magnetite and $\mu_s = 92$ Am^2/kg its spontaneous magnetization. Considering that the CBD extraction yield of sample S0 was 0.1 mg per g of sediment and assuming a 90% efficiency for the chemical preparation method (slightly higher than for a full scale CBD procedure), $\sim 55\%$ of the the extracted iron is originates from ferrimagnetic minerals.

A quantitative estimate of the magnetofossil concentration is more difficult to obtain, because of the uncertain origin of coercivity component EX. Accordingly, the saturation magnetization of magnetofossils is comprised between that of components BS and BH derived from the central ridge of S0-S1, and the bulk M_s. A lower magnetofossil concentration limit is thus given by:

$$c_{\text{Fe-MTB}} > 2\epsilon_{\text{Fe}} \frac{M_{\text{BS}} + M_{\text{BH}}}{\mu_{\text{s}} \overline{S}} \tag{4.13}$$

where $\overline{S} \approx 0.86$ (Tab. (4.4)) is the mean amplitude of magnetization jumps in normalized single-particle hysteresis loops, M_{BS} and M_{BH} are the magnetizations of the corresponding components determined by coercivity analysis (Tab. (4.5)), and the factor 2 derives from $M_{\text{rs}}/M_{\text{s}} = 0.5$ for non-interacting uniaxial particles. Using the values reported in Tab. (4.4) and Tab. (4.5) we obtain $c_{\text{Fe-MTB}} > 2.7 \times 10^{-5}$, corresponding to $> 27\%$ of all CBD extractable iron and $> 24\%$ of all extracted iron. Furthermore, it was shown in Ludwig et al. (2013) that this corresponds to a typical number of $\sim$1000 living cells/cm^3 and a lifetime of individual cells of $0.4 - 20$ days. This is the first reliable, quantitative estimate available on the life cycle of magnetotactic bacteria in marine sediment.

4.4.7. Summary of magnetic characterization results

The combination of the highly selective CBD Fe-extraction technique and novel FORC analysis method enabled a precise identification of primary and secondary magnetic minerals in the sediment horizons of cores 848 and 851 where a supernova ^{60}Fe signature can be expected. Even though only a small fraction of the total Fe in the sediment sits in magnetic minerals, important clues have been obtained about the suitability of the chosen sediment cores as ^{60}Fe reservoirs. The following points summarize the main results of this study:

1. An optimal CBD protocol for Fe extraction from secondary magnetic minerals has been developed. This protocol employs digestion of 35 g of sediment in a 200 ml aqueous solution containing 3.4 g of sodium bicarbonate (B), 12.6 g of sodium citrate (C), and 5.0 g of sodium dithionite (D), at 50°C for 1 hour.
2. The CBD method has been shown to be highly selective towards the extraction of fine magnetite particles of secondary origin, with a maximum contamination from primary magnetic Fe-bearing minerals of $\epsilon_{\text{p}} \approx 7.4\%$. Contaminations from non-magnetic primary minerals are more difficult to estimate: some information is gained from the comparison of high-field susceptibilities χ_{hf} before and after CBD-extraction. χ_{hf} is mainly controlled by paramagnetic minerals, which represent the vast majority of all iron-bearing minerals. The difference in χ_{hf} between pre- and post-CBD values (S0–S1 in Tab. (4.3)) is not consistent with strong dilution of primary iron-bearing minerals within the relatively large errors (± 2 mm^3/kg).
3. The use of the new FORC analysis algorithm VARIFORC allowed for the discovery of a central ridge signature in CBD-treated sediment, where it corresponds to $\sim 19\%$ of the saturation remanence. This hints either to the central ridge being part of the FORC signature of true PSD particles, or to the presence of truly SD particles in the sediment after extraction. The latter can be explained by a fraction of SD particles being embedded in non-CBD dissolvable host-minerals, probably of volcanic origin.

4. Comparison of pre- and post-CBD FORC measurements gives an estimate of the total contribution of primary minerals to the saturation magnetization (30%), the saturation remanence (23%), and the central ridge (3.6%) of the investigated pelagic carbonate. In this example, the whole central ridge of untreated sediment can be attributed to secondary iron oxides without large errors.
5. Differences between pre- and post-CBD measurements define the magnetic signature of CBD-extractable (secondary) minerals. This signature is formally equivalent to a mixture of strictly non-interacting SD particles on one hand, and PSD or strongly interacting SD particles on the other, which contribute to ∼77% and ∼23% of the saturation remanence, respectively. Contributions with intermediate properties (e.g. slightly interacting particles) are absent, as deduced from the sharpness of the central ridge. Magnetic properties of the central ridge are compatible with a mixture of isolated SD particles and isolated magnetosome chains. The coercivity distribution derived from the central ridge can be modeled with three components (called EX, BS, and BH after Egli, 2004a), previously identified with non-interacting SD particles on the basis of elevated ARM ratios. These components have been originally attributed to authigenic magnetite (EX), and to magnetofossils with different elongations (BS and BH). The same components are identifiable in the central ridge of a magnetofossil-bearing lake sediment, supporting the original interpretation of BS and BH. The distance between magnetosome chains, deduced from the residual vertical width of the central ridge, is at least as large as the typical size of magnetotactic bacteria, which means that chain aggregation after cell dissolution was prevented by the sediment matrix.
6. Comparison of the marine sediment sample S0 with another magnetofossil-bearing lake sediment sample (Ely-6) shows that the two materials share similar FORC signatures (Ludwig et al., 2013). In particular, the estimated fraction of saturation remanence associated with the upper quadrant of the FORC diagram is the same in both cases. This signature is related to CBD-extractable minerals, setting an upper grain size limit of ∼1 μm for particles contributing to the FORC function over the upper quadrant. A detrital origin for such particles is unlikely, because different relative contributions of primary and secondary magnetite would be expected for the two samples. Therefore, the most probable source for the observed FORC contributions over the upper quadrant is represented by strong magnetostatic interactions arising from double chains and chain bundles, as observed in some types of magnetotactic bacteria, and/or magnetosome aggregates resulting from chain collapse.
7. Ferrimagnetic minerals contain $\sim 60\%$ of the total CBD-extractable iron, for an estimated mass concentration of 6.0×10^{-5}, of which $> 45\%$ is of magnetofossil origin. The remaining part of CBD-extractable Fe is probably bounded to amorphous or poorly crystalline substances. Accordingly, magnetotactic bacteria produced $> 27\%$ of all CBD extractable iron, which demonstrates their non-negligible contribution

to the sedimentary iron cycle. Not less than 10^8 cells/cm^3 were needed to produce the observed magnetofossil concentration. Combining this estimate with the sedimentation rate and the typical range of depths where magnetotactic bacteria occur in pelagic sediments, $> 2 \times 10^4$ new bacteria per cm^3 sediment must have been produced every year until the sediment could no longer host living cells and the typical life-span of individual cells is estimated to be 0.4-20 days.

8. The CBD-extracted ferrimagnetic minerals are of secondary origin and contain ∼55% of all extractable Fe. The remaining part of extractable Fe is likely to be of secondary origin for the most part, but lacking precise information on the non-ferrimagnetic fraction, it is conservatively assumed that it comes from primary minerals. In this case, $c_{\mathrm{AMS}} = {}^{60}\mathrm{Fe/Fe}$ is reduced by a factor < 2 with respect to the case where all Fe for AMS is of secondary origin. For comparison, the use of a technique that leaches all Fe in the sediment would yield a > 100 times smaller c_{AMS}, which would be below the AMS detection limit. This underlines the advantage of using a well-tuned, selective extraction technique such as CBD. The selectivity of the procedure is once more underlined in Fig. (4.13) by comparing the composition of the untreated sediment (Fig. (4.13a)) with the final AMS sample (Fig. (4.13b)).

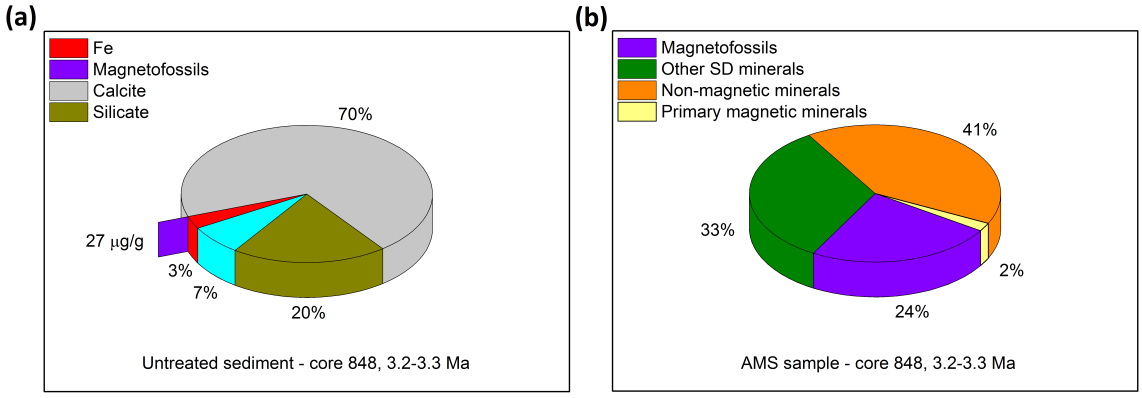

Figure 4.13: (a) Mass fractions of the dry, untreated sediment. Only 27 μg/g (lower limit) of the mass is carried by Fe from magnetofossils. (b) Mass fractions of the final AMS sample. Due to the high selectivity of the CBD procedure, at least 24% of the Fe in the sample originates from magnetofossils.

4.5. Magnetic extraction from sediment

The possibility of a magnetic extraction of Fe-bearing particles from sediment in order to produce AMS samples has also been considered and is part of a work that is still in progress. The Fe yield of from the current extraction setup is still too low to produce suitable AMS samples. Nevertheless, magnetic extracts provide the opportunity to observe the magnetic fraction under the electron microscope, serving as independent confirmation

of the magnetofossil nature of the FORC signature. The Magnetic extraction setup is described in the following, along with a short description of electron microscopy results.

4.5.1. General idea

SD magnetite particles and intact chains of such particles (magnetofossils), are magnetically equivalent to a dipole with magnetic moment $\vec{\mu}$. In an external magnetic field $\vec{B}$, the particle experiences a torque

$$\vec{D} = \vec{\mu} \times \vec{B}, \tag{4.14}$$

and a force

$$\vec{F}_{\mathrm{SD}} = -\vec{\nabla}\left(-\vec{\mu} \cdot \vec{B}\right). \tag{4.15}$$

In homogeneous fields (i.e. $\vec{\nabla}\vec{B} = 0$), the particle's magnetic moment will align with $\vec{B}$ without experiencing a net force, as it is the case for a compass needle in the Earth's magnetic field. On the other hand, magnetic extraction relies on strong gradients attracting ferromagnetic particles toward a magnetic field source.

As seen in Eq. (4.15), the extraction force is proportional to $\vec{\nabla}\vec{B} = 0$ and to the magnetic moment $\vec{\mu}$ of particle. This moment depends in turn on $\vec{B}$ in a manner that is determined by the hysteresis properties of the particles. In case of paramagnetic particles, which represent the main ingredients of most sediments, $\vec{\mu} = V \cdot \chi_{\mathrm{para}} \cdot \vec{B}/\mu_0$, where V is the particle's volume and χ_{para} the paramagnetic susceptibility, so that

$$\vec{F}_{\mathrm{para}} = V \cdot \chi_{\mathrm{para}} \cdot \vec{B} \cdot \vec{\nabla}\vec{B} \cdot \frac{1}{\mu_0}. \tag{4.16}$$

On the other hand, ferro- and ferrimagnetic minerals saturate in moderate fields, so that $\vec{\mu} = V \cdot M_{\mathrm{s}}$, where M_{s} is the spontaneous magnetization. The resulting force on a ferromagnetic particle is thus

$$\vec{F}_{\mathrm{ferr}} = V \cdot M_{\mathrm{s}} \cdot \vec{\nabla}\vec{B}. \tag{4.17}$$

Accordingly, the ratio between the extraction forces exerted on para- and ferro-/ferrimagnetic minerals is given by

$$\frac{|\vec{F}_{\mathrm{ferr}}|}{|\vec{F}_{\mathrm{para}}|} = \frac{\mu_0 \cdot M_{\mathrm{s}}}{\chi_{\mathrm{para}} \cdot |\vec{B}|} \propto \frac{1}{|\vec{B}|}. \tag{4.18}$$

This result demonstrates that the selectivity of magnetic extractions towards ferro- and ferrimagnetic minerals is inversely proportional to $|\vec{B}|$, while the extraction force is proportional to $\vec{\nabla}\vec{B}$. Therefore, magnetic extraction require strong magnetic field gradients with smallest possible field amplitudes. Such gradients are typically obtained along the

sharp edges of strongly magnetized bodies (e.g. the tip of a magnetic needle).

Therefore, efficient extraction setups allow suspensions of magnetic particles to flow as close as possible to the sharp edges of a ferromagnetic material. Practical realizations include magnetic fingers (i.e. soft iron studs attached to a strong permanent magnet), steel wool in a moderate magnetic field, and magnetized Fe wires.

4.5.2. Extractor setup

Samples for electron microscopy were prepared using an extraction setup which was set up in Garching with only minor modifications of a pre-existing setup at Bremen University (Dobeneck et al., 1987). For this purpose 7 g of sediment were well dispersed with an ultrasonic rod in 2 l of water. The sediment was constantly pumped from the water container through a glass extraction vessel by a peristaltic pump. The vessel has a water-tight opening in which a Fe finger with a teflon coating can be inserted. By attaching strong permanent magnets to outer finger end, the finger tip is magnetized and generate a strong field gradient causing magnetic particles to collect on the teflon surface. After about 1 day of extraction, the finger is removed and the magnetic particles can be harvested.

Optionally, the sediment can be pre-treated with 20% acetic acid to remove most calcite. This has two advantages: firstly, the calcite removal increases the total amount of sediment that can be used per extraction from 7 g to about 30 g, and secondly, magnetic particles initially embedded in the calcite matrix now have increased mobility and thus are more likely to be extracted.

Although this extractor design has proven to be effective for the production of samples for electron microscopy, it is not well suited for AMS sample production, since the concentration of Fe in the extract is low (few %), and the amount of extract harvested per day and per extractor is only few mg.

4.5.3. TEM analysis

Magnetic extraction techniques suffer from two major problems. Firstly, the magnetic extraction tends to be more efficient for large ferrimagnetic minerals of primary origin, due to the proportionality of the extraction force to particle volume. Especially in case of incomplete extractions, the magnetic extract is likely enriched of unwanted primary Fe oxides. Secondly, small magnetic particles are often electrostatically attached to large non-magnetic particles, as for instance magnetite on clay (Galindo-González et al., 2005). These problems have been assessed by analyzing magnetic extracts with the transmission electron microscope (TEM) setup at the TUM Chemistry Department. The electron microscopy was performed by Dr. Marianne Hanzlik.

Sample description

For the electron microscopy study, a set of 3 magnetic extractions were performed on 7 g sediment aliquots taken from the $2.40 - 2.62$ Ma age interval of core 851. The sediment was not pre-treated before the extraction. Extracts were harvested after 24 h and the typical extract masses were $\sim 1 - 2$ mg.

SEM of magnetic extract

An initial low-resolution overview of the microscopic composition of the extract was obtained using scanning electron microscopy (SEM). The setup also features EDX analysis, allowing the live determination of the elemental composition of individual grains by comparison of characteristic x-ray line intensities. The bulk of the extract consists of large carbonate and silicate grains (Fig. (4.14a)). Although these minerals are not ferromagnetic, small grained Fe-bearing minerals can stick to larger non-magnetic particles and contribute to their unwanted extraction. This can be clearly seen in Fig. (4.14b,c), where Fe-bearing minerals are visible as bright spots on larger grains. Large Fe-bearing minerals of primary origin can also be found in the extract (Fig. (4.14b)). However, the limited resolution of SEM prevents the direct observation of magnetofossils and other secondary Fe oxides.

TEM of magnetic extract

The observation of individual secondary magnetite particles is possible using high-resolution TEM. An estimate of particle composition can be obtained by electron diffraction analysis. TEM images show abundant particles compatible with bacterial magnetosomes (Fig. (4.15)) made of magnetite, as confirmed by diffraction analysis. Individual magnetosomes are usually clustered (Fig. (4.15d)). Furthermore, linear chains are rare, and often composed of dissimilar crystals (Fig. (4.15b)). This shows that the original magnetic structure deduced from FORC analysis (i.e. isolated chains of magnetofossils) is not preserved through magnetic extraction and subsequent transfer to TEM grids, so that caution should be used when interpreting TEM images. Nonetheless, the observation of magnetosomes by TEM is an important independent confirmation of the results obtained from magnetic measurements. Estimation of the Fe mass in extracted magnetosomes is very difficult. Assuming the magnetosome fraction in the magnetic extract to be 40-80% by rough optical evaluation of TEM images, the magnetosome concentration appears to be compatible with magnetic measurements.

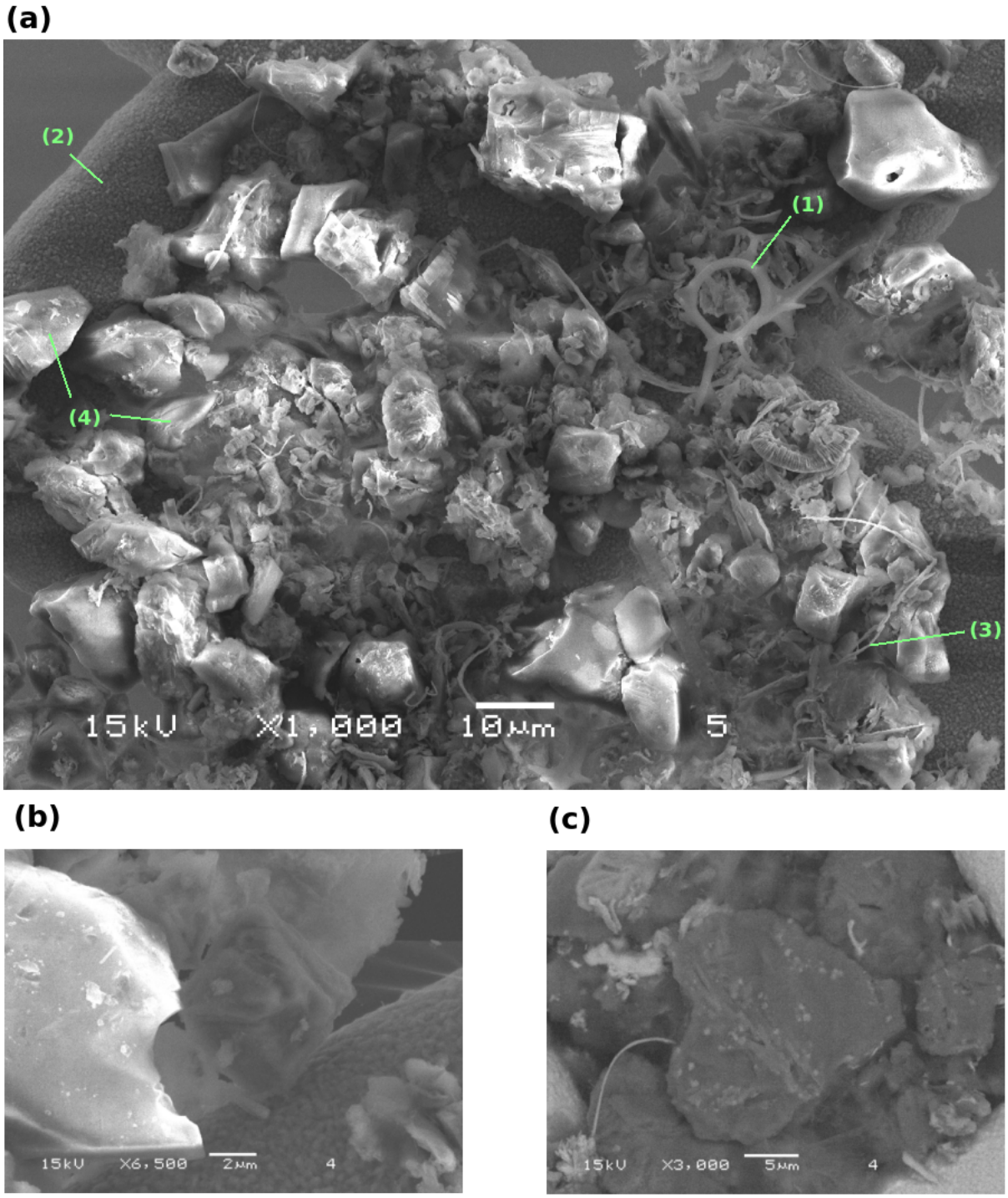

Figure 4.14: SEM images of magnetic extract of sediment from core 851, 2.40-2.62 Ma. (a) Bulk image showing various components of the extract. Highlighted are (1) Diatoms, (2) Copper sample holding grid, (3) Fe-Cr filaments of unknown origin (probably contamination acquired during extraction), (4) Large grains of mainly $CaCO_3$ and SiO_2. (b) High resolution image of a Titanomagnetite grain (in the center, dark grey). (c) Image of a large silicate grain (dark) with bright spots of Fe-bearing small-grained minerals sticking to it.

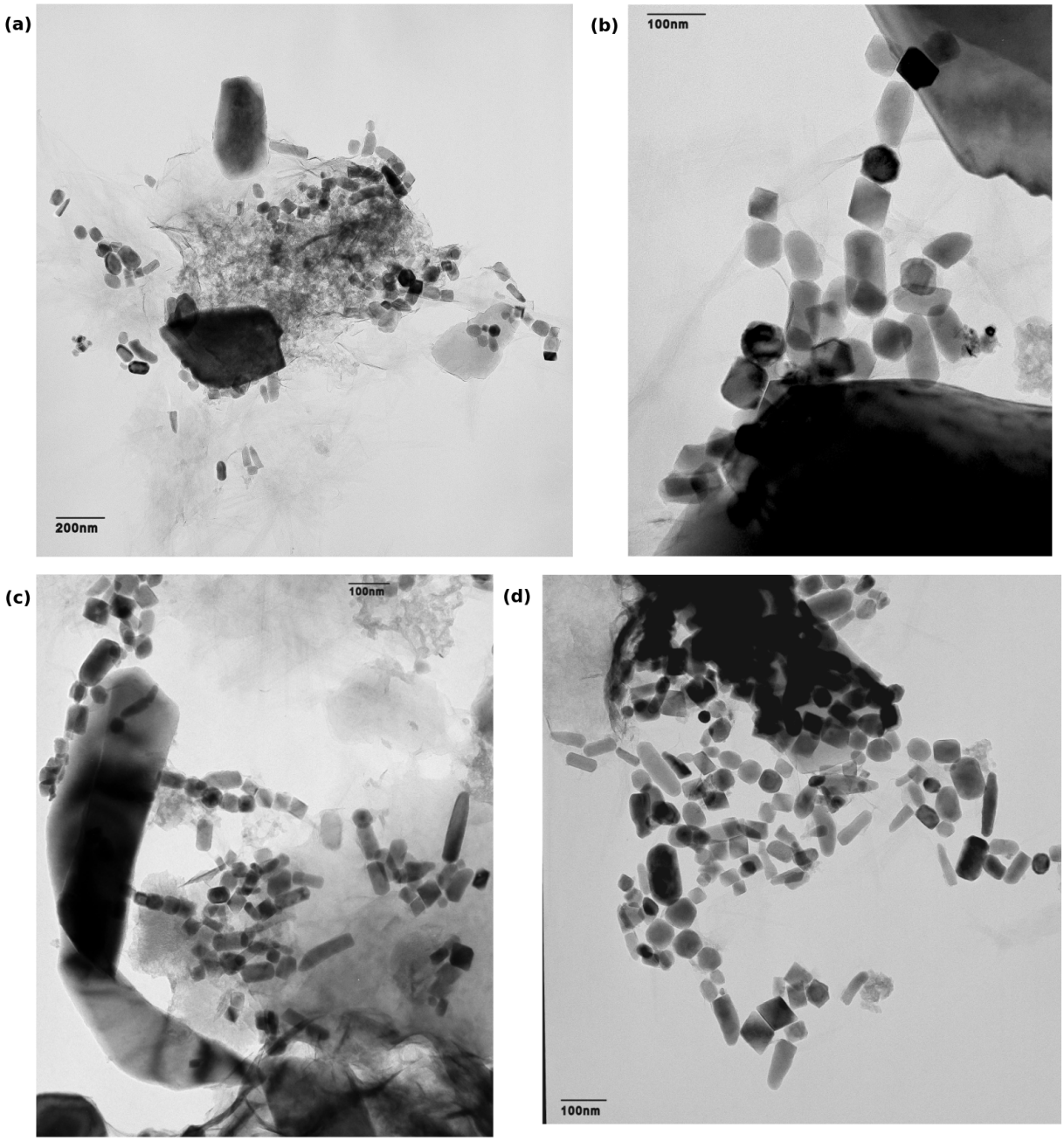

Figure 4.15: TEM images of magnetic extract of sediment from core 851, 2.40-2.62 Ma.

5. AMS setup and measurements

This chapter begins with a short introduction to AMS, based on Tuniz et al. (1998), which is followed by a description of the GAMS setup and the ^{60}Fe measurement procedure.

5.1. Introduction to AMS

AMS is an ultrasensitive ion counting technique that is used to determine extremely low concentrations of (mostly) long-lived radioisotopes, with typical half-lives in the range 10^3 a $\lesssim T_{1/2} \lesssim 10^9$ a. The fundamental difference between AMS and decay counting experiments is that the atoms of the radioactive species itself are detected, not their decay. This allows AMS to outperform decay counting in cases of isotopes with long half-lives and small available sample masses.

Muller (1977) suggested that trace amounts of ^{14}C and ^{10}Be could be measured with the use of accelerators. Shortly after, two groups reported success measuring ^{14}C in natural samples for the first time (Bennett et al., 1977; Nelson et al., 1977). Still today, carbon-dating using ^{14}C is the most widely known and used AMS application, however, over the decades AMS has evolved into a technique with wide-spread applications. Today (2015) there are about 100 AMS laboratories worldwide (many of which focus on ^{14}C), with applications reaching up to the heaviest isotopes. The applications of AMS are different for each isotope and span the fields of material sciences, extraterrestrial physics, geophysics, bio-medicine, environmental science, and nuclear astrophysics.

The goal of an AMS measurement is the determination of the atom ratio of the number of particles of a long-lived radioactive species to a stable isotope of the same element (e.g. ^{14}C/^{12}C, ^{60}Fe/^{54}Fe). To this end, typically, few milligrams of sample material are put in a sample holder and inserted into a (usually Cs-sputtering) ion source. The beam is then extracted as negative ions and injected into the beamline. Almost all AMS systems feature a tandem accelerator with terminal voltages reaching from 200 kV (modern table-top machines) up to 14 MV. Such high voltages accelerate the beam to high energies (MeV range), which is necessary for two reasons: firstly, the high ion beam energy is necessary to employ nuclear physics particle identification techniques in order to distinguish the radioisotope from other ions. Secondly, the electron stripping process (either foil or gas stripping) in tandem accelerators suppresses any molecular background (Coulomb explosion).

On the high-energy side of the accelerator, AMS systems normally feature a combina-

tion of magnetic dipoles, electrostatic analyzers, and/or Wien-velocity filters, to separate all undesired particles with different mass number out of the beam and thereby allow only the interesting species through. For many measurements, the main challenge is the correct identification of individual atoms using a particle detection system. This is necessary since, in most AMS measurements, background is expected from isobars and from particles with the same magnetic rigidity as the target AMS isotope. Particle identification is normally achieved by measurements of energy loss (e.g. in an ionization chamber), energy (e.g. in a silicon detector), and/or velocity (using a time of flight measurement). Atoms of the radioisotope in question can then be counted individually. A comparison of the number of counted ions with the stable ion beam current of the reference isotope then yields the atom ratio of interest in the sample material. A quantitative result can be achieved by comparing the measured concentrations of a sample with those in a standard material (known concentration) and in a blank (no, or little radioisotope expected). The production of suitable standard and blank materials is, depending on the radioisotope in question, one of the most important and challenging issues for AMS. The isotopic ratios which can be reached with this ultrasensitive technique are as low as few 10^{-17} (e.g. in the case of ^{60}Fe).

The challenge of performing an AMS measurement is different for every isotope. In most cases, it is desired to achieve a good enough background suppression in order to observe the radionuclide of interest at natural concentrations. On the one hand, there are relatively easy measurements, like ^{14}C, where the isobar ^{14}N doesn't form negative ions in the source and is thus already completely suppressed. This means that even low-energy AMS machines are able to reach good sensitivities, and can focus on other challenges, like measurement precision and lowering necessary sample masses. On the other hand, there are isotopes which are much more demanding to measure. In cases like ^{53}Mn, ^{60}Fe, or ^{93}Zr, the stable isobars (^{53}Cr, ^{60}Ni, and ^{93}Nb, respectively), are difficult to suppress in the ion source and thus, have to be separated in the detection system, e.g. using passive absorbers or a gas-filled magnet. Additionally, for heavier nuclei, the relative difference in mass between neighboring isotopes gets smaller, which makes them harder to separate, favoring large accelerator systems with high terminal voltage and thus higher ion energies.

5.2. AMS setup GAMS in Garching

The MLL in Garching, Germany, features a 14 MV Tandem accelerator, which is used in various fields of research. The accelerator supplies ion beams of most elements to about 15 different experimental stations in the fields of nuclear physics, astro-particle physics, medicine, and others. There are two beamlines dedicated to AMS (Fig. (5.1)). The Actinide-beamline is equipped with a powerful Wien-filter and a Time-of-Flight (TOF) detection system, specifically designed for the detection of heavy isotopes, such as actinides (Famulok et al., 2015) and superheavy elements (Ludwig et al., 2012). The mea-

surements of ^{60}Fe for this work were carried out at the GAMS setup (Knie et al., 1997, 2000). It features an optional TOF line, a gas-filled magnet, and a multi-anode ionization chamber, and is specifically designed to provide isobar suppression for AMS isotopes in the medium mass range. The following section describes the key elements of the GAMS beamline in detail.

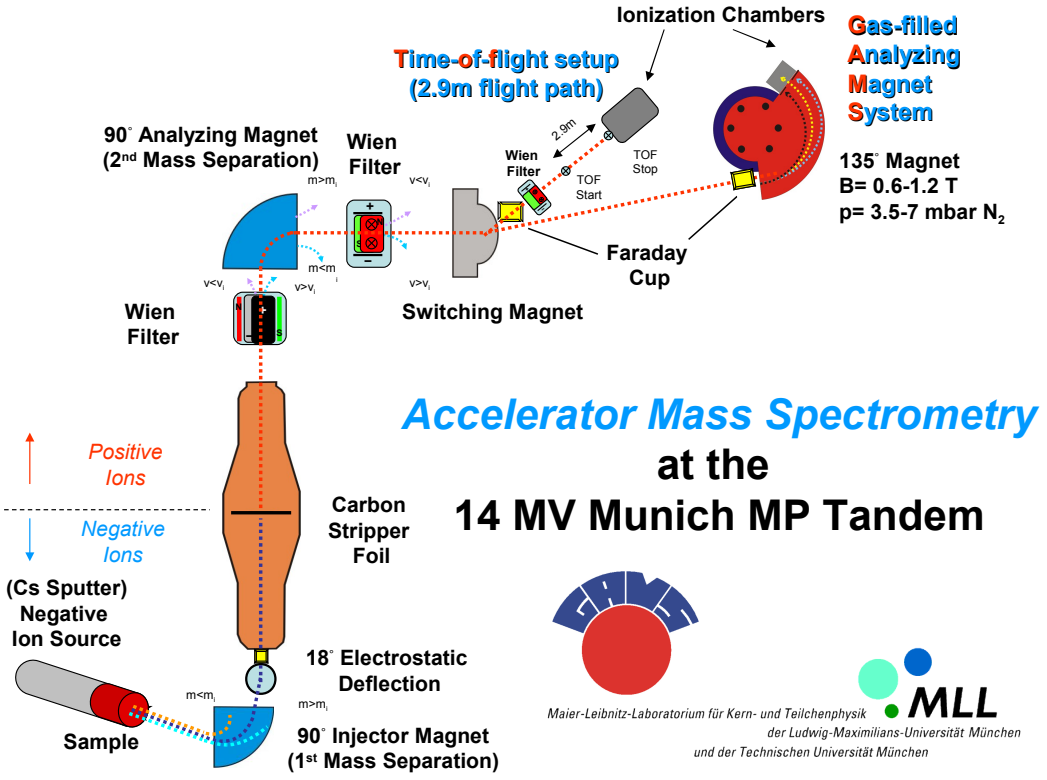

Figure 5.1: The figure shows a schematic overview of the two AMS beamlines at the MLL. Key features are the 14 MV Tandem accelerator, the Time of Flight beamline for detection of heavy isotopes, and the GAMS beamline, equipped with a gas-filled magnet for isobar suppression.

5.2.1. Ion source and injector magnet

In order to form the negative ion beam required for injection into the tandem accelerator, the sample material is hammered into a 1.5 mm wide and 2 mm deep hole which has been drilled into a silver sample holder. The sample holder is then screwed onto a water-cooled holding-rod, and inserted into a Middleton-type (Middleton, 1983) cesium sputter source with a spherical ionizer Fig. (5.2a). Cs-vapor is introduced into the otherwise evacuated (pressure $< 1 \times 10^6$ mbar) ion source from a heated Cs-reservoir below and is ionized on a $(1000 - 1300)$°C ionizer surface made from tantalum. By applying a sputtering voltage $U_{\mathrm{sp}} = 5$ kV, the Cs^+ ions are accelerated towards the sample and sputter out atoms and molecules from the sample material, mostly neutrally charged, but also as ions. Cs

settles down on the cooled sample surface and enhances the probability for the formation of negative ions because of its low electronegativity. By this method, it is possible to convert on the order of $10^{-4} - 10^{-2}$ of the sample material into a negatively charged ion beam. This beam is extracted out of the source by applying an extraction voltage of $U_{\text{ex}} = 23$ kV.

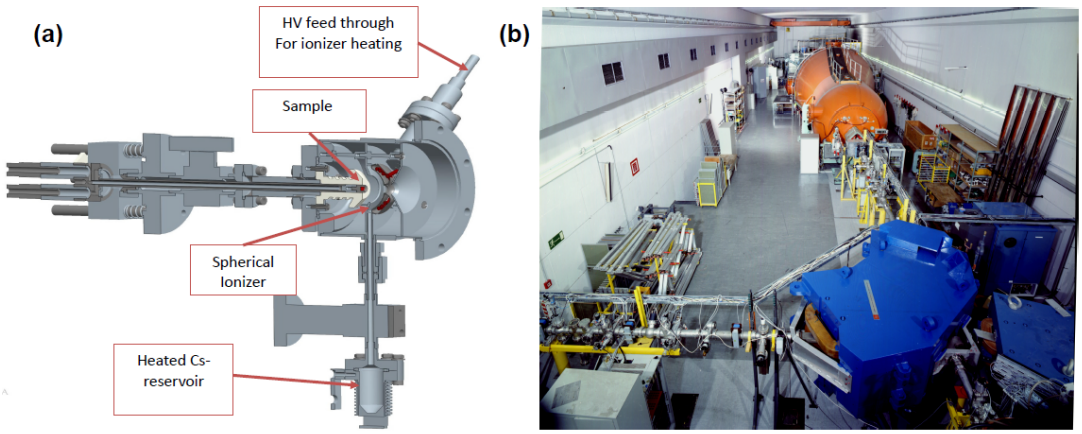

Figure 5.2: (a) Cross-section through the ion source. Courtesy of Peter Hartung. (b) Photograph of the accelerator hall with the tandem accelerator tank (orange) and the analyzing magnet on the high energy side (blue).

After leaving the ion source, the particles have a fixed energy of 28 keV, pass through a pair of electrostatic lenses (an Einzel-and a Quadrupole lens), and pass a 90° dipole bending magnet with a maximum field strength of 1.2 T and a bending radius of 0.38 m. The trajectory of the particles depends on their mass, thus a first mass selection on the low energy side is possible. The mass resolution of the injector magnet can be determined on a Faraday cup at the entrance of the tandem accelerator and is typically $\frac{\Delta m}{m} = 2 \cdot \frac{\Delta B}{B} \approx 1 : 400$ (depending on aperture openings along the beamline). Afterward, the beam is transported towards the entrance of the accelerator using a system of 7 electrostatic lenses, steerers, and an 18° electrostatic deflector.

5.2.2. Tandem accelerator

The 14 MV Tandem accelerator uses a pelletron charging system for increased voltage stability and SF_6 gas for suppression of high-voltage discharges. The maximum stable voltage during the course of this project varied between 11.2 and 12.0 MV. The negatively charged particles enter the tandem and are accelerated towards the positively charged terminal in the center. There, they pass through a thin (4 μm) carbon stripping foil, which removes several electrons. Typical charge states for medium mass isotopes at 11-12 MV are in the range 8+ to 13+. The positive ions are then further accelerated by the terminal towards ground potential at the high energy end of the tandem, reaching a final kinetic energy E_{kin} of

$$E_{\mathrm{kin}} = e \cdot (U_{\mathrm{sp}} + U_{\mathrm{ex}}) \cdot \frac{M_{\mathrm{ion}}}{M_{\mathrm{molecule}}} + e \cdot U_{\mathrm{tandem}} \cdot \frac{M_{\mathrm{ion}}}{M_{\mathrm{molecule}}} + q \cdot U_{\mathrm{tandem}}, \qquad (5.1)$$

which is typically in the range 80 MeV to 140 MeV for the parameters mentioned above. The energy stability of the tandem is one of the critical parameters that influences the quality of AMS measuring conditions, and is as good as $\Delta U = 3$ kV, corresponding to $\frac{\Delta U}{U} \approx 1:3500$.

5.2.3. Beamline features

On the high energy side of the accelerator, the ion beam first passes a Wien-filter ($\frac{\Delta M}{M} \approx 1:80$), and then a 90° dipole bending magnet Fig. (5.2b) with a maximum field of 1.6 T an a bending radius of 1.65 m, which fixes the magnetic rigidity for the transported particles. This is followed by another Wien-filter ($\frac{\Delta M}{M} \approx 1:40$), after which the beam is directed towards the dedicated GAMS beamline using a switching magnet. This beamline features a TOF system with start and stop signals being generated by two micro channel plate detectors, which was not used for the experiments discussed here, since TOF is normally needed only in cases with interfering isotopes with $\Delta A = 1$ from the radioisotope.

5.2.4. Gas-filled magnet

In order to separate isobars, the AMS setup features a gas-filled magnet. The GAMS magnet (bending radius 90 cm, bending angle 135°) is typically operated between 600 mT and 900 mT and filled with 3-7 mbar of N_2. The maximum field of 1.25 T is sufficient to bend particles up to $A \lesssim 130$ for typical operating parameters. For a more detailed description, the reader is referred to Knie et al. (1997). Isobars, for example ^{60}Fe and ^{60}Ni, enter the magnet through a thin mylar foil and experience electron-exchange reactions with the nitrogen gas. These reactions alter the charge state of the ions, depending on the original electron shell configuration, and thus on the element number Z, which is different for isobars. Thus, ^{60}Fe and ^{60}Ni form different average charge states $\overline{q} \propto Z^{0.4}$ and thus obtain different magnetic rigidities $B\rho \propto MZ^{-0.4}$. This means that the isobars are forced on different trajectories inside the magnetic dipole field, allowing for an a spatial separation in x-direction on the order of a few centimeters between isobars, with the isobar of higher Z on the inner trajectory. This isobar suppression technique is also illustrated in Fig. (5.3).

5.2.5. Ionization chamber

Particle identification is essential for AMS measurements, and is especially demanding in the case of interfering isobars. The GAMS setup features an ionization chamber (Fig. (5.3c)) with a split anode (5 ΔE signals) and a Frisch-grid, and is filled with typically 30-60 mbar of isobutane (C_4H_{10}) gas. Voltages of -700 V and -280 V are applied

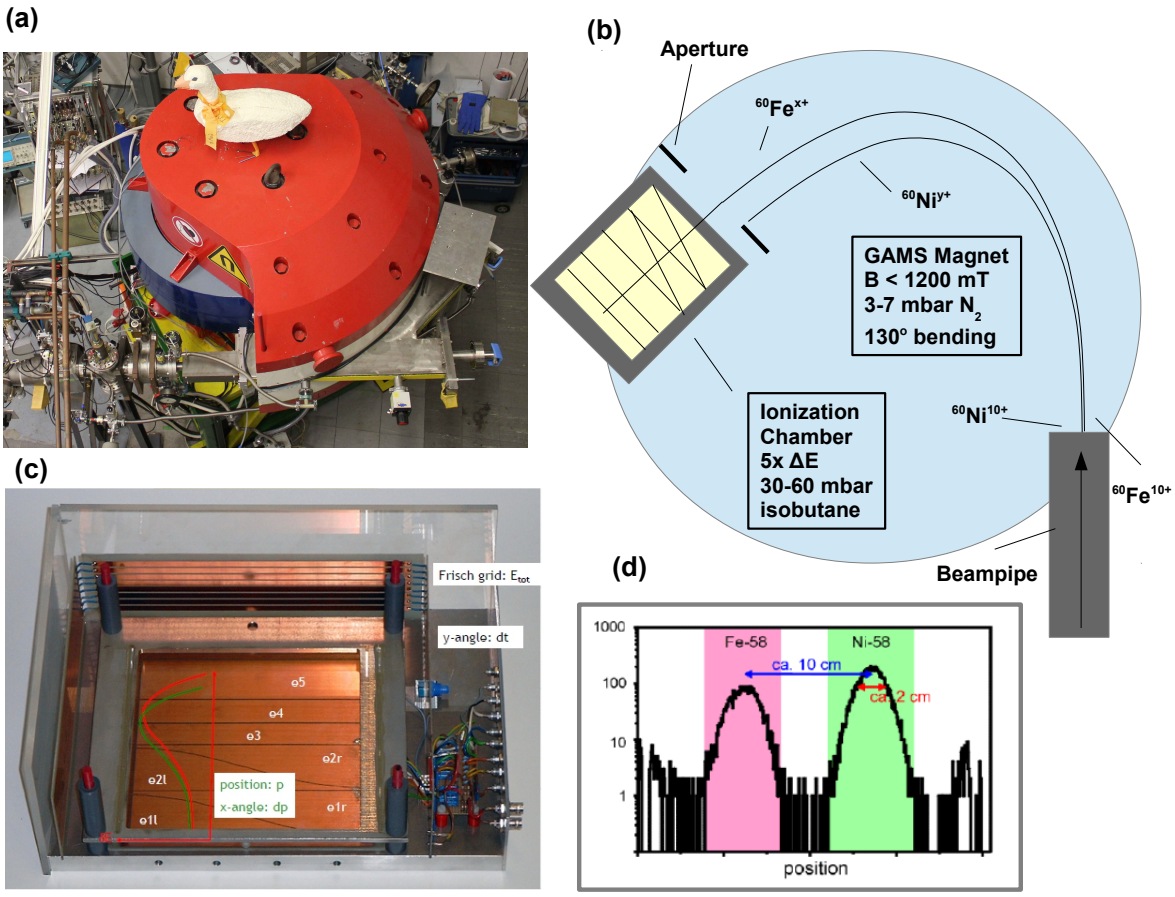

Figure 5.3: (a) Aerial view photograph of the GAMS setup with beam coming from the left side. (b) Sketch of the GAMS and the isobar suppression principle. The magnet is filled with few mbar N_2, and forces different elements to form different average charge states. In this case, ^{60}Ni and ^{60}Fe form charge states $y+$ and $x+$, respectively, with $y > x$. The element with higher Z is thus forced onto the inner trajectory. In this way, most of the unwanted isobar can be rejected by blocking it with an aperture. (c) Photograph of the ionization chamber. It features a Frisch-grid and five anodes, the first two of which are diagonally separated for x-position determination. Green and red curve are qualitative energy loss curves for ^{60}Ni and ^{60}Fe, respectively. (d) Example of spatial isobar separation of the two stable counterparts ^{58}Fe and ^{58}Ni obtained from the ratio of the left and right signal of the first anode in the detector. Image taken from Knie (1997).

to the cathode and the Frisch-grid, respectively. The first two anodes are split diagonally in order to reconstruct the particle's x-position (Fig. (5.3d)). The maximum count-rate supported is in the range of a few kHz, after which dead-time effects become dominant. Being different elements, isobars passing the detector will each have a characteristic Bragg curve, leading to different energy depositions in the ΔE signals, allowing for additional discrimination between them.

5.3. ^{60}Fe measurements at the MLL

5.3.1. Ion source and beam tuning

All samples for ^{60}Fe measurements were prepared as Fe_2O_3, mixed 1:1 (by mass) with silver powder (to provide electrical and thermal conductivity). The sample holders were manufactured from high purity silver (> 99.99%, Alfa Aesar, Lot Nr.: 231-131-3). Typically, a sample contained about 7 mg of Fe_2O_3. The highest current could be achieved by extracting Fe as FeO^- from the source. The beam was tuned to a Faraday cup after the injector magnet, which was set to mass $M = 70$, allowing stable $^{54}Fe^{16}O$ to pass. The choice of ^{54}Fe has the advantage that the current from the ion source is typically only between 50 nA and 150 nA of $^{54}Fe^{16}O^-$, whereas the current from $^{56}Fe^{16}O^-$ would typically be few microamperes. This lower current is easier to handle during beam tuning and is also less harmful to the stripping foil in the accelerator.

The beam of $^{54}Fe^{16}O^-$ was tuned to a Faraday cup at the entrance of the Tandem accelerator. This could normally be achieved without significant loss of particles using a set of 8 electrostatic lenses. The beam was then injected into the accelerator with an energy of 178 keV and accelerated further by a terminal voltage of typically 11.5 MV. The voltage was different in many beamtimes, since it had to be adapted to the condition of the accelerator and varied between 11.2 MV and 12 MV. This corresponds to beam energies of $120 - 130$ MeV for $^{60}Fe^{10+}$. The transmission through the accelerator was about 50%. This, and also the stripping yield probability of around 20% for charge states of interest (9+, 10+, or 11+) lead to unavoidable losses. For most beamtimes,4 the beamline was tuned using $^{54}Fe^{9+}$. The current of this isotope at a Faraday cup in from of the GAMS was then typically $50 - 150$ enA.

Afterward, the beamline could be set to ^{60}Fe, which was measured in the charge state 10+. Unfortunately, the setup does not feature a fast cycling system (e.g. using a bouncing injector magnet), meaning that using the same energy on the low energy side and the same magnetic rigidity on the high energy side, one has to change the field of the injector magnet, the terminal voltage of the tandem, and the electric field of the Wien-filters. Although this procedure is automated, is takes roughly 30 seconds to switch between isotopes. At this point, choosing $^{54}Fe^{9+}$ for stable current has another advantage over other Fe isotopes, since $^{60}Fe^{10+}$ has the same magnetic rigidity and requires only a small change

in terminal voltage (around 200 kV) and no change in the voltage of the Wien-filters.

For some beamtimes, the isotope used for tuning was $^{58}Fe^{10+}$. The advantage of this choice was that the beam tuning could be performed for an isotope in the same charge state as the AMS isotope which does not suffer from the possibility that isotopes of different charge states have slightly different trajectories after the high voltage terminal of the accelerator. The drawback, however, was the considerable change in terminal voltage necessary to switch between $^{58}Fe^{10+}$ and $^{60}Fe^{10+}$. For simplicity reasons, the following discussion of the measurement procedure will use the current of $^{54}Fe^{9+}$ for normalization, but all arguments and equations are also valid for $^{58}Fe^{10+}$.

5.3.2. Sequence of a data run

First, the current I_1 of $^{54}Fe^{9+}$ on the Faraday cup in front of the GAMS is recorded on an analogue ammeter. Afterward, the injector magnet, the terminal voltage, and the Wien-filter are set to $^{60}Fe^{10+}$ and data acquisition is started. The number of events of ^{60}Fe, n_p, is recorded along with the number of background events and the number of triggers yielding the live-time fraction of the detector f_{live}. After a time t ($2 - 60$ min, depending on the sample and stability of the system), data taking is terminated and the system is set back to $^{54}Fe^{9+}$ to measure the current on the Faraday cup again (I_2) to calculate the average current during the run as $I = (I_1 + I_2)/2$.

5.3.3. Transmission T

Using a standard sample (known concentration c_s of $^{60}Fe/Fe$), the GAMS settings (pressure, magnetic field), and the detector pressure can be optimized to allow for a good transmission of ^{60}Fe into the detector, while suppressing the isobar ^{60}Ni using the aperture on the inside trajectory, and keeping the count-rate in the detector low, in order to avoid pile-up and dead-time. The physical transmission through the GAMS magnet for ^{60}Fe is typically $80 - 90\%$, however, after applying software cuts, the transmission from the Faraday cup in front of the GAMS to the detector is usually $T \approx 50 - 70\%$. This can be calculated using the known concentration of a standard sample and the current of stable ^{54}Fe as

$$T = \frac{n_s \times e}{c_s \times I \times t}, \tag{5.2}$$

where t is the measurement time, n_s is the number of ^{60}Fe events in the standard sample run, and e is the elementary charge. A standard measurement typically consists of 3 data runs with a total of at least 100 events of ^{60}Fe, which can be summed up to calculate the transmission T.

5.3.4. Sample order

After confirming good transmission T, a measurement of a blank sample is performed. This is necessary to show that a sample containing no ^{60}Fe does not produce false positive events. Since ^{60}Fe events should not occur in a natural sample of Fe, any ^{60}Fe-like events could be scattered events from other species, or cross-talk between samples in the ion source. The ^{60}Fe/Fe concentration determined in the blank sample is known as the blank level, which is also a measure for the highest sensitivity possible. After a sufficiently small blank level is reached (should be at least 1 order of magnitude lower than the expected signal of the radioisotope), a real sample can be measured. A measurement of a set of samples with unknown concentration is typically performed in the following order:

1. Standard sample, 3 runs, 5 min each, $\sim$ 100 events of ^{60}Fe total.
2. Blank sample, 1 run, 30 min.
3. Samples of interest, 3 runs each, t depends on concentration.
4. Standard sample, 3 runs, 5 min each, $\sim$ 100 events of ^{60}Fe total.

This type of measuring order allows to correct for a drift in transmission during the measurements. In most cases with stable conditions, standard measurements are performed every 5-10 h. The transmission used for samples of unknown concentration is the average of the transmissions obtained in the standard measurements before and after.

5.3.5. Calculation of concentration

The final result of the AMS measurement is the concentration

$$c_p = \frac{N\,(^{60}\mathrm{Fe})}{N(\mathrm{Fe})}. \tag{5.3}$$

It can be calculated for any data run using

$$c_p = \frac{n_p}{Q_{\mathrm{eff}}} \tag{5.4}$$

where n_p is the number of events of ^{60}Fe during the run and Q_{eff} is the number of examined Fe atoms, which can be calculated with

$$Q_{\mathrm{eff}} = \frac{t \times I_{54} \times T \times f_{\mathrm{live}}}{e \times f_{54}} \tag{5.5}$$

where f_{live} is the fraction of live-time of the detector and $f_{54} = 5.845\%$ is the isotopic fraction of ^{54}Fe.

5.3.6. Challenges of measuring ^{60}Fe

Although ^{60}Fe is generally considered an AMS isotope which is difficult to measure by most groups, this normally refers to the need for high energy, and thus large accelerators,

and an isobar suppression system, in order to separate ^{60}Fe from ^{60}Ni. Other than that, the case of ^{60}Fe is relatively fortunate: the isobar is at $\Delta Z = 2$, which makes the spatial separation after the GAMS magnet twice as large as for $\Delta Z = 1$ and Fe has no stable isotopes heavier than ^{60}Fe, which could interfere in the detector, while lower mass isotopes in the same charge state are suppressed by the aperture, just like ^{60}Ni. This situation allows us to reach blank levels in the $\mathcal{O}(^{60}\text{Fe}/\text{Fe}) \approx 10^{-17}$. A few critical points that influence data quality should, however, be mentioned separately.

Choice of charge-states

While a charge state as high as possible is usually desirable in AMS, since it leads to higher energy and thus better separation between different particles (e.g. ^{60}Fe and ^{60}Ni), the choice of charge states is limited by the available maximum terminal voltage, which determines the charge state distribution. An additional challenge is that certain charge states might have a high background count-rate caused by particles in other charge states, which have the same, or only slightly different magnetic rigidity. For the ^{60}Fe measurements discussed in this work, the terminal voltage was the limiting factor for the choice of charge state. With a maximum voltage of 11.2-12.0 MV, the charge state 10+ was chosen for ^{60}Fe, corresponding to 9+ for ^{54}Fe. Although experience shows that particle discrimination between ^{60}Fe and background sources is much easier measuring ^{60}Fe in 11+, this would have cost roughly 50% in transmission due to lower stripping yields for the higher charge state at low terminal voltage. This has an impact on the particle identification procedure, which becomes more challenging for two reasons. Firstly, the isotope $^{60}\text{Fe}^{10+}$ has an integer mass-to-charge ratio. This can potentially cause strong background of lower mass ions with similar mass-to-charge ratio. Secondly, particle discrimination between $^{60}\text{Fe}^{10+}$ and e.g. $^{60}\text{Ni}^{10+}$ becomes more difficult at lower particle energy, which was only about 125 MeV for $^{60}\text{Fe}^{10+}$ at 11.5 MV terminal voltage compared to 150 MeV for $^{60}\text{Fe}^{11+}$ at 12.5 MV.

Suppression of ^{60}Ni

Isobaric suppression is key for high sensitivity AMS measurements. In order to reach down to a blank level on the order of $\mathcal{O}(^{60}\text{Fe}/\text{Fe}) \approx 10^{-17}$, it is necessary to reduce the number of ^{60}Ni particles arriving at the detector, which might cause false identification as ^{60}Fe, when too abundant. This suppression is reached in four steps. First: the chemical preparation of our samples always includes several steps aimed to suppress the isobar. Second: the choice of extracting oxides from the ion source favors the production of FeO^- and suppresses NiO^- by about one order of magnitude. The third suppression has already been discussed above, and is performed by denying most of the Ni ions passage into the detector using an aperture in the GAMS. The fourth suppression can be made using software cuts on the signals of the ionization chamber that specifically reject ^{60}Ni.

Crosstalk

It is also very important to understand possible crosstalk between samples. This can happen when sputtered material from a sample is still present in the ion source when measuring the next sample. This can lead to additional ^{60}Fe events and falsify the measured concentration. This problem is especially critical when measuring samples with radioisotope concentrations which differ by several orders of magnitude. For the measurements presented here, the standard material with $c_s = 1.25 \times 10^{-12}$ (See description in Sec. (5.3.9)) has a concentration 4-5 orders of magnitude above the desired sensitivity. Two types of cross-talk can be distinguished: short-term crosstalk, which would manifest as an abundance of events in a sample measured directly after measuring a standard, and long-term crosstalk, which can occur when material from the standard which is still present in the ion source is re-ionized, e.g. by discharges in the source, which can occur even hours after the last standard has been measured.

The average effect of long-term crosstalk can be analyzed by measuring large amounts of blank samples spread out over the beamtimes. The blank levels which were obtained were always on the order of ^{60}Fe/Fe $< 1 \times 10^{16}$ and will be discussed further in Sec. (5.3.9). In order to investigate the short-term cross-talk behavior of the ion source, at the end of beamtimes, a sample with a high concentration can be measured, typically with ^{60}Fe/Fe $\approx (10^{-10} - 10^{-9})$. In a subsequent blank measurement, no cross-talk could be identified down to 5 orders of magnitude below the standard concentration, confirming that cross-talk is usually not critical in ^{60}Fe measurements. Additionally, the danger of cross-talk is reduced by the use of a single-cathode ion source, where the standard sample is completely removed before inserting a sample of interest or a blank.

5.3.7. Total efficiency/transmission

A big challenge for high sensitivity AMS is the overall efficiency of the system. This number states what fraction of atoms is actually transported from the sample to the detector. Since this is an important aspect which can limit the possible resolution of ^{60}Fe/Fe, it is estimated in the following: A sample of 5 mg of Fe (corresponding to 7 mg of Fe_2O_3) contains about 5×10^{19} atoms of Fe. Using an average current of 30-100 nA of $^{54}Fe^{9+}$ at the Faraday cup in front of the GAMS, over 5 hours until the sample is empty, and a transmission $T = 60\%$, a total number of $Q_{\text{eff}} = (5 - 10) \times 10^{15}$ atoms of Fe could be examined, leading to a total efficiency of $\epsilon_{\text{tot}} \approx (1 - 2) \times 10^{-4}$.

This number is made up of six different contributions. The biggest loss occurs already in the ion source, where only a small fraction of particles get extracted as negative ions. Assuming a current of 2 μA of $^{56}FeO^-$ can be extracted from the ion source for 5 hours using the same sample with 5 mg Fe corresponds to an ion source extraction efficiency (including transport through the injector magnet) of $\epsilon_{\text{inj}} \approx 0.5\%$.

The additional factors which are included in ϵ_{tot} are the transmission to the tandem

entrance ($T_{\mathrm{LE}} \approx 70\%$), the transmission through the accelerator ($T_{\mathrm{acc}} \approx 50\%$), the stripping yield ($Y \approx 20\%$), and the transmission through the high energy side of the beamline until the Faraday cup in front of the GAMS ($T_{\mathrm{HE}} \approx 70\%$). These transmissions can be obtained by measuring the ion current at different retractable Faraday cups along the beamline. Finally, the transmission from the last Faraday cup (in front of the GAMS) to the detector (including software cuts) is given as

$$\epsilon_{\mathrm{tot}} = \epsilon_{\mathrm{inj}} \times T_{\mathrm{LE}} \times T_{\mathrm{acc}} \times Y \times T_{\mathrm{HE}} \times T \approx 1 - 2 \times 10^{-4}. \tag{5.6}$$

5.3.8. Data acquisition and analysis

This section gives a short account of the data signal analysis procedure and data processing, while a more detailed description is given in appendix C.

The GAMS ionization chamber produces a total of 8 raw signals: 7 ΔE signals (left and right each for the first two anodes) and the signal from the Frisch-grid. The collected charge on the anodes is converted into a voltage pulse in a charge sensitive pre-amplifier. The y-angle is generated from the time delay between anode signals 1 and 3. For peak-height determination (and thus ΔE measurements), the signals pass through a shaping amplifier, which increases the peak voltages to $1-10$ V, which can then be digitized by an ADC. The particle's x-position is calculated from the ratio of the signals on either side of the split anodes 1 and 2. The difference of position determined by anodes 1 and 2 serves to calculate the x-angle. The system also features pile-up-rejection, which is especially important for high count-rates. All signals are digitized and stored in their raw form including a time stamp, allowing for a complete offline analysis after the experiment. For on-line analysis, 1- and 2-dimensional spectra of all important signals are created live using the software package ROOT (Brun and Rademakers, 1997) and can be viewed instantaneously during measurements.

As for any AMS measurement, reliable results can only be achieved using a reference sample (standard) with a well-known concentration of ^{60}Fe/Fe. The process of isolating the correct position of ^{60}Fe in the spectra with complete background suppression is illustrated using sample spectra displayed in Fig. (5.4). The signals of the standard sample are compared with a blank sample (no ^{60}Fe). The GAMS parameters (detector pressure, magnet pressure, magnetic field) are adjusted to make the signal of ^{60}Fe easily distinguishable from background in at least one of the five energy loss signals, e.g. dE3 (Fig. (5.4a)). A cut on that energy signal and the x-position in the detector is usually sufficient to isolate ^{60}Fe in the standard sample spectra (black ellipse). This allows to obtain the position of ^{60}Fe in all signals. However, there is still background present, as can be seen by numerous events in that region in the spectrum of the blank sample (Fig. (5.4b)). Nonetheless, the position of ^{60}Fe in all signals is now isolated which allows to make 1-dimensional cuts on all of them.

A powerful tool for background discrimination is a χ^2 analysis. Each event is assigned a value in an approximate χ^2 distribution calculated from all 5 energy loss signals (E_i; $i = 1..5$) and the Frisch-grid signal E_0 as

$$\chi^2 = \sum_{i=0}^{5} \frac{(E_i - \mu_i)^2}{\sigma_i^2}, \tag{5.7}$$

where E_i are the measured signals of a candidate event and μ_i and σ_i are the expected mean signal and its standard deviation determined with a standard. This distribution is not an ideal χ^2 distribution, since the energy signals are neither perfect Gaussians, nor are they completely statistically independent. Nonetheless, it is a useful tool to reduce the 6-dimensional problem of energy signal discrimination to a 1-dimensional number of high predictive power. During a beamtime of one week, an average of 1000 events ^{60}Fe of a standard sample are collected. The χ^2 distribution of these events generated from a 2-dimensional cut on Fig. (5.4a) is shown in Fig. (5.4d). The maximum of the black distribution is approximately at $\chi^2 = 2.5$. The number of degrees of freedom is 6 (6 signals), and thus the maximum should be at $6 - 2 = 4$. This shows that the signals are, as expected, not completely statistically independent.

Fig. (5.4e) shows a superposition of this distribution and the χ^2 values calculated for the events of Fig. (5.4b) and Fig. (5.4c). Any candidate events (green events with low χ^2 in Fig. (5.4e)) now have to be discriminated from background. This is done by applying cuts to all energy signals (possible since the real position of ^{60}Fe is known from the standard). The process of selecting such cuts using the data from Fig. (5.4) is explained in more detail in appendix C. The resulting spectra, again plotted as dE3 over x-position for the standard (Fig. (5.4f)), the blank (Fig. (5.4g)), and the sediment sample (Fig. (5.4h)) then yield the final number of events of ^{60}Fe, which can be used to calculate the concentration in the sample relative to the standard. Every applied cut, however, reduces the number of ^{60}Fe events in the standard, and thus the transmission T. A detector event is only accepted as a ^{60}Fe event, if it lies within all energy cuts and has a $\chi^2 < 15$. This χ^2 cut corresponds to a rejection of about 10% of ^{60}Fe events in the standard.

5.3.9. Standard and Blank materials

Standard material PSI-12

The standard material used for all ^{60}Fe measurements in this work is PSI-12. This material was originally used for the half-life measurement by Rugel et al. (2009). Originally, the ^{60}Fe was created in a beam dump at the Paul-Scherrer-Institute, where a large number of protons were stopped over a period of about 12 years until 1992. After the facility had been decommissioned, the beam-dump was stored to let short-lived radioactivities decay. After chemical Fe extraction and adding of carrier Fe material, a solution containing the Fe isotopes was produced. An aliquot of this solution was used by Rugel et al. (2009) for

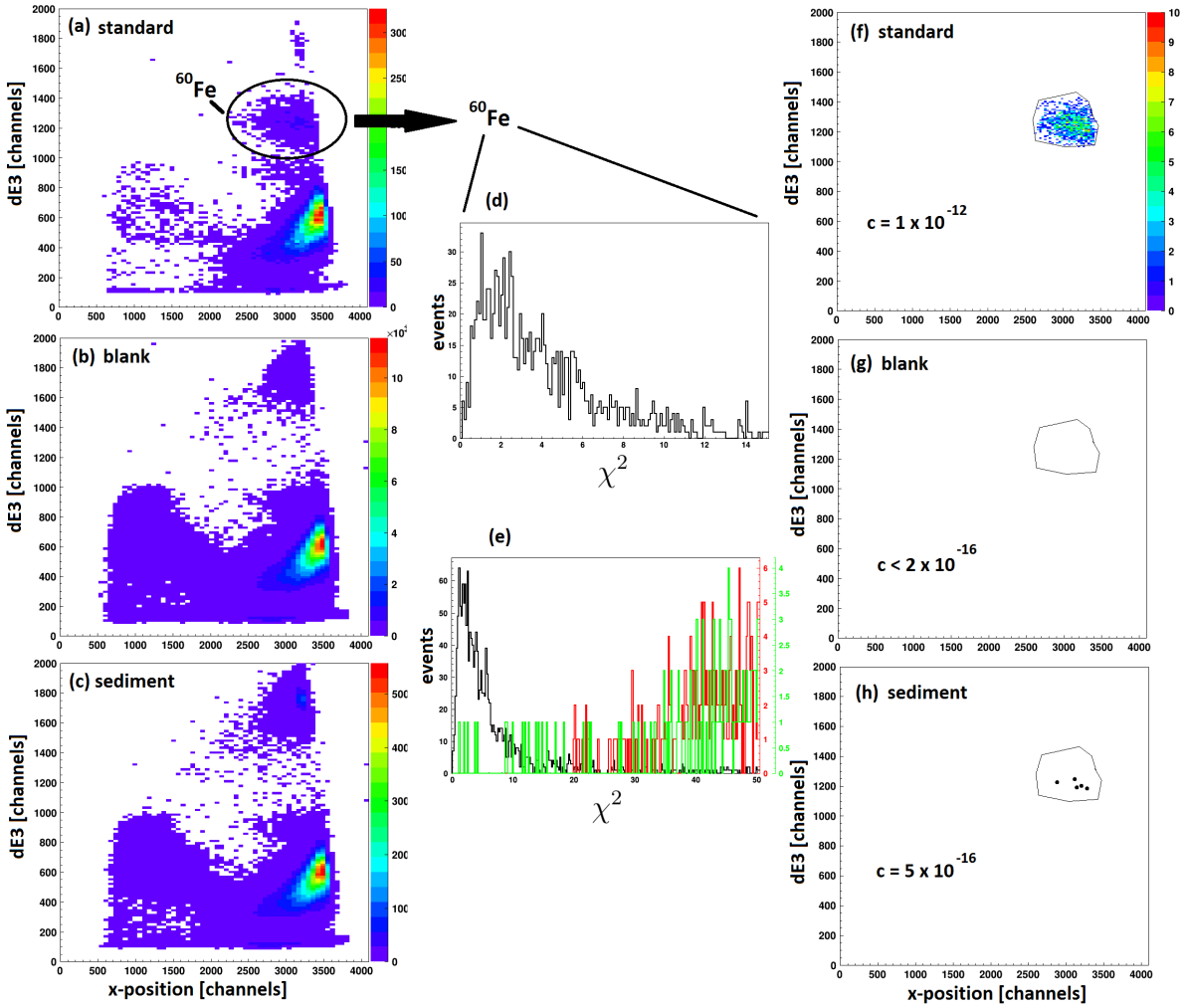

Figure 5.4: Sample spectra from data obtained from the PSI standard sample, a chemistry blank, and a representative sediment sample (core 851 – age: 2.35-2.36 Ma). (a,b,c) Energy loss of anode 3 (dE3) plotted over x-position in the detector chamber of raw data (no cuts). (d) χ^2 distribution of real ^{60}Fe events obtained from the standard (a). (e) superposition of χ^2 data from all three samples, black: standard, red: blank, green: sediment. (f,g,h) same as (a,b,c), but with cuts on all signals, isolating ^{60}Fe. Concentrations of ^{60}Fe/Fe are also given for these specific samples. The black 2D-cut in this case only serves as a visual aid. However, if necessary, any arbitrary 2-dimensional cut can be applied to counter a specific background situation.

the half-life measurement, while the bulk of the solution remained, with a concentration of $^{60}\mathrm{Fe/Fe} = (2.0483 \pm 0.035) \times 10^{-4}$. Since this concentration is much too high for AMS measurements, it was diluted down to produce the standard material PSI-12 with $^{60}\mathrm{Fe/Fe} = (1.25 \pm 0.06) \times 10^{-12}$. Although other standards would have been available, PSI-12 was chosen, since its concentration is ideal for a high-sensitivity measurement. On the one hand, the concentration is not too high, as to produce much cross-contamination in the ion source from sample to sample. On the other hand, it is still high enough to allow for standard runs with ~ 100 counts in a few minutes (depending on ion current). In this way, not much time is lost for standard measurements, while the number of counts is still high enough to keep statistical errors reasonably low.

Blank materials

The conditions for a good AMS blank material can be summarized as such:

1. As low as possible concentration of the radioisotope.
2. Same chemical form as actual sample.
3. Similar contamination of other isotopes as actual sample.

Unfortunately, such a material is not easy to come by for our experiment, but there are several possibilities to improvise. Since all ^{60}Fe samples for this work were prepared as Fe_2O_3, all candidates for blank material should be in the same form in order to comply with condition (3).

Pure Fe_2O_3 For beam tuning, samples of pure Fe_2O_3 (Alfa Aesar, Lot: 24344) were used. Though this material does not meet condition (3), this choice is very suitable for condition (1). Thus, during beamtimes, at least some data are usually taken using this sample as blank material, since it is a reliable check for cross-contamination between samples. The achieved sensitivity for this material was on the order of $\mathcal{O}\left(\frac{^{60}\mathrm{Fe}}{\mathrm{Fe}}\right) = 10^{-17}$, showing that cross-contamination, as well as machine background are not a large concern for this experiment.

Chemistry blank In order to approach condition (2), it makes sense to subject the blank samples to the same chemical pre-treatment as the real samples. In this way, any contaminant originating from chemicals used will also be present in the blank, thus providing a more realistic background approximation. For this purpose a total of 25 samples, which were also used to test the yield of the CBD extraction technique, were prepared from pure Fe_3O_4 (Alfa Aesar, Lot: E08T027, grain size 40-60 nm) and underwent the exact same chemical treatment as the sediment samples. These blanks performed very well during measurements. Over several beamtimes, the blank level determined from the chemistry blank was $\frac{^{60}\mathrm{Fe}}{\mathrm{Fe}} = 1.8 \times 10^{-17}$ with a 1-σ upper limit of $\frac{^{60}\mathrm{Fe}}{\mathrm{Fe}} < 5.1 \times 10^{-17}$, with one count of ^{60}Fe observed. The only source of unwanted background which cannot be estimated using the chemistry blank are contaminations originating from the sediment.

Multiple extraction blanks from sediment Assuming a perfect chemical extraction procedure, which extracts all ^{60}Fe, and leaves the bulk material unchanged, performing an additional chemical extraction on the residue of the first one would yield excellent blank samples. This possibility was explored and tested with a few sediment samples, however, due to the limited available beamtime, insufficient data was collected to reach a conclusive result.

Strongly leached samples During the multi-isotope study described in appendix B, a set of 14 ^{60}Fe AMS samples of core 851 were prepared. These samples ($\sim$ 3 mg Fe_2O_3 each) were produced from only 3 g of sediment each in a strong leaching procedure. If all ^{60}Fe is extracted by both, CBD and this strong leaching, then the additional Fe extracted should dilute the ratio of ^{60}Fe/Fe in strongly leached samples down by a factor of ~ 7. Unfortunately, the samples did not yield good current from the ion source and only 3 samples in the age range 2.10-2.36 Ma were partially measured (corresponding to samples PL5, PL6, and PL7 in appendix B). No events were detected and the upper limit reached by combining all three samples was $^{60}\mathrm{Fe/Fe} < 2.9 \times 10^{-16}$, which is too high to make a clear statement. The remaining samples are to be measured in a future beamtime.

Old sediment samples The only way to guarantee the same expected background in the blank sample and in the actual samples, is to use actual sample material to produce blanks. Fortunately, part of the sediment available for this study is from an age of 7-8 Ma. Here, the already low average concentration observed in younger samples ($0 - 1.5$ Ma) is attenuated by natural radioactive decay of ^{60}Fe by a factor of $\sim 7 - 8$. In this way, the measurement does not directly require an additional blank, since the lowest concentration measured in the study can serve as the blank level. Using only samples with an age of > 6 Ma, a blank level of $\frac{^{60}\mathrm{Fe}}{\mathrm{Fe}} < 8 \cdot 10^{-17}$ could be reached. Considering the similarity of both sediment cores, even though such old samples were only available from site 848 it is safe to assume that this also provides a reliable blank level for measurements at site 851.

Environmental blanks AMS sensitivity for ^{60}Fe can be limited by naturally occurring ^{60}Fe on the Earth's surface (e.g. by cosmic ray production) and possible anthropogenic background, which could contaminate blank materials. In order to investigate this possibility, surface soil and vegetation samples from the Fukushima region (after the Fukushima incident) at a distance of $\lesssim 2$ km from the Daiichi power plant were measured. A total of 5 samples were measured in November 2014 with 0 counts of ^{60}Fe observed, corresponding to a 1-σ upper limit of $^{60}\mathrm{Fe/Fe} < 8 \times 10^{-17}$. This shows that for concentrations of $^{60}\mathrm{Fe/Fe} > 10^{-16}$, neither cosmogenic, nor anthropogenic background appear to be a limiting factor for AMS with ^{60}Fe.

5.3.10. Uncertainty treatment for ^{60}Fe

There are a number of sources for uncertainties to be included in AMS measurements at the MLL. The following section discusses the sources, nature, and impact of these uncertainties. The concentration of ^{60}Fe/Fe is calculated using Eq. (5.4), in which the statistical uncertainty of n has to be included. Splitting Q_{eff} up using Eq. (5.5), it is obvious that uncertainties of the current reading I_{54} and the transmission T also have to be taken into account. Compared to these contributions, uncertainties in the other variables are small and were neglected. Additionally, the value of T is subject to a systematic uncertainty in the standard concentration c_s. In the following section, each of these contributions to the uncertainty will be discussed.

Concentration of standard sample

The uncertainty in the concentration of the standard sample will directly affect any measured concentration of ^{60}Fe/Fe, because all samples are measured relative to the standard sample. This error is of systematic nature and cannot be avoided without changing the standard material. For the standard sample used in this work, PSI-12, the concentration is $(1.25 \pm 0.06) \times 10^{-12}$. This error includes the original uncertainty of the concentration of the master sample from Rugel et al. (2009), and the uncertainty introduced by the dilution process.

This is the only purely systematic error which is taken into account for measuring ratios of ^{60}Fe/Fe. This is due to the fact that all other systematic errors apply both to the sample under investigation, and the standard sample, and will thus cancel out since all measurements are made relative to the standard.

Uncertainty in current reading I_{54}

All currents I are read from an analogue ammeter by eye. This means that a random error is introduced by reading, which depends on high-frequency (compared to reading time of few seconds) fluctuations of the beam, as well as low-frequency drifts. An uncertainty of mostly statistical nature of 13% is estimated for each reading. This means that for calculating I_{54} as the average of the reading before and after the run with relatively stable current ($I_1 \approx I_2$), the uncertainty is given as

$$\frac{\Delta I_{54}}{I_{54}} = \frac{1}{\sqrt{2}} \times \frac{\Delta I_1}{I_1} \approx 9\%. \tag{5.8}$$

Uncertainty in transmission T

As can be seen in Eq.(5.2), the uncertainty of T has to include the statistical uncertainty of counting n events and that of another current measurement. While Δn can be estimated as $\sqrt{n}$ due to the large number of counts in a standard measurement ($n > 100$), the

current is read a total of 12 times for determining T for a set of samples between two standard measurements with three data runs each. Additionally, there can be long-term fluctuations of T, due to slow changes in beam tuning. Thus, instead of estimating these contributions individually, the standard deviation of T over several days can be used, which is typically 12%.

Uncertainty for low count-rates in n

In counting experiments such as AMS, the uncertainty of counting a number of events n can only be estimated as $\sqrt{n}$ for large n. In this work, that approximation was used only for data runs with $n > 20$ events. For smaller n, the confidence intervals and upper limits suggested by Feldmann and Cousins (1998), constructed using a likelihood-ratio approach, were employed. Especially for small n, this statistical uncertainty dominates.

Final 1-σ intervals and discussion

All statistical uncertainties mentioned above are used to estimate 1-σ confidence intervals in the following way. The uncertainties for the current reading ΔI and the transmission T are added quadratically to yield 15%. This 15% statistical uncertainty was quadratically added to the relative uncertainty of the error intervals of Feldmann and Cousins (1998). Technically, this is not correct since the error intervals should be constructed from the Poisson contribution of low counting statistics and the Gaussian contribution of other statistical uncertainties. However, since the uncertainty introduced by counting statistics dominates other errors, the resulting confidence intervals still represent a sensible estimate. In the case of zero events, the upper confidence limit is artificially increased by 0.15 corresponding to 15% error at 1 event (instead of 0). The resulting confidence intervals for up to 20 events are shown in Tab. (5.1).

Events	u.l. FC	l.l. FC	new u.l.	new l.l.
0	1.29	0	1.44	0
1	2.75	0.37	2.76	0.35
2	4.25	0.74	4.27	0.70
3	5.30	1.10	5.34	1.05
4	6.78	2.34	6.84	2.23
5	7.81	2.75	7.91	2.63
6	9.28	3.82	9.40	3.64
7	10.30	4.25	10.46	4.06
8	11.32	5.30	11.53	5.05
9	12.79	6.33	13.02	6.01
10	13.81	6.78	14.09	6.45
11	14.82	7.81	15.16	7.41
12	16.29	8.83	16.65	8.35
13	17.30	9.28	17.72	8.80
14	18.32	10.30	18.80	9.75
15	19.32	11.32	19.87	10.69
16	20.80	12.33	21.37	11.61
17	21.81	12.79	22.44	12.08
18	22.82	13.81	23.52	13.02
19	23.82	14.82	24.60	13.94
20	25.30	15.83	26.09	14.86

Table 5.1.: Confidence intervals depending on the number of events observed. Columns 2 and 3 show the 1-σ intervals (u.l. = upper limit, l.l. = lower limit) suggested by Feldmann and Cousins (1998) for measurements without background. Columns 4 and 5 are the 1-σ intervals used in this work, calculated by adding 15% statistical uncertainty quadratically to columns 2 and 3, with the exception of the intervals for 0 events, where the upper limit was estimated by adding 0.15 to the original limit.

6. ^{60}Fe AMS results and discussion

Over a period of three years, 109 ^{60}Fe AMS samples were measured at the GAMS setup: 65 samples from core 848 and 44 samples of core 851. All results will be presented in this chapter, followed by a discussion of the ^{60}Fe data.

The results are calculated as concentration of ^{60}Fe to stable Fe in the sample material. All uncertainties included in the results of individual samples only take statistical errors into account and are given as 1-σ confidence intervals. The systematic uncertainty of the concentration of the standard sample is not shown. All x-error bars in the AMS data plots of this chapter denote the range of time span across which sediment material was used for the measurements obtaining the data point. sampling range of sediment for obtaining the data point. For samples which were grouped together, the x-interval is the entire sampling range, and the x-position of the data point itself is the mean of all samples used to obtain it, weighed by their statistical significance (Q_{eff}). The x-intervals of neighboring grouped samples can overlap in some cases, since the available individual samples often had different time resolutions.

6.1. Observed signal

In all 109 samples of both sediment core combined, a total of 87 events of ^{60}Fe were detected. At the same time, only 1 single event was observed in the chemistry blank, leading to a cumulative blank level over all beamtimes of 1.8×10^{-17}, corresponding to a 1-σ upper limit of the blank level of $^{60}\text{Fe/Fe} < 5.1 \times 10^{-17}$.

In order to exclude false positive events it is important to show that the detector signals of ^{60}Fe events in actual samples are similar to those of the standard material (Sec. 5.3.9). Since pressure and detector settings were slightly different in each beamtime, the individual signals cannot be compared between beamtimes. As introduced in chapter 5 and described in detail in appendix C, the χ^2 distribution constructed from the 6 energy signals is a powerful tool for this purpose. The χ^2-distribution of 30.000 events of ^{60}Fe recorded over all beamtimes (Fig. (6.1a)) is compatible with an ideal χ^2 distribution with NDF = 4.5. This mathematical coincidence (reduced χ^2-value of the fit is 1.7) should not be over-interpreted, since the individual energy signals are neither ideal Gaussians, nor statistically independent. Nonetheless, the distribution (no matter what specific shape) must be reproduced by the ^{60}Fe events in the sediment samples in order to confirm the authenticity of the signal. A comparison of the χ^2-distribution of the 87 events of the

sediment with the expected number of events for a χ^2-distribution with NDF = 4.5 is shown in Fig. (6.1b). The two distributions are in excellent agreement and show that the events observed in the sediment samples are fully compatible with ^{60}Fe.

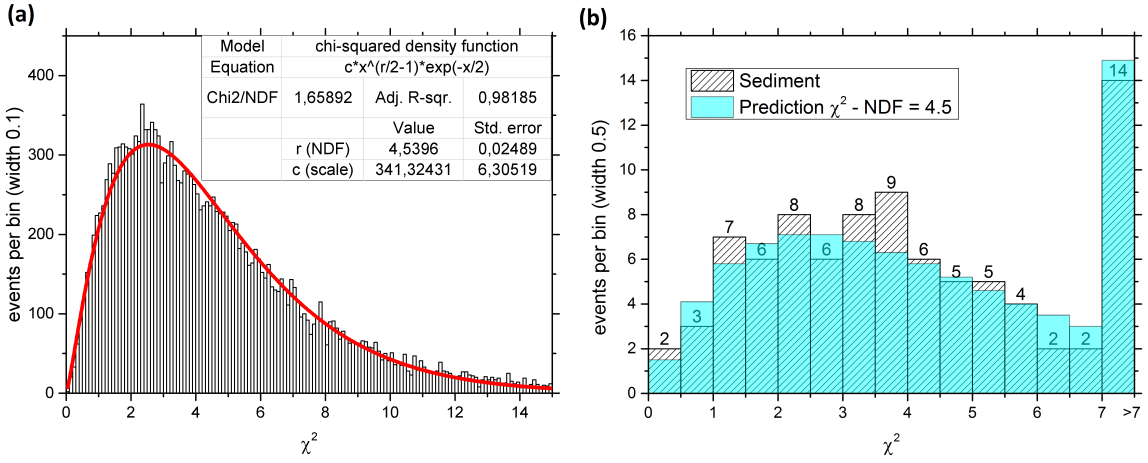

Figure 6.1: (a) χ^2 of 30.000 events of ^{60}Fe in the standard sample recorded over all beamtimes. Red curve is a fit of an ideal χ^2-distribution with variable height and NDF. (b) χ^2 of all 87 events of ^{60}Fe in sediment samples recorded over all beamtimes (striped black) with a bin width of 0.5. Numbers above columns indicate the number of events per bin. The cyan-colored columns are the expected values for a χ^2 distribution with NDF = 4.5 (see (a)). The last bin corresponds to $7 \leq \chi^2 \leq 15$. Events with $\chi^2 > 15$ were rejected.

6.2. ^{60}Fe result core 848

A total of 65 AMS samples were measured for core 848 spread out over a depth range corresponding to an age of $0-8$ Ma. However, there was no sample material available in the range $3.2-7.4$ Ma Details on the individual samples and the measured concentrations are presented in appendix A. A signal of ^{60}Fe/Fe significantly above the blank level is observed only in the time range from ~ 1.8 to ~ 2.6 Ma. This age range estimate is based on the assumption of a 800 ka long signal, but is not the only estimate possible. This will be discussed in detail in Sec. (6.4.2). The average concentration observed over that time range was $^{60}\text{Fe/Fe} = 4.2 \times 10^{-16}$. This average was determined by summing up all data points in this age region (sum over both the number of events, as well as Q_{eff}). In order to estimate the significance of the observed signal, the age range can be divided into three intervals: young sediment, the signal region, and old sediment, as shown in Tab. (6.2). The possibility of the signal observed in the peak region being of random background origin is mainly determined by the large statistical error on the observed average concentration (22%). This concentration is about 3.9 σ above the conservative $1-\sigma$ upper limit of the blank level. The probability p_{848} of the signal being random background can be

estimated by assuming a Poisson distribution for the background with $\lambda = 1.8 \times 10^{-17}$, corresponding to the one event observed in the chemistry blank. The probability for this distribution producing a signal that overlaps or exceeds the the $1-\sigma$ confidence interval of the observed average concentration $(4.2 \pm 0.9) \times 10^{-16}$ is $p_{848} = 3 \times 10^{-7}$.

Region name	Age [Ma]	events	Q_{eff}	avg. ^{60}Fe/Fe	$1-\sigma$ up	$1-\sigma$ down
young	0-1.8	4	1.2×10^{17}	3.3×10^{-17}	2.3×10^{-17}	1.5×10^{-17}
peak	1.8-2.6	36	8.6×10^{16}	4.2×10^{-16}	9.4×10^{-17}	9.4×10^{-17}
old	2.6-8.0	0	3.8×10^{16}	0	3.8×10^{-17}	0
entire	0-8.0	40	2.5×10^{17}	1.6×10^{-16}	3.6×10^{-17}	3.6×10^{-17}
Chem. blank	–	1	5.4×10^{16}	1.8×10^{-17}	3.3×10^{-17}	1.2×10^{-17}

Table 6.1.: Overview of samples of core 848 divided into three parts: young sediment, sediment in the peak region, and old sediment, supplemented by the average over the entire data-set, and data for chemistry blank material. Columns show from left to right: sample name, age range (not available for chemistry blank), number of events of ^{60}Fe, number of sample atoms examined, determined concentration of ^{60}Fe/Fe, and its $1-\sigma$ statistical uncertainty up and down.

Due to the low number of events observed per sample (0-5), it is favorable to combine several samples to increase the statistics per data point. A sensible grouping should attempt to keep age intervals for grouped data points small and also, each grouped data point should have roughly the same statistics (Q_{eff}). Three such groupings were preformed, one with $Q_{\text{eff}} \approx (1-1.5) \times 10^{16}$ (Fig. (6.2a)), one with $Q_{\text{eff}} \approx (1.5-2) \times 10^{16}$ (Fig. (6.2b)), and one with $Q_{\text{eff}} \approx (2-3) \times 10^{16}$ (Fig. (6.2c)). The groupings were preformed from left to right (i.e. from present time to the past) until the summed Q_{eff}-value was withing the specified range. The resulting data points can overlap in x-direction. This can happen because some individual samples (see appendix A) also have overlapping age ranges. The same data is shown again in Fig. (6.3) after correction for radioactive decay of ^{60}Fe.

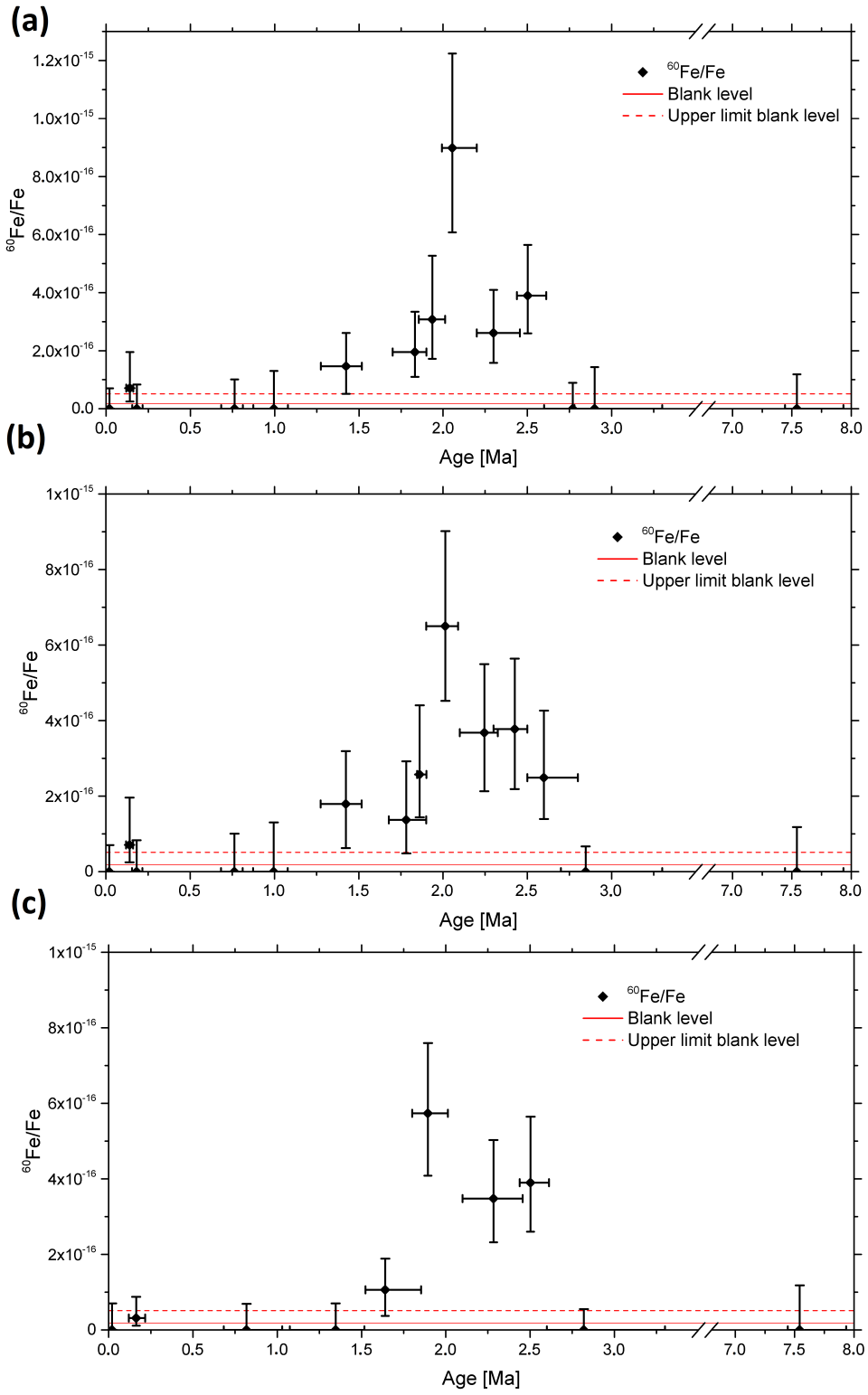

Figure 6.2: Isotopic ratio of ^{60}Fe to stable Fe obtained for all 65 samples of sediment core 848. Adjacent samples were grouped together to increase statistics per data-point. (a) Samples grouped to obtain $Q_{\text{eff}} \approx (1 - 1.5) \times 10^{16}$ per data-point. (b) Same, with $Q_{\text{eff}} \approx (1.5 - 2) \times 10^{16}$. (c) Same, with $Q_{\text{eff}} \approx (2 - 3) \times 10^{16}$.

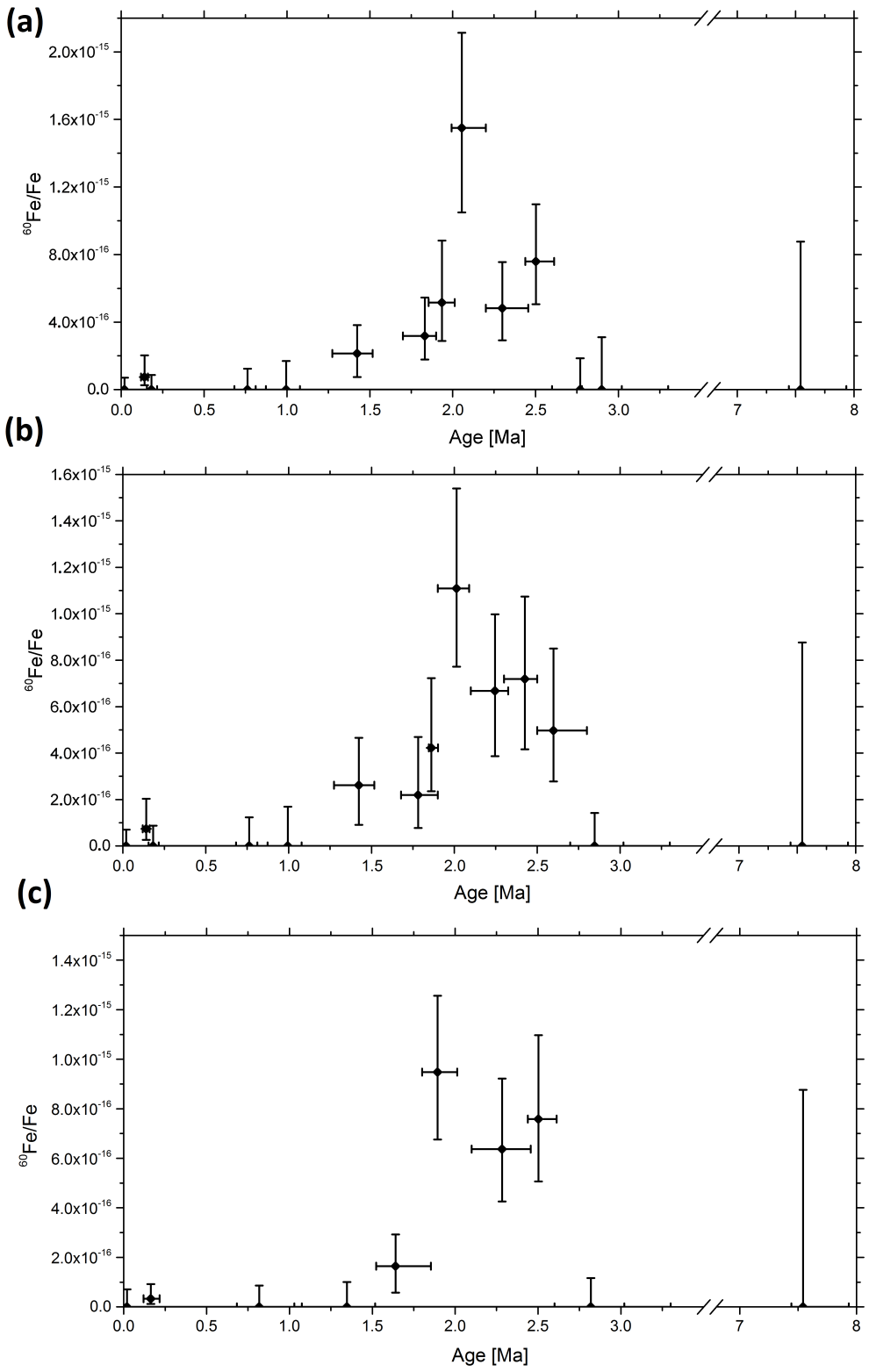

Figure 6.3: Same as Fig. (6.2) after correction for radioactive decay of ^{60}Fe.

6.3. ^{60}Fe result core 851

A total of 44 samples were measured for sediment core 851. Unfortunately, there was no sample material available outside a range of 1.6-3.3 Ma. The individual samples are presented in appendix A. Due to the low observed average concentration in the peak range indicated by the data from core 848 of $^{60}\mathrm{Fe/Fe} = 2.7 \times 10^{-16}$ and several events in the adjacent regions, the profile cannot be interpreted as a significant peak by observing individual samples, making a grouping of data points necessary. Nonetheless, the concentration in the age range 1.8-2.6 Ma is still above the $1-\sigma$ upper limit of the blank level by 3.7 σ, comparable to the significance observed in core 848. As in core 848, the probability p_{851} of the signal being random background is estimated as the probability of a Poisson distribution with $\lambda = 1.8 \times 10^{-17}$ reaching or exceeding the signal range of $(2.7 \pm 0.5) \times 10^{-16}$ is $p_{851} = 1 \times 10^{-4}$.

Region name	Age [Ma]	events	Q_{eff}	avg. ^{60}Fe/Fe	$1-\sigma$ up	$1-\sigma$ down
young	1.6-1.8	2	1.3×10^{16}	1.6×10^{-16}	1.8×10^{-16}	1.0×10^{-16}
peak	1.8-2.6	40	1.5×10^{17}	2.7×10^{-16}	5.9×10^{-17}	5.9×10^{-17}
old	2.6-3.7	5	4.7×10^{16}	1.1×10^{-16}	6.2×10^{-17}	5.1×10^{-17}
entire	0-3.7	47	2.1×10^{17}	2.2×10^{-16}	4.7×10^{-17}	4.7×10^{-17}
Chem. blank	–	1	5.4×10^{16}	1.8×10^{-17}	3.3×10^{-17}	1.2×10^{-17}

Table 6.2.: Overview of samples of core 851 divided into the same regions as for core 848 in Tab. (6.2) for comparison: young sediment, sediment in the peak region, and old sediment, supplemented by the average over the entire dataset, and data for chemistry blank material. Columns show from left to right: sample name, age range (not available for chemistry blank), number of events of ^{60}Fe, number of sample atoms examined, determined concentration of ^{60}Fe/Fe, and its $1-\sigma$ statistical uncertainty up and down.

The smoothed data plots are similar to the ones for core 848: three plots with grouped samples for $Q_{\mathrm{eff}} \approx (1-1.5) \times 10^{16}$ (Fig. (6.4a)), $Q_{\mathrm{eff}} \approx (1.5-2) \times 10^{16}$ (Fig. (6.4b)) and $Q_{\mathrm{eff}} \approx (2-3) \times 10^{16}$ (Fig. (6.4c)), respectively. The same data is shown again in Fig. (6.5) after correction for radioactive decay of ^{60}Fe.

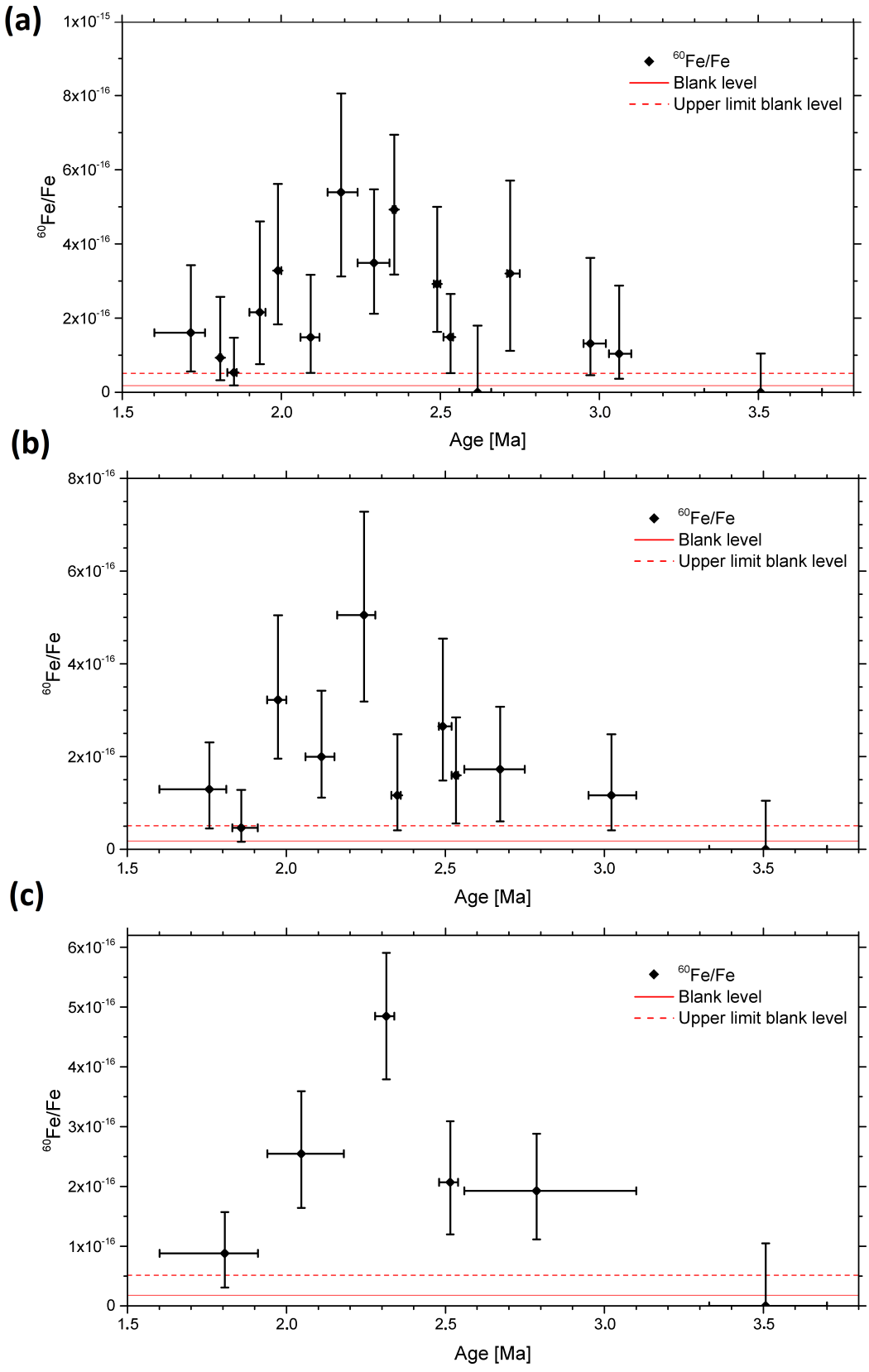

Figure 6.4: Isotopic ratio of ^{60}Fe to stable Fe obtained for all 44 samples of sediment core 851. Adjacent samples were grouped together to increase statistics per data-point. (a) Samples grouped to obtain $Q_{\text{eff}} \approx (1 - 1.5) \times 10^{16}$ per data-point. (b) Same, with $Q_{\text{eff}} \approx (1.5 - 2) \times 10^{16}$. (c) Same, with $Q_{\text{eff}} \approx (2 - 3) \times 10^{16}$.

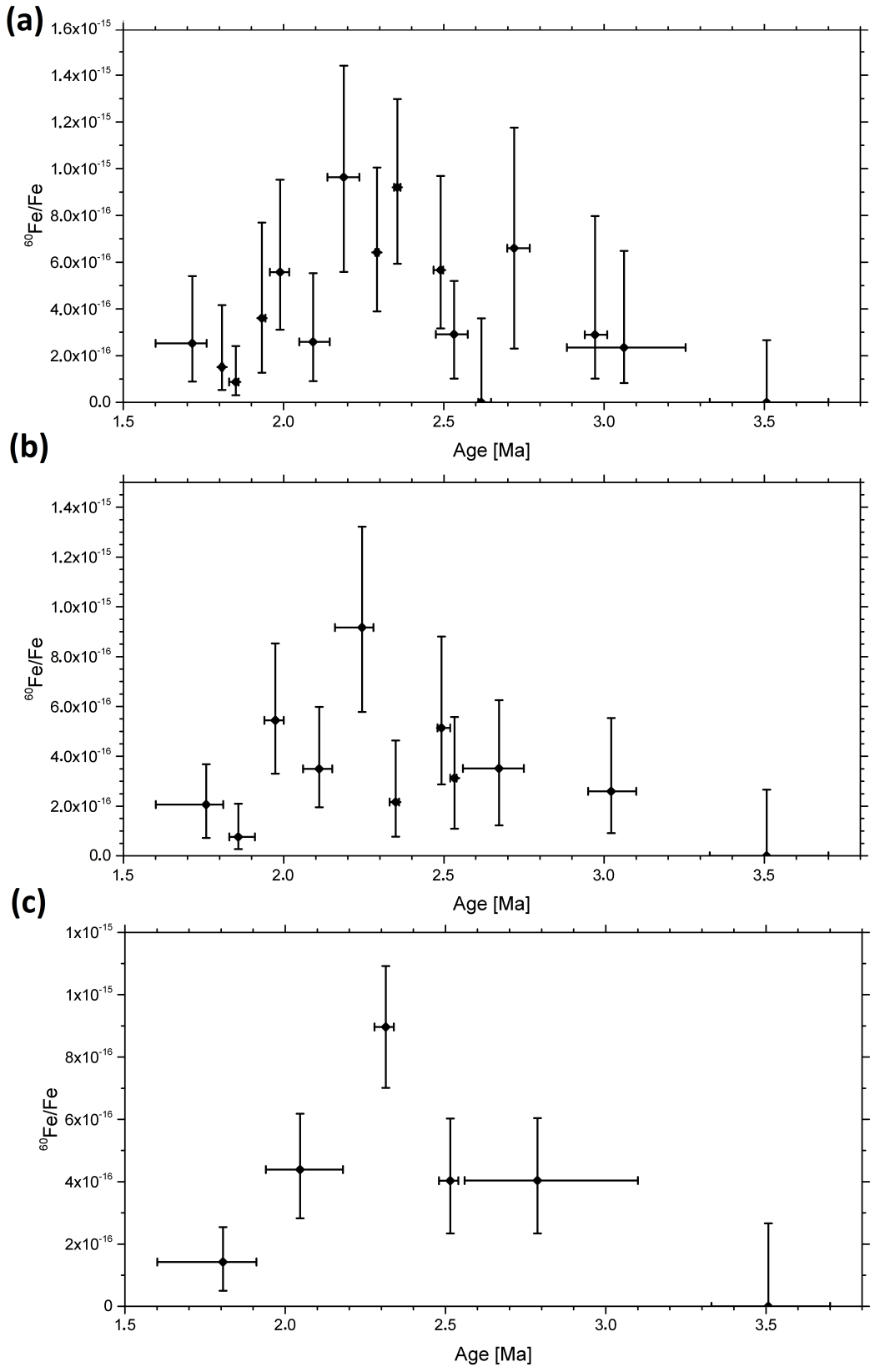

Figure 6.5: Same as Fig. (6.4), after correction for radioactive decay of ^{60}Fe.

6.4. Interpretation and analysis of ^{60}Fe results

An enhancement of ^{60}Fe above expected background was detected in both sediment cores. The ^{60}Fe signal is highly significant, being 3.9σ and 3.7σ above the upper limit of the blank level in core 848 and 851, respectively. The probabilities of these signals being due to random background were estimated as $p_{848} = 3\times10^{-7}$ and $p_{851} = 1\times10^{-4}$. This section is dedicated to the detailed analysis of the nature, amplitude and temporal structure of this observation.

6.4.1. Estimation of cosmogenic ^{60}Fe fraction

In order to positively identify the ^{60}Fe signature as being of SN origin, it is imperative to rule out a cosmogenic signal. It was pointed out by Basu et al. (2007) and Stuart and Lee (2012) that a possible explanation for the ^{60}Fe signal observed by Knie et al. (2004) was the deposition of interplanetary (in contrast to interstellar) grains which have been irradiated by GCR, producing ^{60}Fe.

Since GCR produce ^{60}Fe mainly by spallation on Ni targets, appreciable concentrations can be found in iron meteorites, which contain a high Ni fraction. However, since the main component of those bodies is Fe, a high amount of ^{53}Mn is produced also. ^{53}Mn was measured in 6 samples of core 851, which is described in detail in appendix 2. The measurements resulted in an upper limit on the deposition rate of ^{53}Mn into the sediment of $r_{(^{53}\mathrm{Mn})} < 130\ \frac{\mathrm{at}}{\mathrm{cm}^2\ \mathrm{a}}$. In a recent measurement of ^{60}Fe and ^{53}Mn in 7 iron meteorites (Fimiani, 2014) the saturation ratio of the activities of the two radioisotopes is on average

$$\frac{A\,(^{53}\mathrm{Mn})\left[\frac{\mathrm{dpm}}{\mathrm{kg\ Fe}}\right]}{A\,(^{60}\mathrm{Fe})\left[\frac{\mathrm{dpm}}{\mathrm{kg\ Ni}}\right]} \approx 300, \tag{6.1}$$

in good agreement with theoretical models (Ammon et al., 2009). Pessimistically assuming a high average Ni content (20%) and low average Fe content (80%) of the possible meteoritic carriers of the observed ^{60}Fe signature in the sediment samples, this would correspond to an atomic ratio of

$$\frac{^{53}\mathrm{Mn}}{^{60}\mathrm{Fe}} \approx 1700. \tag{6.2}$$

With this result, the upper limit obtained on the ^{53}Mn concentration in sediment core 851 can be converted to an upper limit on the expected ^{60}Fe concentration due to meteoritic influx independent of a possible SN signal. Assuming a steady deposition without chemical selection, the corresponding ^{60}Fe concentration in core 848 can be estimated by scaling the result from core 851 by the ratio of the sedimentation rates. The resulting upper limits on the cosmogenic contributions to the observed ^{60}Fe signal in both sediment cores are shown in Fig. (6.6). This clearly shows that the observed ^{60}Fe signature cannot be

explained by GCR production, since significant variations in GCR flux over the last few Ma have not been observed (Poutivtsev, 2007). It may, however, explain the small surface activity observed in core 848. The only other way to explain the signal as GCR produced is the local deposition of high amounts of cosmogenic material during the time of the ^{60}Fe signal, which would have been detected as a much stronger (at least 1 order of magnitude) ^{53}Mn signal in that age range.

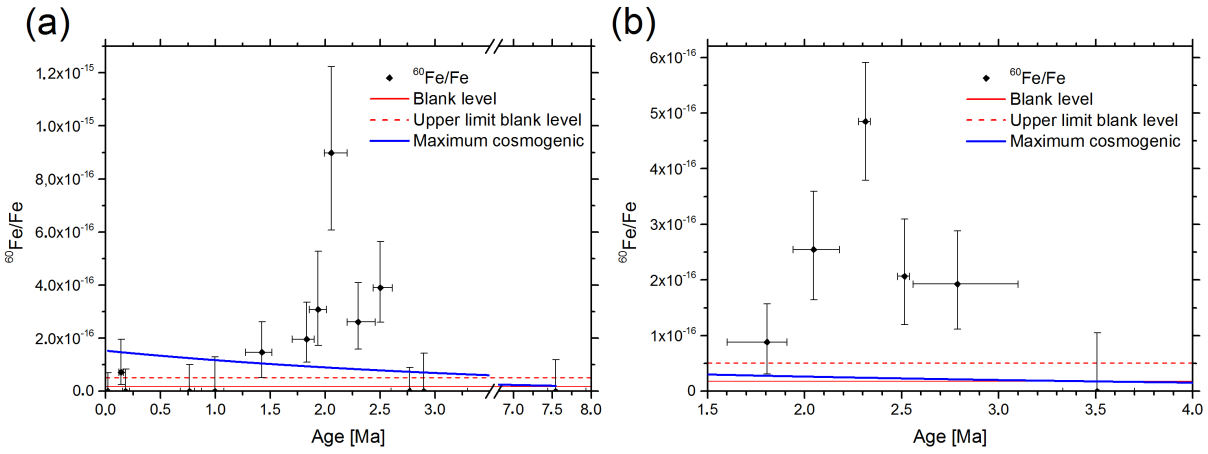

Figure 6.6: (a) Grouped data points from core 848. Blue line represents the upper limit on the expected contribution of cosmogenic, non-SN, ^{60}Fe/Fe. (b) Same for core 851.

Finally, it should be mentioned that the assumed upper limit is very conservative, since the isotope ^{53}Mn was extracted with a strong leaching technique able to dissolve MMs (same procedure used as in Feige, 2014), while ^{60}Fe was prepared using the mild CBD technique. This means that any ^{60}Fe deposited by MMs which survived atmospheric entry and are still sufficiently large ($\sim \mu$m) cannot contribute to the total signal, since CBD does not dissolve large Fe minerals. For a more conclusive analysis of the relationship between ^{53}Mn and ^{60}Fe, further measurements of ^{53}Mn would be interesting for the future.

6.4.2. Temporal structure

One of the unresolved issues left behind after the publication of the ferromanganese crust data (Knie et al., 2004), was the exact temporal structure of the ^{60}Fe input. A variation of the concentration of ^{60}Fe/Fe cannot be explained by variations in the sedimentation rates of the cores, which were constant within $\sim 5\%$ (Sec. 3.1.3). Due to the higher time resolution available in the sediment data from this work, a more thorough analysis is possible. Since there is more data available fore core 848, the following analysis will focus on 848, followed by a short comparison with 851.

Running mean analysis

In order to better reconstruct the time profile of the signal, it is possible to smooth the data by applying a moving average. This procedure replaces each data point by an average over itself, and a number of neighboring data points, where the total number of points used to obtain each average is defined as the degree n. Although this method should be used with prudence, since it artificially increases statistics, it is well-suited to filter high-frequency fluctuations and present the data in a smoothed way. Running means have been calculated for data from core 848 with $n = 3$,5, and 7, as displayed in Fig. (6.7).

The time profile of the ^{60}Fe signal revealed in this way is compatible with a short, strong exposure at around $2.0 - 2.2$ Ma, superimposed onto a longer signal in the range $1.5 - 2.8$ Ma. This interpretation is, however, to be taken cautiously, because of the low statistics available.

Signal duration

One of the main tasks of this work was the determination of the total exposure time of Earth to the ^{60}Fe signal. In order to answer this question, a definition of the edge of the signal is necessary. Possible approaches include:

1. First to last data points showing ^{60}Fe events.
2. Intersects of running means with blank level.
3. Running means continuously non-zero in signal region.
4. Intersects of fits to the data with the blank level.
5. Grouped data above blank level.

Option (1) is only reliable with zero background, which is not the case, as seen by the non-zero blank level. However, omitting the event at 0.131 Ma, this would lead to a signal range of $1.52 - 2.61$ Ma. In the case of (2), the intersects of the running means with the upper limit of the blank level ($^{60}\mathrm{Fe/Fe} < 5.1 \times 10^{-17}$) can be calculated, yielding ranges between $1.50 - 2.67$ Ma for $n = 3$. Option (3) for $n = 3$ takes into account the fact that the signal at 1.528 Ma could be a statistical artifact, which cannot be excluded since the data point lies only 1.2 σ above the blank level. Option (3) for $n = 3$ then yields a signal interval of $1.80 - 2.68$ Ma. Next, option (4) represents a more complicated approach. Assuming a single Gaussian–shaped exposure is the source of the signal (which is not physical), then a fit as a superposition of a Gaussian and constant machine background could yield reasonable results. However, the error bars on single data points are so large, that a Gaussian fit would yield non-unique results and thus this option was dismissed. Finally, option (5) is using the age interval where grouped data points are above the blank level. Applying this to Fig. (6.2a and b) yields signal intervals of $1.70 - 2.61$ Ma and $1.80 - 2.56$ Ma, respectively. Similar examinations for core 851 yield intervals ranging from $1.94 - 2.50$ Ma (shortest signal) to $1.73 - 3.05$ Ma (longest signal), however much less reliable than for fore 848. The average over all these possibilities yields a value for

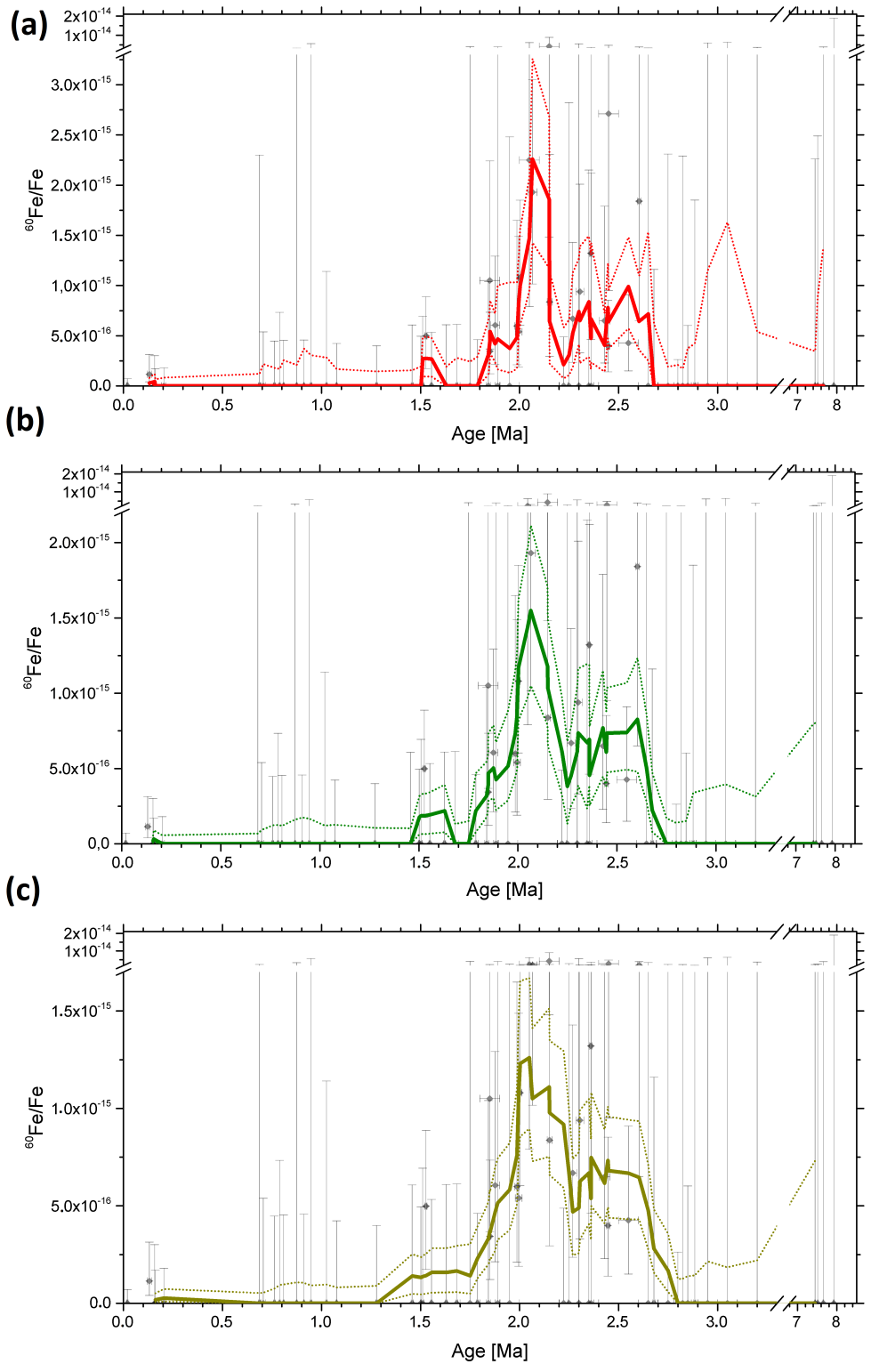

Figure 6.7: Running means (full lines) applied to the decay corrected data from core 848. Dotted lines represent 1-σ statistical uncertainties. The underlying data points (gray) are the concentrations in each individual sample. Running means are calculated by averaging over n data points each: (a) $n = 3$, (b) $n = 5$, (c) $n = 7$.

the center t_c, as well as the duration t_{SN} of the ^{60}Fe signal:

$$t_c = (2.19 \pm 0.11)\ \text{Ma} \qquad \text{and} \qquad t_{SN} = (0.96 \pm 0.25)\ \text{Ma} \tag{6.3}$$

This corresponds to a time interval of $1.71 - 2.67$ Ma.

6.4.3. Influence of sedimentation rate

A remarkable result of this work is revealed when examining the ^{60}Fe/Fe signal amplitudes compared to the sedimentation rates in both cores. While the average sedimentation rate of core 848 is by about a factor of 3 lower than that of core 851, the average ^{60}Fe/Fe ratio in core 848 is only 1.5 times higher than in 851. Naively, one would expect a factor 3, by assuming that the number of ^{60}Fe atoms deposited onto the sediment surface is the same for both cores, and that the higher sedimentation rate in 851 would cause dilution.

A possible explanation of this observation is that the concentration of ^{60}Fe/Fe is not primarily determined by the sedimentation rate, but by the abundance of secondary iron bearing minerals, which are able to consume ^{60}Fe from the water and bind it into their mineral structure. The SD particles such as magnetofossils are the most likely representative of these minerals. Thus, a more reliable relation between the ^{60}Fe/Fe concentrations of the two cores could be established by comparing not the sedimentation rates, but the average SD Fe fraction reported from ARM/IRM measurements in chapter 4, which was $\sim$30 μg/g for core 848, and $\sim$20 μg/g for core 851, explaining the 1.5x lower ^{60}Fe/Fe in 851.

6.4.4. Local interstellar fluence of ^{60}Fe

The local interstellar fluence Φ_{LIF} is defined as the total number of ^{60}Fe atoms originally passing through 1 cm^2 of space, and is thus the time integrated flux. If a complete time profile of the ^{60}Fe input was measured, then an integration over the entire signal range can yield Φ_{LIF}. For the sediment samples examined in this work, a rough estimate of $\Phi_{LIF\text{-}sed}$ can be calculated making a series of assumptions. The quantities required for this calculation are summarized in Tab. (6.3). This estimation can be performed by calculating the average concentration of ^{60}Fe over the signal region and then the number of ^{60}Fe atoms per cm^2 of sediment. For a calculation of the average decay-corrected concentration of ^{60}Fe/Fe in the signal range ($1.7 - 2.7$ Ma), the result from each individual data point is first corrected for radioactive decay (as in Fig. (6.8)). An average over the entire range can then be obtained in two different ways. (1) All samples are grouped together and weighed by their individual Q_{eff}. (2) The concentration is integrated over the time range of interest (e.g. $1.7 - 2.7$ Ma) and divided by its length (in this case 1 Ma), which can be approximated by a sum over all data points i:

$$\left(\frac{^{60}\mathrm{Fe}}{\mathrm{Fe}}\right)_{\mathrm{avg}} = \frac{\int_{t_1}^{t_2}\left(\frac{^{60}\mathrm{Fe}}{\mathrm{Fe}}\right)(t)dt}{t_2 - t_1} \approx \frac{\sum_i \left(\frac{^{60}\mathrm{Fe}}{\mathrm{Fe}}\right)_i \Delta t_i}{t_2 - t_1}\frac{1}{f_{\mathrm{corr}}}, \tag{6.4}$$

where Δt_i is the width of each data point and f_{corr} is a correction factor accounting for over and under-coverage of time intervals between t_1 and t_2 by the data (typically $f_{\mathrm{corr}} = 0.8 - 0.9$). Both (1) and (2) yielded similar values for the average decay-corrected concentration ^{60}Fe/Fe of $(7.4 \pm 1.1) \times 10^{-16}$ in core 848 and $(4.7 \pm 0.7) \times 10^{-16}$ in core 851, respectively. Depending on the exact choice of t_1 and t_2, the resulting average concentration will be different. This is also depicted in Fig. (6.8), which shows the decay corrected concentrations of ^{60}Fe/Fe determined in core 848 and two possible estimates of the integral signal as a red and a green box. For simplicity, ^{60}Fe is assumed to reside only CBD extractable minerals and thus is completely removed from the sediment during extraction. $\Phi_{\text{LIF-sed}}$ is then obtained by multiplying this number with a factor 4, which is the ratio between the surface area of Earth ($4\pi r_{\mathrm{E}}^2$) and its projection (πr_{E}^2). Since in reality ^{60}Fe may also be present in non-CBD extractable minerals, the actual input into the sediment might be higher than estimated using Φ_{LIF}. The average $\Phi_{\text{LIF-sed}}$ deduced from both sediment cores is $\Phi_{\text{LIF-sed}} = (2.0 \pm 0.6) \times 10^6$ at/cm^2. The actual interstellar fluence Φ_{LIF} is larger than $\Phi_{\text{LIF-sed}}$, because not all ^{60}Fe atoms can be expected to be incorporated into the sediment. The fraction of atoms of ^{60}Fe incorporated is defined as the uptake factor U_{sed}.

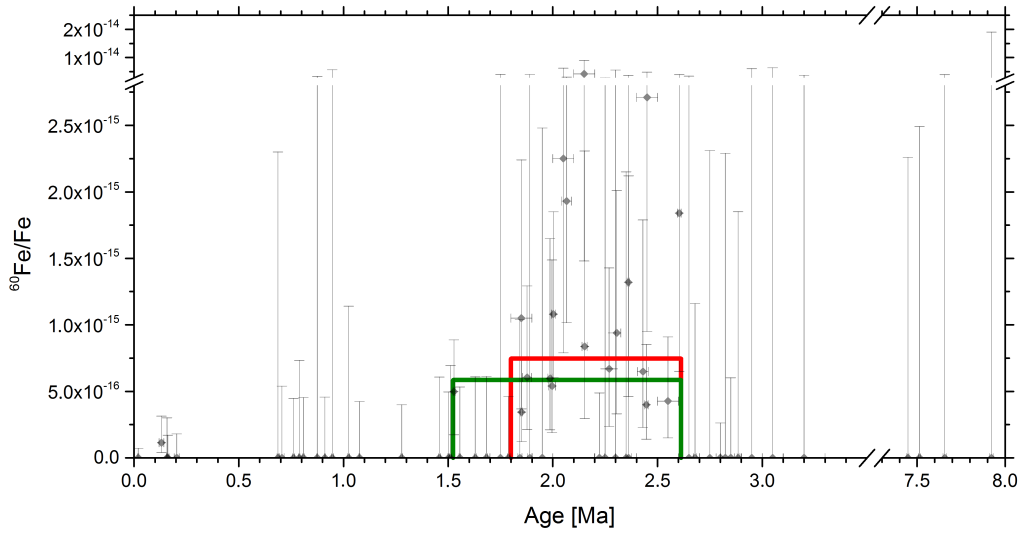

Figure 6.8: Concentrations of ^{60}Fe/Fe determined for individual samples of core 848, corrected for radioactive decay of ^{60}Fe. Superimposed are two possible averages in order to determine Φ_{LIF}.

Quantity	Core 848	Core 851	Description
ϵ_{chem}	$(85 \pm 5)\%$	$(85 \pm 5)\%$	efficiency of chemistry
y_{chem} [mg/g]	0.12 ± 0.02	0.11 ± 0.02	average Fe yield
Y_{chem} [mg/g]	0.14 ± 0.02	0.13 ± 0.02	$Y_{\text{chem}} = y_{\text{chem}}/\epsilon_{\text{chem}}$ y_{chem} corrected for efficiency
N_{Fe} [at/g]	$(1.5 \pm 0.2) \times 10^{18}$	$(1.4 \pm 0.2) \times 10^{18}$	$N_{\text{Fe}} = Y_{\text{chem}} \times N_A/M_{\text{Fe}}/1000$ Fe atoms extracted g^{-1} sed.
R_{dc}	$(7.4 \pm 1.1) \times 10^{-16}$	$(4.7 \pm 0.7) \times 10^{-16}$	avg. (dec. corr.) ^{60}Fe/Fe in peak
N_{60} [at/g]	1120 ± 250	650 ± 140	$N_{60} = N_{\text{Fe}} \times R_{\text{dc}}$ ^{60}Fe atoms extracted g^{-1} of sed.
ρ_{sed} [g/cm^3]	0.63 ± 0.09	0.68 ± 0.10	average dry sed. density
t_{peak} [Ma]	1.0 ± 0.2	1.0 ± 0.2	time duration of ^{60}Fe signal
r_{sed} [m/Ma]	6.1 ± 0.3	19.3 ± 1.0	avg. sed. rate in peak region
h_{peak} [m]	6.1 ± 1.5	19.3 ± 4.8	$h_{\text{peak}} = t_{\text{peak}} \cdot r_{\text{sed}}$ height of peak sediment column
V_{peak} [cm^3]	480 ± 120	1520 ± 380	$V_{\text{peak}} = \pi(0.5)^2 \times 100 \times h_{\text{peak}}$ volume of peak sed. under 1 cm^2
M_{peak} [g]	300 ± 90	1030 ± 300	$M_{\text{peak}} = V_{\text{peak}} \times \rho_{\text{sed}}$ mass of peak sed. under 1 cm^2
$N_{\text{60-peak-dc}}$ [at]	$(3.4 \pm 1.2) \times 10^5$	$(6.7 \pm 2.5) \times 10^5$	$N_{\text{60-peak-dc}} = N_{60} \times M_{\text{peak}}$ ^{60}Fe atoms per cm^2 dec. corr.
$\Phi_{\text{LIF-sed}}$ [at/cm^2]	$(1.4 \pm 0.6) \times 10^6$	$(2.7 \pm 1.1) \times 10^6$	$\Phi_{\text{LIF-sed}} = 4 \times N_{\text{60-peak-dc}}$ local interstellar fluence

Table 6.3.: Key quantities required for an estimation of the local interstellar fluence. N_A is Avogadro's number and M_{Fe} is the atomic mass of iron. Abbreviations: sed. - sediment, sed. rate - sedimentation rate, dec. corr. - decay corrected.

6.4.5. Uptake factor

Recent measurements of ^{60}Fe in lunar samples allowed for a more reliable estimation of $\Phi_{\text{LIF-moon}} = (4 - 20) \times 10^7$ at/cm^2 (not decay corrected since a time-resolved measurement is not possible due to the lack of sedimentation) (Fimiani et al., 2014). The lunar surface is very well suited as a sampling site to obtain the local interstellar fluence of ^{60}Fe, since any input just collects on the surface and remains there. This result is thus a much more reliable estimate of the actual Φ_{LIF} than $\Phi_{\text{LIF-sed}}$ obtained from sediment. The discrepancy between $\Phi_{\text{LIF-sed}}$ and $\Phi_{\text{LIF-moon}}$ can be explained with a low uptake factor into the sediment:

$$U_{\text{sed}} = \frac{\Phi_{\text{LIF-sed}}}{\Phi_{\text{LIF}}} \approx \frac{\Phi_{\text{LIF-sed}}}{\Phi_{\text{LIF-moon-HL}}} = (0.2 - 3.8)\% \tag{6.5}$$

where $\Phi_{\text{LIF-moon-HL}}$ is the decay-corrected fluence on the lunar surface by applying a correction factor of 1.8, corresponding to an average deposition time of 2.2 Ma. Assuming that the same number of atoms of ^{60}Fe arrive on Earth and on the moon, then there are several possible explanations for this low uptake factor. Firstly, since the ocean mixing time (> 1000 a) is longer than the typical residence time of Fe in the ocean, it cannot be expected that the deposition is the same in all parts of the ocean. Depending on wind patterns upon atmospheric deposition and ocean currents, the number of ^{60}Fe atoms finally available for sediment deposition can vary from site to site. This is also supported by a recent ^{60}Fe measurement in Indian Ocean sediment

cores, where the uptake factor was found to be about one order of magnitude higher (Feige, 2014). Secondly, a fraction of ^{60}Fe can be in the form of non-CBD extractable minerals, such as MMs (not completely ablated dust grains) or CBD-extractable minerals embedded in a non-extractable host mineral, which would remain in the sediment residue after CBD extraction.

6.4.6. Compatibility with ferromanganese crust

Assuming that the observed ^{60}Fe signal in the sediment in this work is the same one which was observed in the ferromanganese crust (Knie et al., 2004; Fitoussi et al., 2008), then the temporal-signature should be similar (assuming correct dating methods). Fig. (6.9) shows a compilation of the ferromanganese crust data and one possible data grouping of each, core 848 and core 851. The time-structure of the profile measured in the sediment is clearly compatible with the one in the crust within the given uncertainties. This is an indication that the signatures observed in the sediment and the crust actually have the same origin.

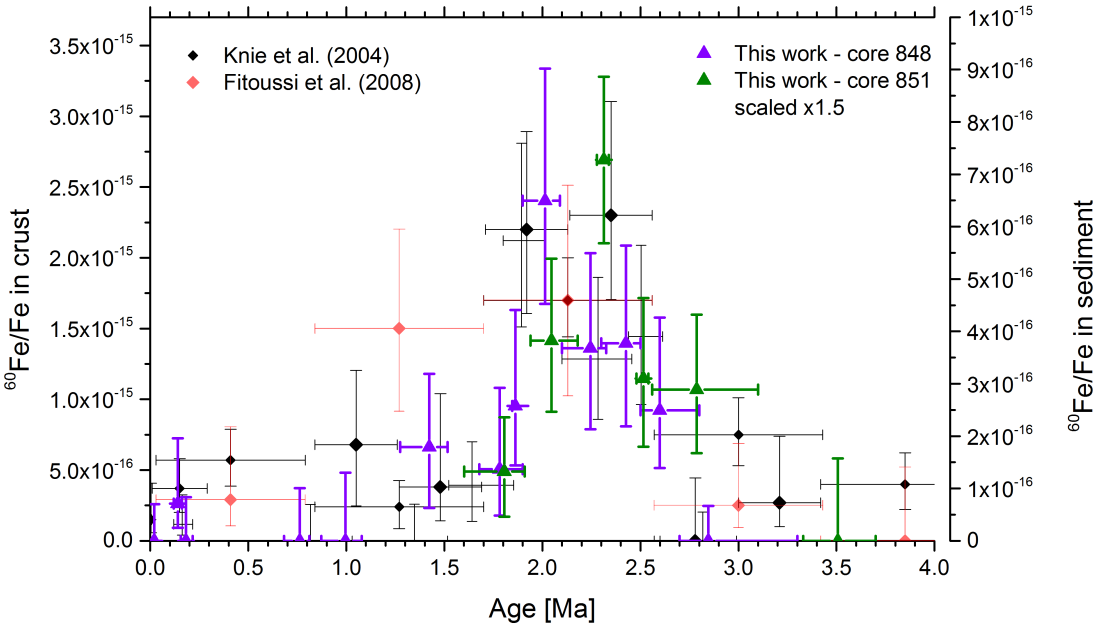

Figure 6.9: Comparison of ^{60}Fe/Fe data from Knie et al. (2004) and Fitoussi et al. (2008) for the ferromanganese crust (left y-axis) with data for sediment core 848 (unscaled) and core 851 (scaled by 1.5) (right y-axis).

The concentration of ^{60}Fe/Fe in the sediments is lower than in the crust. This also results in a lower uptake factor for the sediment. For a comparison of the uptake factors, it should be mentioned that the crust data was measured against a different AMS standard, which is currently being re-evaluated in advanced cross-calibration measurements (unpublished). Taking the preliminary result from this re-evaluation into account, the crust ^{60}Fe/Fe ratio in the crust needs to be corrected up by a factor $\sim 1.8 \pm 0.2$. Taking this and the updated half-life (2.61 Ma) into account, the local interstellar fluence estimate from the crust becomes $\Phi_{\text{LIF-crust}} = (1.0 \pm 0.5) \times 10^7$ at/cm^2. The uptake factor into the crust can be estimated as

$$U_{\text{crust}} = \frac{\Phi_{\text{LIF-crust}}}{\Phi_{\text{LIF}}} \approx \frac{\Phi_{\text{LIF-crust}}}{\Phi_{\text{LIF-moon-HL}}} = (3-14)\%. \tag{6.6}$$

This means that the uptake factor of the crust is about one order of magnitude larger than for the sediment. As previously mentioned, this is most likely a combination of two effects: the local variation of ^{60}Fe deposition and the uptake efficiency into the respective geological reservoir, leading to different uptake factors.

6.4.7. Astrophysical interpretation

After excluding a GCR origin or statistical background as the cause of the observed ^{60}Fe signature in both sediment cores, it is interpreted as the deposition in interstellar material into our solar system by one or more SN explosions. In a recent model calculation by Fry and Fields (2014), the shape of SN ejecta from a single SN event arriving at Earth is expected to be cusp-shaped. This means that these authors expect a sharp rise at the time of arrival of the ejecta, and a slow decay of the signal over about half of the travel time from the SN explosion. Assuming a relatively distant SN event ($150-200$ pc) with a high mass ejection of ^{60}Fe, the long travel time could cause an exposure of Earth that is even longer than 1 Ma. This means that the observed signature of ^{60}Fe in the sediment might be explained by a single SN event. However, it cannot be excluded that a superposition of multiple SNe is responsible. Unfortunately, a clear distinction between these scenarios is still out of reach, but might be possible in the future, when more depth-resolved studies of ^{60}Fe in terrestrial reservoirs become available.

7. Conclusion

Over the course of this work, an isotopic anomaly of ^{60}Fe was studied in 109 samples from two Pacific Ocean sediment cores. This sediment was characterized using magnetic measurements and it has been shown to be rich in magnetofossils ($15 - 60$ μg/g).

The AMS samples were prepared using the very mild CBD leaching technique, which was specifically fine-tuned to leave primary minerals mostly intact and dissolve mainly secondary iron oxides, such as magnetofossils. It was shown using novel magnetic analysis methods, including high-resolution FORC diagrams (Ludwig et al., 2013) that for a representative sediment sample, about 24% of the Fe in the final AMS sample originates from magnetofossils. In this way, the expected ratio of ^{60}Fe/Fe could be maximized, since magnetofossils, as secondary minerals, can be expected to carry the original ^{60}Fe/Fe signal without dilution. This work produced the first fully quantitative description of magnetofossils in a marine sediment by combining chemical and magnetic unmixing techniques.

The 109 AMS samples were measured at the GAMS setup in Garching, which is uniquely suited for low-level measurements of ^{60}Fe because it allows for complete suppression of the stable isobar ^{60}Ni in a gas-filled magnet. The measurements were distributed over the course of three years in ten separate beamtimes.

A signature of ^{60}Fe was observed in both sediment cores. The average concentrations observed is relatively low (^{60}Fe/Fe $\approx (3-8)\times 10^{-16}$). The signal is centered around $t_c = (2.19 \pm 0.11)$ Ma and has a total duration of $t_{SN} = (0.96 \pm 0.25)$ Ma. This corresponds to a total of 87 events of ^{60}Fe were detected.

The origin of the observed enhanced ^{60}/Fe ratios was narrowed down: (1) An anthropogenic, i.e. ^{60}Fe contaminations by nuclear bombs, plants, and reprocessing facilities can be excluded for deep sediment layers and could only contribute to the surface concentration of ^{60}Fe. (2) Cosmogenic production of ^{60}Fe, i.e. in GCR spallation on targets on Earth is strongly suppressed by atmospheric shielding. A possible contamination by such, in situ produced ^{60}Fe can be excluded, since the depth profile of such a contribution would be similar to an exponential decay curve, modulated by GCR intensity, and thus cannot explain the peak-shaped ^{60}Fe which was observed. This is also supported by the lack of an increased ratio of ^{53}Mn/Mn in core 851. (3) The local deposition of ^{60}Fe of MMs from non-SN sources, e.g. IDPs, could also be dismissed: firstly, because the CBD procedure mainly targets fine-grained iron-bearing minerals. Secondly, a localized input of MMs could not explain that the ^{60}Fe signature has been observed in other reservoirs as well (e.g. in the ferromanganese crusts (Knie et al., 2004)).

After excluding all other possibilities, the observation of an increased ^{60}Fe/Fe ratio which was observed in this work is attributed to the deposition of SN debris into our solar system ~ 2.7 Ma ago. The integrated number of atoms of ^{60}Fe, could be used to obtain a value for the local interstellar fluence, $\Phi_{\text{LIF-sed}} = (2.0 \pm 0.6) \times 10^6$ at/cm^2. This number is by 1-2 orders of

magnitudes lower than recent values from the lunar surface (Fimiani et al., 2014), corresponding to an uptake factor of the sediment in the range $U_{\mathrm{sed}} = (0.2 - 3.8)\%$. A likely explanation for this observation is that the deposition of ^{60}Fe atoms was not constant everywhere on Earth. This can be explained by taking into account that the residence time of soluble Fe in water is shorter than the typical ocean mixing timescale. This means that deposition depends on wind and water flow patterns and can locally enhance or reduce the number of deposited atoms of ^{60}Fe. This is also supported by a recent ^{60}Fe measurement in Indian Ocean sediment cores (Feige, 2014), where a larger uptake factor was observed.

The temporal signature of the observed ^{60}Fe exposure is compatible with earlier measurements ferromanganese crust samples (Knie et al., 1999, 2004; Fitoussi et al., 2008). An important remaining question is whether the observed signature was caused by a single SN, or a superposition of two or more SN events. While long exposures (even > 1 Ma) could possibly be produced by a single SN event (Fry and Fields, 2014), a superposition of several SN events cannot be excluded.

A. Appendix: Individual sample results

Detailed information on all ^{60}Fe sediment samples measured for this work is displayed in Tab. (A) for sediment core 848 and in Tab. (A) for sediment core 851.

The concentrations of ^{60}Fe/Fe obtained for both cores are displayed in Fig. (A.1).

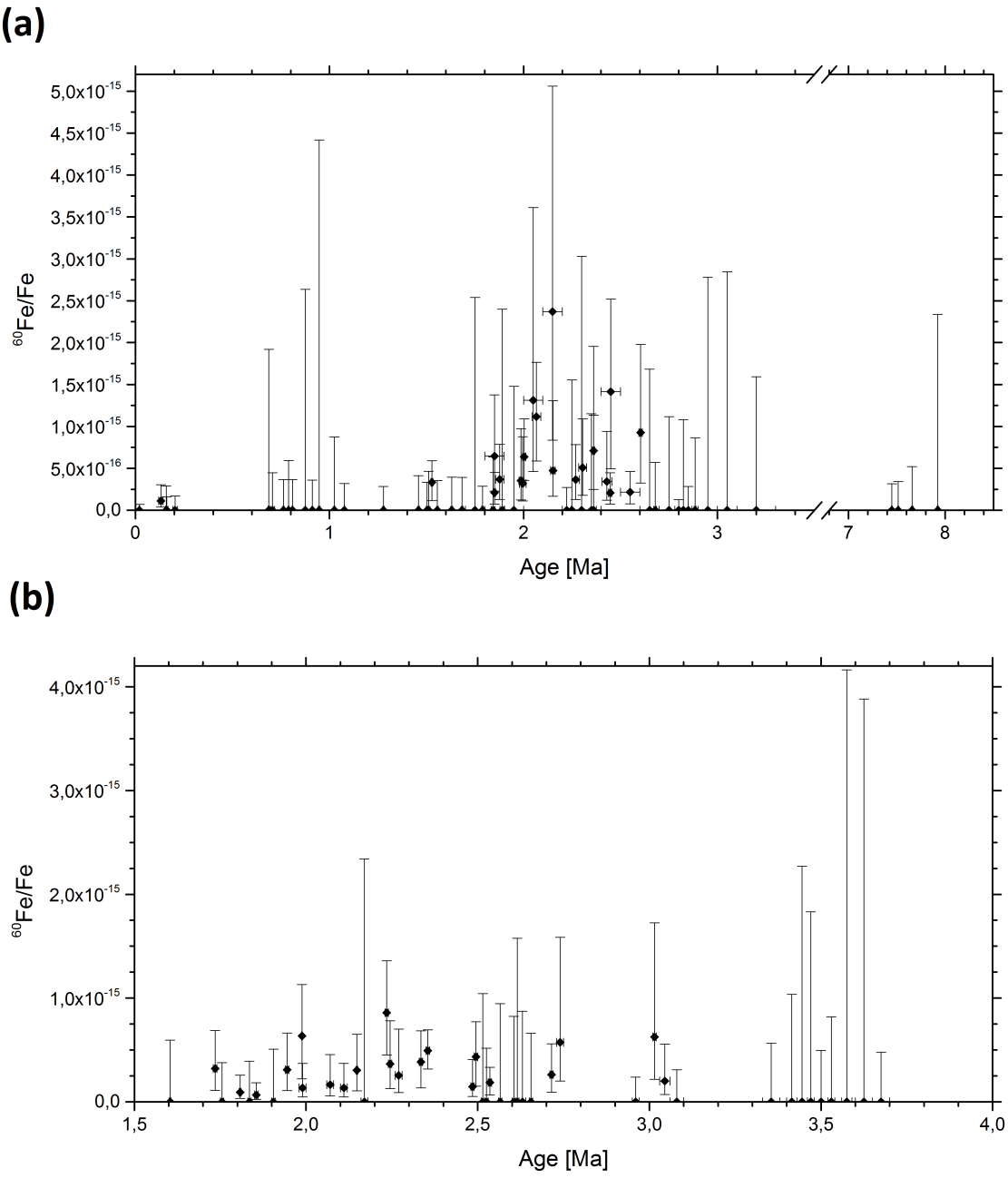

Figure A.1: (a) Isotopic ratio of ^{60}Fe/Fe measured (not decay corrected) for all 65 samples of sediment core 848. (b) Same for all 44 samples of core 851.

Age [Ma]	Sed. mass [g]	Fe [mg/g]	Q_{eff} $\times 10^{15}$	Events	$^{60}Fe/Fe$ $\times 10^{-16}$
0.020 ± 0.003	74.0*	0.17	20.50	0	< 0.70
0.131 ± 0.011	78.7*	0.11	9.07	1	$1.1^{+1.9}_{-0.7}$
0.158 ± 0.003	43.0	0.19	4.99	0	< 2.9
0.161 ± 0.006	48.7	0.17	8.86	0	< 1.6
0.204 ± 0.012	43.1	0.22	8.46	0	< 1.7
0.687 ± 0.004	42.7	0.15	0.75	0	< 19
0.706 ± 0.011	42.5	0.16	3.22	0	< 4.5
0.762 ± 0.004	49.6	0.08	3.94	0	< 3.7
0.789 ± 0.003	48.2	0.15	2.42	0	< 5.9
0.809 ± 0.003	45.1	0.10	3.94	0	< 3.7
0.875 ± 0.002	40.1	0.19	0.55	0	< 26
0.911 ± 0.002	41.4	0.10	4.01	0	< 3.7
0.947 ± 0.005	37.5	0.14	0.33	0	< 44
1.025 ± 0.004	43.7	0.18	1.65	0	< 8.7
1.077 ± 0.002	38.2	0.13	4.53	0	< 3.2
1.278 ± 0.004	39.9	0.15	5.06	0	< 2.9
1.458 ± 0.005	34.7	0.17	3.49	0	< 4.1
1.502 ± 0.003	35.0	0.09	4.33	0	< 3.3
1.511 ± 0.006	34.1	0.13	3.10	0	< 4.7
1.528 ± 0.005	35.7	0.17	9.03	3	$3.3^{+2.6}_{-2.2}$
1.556 ± 0.004	44.1	0.10	4.08	0	< 3.5
1.630 ± 0.005	46.1	0.12	3.64	0	< 4.0
1.683 ± 0.005	41.1	0.11	3.67	0	< 3.9
1.75 ± 0.05	30.0	0.07	0.57	0	< 25
1.788 ± 0.004	45.2	0.14	5.01	0	< 3.0
1.84 ± 0.01	50.0*	0.09	2.26	0	< 6.4
1.85 ± 0.05	20.0	0.15	3.10	2	$6.5^{+7.3}_{-4.2}$
1.851 ± 0.005	36.1	0.11	9.50	2	$2.1^{+2.4}_{-1.4}$
1.877 ± 0.022	63.0*	0.10	5.43	2	$3.7^{+4.2}_{-2.4}$
1.890 ± 0.012	42.6	0.09	0.60	0	< 24
1.95 ± 0.05	30.1	0.10	0.97	0	< 15
1.99 ± 0.01	40.1	0.10	2.83	1	$3.5^{+6.2}_{-2.3}$
1.996 ± 0.017	40.0	0.10	3.14	1	$3.2^{+5.6}_{-2.1}$
2.003 ± 0.009	32.6	0.20	6.28	4	$6.4^{+4.5}_{-2.8}$
2.05 ± 0.05	26.0	0.11	0.76	1	13^{+23}_{-8}
2.066 ± 0.023	31.0	0.09	4.48	5	$11.2^{+6.5}_{-5.3}$
2.15 ± 0.05	30.0	0.11	0.84	2	23^{+27}_{-15}
2.152 ± 0.012	37.6	0.07	2.11	1	$4.7^{+8.3}_{-3.1}$
2.223 ± 0.023	33.0	0.16	5.31	0	< 2.7
2.25 ± 0.05	38.0	0.08	0.93	0	< 16
2.27 ± 0.02	40.0	0.09	5.45	2	$3.7^{+4.2}_{-2.4}$
2.3 ± 0.1	40.8	0.11	0.48	0	< 30
2.31 ± 0.02	30.0	0.14	3.92	2	$5.1^{+5.8}_{-3.3}$
2.35 ± 0.05	30.0	0.06	1.25	0	< 12
2.361 ± 0.006	32.0	0.07	1.41	1	7^{+12}_{-5}

Table A.1.: Continued in Tab. (A.2).

Age [Ma]	Sed. mass [g]	Fe [mg/g]	Q_{eff} $\times 10^{15}$	Events	$^{60}Fe/Fe$ $\times 10^{-16}$
2.362 ± 0.013	38.0	0.12	1.27	0	< 11
2.430 ± 0.026	35.0	0.10	2.93	1	$3.4^{+6.0}_{-2.2}$
2.447 ± 0.008	39.2	0.10	9.57	2	$2.1^{+2.4}_{-1.4}$
2.45 ± 0.05	25.7	0.20	2.12	3	14^{+11}_{-9}
2.55 ± 0.05	69.3*	0.14	9.22	2	$2.2^{+2.5}_{-1.4}$
2.604 ± 0.009	32.0	0.12	2.16	2	9^{+10}_{-6}
2.65 ± 0.05	30.1	0.11	0.86	0	< 16
2.679 ± 0.007	48.0	0.05	2.53	0	< 5.7
2.75 ± 0.05	41.0	0.07	1.29	0	< 11
2.8 ± 0.1	34.6	0.08	11.5	0	< 1.3
2.824 ± 0.044	35.0	0.08	1.33	0	< 11
2.85 ± 0.05	46.0	0.06	5.08	0	< 2.8
2.885 ± 0.005	46.0	0.06	1.67	0	< 8.6
2.95 ± 0.05	36.0	0.05	0.52	0	< 28
3.05 ± 0.05	38.0	0.07	0.51	0	< 28
3.2 ± 0.1	26.8	0.15	0.91	0	< 16
7.448 ± 0.006	48.0	0.16	4.57	0	< 3.2
7.514 ± 0.006	38.0	0.08	4.22	0	< 3.4
7.66 ± 0.01	45.0	0.20	2.77	0	< 5.2
7.92 ± 0.01	41.8	0.17	0.62	0	< 23

Table A.2.: Continuation of Tab. (A.1). Summary of individual samples measured from sediment core 851. Samples with > 50 g (marked with a *) available mass were split into two chemical preparations, but the data was summed up in the end.

Age [Ma]	Sed. mass [g]	Fe [mg/g]	Q_{eff} $\times 10^{15}$	Events	$^{60}Fe/Fe$ $\times 10^{-16}$
1.604 ± 0.003	32.5	0.11	2.42	0	< 6.0
1.735 ± 0.005	22.1	0.15	6.22	2	$3.2^{+3.6}_{-2.1}$
1.755 ± 0.005	33.1	0.12	3.82	0	< 3.8
1.808 ± 0.003	31.8	0.09	10.70	1	$0.93^{+1.6}_{-0.61}$
1.835 ± 0.005	26.9	0.09	3.68	0	< 3.9
1.855 ± 0.005	38.0	0.11	15.00	1	$0.67^{+0.29}_{-0.67}$
1.905 ± 0.005	33.0	0.10	2.83	0	< 5.1
1.945 ± 0.005	33.5	0.11	6.44	2	$3.1^{+3.5}_{-2.0}$
1.99 ± 0.01	29.6	0.09	7.46	1	$1.3^{+2.4}_{-0.9}$
1.998 ± 0.001	35.4	0.09	4.72	3	$6.4^{+5.0}_{-4.1}$
2.07 ± 0.01	36.4	0.12	6.04	1	$1.6^{+2.9}_{-1.1}$
2.11 ± 0.01	31.9	0.13	7.43	1	$1.4^{+2.4}_{-0.9}$
2.148 ± 0.003	38.9	0.09	6.55	2	$3.1^{+3.5}_{-2.0}$
2.17 ± 0.01	28.5	0.04	0.62	0	< 23
2.235 ± 0.005	42.1	0.11	5.82	5	$8.6^{+5.0}_{-4.1}$
2.245 ± 0.005	45.8	0.09	5.47	2	$3.7^{+4.2}_{-2.4}$
2.27 ± 0.01	34.5	0.13	3.93	1	$2.5^{+4.5}_{-1.7}$
2.235 ± 0.005	42.4	0.10	7.79	3	$3.9^{+3.0}_{-2.5}$
2.355 ± 0.005	51.1*	0.14	20.3	10	$4.9^{+2.0}_{-1.8}$
2.485 ± 0.005	38.5	0.14	6.77	1	$1.5^{+2.6}_{-1.0}$
2.495 ± 0.005	31.0	0.15	6.92	3	$4.3^{+3.4}_{-2.8}$
2.515 ± 0.005	28.6	0.15	1.38	0	< 10
2.525 ± 0.005	39.0	0.13	2.78	0	< 5.2
2.535 ± 0.005	44.0	0.08	16	3	$1.9^{+1.5}_{-1.2}$
2.565 ± 0.005	30.5	0.09	1.52	0	< 9.5
2.605 ± 0.005	42.4	0.11	1.75	0	< 8.2
2.615 ± 0.005	30.6	0.10	0.91	0	< 16
2.63 ± 0.01	34.1	0.10	1.65	0	< 8.7
2.655 ± 0.005	46.1	0.07	2.18	0	< 6.6
2.715 ± 0.005	35.5	0.13	7.62	2	$2.6^{+3.0}_{-1.7}$
2.74 ± 0.01	49.0	0.15	1.74	1	6^{+11}_{-4}
2.96 ± 0.01	39.7	0.14	6.01	0	< 2.4
3.015 ± 0.005	40.1	0.12	1.60	1	6^{+11}_{-4}
3.045 ± 0.015	26.0	0.16	4.95	1	$2.0^{+3.6}_{-1.3}$
3.08 ± 0.02	38.1	0.12	4.64	0	< 3.1
3.355 ± 0.025	25.7	0.12	2.55	0	< 5.7
3.415 ± 0.015	29.8	0.11	1.39	0	< 10
3.445 ± 0.015	36.0	0.02	0.63	0	< 23
3.47 ± 0.01	36.2	0.08	0.79	0	< 18
3.50 ± 0.02	45.3	0.12	2.90	0	< 5.0
3.53 ± 0.01	61.4*	0.12	1.76	0	< 8.2
3.575 ± 0.015	38.0	0.07	0.35	0	< 42
3.625 ± 0.025	38.0	0.07	0.37	0	< 39
3.675 ± 0.025	30.0	0.10	3	0	< 4.8

Table A.3.: Summary of individual samples measured from sediment core 851. Samples with > 50 g (marked with a *) available mass were split into two chemical preparations, but the data was summed up in the end.

B. Appendix: Multi-isotope measurements

In addition to ^{60}Fe, there are several other AMS isotopes which can be measured in marine sediments. While ^{10}Be and ^{26}Al can serve as an independent dating method of sediment cores, there are several isotopes which might also show an enhancement from SN input, including ^{26}Al and ^{53}Mn. This study was limited to 14 samples of sediment core 851 in the age range 1.75-3.48 Ma, due to limited time for sample preparation and beamtime. All concentrations measured for ^{10}Be, ^{26}Al, and ^{53}Mn are summarized in Tab. (B.5.3) at the end of the chapter.

B.1. Chemical extraction

The preparation of all samples for the multi-isotope-analysis was performed by Dr. Silke Merchel at the HZDR. The procedure described in Feige et al. (2013) was employed, which uses a strong hydroxylamine leaching described by Bourlès et al. (1999) and Fitoussi and Raisbeck (2007), which was adapted by to produce samples from higher mass of marine sediment (i.e. 3 g instead of 1 g). Specifically, in the procedure described in Feige et al. (2013), a separation of the fraction containing Fe, Al, and Be from Mn is achieved by precipitation of the hydroxides of Fe, Al, and Be with NH_3(aq). Mn(II), exposed to oxygen in the air, is then slowly oxidized to Mn(IV) and undergoes a delayed precipitation as $MnO(OH)_2$ after few hours. A suppression of ^{53}Cr necessary for AMS measurements of ^{53}Mn is then achieved by dissolving the Mn in HNO_3 and H_2O_2 and precipitating it again using $KClO_3$.

For each sample, 3 g of sediment were used. Two batches of 7 samples each were processed, yielding 14 AMS samples for measurements of the radioisotopes ^{10}Be, ^{26}Al, ^{53}Mn, and ^{60}Fe, and 2 processing blanks for ^{10}Be. Due to the low abundance of stable Be, about 0.3 mg of ^{9}Be were added as carrier to each sample. After leaching, but before carrier addition, an aliquot of the solution was taken for ICP-MS analysis.

Since AMS only allows for the determination of isotopic ratios, it needs to be supplemented with an absolute measurement technique for the stable isotope in order to obtain an absolute count of the number of atoms in a sample of the radioactive counterpart. To this end, an ICP-MS measurement at the Institut für Resourcenökologie at HZDR in Dresden was performed for each sample, determining the amounts of stable Be, Al, Mn, and Fe in each sample.

The measurements of the ^{60}Fe samples were described in Sec. (5.3.9). The measurements of the other isotopes are discussed in the following.

B.2. DREAMS setup at HZDR

Measurements of ^{10}Be and ^{26}Al were performed at the DREAMS setup at the HZRD, Germany. A short description of the setup follows, however, for a more detailed account, the reader is referred to Akhmadaliev et al. (2013).

The ion beam is formed using one of two identical Cs-sputter ion sources (model SO-110), which feature sample wheels for 200 samples each. After energy selection in a 54° electrostatic analyzer, the beam passes a 90° bouncing magnet, which allows for fast cycling (about 70 Hz) by alternating the injection of radioactive and stable beam. The accelerator is a 6 MV Tandetron (HVEE) using argon as a stripper gas. On the high-energy side of the accelerator, the ions pass a 90° analyzing magnet and then a system of of 2 moveable Faraday cups. This allows for current measurement of up to two stable isotopes during AMS measurements using the bouncing magnet. Afterward, the ions pass an optional absorber foil of 1 μm silicon nitride for isobar suppression, and then a 35° ESA. Particle identification and counting are performed with an isobutane-filled ionization chamber with 4 anodes.

The typical measurement procedure consists of a block of 30 second runs for each sample, during which the AMS isotope is injected for about 29.5 s, and the remaining 0.5 s are used for injecting the stable isotope for a current measurement. Depending on the type of sample and the desired statistics, a block typically consists of 10 to 50 runs, before the sample is changed. A measurement cycle usually begins with a standard sample, then a blank, and afterward the samples of interest.

B.3. ^{10}Be

In stars, light elements (Li, Be, B) are quickly consumed by capture reactions at high temperature. Their observed abundance on Earth is mainly due to spallation reactions. ^{10}Be, with a half-life of (1.387 ± 0.012) Ma (Korschinek et al., 2010; Chmeleff et al., 2010) on Earth is almost exclusively produced in solar and galactic cosmic ray (SCR and GCR) spallation reactions on the atmosphere. It can then be transported to the Earth's surface by dust, rain or snow and be incorporated into geological reservoirs and can be used for dating over several Ma (Bourlès et al., 1999).

B.3.1. ^{10}Be measurement at DREAMS

^{10}Be samples are prepared as BeO, mixed 1:4 by weight with Nb powder. Measurements of ^{10}Be are performed at a terminal voltage of 4.5 MV, leading to an energy of 10.7 MeV for $^{10}Be^{2+}$. Be is extracted from the ion source as BeO^- with a typical current of several μA of stable $^9BeO^-$. The main challenge for ^{10}Be measurements is the suppression of the stable isobar ^{10}B, which is realized by inserting a 1 μm thick silicon nitride foil on the high-energy side, where ^{10}B ($Z = 5$) loses more energy than ^{10}Be ($Z = 4$). Due to this energy difference between the isobars, they can be separated in an electrostatic analyzer. This allows most of the ^{10}Be, but only a small fraction of ^{10}B to reach the ionization chamber, where the remaining ^{10}B is completely suppressed because it does not reach the last anode. For normalization, the secondary in-house standard

SMD-Be-12 with $^{10}Be/^{9}Be = (1.704 \pm 0.036) \times 10^{-12}$ (Akhmadaliev et al., 2013) is used. As blank sample, two processing blanks which have undergone the same chemical procedure as the sediment samples, were measured. The amount of stable ^{9}Be is also required to reconstruct the original concentration of $^{10}Be/^{9}Be$ in the sediment, since carrier material was used. This was also performed at HZDR with a total uncertainty of the ^{9}Be measurements of 5%.

B.3.2. ^{10}Be AMS results

All 14 sediment samples were measured twice, in two separate beamtimes. All of them performed very well during the experiment and yielded an average of 10^6 events of ^{10}Be each. The average blank level was determined several times during the measurements to be $^{10}Be/^{9}Be = (5.9 \pm 0.9) \times 10^{-15}$, which was several orders of magnitudes below the concentrations of all samples.

Due to the addition of stable carrier material, the determined concentrations of $^{10}Be/^{9}Be$ in the AMS samples was on the order of $^{10}Be/^{9}Be \approx 10^{-11} - 10^{-10}$. This data then needed to be corrected for the ^{9}Be carrier, which was possible using the determined amount of natural ^{9}Be in the aliquot by ICP-MS. The corrected concentrations of $^{10}Be/^{9}Be$ are then about 2-3 orders of magnitude higher. The results are displayed in Fig. (B.1), on a logarithmic scale, and show an exponential decrease with depth. The plot also includes an exponential fit to the data, taking only the y-errors into account. The fit agrees well with the data (reduced $\chi^2 = 1.9$), confirming that the sedimentation rate of core 851 was relatively constant during the time interval under consideration, as could also be seen in the age model (Sec. (3.1.3)). This result provides an independent confirmation of an undisturbed sediment core.

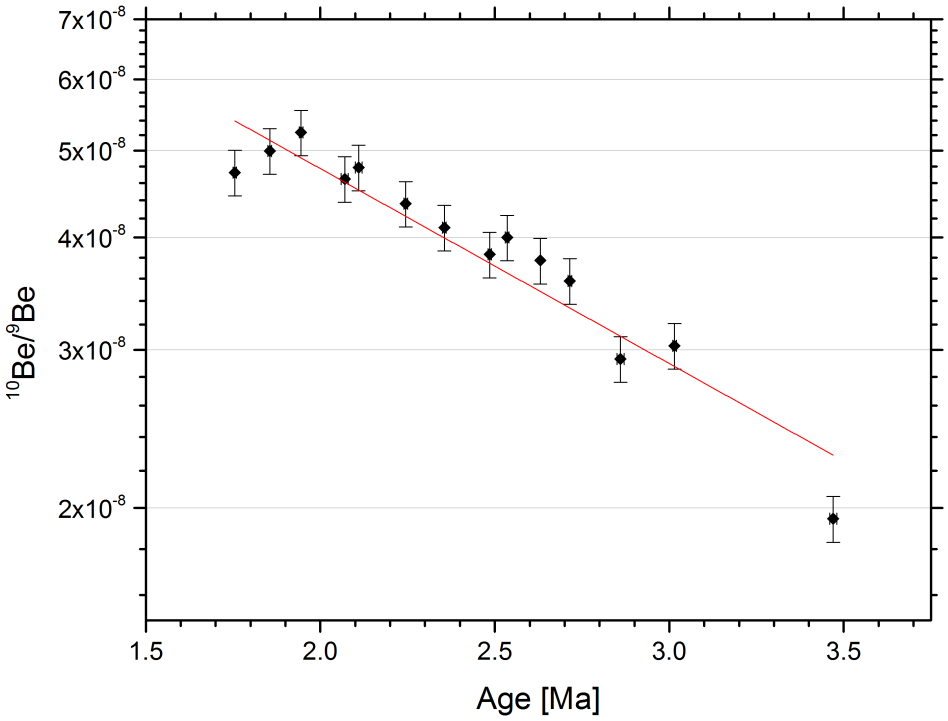

Figure B.1: AMS results of $^{10}Be/^{9}Be$ samples of sediment core 851 corrected for carrier. x-error bars represent sampling range, y-errors correspond to 1-sigma confidence intervals. The red line is an exponential fit using a fixed half-life of 1.387 Ma (reduced $\chi^2 = 1.9$).

B.4. ^{26}Al

The radioisotope ^{26}Al has a half-life of (0.717 ± 0.017) Ma (weighted mean over all available values, see Auer et al., 2009, and references therein) and decays to ^{26}Mg via electron capture or β^+ decay. For decades it has been used in different fields, among others for γ-ray observations of ongoing nucleosynthesis in our galaxy, as a medical tracer isotope, and as a tool to study cosmic ray exposures of meteorites and the lunar surface.

In the universe, ^{26}Al is produced abundantly in massive stars and their subsequent supernova explosions (Limongi and Chieffi, 2006b). ^{26}Al on Earth is mainly produced by cosmic ray spallation on argon in the atmosphere. Similar to beryllium, it can attach to aerosols and be transported to the Earth's surface by both dry and wet deposition mechanisms. Other components which can contribute to the total ^{26}Al content on Earth are the influx of extraterrestrial material (mostly IDPs), cosmic ray spallation on Earth's surface, and secondary reactions induced by natural radioactivities. The background sources are very strong compared to ^{60}Fe, making the discovery of the ^{26}Al counterpart of the ^{60}Fe signature observed by Knie et al. (2004) in our samples unlikely, especially considering a rather long interaction time of Earth with the SN-ejecta enriched ISM.

B.4.1. ^{26}Al measurement at DREAMS

^{26}Al samples are prepared as Al_2O_3 and mixed 1:1 by weight with Ag powder. The method for suppression of the stable isobar ^{26}Mg occurs already in the source, since the beam is extracted as Al^- and Mg does not form negative ions. Thus, in contrast to ^{10}Be, an absorber foil on the high energy side is not necessary for ^{26}Al measurements. The cost of this procedure is the relatively low current of stable $^{27}Al^-$ of several hundred nanoamperes. A terminal voltage of 2.7 MV was used and a charge state of 3+ was selected. The standard material used was the secondary in-house standard SMD-Al-11 with a concentration of $^{26}Al/^{27}Al = (9.660 \pm 0.158) \times 10^{-12}$ (Merchel, 2015, private communication).

B.4.2. ^{26}Al AMS results

All 14 samples were measured in a single beamtime. Unfortunately, the average ion current during the beamtime was low and thus only an average of 25 events of ^{26}Al per sample were detected, causing large statistical uncertainties. Fig. (B.2) shows the results of all samples on a logarithmic scale, including an exponential fit (using $T_{1/2} = 0.717$ Ma) taking only y-errors into account. The fit (reduced $\chi^2 = 1.0$) shows that the data is compatible with a steady influx and radioactive decay.

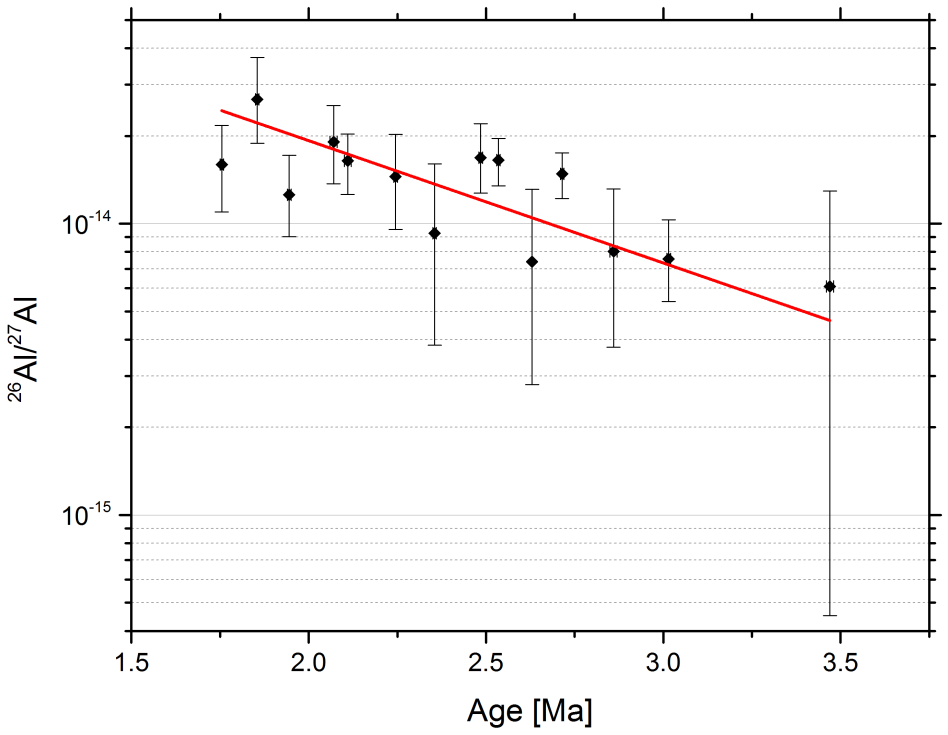

Figure B.2: AMS results of $^{26}Al/^{27}Al$ samples of sediment core 851. x-error bars represent sampling range, y-errors correspond to 1-sigma confidence intervals. The red line is an exponential fit using a fixed half-life of 0.717 Ma (reduced $\chi^2 = 1.0$).

B.5. ^{53}Mn

As an AMS isotope, ^{53}Mn ($T_{1/2} = (3.7 \pm 0.4)$ Ma)(Honda and Imamura, 1971) has various applications. For example, its long half-life could allow for dating of geological reservoirs like manganese crusts and sediments over very long time scales and allow for drawing conclusions on the influx of interplanetary dust particles. Additionally, ^{53}Mn measurements of extraterrestrial material such as meteorites can yield exposure ages to cosmic radiation. AMS measurements of ^{53}Mn are very challenging, but AMS has proven to be the most sensitive detection technique for this isotope, outperforming neutron activation analysis, which had been used for many decades.

There is only one stable Mn isotope, ^{55}Mn, and thus the ratio of ^{53}Mn/^{55}Mn in terrestrial samples determined in AMS, is a measure for the ratio of the input of extraterrestrial and in situ-produced ^{53}Mn to the dilution by stable ^{55}Mn. This stable Mn can reach marine reservoirs like sediments and hydrogenetic crusts by weathering and subsequent water transport, usually dissolved as Mn(II+). Under oxidizing conditions, it can then be found as Mn(IV+) in minerals like MnO_2.

Since ^{53}Mn does not occur as a primordial isotope on Earth ($T_{1/2} <<$ age of the Earth), it has to originate from extraterrestrial sources, or be produced by nuclear reactions here on Earth.

B.5.1. Production and sources of ^{53}Mn

Cosmic ray interactions

The main production mechanism for ^{53}Mn is nuclear spallation reactions involving cosmic radiation, which consists mostly of protons and α particles. While SCR particles have typical energies of $<$ 100 MeV, GCR particles can reach energies of several GeV per nucleon. The most common target material for ^{53}Mn production is Fe. Typical reactions include ^{nat}Fe(p,x)^{53}Mn and ^{nat}Fe(n,y)^{53}Mn, where x and y depend on the target isotope of Fe. A small contribution ($<$ 5%) also comes from spallation on Ni targets.

As an example, one can consider an iron meteoroid, exposed to cosmic radiation for a long time. The production rate of ^{53}Mn in the meteoroid depends on the depth under the surface and the size of the object. After being subjected to irradiation by cosmic rays for several half-lives, the amount of ^{53}Mn will reach a saturation value of p/λ, where p is the production, and λ is the decay rate. Ammon et al. (2009) showed that typical production rates in iron meteorites are 300-400 dpm/kg (disintegrations per minute per kg) and that production is mostly limited to the top 50 cm below the surface due to the limited penetration depth of GCR. Objects smaller than 50 cm can reach a factor 2 higher values due to the larger exposure angle. Since the SCR component has a much lower penetration depth, its contribution is limited to the top layers of larger objects. However, these layers are lost during atmospheric entry of the meteorite, thus GCR production is more important in this case. Similar production rates have been estimated for SCR production in IDPs.

Extraterrestrial sources

The main source of influx of extraterrestrial material onto Earth are fragments originating from the asteroid belt between Mars and Jupiter, as well as from the Oort Cloud, which surrounds our solar system. Fragments of different sizes, from μm sized dust grains to large meteoroids ejected from these sources can intersect Earth's orbit. The total deposition mass of extraterrestrial material onto Earth is estimated to be on the order of $10^7 - 10^8$ kg/a (Kortenkamp and Dermott, 1998; Merchel, 1998). The total amount of ^{53}Mn arriving on Earth in this manner has been estimated to lie between 200 and 2000 at cm^{-2}a^{-1} (Auer, 2008; Nishiizumi et al., 1980).

In-situ production

Interpreting the origin of radioisotopes found on Earth as extraterrestrial can be challenging due to other production mechanisms. In the case of ^{53}Mn, atmospheric production by cosmic rays can be neglected, due to the lack of a heavy atmospheric spallation target with $A > 53$. However, since the Earth's surface is rich in Fe, the primary spallation target for production of ^{53}Mn, in-situ production of unshielded reservoirs has to be expected. Depending on the shielding of the reservoir, the production is a superposition of production rates from several primary and secondary cosmic ray particles, such as muons. For the sediment samples, however, direct in-situ production can be neglected due to the 4000 meters of water depth. A small contribution could nonetheless be transported to the sediment by erosion after in-situ production in less shielded reservoirs, which was estimated by Poutivtsev (2007) to be at least one order of magnitude lower than typical results from ferromanganese crusts and marine sediments.

Massive stars

In massive stars, ^{53}Mn is mainly produced in explosive burning (Meyer, 2005). The most favorable site is the α-rich freeze-out. When the SN shockwave heats Si-rich material to high temperatures (> 5 GK), where nuclei are disintegrated into neutrons, protons, and α-particles and NSE is established for a short time. Upon cooling, not all α's are consumed, leading to the term α-rich freeze-out, where most nuclei are assembled into isotopes in the iron region, and also ^{53}Fe, which quickly decays to ^{53}Mn. Another site is explosive O-burning, which occurs when the SN shockwave penetrates O-rich layers. In this scenario, ^{53}Fe can be produced when temperatures reach ~ 3 GK, yielding ^{53}Mn after decay (Huss et al., 2009). The total amount of ^{53}Mn ejected is difficult to estimate, since it is produced close to the range of masses which might not be ejected, but fall back onto the neutron star or black hole. Typical yields for ^{53}Mn in stars in the mass range $20 - 40\ M_\odot$ are typically between 10^{-5} and $10^{-3}\ M_\odot$ (see e.g. Rauscher et al., 2005), and thus about one order of magnitude higher than for ^{60}Fe.

B.5.2. ^{53}Mn measurement at the MLL

General procedure

All ^{53}Mn measurements were performed at the GAMS setup in Garching using the measurement procedure described by Poutivtsev et al. (2010). The samples are prepared as MnO_2 and mixed

with Ag powder (50% by volume). A beam of $^{55}MnO^-$ is extracted from the ion source and tuned through the beamline. At a terminal voltage of about 11.5 MV, a charge state 11+ is selected on the high-energy side of the accelerator. The concentration of $^{53}Mn/Mn$ is obtained by measuring the current of ^{55}Mn at a cup in front of the GAMS, the number of counts of ^{53}Mn in the detector, and comparing it with a standard sample. The standard sample used for this work is Grant GLS. The original published concentration of this material, $(2.96 \pm 0.06) \times 10^{-10}$, (Schaefer et al., 2006), was slightly lowered due to advanced cross-calibration measurements: $^{53}Mn/Mn = (2.83 \pm 0.14) \times 10^{-10}$ (Poutivtsev et al., 2010).

Isobaric background

The main challenge for ^{53}Mn measurements is isobaric background of ^{53}Cr. A suppression of Cr background can be achieved in several steps. The chemical preparation of the MnO_2 sample suppresses Cr by several orders of magnitude. During the measurement, additional suppression of Cr is achieved in the GAMS magnet. Since Cr ($Z = 24$) will form a lower average charge state than Mn ($Z = 25$) in the gas-filled magnet, it is forced on an outside track through the magnet chamber and can be spatially separated and thus suppressed by several orders of magnitude. A final discrimination between Cr and Mn events can be made in the detector due to the different energy deposition curves of the isobars.

Another problem is that the Cr background is different for each sample. As suggested by Poutivtsev et al. (2010), in order to compensate for this, a sample with about 1000 μg/g of Cr was measured. Using this sample, a Cr suppression factor of the data analysis software can be calculated, dividing the number of Cr events falsely identified as ^{53}Mn, divided by the total number of Cr events in the detector, resulting in a software suppression of around 10^{-6}, which means that every one million Cr background counts, there is on average one false positive count of ^{53}Mn. Using this information, the expected background in every sample can be calculated by multiplying the software suppression factor with the number of Cr background counts in that sample.

For this work, a small adaptation had to be made to this procedure to estimate the Cr background more reliably. Since Cr is suppressed by the GAMS, some of the Cr background consists of scattered particles and may this appear as several species in the detector. Since the ratio of those species can vary (e.g. due to small fluctuations in beam tuning), and since usually only one species is responsible for most of the background close to the region of interest for ^{53}Mn, the suppression factor was calculated using only events with a χ^2-values between 20 and 100. In this way, no real events are taken (since they have lower χ^2, and other species (other Cr background or background by other elements) with higher χ^2 are dismissed.

The uncertainties included in the results for ^{53}Mn are comprised of the statistical 1-σ intervals from Feldmann and Cousins (1998) with background, combined with the additional 15% statistical uncertainty in Q_{eff} similar to ^{60}Fe.

B.5.3. ^{53}Mn AMS results

Due to limited beamtime, only 6 of the 14 available samples have been measured. The blank level reached during the measurement was 2.15×10^{-14}. This was determined by measuring a

blank sample of MnO_2 from Alfa Aesar (Purity 99.997%, Lot: 23595), in which a concentration of ^{53}Mn/Mn of $1.2^{+1.0}_{-0.7} \times 10^{-14}$ was measured with 4 events of ^{53}Mn. The blank level was then calculated as the 1-σ upper limit on that concentration. The blank level during that beamtime was limited mostly by cross-talk in the ion source. An plot of all determined concentrations is seen in Fig. (B.3).

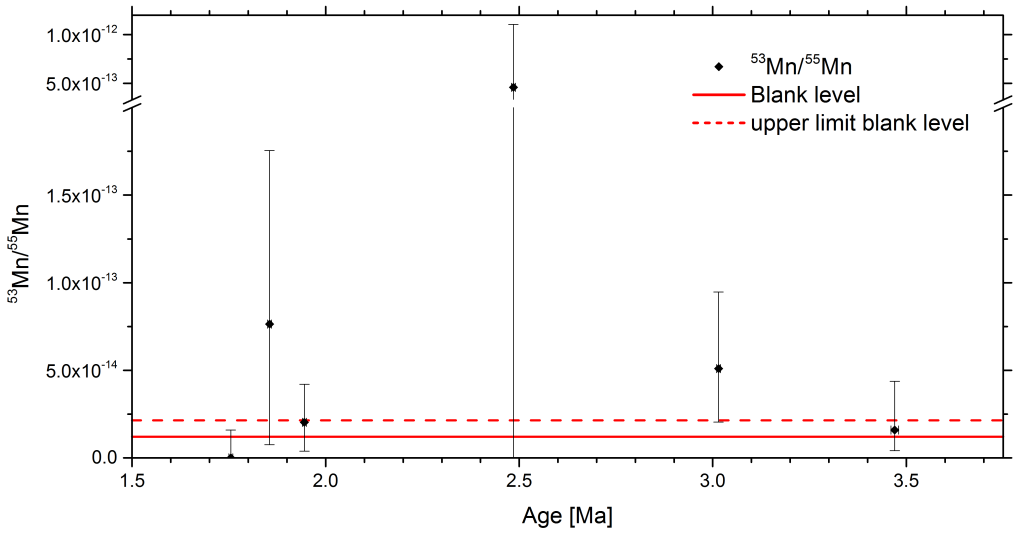

Figure B.3: All data obtained from AMS measurements of ^{53}Mn/^{55}Mn. x-errors show sampling intervals, y-errors correspond to 1-σ statistical uncertainties.

Sample	Age [Ma]	$\frac{^{10}Be}{^{9}Be}_{AMS}$ $[10^{-11}]$	$\frac{^{10}Be}{^{9}Be}_{sed}$ $[10^{-8}]$	$\frac{^{26}Al}{^{27}Al}$ $[10^{-14}]$	$\frac{^{53}Mn}{^{55}Mn}$ $[10^{-14}]$
PL01	1.75-1.76	9.37 ± 0.28	4.73 ± 0.27	$1.59^{+0.58}_{-0.50}$	< 1.8
PL02	1.85-1.86	9.61 ± 0.29	5.00 ± 0.29	$2.67^{+1.06}_{-0.79}$	$7.6^{+10.0}_{-7.0}$
PL03	1.94-1.95	10.5 ± 0.34	5.24 ± 0.30	$1.25^{+0.47}_{-0.36}$	$2.0^{+2.2}_{-1.7}$
PL04	2.06-2.08	8.86 ± 0.27	4.65 ± 0.27	$1.91^{+0.64}_{-0.55}$	
PL05	2.10-2.12	9.09 ± 0.27	4.79 ± 0.28	$1.64^{+0.39}_{-0.39}$	
PL06	2.24-2.25	7.79 ± 0.23	4.36 ± 0.25	$1.45^{+0.58}_{-0.50}$	
PL07	2.35-2.36	5.21 ± 0.16	4.10 ± 0.24	$0.93^{+0.68}_{-0.55}$	
PL08	2.48-2.49	5.03 ± 0.15	3.83 ± 0.22	$1.68^{+0.53}_{-0.42}$	46^{+65}_{-46}
PL09	2.53-2.54	7.86 ± 0.23	4.00 ± 0.23	$1.65^{+0.32}_{-0.32}$	
PL10	2.62-2.63	5.40 ± 0.16	3.77 ± 0.22	$0.74^{+0.57}_{-0.46}$	
PL11	2.71-2.72	4.73 ± 0.15	3.58 ± 0.21	$1.48^{+0.27}_{-0.27}$	
PL12	2.85-2.87	3.82 ± 0.12	2.93 ± 0.17	$0.80^{+0.51}_{-0.43}$	
PL13	3.01-3.02	4.62 ± 0.14	3.03 ± 0.18	$0.76^{+0.28}_{-0.22}$	$5.1^{+4.4}_{-3.2}$
PL14	3.46-3.48	3.08 ± 0.09	1.95 ± 0.11	$0.61^{+0.68}_{-0.57}$	$1.6^{+2.8}_{-1.2}$
Blank	—	$(5.91 \pm 0.90) \times 10^{-4}$	-	$0.28^{+0.20}_{-0.12}$	$1.2^{+1.0}_{-0.7}$

Table B.1.: Summary of all AMS results for ^{10}Be, ^{26}Al, and ^{53}Mn. For ^{26}Al, blank levels were subtracted. Errors correspond to 1-σ statistical uncertainties. $^{10}Be/^{9}Be_{AMS}$ are the concentrations measured in the AMS samples. $^{10}Be/^{9}Be_{sed}$ values represent the original concentrations in the sediment samples, reconstructed using ICP-MS data for stable ^{9}Be.

B.6. Analysis of $^{26}Al/^{10}Be$ ratio

It was observed by Auer et al. (2009) that the atmospheric ratio of $^{26}Al/^{10}Be$ is globally constant within 5% of $^{26}Al/^{10}Be = 1.89 \times 10^{-3}$. They further suggest using this ratio as a chronometer for ice cores. The ratio of $^{26}Al/^{10}Be$ decreases with an effective half-life of (1.49 ± 0.07) Ma.

By using the concentrations of stable ^{27}Al and ^{9}Be obtained with ICP-MS and the AMS results, the number of atoms of the respective radioisotopes, ^{26}Al and ^{10}Be in the sediment samples can be calculated. The ratios of these two radioisotopes and their stable counterparts are depicted in Fig. (B.4).

The average ratio $^{26}Al/^{10}Be = (0.80 \pm 0.08) \times 10^{-3}$ which is less than half of the atmospheric ratio. This is not unusual, since the the input of ^{26}Al into the sediment is a superposition of atmospheric and continental deposition, which is subject to spatial and temporal variations.

Using the average sedimentation rate (19.3 m/Ma) and the dry density of the sediment (0.68 g/cm^3), it is also possible to calculate the average deposition rates for both isotopes.

$$r_{(^{10}Be)} = (1.8 \pm 0.2) \times 10^6 \ \frac{\text{at}}{\text{cm}^2\text{a}} \qquad \text{and} \qquad r_{(^{26}Al)} = (1.7 \pm 0.2) \times 10^3 \ \frac{\text{at}}{\text{cm}^2\text{a}} \tag{B.1}$$

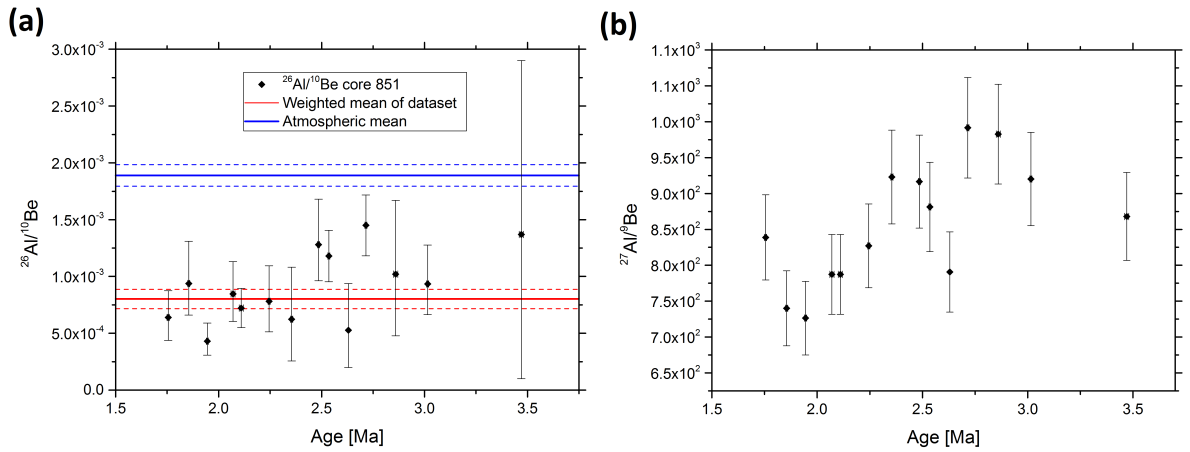

Figure B.4: (a) Decay-corrected ratio of ^{26}Al/^{10}Be in sediment core 851. For comparison, the average atmospheric value from Auer et al. (2009) is also shown (blue line). (b) Ratio of ^{27}Al/^{9}Be calculated as fraction of atoms leached using ICP-MS.

B.7. Extraterrestrial ^{53}Mn and ^{26}Al

The concentrations of ^{53}Mn/Mn shown in Fig. (B.3) only include a subtraction of expected Cr background. Since cross-talk is a likely source of the relatively high blank level, the blank level was subtracted from the individual samples for further analysis. The large errors and low number of samples does not allow for a thorough analysis of the depth profile and the average ^{53}Mn signal is compatible with zero on a 1-σ confidence level. Nonetheless, in combination with ICP-MS measurements, it is possible to calculate an upper limit on the average concentration of ^{53}Mn in the sediment. After decay correction of the isotopic ratios, upper limit on the number of atoms of ^{53}Mn per gram of dry sediment is $< 9.1 \times 10^4$ at/g. Factoring in the average sedimentation rate and dry density of core 851, this results in an upper limit on the average deposition rate $r_{(^{53}\mathrm{Mn})}$ of ^{53}Mn of

$$r_{(^{53}\mathrm{Mn})} < 130 \ \frac{\mathrm{at}}{\mathrm{cm}^2 \ \mathrm{a}} \tag{B.2}$$

which is compatible with (Auer, 2008).

The observed signal of ^{26}Al is a superposition of atmospheric in-situ production and extraterrestrial influx. A possible way to distinguish between these two sources is a comparison with ^{53}Mn. The atomic ratio of $(^{26}\mathrm{Al}/^{53}\mathrm{Mn})_{\mathrm{ext}}$ in extraterrestrial material has been estimated to be 0.26 (Auer et al., 2009). In this work, an average ratio of $(^{26}\mathrm{Al}/^{53}\mathrm{Mn})_{\mathrm{sed}} > 12.7$ was observed in the sediment samples. Assuming further that the atmospheric and surface production of ^{53}Mn is negligible, the fraction of ^{26}Al of extraterrestrial origin f_{ext} can be estimated in the way of

$$f_{\mathrm{ext}} = \frac{(^{26}\mathrm{Al}/^{53}\mathrm{Mn})_{\mathrm{ext}}}{(^{26}\mathrm{Al}/^{53}\mathrm{Mn})_{\mathrm{sed}}} < 2.1\%, \tag{B.3}$$

which is also compatible with the result from aerosol samples by Auer et al. (2009).

C. Appendix: Electronics and data analysis

C.1. Electronics setup and signal processing

The ionization chamber of the GAMS setup features a split anode with five segments. In addition to the energy loss of the last three segments (E3, E4, E5), the first two anodes are split diagonally, thus providing an energy loss signal on each side (E1l, E1r, E2l, E2r). The influenced signal on the Frisch-grid, corresponding to the total energy loss (Et) of the particles is also measured. The individual signals then pass through a pre-amplifier and are then further processed in a NIM crate as displayed schematically in Fig. (C.1).

After shaping and further amplification of each signal in a spectroscopic amplifier (model Canberra 2022), they are forwarded to a VME crate and digitized in an ADC. In addition to the energy signals, signals for measuring the y-angle of particles, a pile-up rejection, and a time-of-flight measurement (not used in this work) are also generated. The pile-up rejection is performed examining the coincident signal of a gate, generated from E1, with E1 itself. If a second signal occurs withing the gate length, a pile-up signal is forwarded to the ADC and the corresponding events can be discarded. The y-angle of the incident particles is not measured directly, but a quantity which carries at least some of this information is the time-difference between the energy signals E1 and E3, called dt. The master trigger for data acquisition is generated from Et.

In addition to the raw signals, the particle positions p1 and p2 are calculated from the difference in the left and right part of E1 and E2, respectively. The difference between p1 and p2 is proportional to the x-angle of the particles (for small angles) and the corresponding signal is named dp. To obtain the total energy loss in anode segments 1 and 2, the respective left and right contributions are summed. In total, this yields 5 energy loss signals E1, E2, E3, E4, and E5, the Frisch-grid signal Et, two x-position signals p1 and p2, and the two angles dp (x-angle) and dt (y-angle).

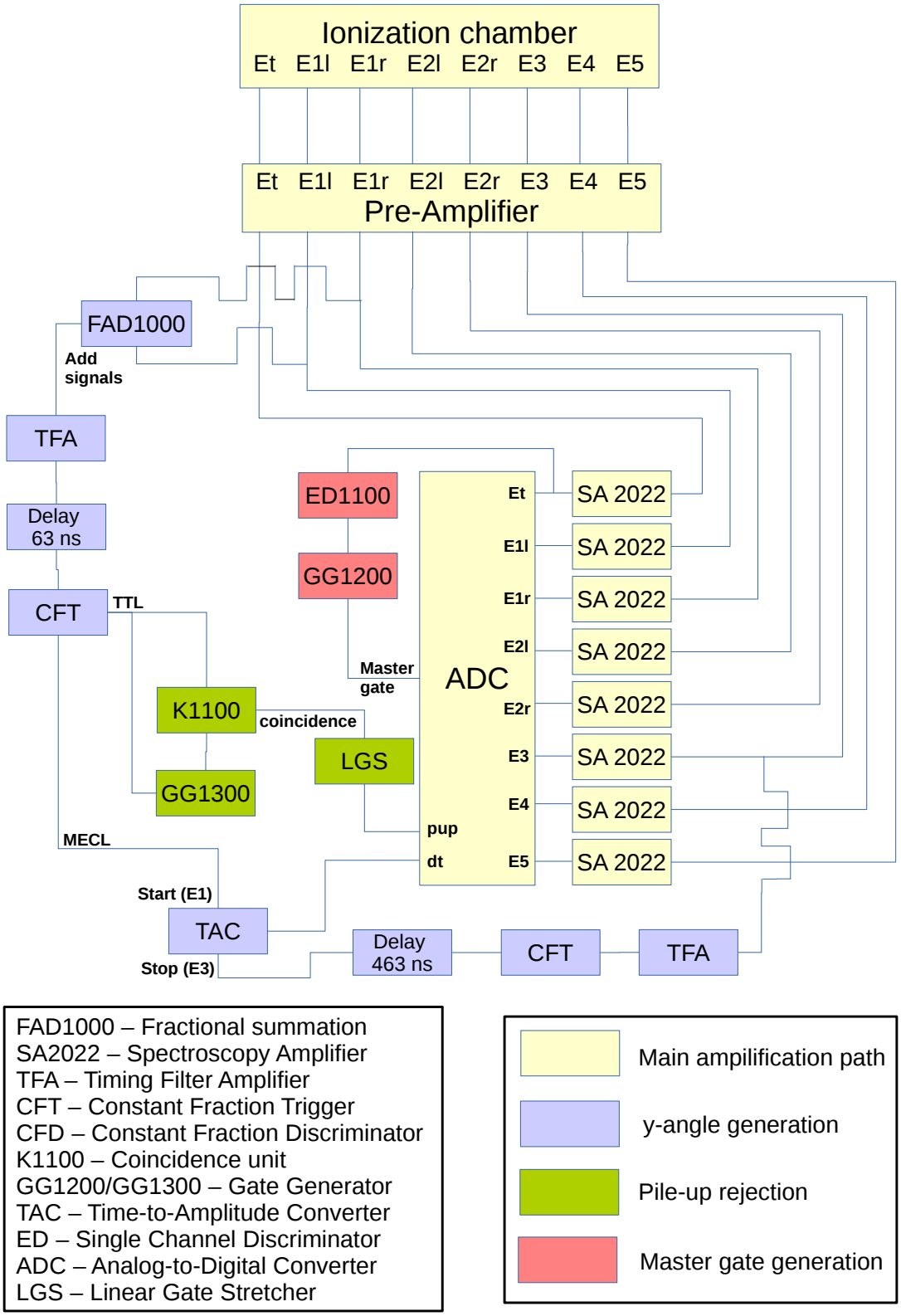

Figure C.1: Analog signal processing setup for particle identification with the GAMS setup.

C.2. Data analysis

The main difficulty for data analysis is the discrimination between actual ^{60}Fe events and background. This is especially important when measuring samples with very low ^{60}Fe/Fe, where only few events are observed and even the smallest background source can influence the final result. The analysis procedure employed in this work is illustrated in the following section using data from a beamtime of June 2014 as a representative example.

As a starting point a visual discrimination between ^{60}Fe events in the standard sample in several two dimensional representations of the signals should be possible, as seen in Fig. (5.4a). The main background suppression is achieved by the GAMS system, which forces the isobar ^{60}Fe on an inner trajectory through the magnet (right = high x-position). This is why Fig. (5.4a,b,c) only show a small fraction of the actual ^{60}Ni, since the majority of the particles are blocked by an aperture. The remaining ^{60}Ni ions arrive on the right side of the detector. The GAMS magnetic field is then adjusted to suppress ^{60}Ni until the countrate in the detector is small (always $<$ 500 Hz, but typically a few Hz). The cost of this procedure is that ^{60}Fe, which arrives further left in the detector, is also partly blocked (typically 10%).

The suppression of the stable isobar ^{60}Ni is mostly achieved by increasing the GAMS magnetic field until most of the ^{60}Ni cannot enter the detector anymore. However,there are a few species (typically 4), which arrive at a similar x-position as ^{60}Fe (Fig. (5.4a)). Besides the tail of ^{60}Ni, there are other species which can interfere, depending on the magnetic rigidity selected for the experiment. In the case of $^{60}Fe^{10+}$, possible interferences (background A and B in Fig. (C.2)) arriving at the detector at roughly the same x-position as ^{60}Fe are $^{72}Ge^{11+}$, $^{55}Mn^{9+}$, $^{62}Ni^{10+}$ and $^{59}Co^{10+}$. This is illustrated in Fig. (C.2), where cuts in both E3 and x-position were made to isolate each of the 4 species on the same dataset as in Fig. (5.4).

Complete suppression of background can be achieved by applying a suitable set of software cuts. This procedure is displayed in Fig. (C.3). Placement of software cuts in all energy signals on ^{60}Fe is possible since the position of ^{60}Fe in all signals is known from the standard sample (Fig. (C.3a)). The same cuts can then be applied to sediment samples (Fig. (C.3b)). The resulting spectra are usually free of background, but in some cases, scattered particles of other species can still be difficult to distinguish from ^{60}Fe.

Additional background suppression is then achieved by including a software cut on the χ^2 distribution calculated using Eq. (5.7). The usual cut on the χ^2 distribution is $\chi^2 < 15$, as shown in Fig. (C.4a). A final discrimination is usually performed by applying a 2-dimensional, roughly elliptical cut on the x-position and one of the energy signals, as shown in Fig. (C.4b). This final cut can be adapted to counter a specific background situation, e.g. background coming from top right, which can be different in each beamtime, and also from sample to sample. In most cases, the 2-dimensional cut was not even necessary. Candidate events are only accepted as ^{60}Fe if their χ^2 value is < 15 and if they are inside all other cuts. The remaining events for the representative sediment sample are shown in Fig. (C.4c). Knowing the currents and measuring times for standard and sediment samples, the concentration of ^{60}Fe/Fe can now be calculated.

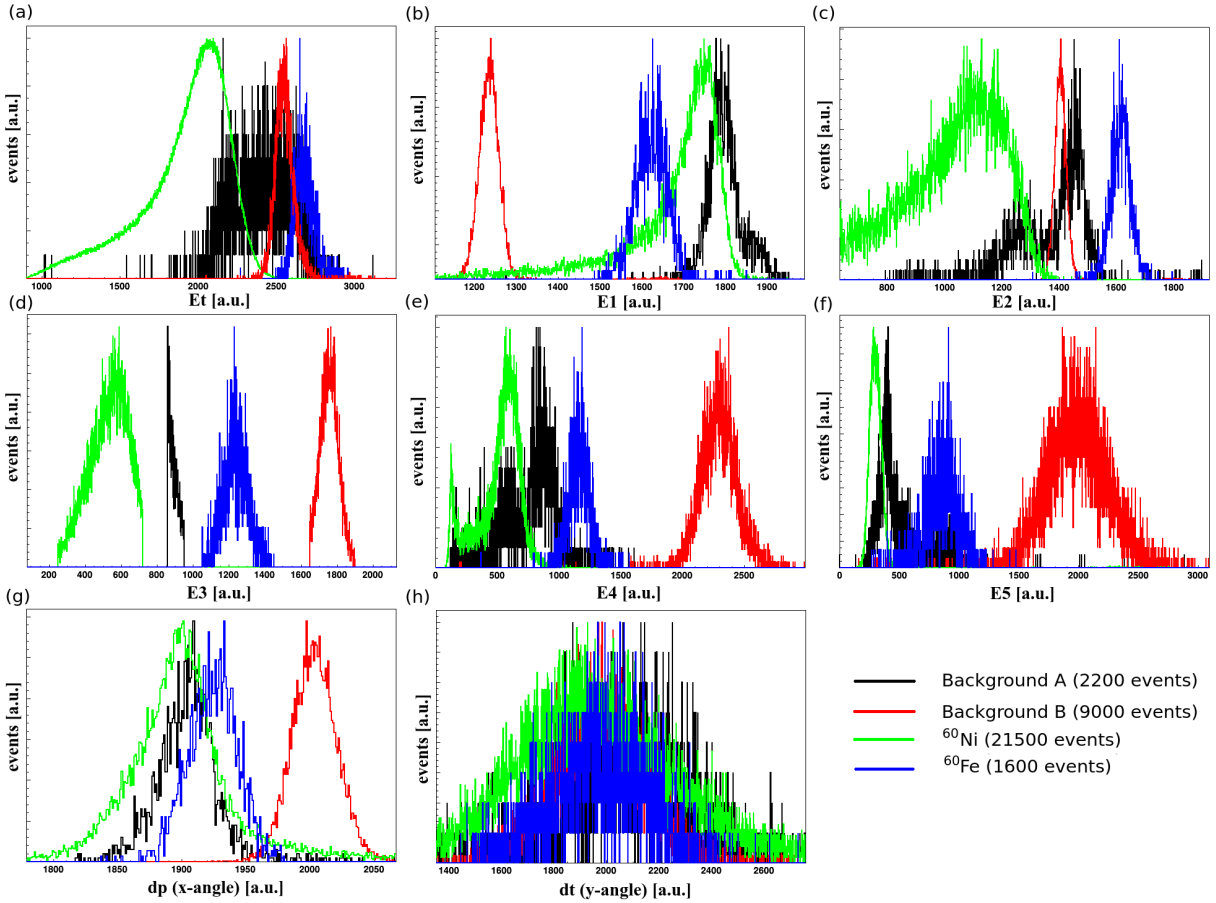

Figure C.2: Comparison of all individual signals for the four main species to be discriminated. The individual species were isolated by applying rectangular, 2-dimensional cuts on Fig. (5.4a). This can be seen in (d), where the different E3-cuts are visible.

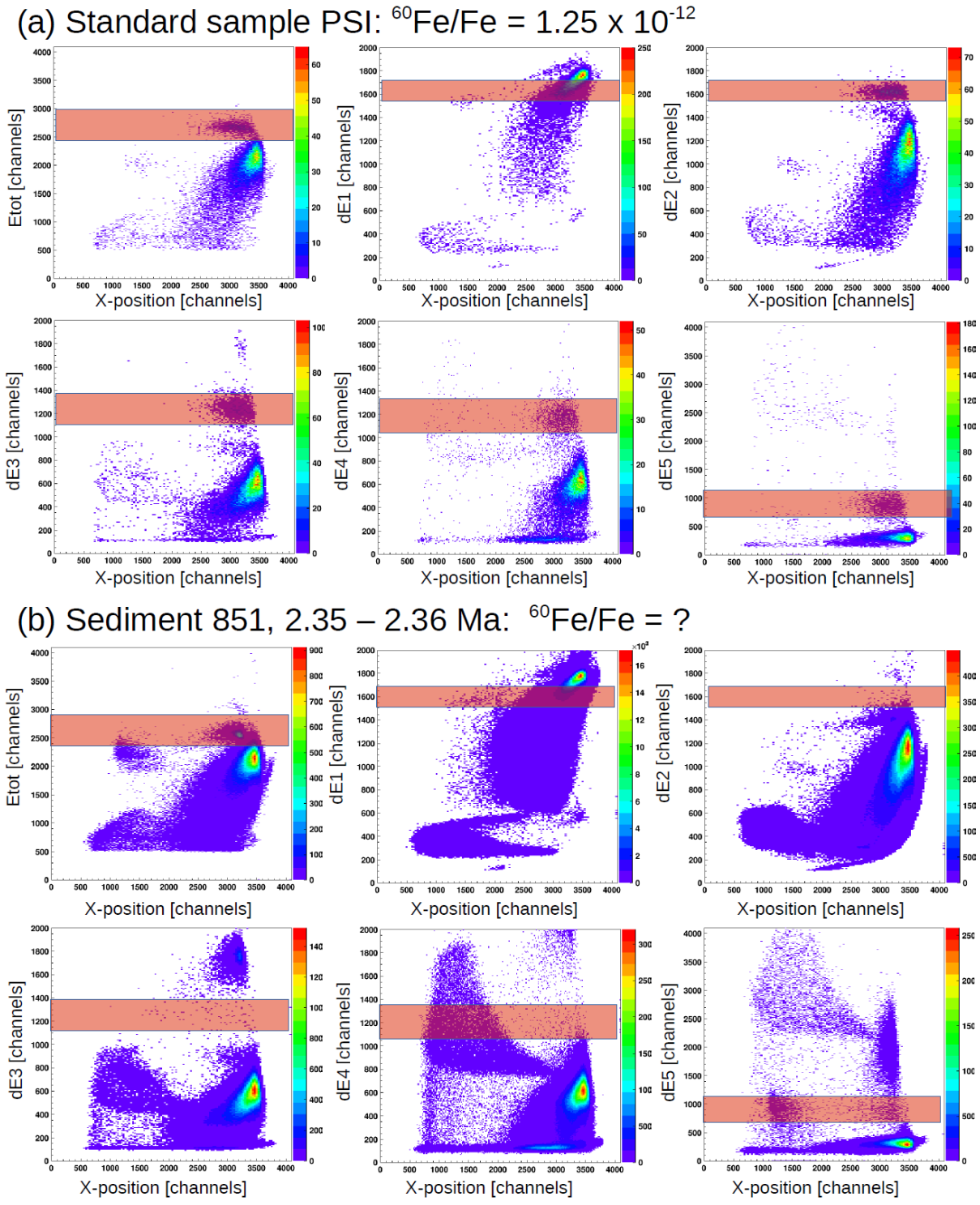

Figure C.3: All energy signals for a representative set of data obtained from a standard sample (a), and a sediment sample (b). 1-dimensional cuts can be applied to the known positions of ^{60}Fe (shaded red areas).

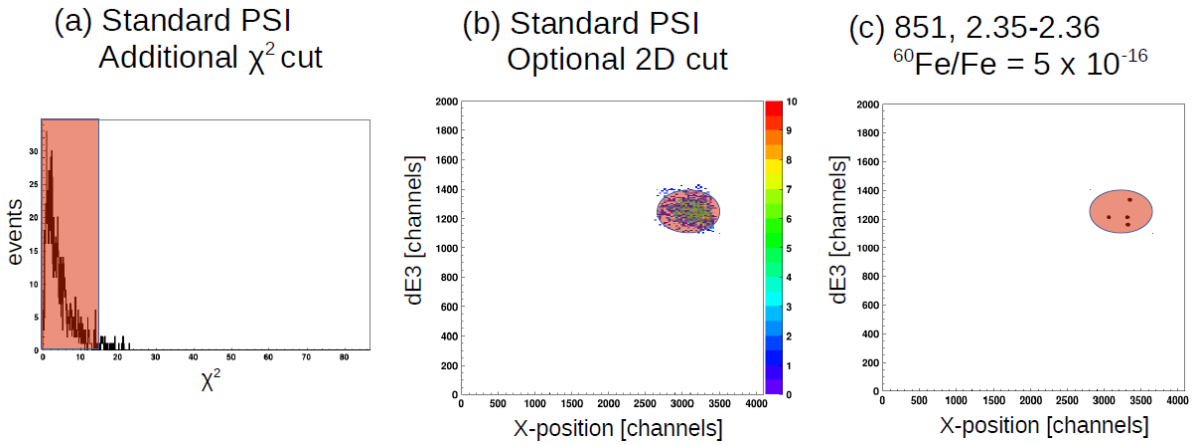

Figure C.4: (a) χ^2 distribution of all events from Fig. (C.3a) after applying the indicated software cuts. An additional cut ($\chi^2 < 15$) is placed (shaded red box). (b) Same events as in (a), displayed as dE3 over x-position. An optional 2-dimensional cut is applied (red shaded ellipse). (c) Sediment data from Fig. (C.3b) after all cuts are applied, including those of (a) and (b).

Index

The following abbreviations are employed in this work:

- **AGB**– Asymptotic Giant Branch
- **AMS**– Accelerator Mass Spectrometry
- **ARM**– Anhysteretic Remanent Magnetization
- **CBD**– Citrate-Bicarbonate-Dithionite
- **CCSN**– Core-Collapse supernova
- **DREAMS**– DREsden AMS
- **EDX**– Energy Dispersive X-ray Spectroscopy
- **GAMS**– Gas-filled Analyzing Magnet System
- **GCR**– Galactic Cosmic Rays
- **HZDR**– Helmholtz-Zentrum Dresden-Rossendorf
- **ICP-MS**– Inductively Coupled Plasma Mass Spectrometry
- **IDP**– Interplanetary Dust Particles
- **ISD**– Interstellar Dust
- **ISM**– Interstellar Medium
- **IRM**– Isothermal Remanent Magnetization
- **mcd**– Meters Core Depth
- **MD**– Multi-Domain
- **MLL**– Maier-Leibnitz-Laboratorium
- **MM**– Micro-Meteorite
- **NSE**– Nuclear Statistical Equilibrium
- **OATZ**– Oxic-Anoxic Transition Zone
- **ODP**– Ocean Drilling Program
- **PNS**– Proto Neutron Star
- **PSD**– Pseudo Single-Domain
- **r-process**– Rapid neutron capture process
- **s-process**– Slow neutron capture process
- **SCR**– Solar Cosmic Rays
- **SD**– Single-Domain
- **SEM**– Scanning Electron Microscopy
- **SF**– Smoothing Factor
- **SN**– Supernova
- **SNR**– Supernova Remnant
- **SP**– Super-Paramagnetic

- **TEM**– Transmission Electron Microscopy
- **TNSN**– Thermonuclear Supernova
- **UNISD**– Uniaxial Single Domain
- **WD**– White Dwarf

List of Figures

List of Tables

Bibliography

Abrajevitch, A., Kodama, K., 2009. Biochemical vs. detrital mechanism of remanence acquisition in marine carbonates: A lesson from the K-T boundary interval. Earth Planet. Sc. Lett. 286, 269–277.

Abrajevitch, A., Kodama, K., 2011. Diagenetic sensitivity of paleoenvironmental proxies: A rock magnetic study of Australian continental margin sediments. Geochem. Geophy. Geosy. 12, Q05Z24.

Adams, S., Kochanek, C., Beacorn, J., Vagins, M., Stanek, K., 2013. Observing the next galactic supernova. Astrophys. J. 778, 164.

Akhmadaliev, S., Heller, R., Hanf, D., Rugel, G., Merchel, S., 2013. The new 6 MV AMS-facility DREAMS at Dresden . Nucl. Instrum. Methods Phys. Res., Sect. B 294, 5–10.

Ammon, K., Masarik, J., Leya, I., 2009. New model calculations for the production rates of cosmogenic nuclides in iron meteorites. Meteorit. Planet. Sci. 44, 485–503.

Argast, D., Samland, M., Thielemann, F.K., Qian, Y.Z., 2004. Neutron star mergers versus core-collapse supernovae as dominant r-process sites in the early Galaxy. Astron. Astrophys. 416, 997–1011.

Arnett, D., 1996. Supernovae and Nucleosynthesis. Princeton University Press.

Asplund, M., Grevesse, N., Sauval, A., Scott, P., 2009. The chemical composition of the Sun. Annu. Rev. Astro. Astrophys. 470, 481–522.

Athanassiadou, T., Fields, B., 2011. Penetration of nearby supernova dust in the inner solar system. New. Astron. 16, 229–241.

Auer, M., 2008. Applications of ^{26}Al in Atmospheric Research. Ph.D. thesis. University of Vienna.

Auer, M., Wagenbach, D., Wild, E., Wallner, A., Priller, A., Miller, H., Schlosser, C., Kutschera, W., 2009. Cosmogenic ^{26}Al in the atmosphere and the prospect of a ^{26}Al/^{10}Be chronometer to date old ice. Earth Planet. Sci. Lett. 287, 453–462.

Barron, J., 1985a. Late Eocene to Holocene diatom biostratigraphy of the equatorial Pacific Ocean, Deep Sea Drilling Project Leg 85, pp. 413–456.

Barron, J., 1985b. Miocene to Holocene planktic diatoms, in: Bolli, H., Saunders, J., Perch-Nielsen, K. (Eds.), Plankton Stratigraphy, Cambridge Univ. Press. pp. 763–809.

Basu, S., Stuart, F., Schnabel, C., Klemm, V., 2007. Galactic-cosmic-ray-produced ^{3}He in a ferromanganese crust: any supernova ^{60}Fe excess on Earth? Phys. Rev. Lett. 98, 141103–141107.

Bellini, S., 2009a. Further studies on 'magnetosensitive bacteria'. Chin. J. Oceanol. Limn. 27, 6–12.

Bellini, S., 2009b. On a unique behaviour of freshwater bacteria. Chin. J. Oceanol. Limn. 27, 3–5.

Benítez, N., Maíz-Apellániz, J., Canelles, M., 2002. Evidence for Nearby Supernova Explosions. Phys. Rev. Lett. 88, 081101.

Bennett, C., Beukens, R., Clover, M., Gove, H., Liebert, R., Litherland, A., Purser, K., 1977. Radiocarbon dating using electrostatic accelerators: negative ions provide the key. Science 198, 508.

Berggren, W., Kent, D., Van Couvering, J., 1985. The Neogene: Part 2. Neogene geochronilogy and chronostratigraphy. Geol. Soc. London Mem. 211-260.

Berghöfer, T., Breitschwedt, D., 2002. The origin of the young stellar population in the solar neighborhood – A link to the formation of the Local Bubble? Astron. Astrophys. 390, 299–306.

Bishop, S., Egli, R., 2011. Discovery prospects for a supernova signature of biogenic origin. Icarus 212, 960–962.

Blakermore, R., 1975. Magnetotactic bacteria. Science 190, 377–379.

Blakermore, R., 1982. Magnetotactic bacteria. Annu. Rev. Microbiol. 36, 217–238.

Blanchard, M., Brownlee, D., Bunch, T., Hodge, P., Kyte, F., 1980. Meteoroid ablation spheres from deep-sea sediments. Earth Planet. Sci. Lett. 46, 178–190.

Blow, W., 1967. Late middle Eocene to recent planktonic foraminiferal biostratigraphy. Proc. First Int. Conf. Planktonic Microfossils, Geneva 1, 199–422.

Bouchet, L., Jourdain, E., Roques, J.P., 2015. The galactic ^{26}Al emission map as revealed by INTEGRAL SPI. Astrophys. J. 801, 142.

Bourlès, D., Raisbeck, G., Yiou, F., 1999. ^{10}Be and ^{9}Be in marine sediments and their potential for dating. Geochim. Cosmochim. Ac. 53, 443–452.

Breitschwerdt, D., de Avillez, M., Feige, J., Dettbarn, C., 2012. Interstellar Medium Simulations. Astron. Nachr. 333, 486–496.

Breitschwerdt, D., de Avillez, M., Fuchs, B., Dettbarn, C., 2009. What Physical Processes Drive the Interstellar Medium in the Local Bubble? Space Sci. Rev. 143, 263–276.

Briani, G., Pace, E., Shore, S., Pupillo, G., Passaro, A., Aiello, S., 2013. Simulations of micrometeoroid interactions with the Earth atmosphere. Astron. Astrophys. 552, A53.

Brun, R., Rademakers, F., 1997. ROOT - An Object Oriented Data Analysis Framework. Nucl. Instrum. Meth. A 389, 81–86.

Burbridge, E., Burbridge, G., Fowler, W., Hoyle, F., 1957. Synthesis of Elements in Stars. Rev. Mod. Phys. 29, 547–654.

Burrows, A., 2013. Perspectives on core-collapse supernova theory. Rev. Mod. Phys. 85, 245–261.

Canfield, D., Berner, R., 1987. Dissolution and hydritization of magnetite in anoxic sediments. Geochim. Cosmochim. Ac. 511, 645–659.

Canfield, D., Raiswell, R., Bottrell, S., 1992. The reactivity of sedimentary iron minerals toward sulphide. Am. J. Sci. 292, 659–683.

Cappellaro, E., Riello, M., Altavilla, G., Botticella, M., Benetti, S., Clocchiatti, A., Danziger, J., Mazzali, P., Pastollero, A., Patat, F., Salvo, M., Turatto, M., Valenti, S., 2005. Death rate of massive stars at redshift $\sim$0.3. Astron. Astrophys. 430, 83–93.

Carvallo, C., Dunlop, D., Özdemir, Ö., 2005. Experimental comparison of FORC and remanent Preisach diagrams. Geophys. J. Int. 162, 747–754.

Carvallo, C., Muxworthy, A., Dunlop, D., Williams, W., 2003. Micromagnetic modeling of first-order reversal curve (FORC) diagrams for single-domain and pseudo-single-domain magnetite. Earth Planet. Sci. Lett. 213, 375–390.

Chen, A., Egli, R., Moskowitz, B., 2007. First-order reversal curve (FORC) diagrams of natural and cultured biogenic magnetic particles. J. Geophys. Res. 112, B08S90.

Cherchneff, I., 2014. Dust production in supernovae. PoS LCDU2013, 018.

Chester, R., Jickells, T., 2012. Marine Geochemistry - 3rd edition. Wiley-Blackwell.

Chieffi, A., Limongi, M., 2013. Pre-supernova evolution of rotating solar metallicity stars in the mass range 10-120 $M_{\odot}$ and their explosive yields. Astrophys. J. 764, 21.

Chmeleff, J., Blanckenburg, F.V., Kossert, K., Jakob, D., 2010. Determination of the ^{10}Be half-life by multicollector ICP-MS and liquid scintillation counting. Nucl. Instrum. Methods Phys. Res., Sect. B 268, 192–199.

Church, N., Feinberg, J., Harrison, R., 2011. Low-temperature domain wall pinning in titano-magnetite: Quantitative modeling of multidomain first-order reversal curve diagrams and AC susceptibility. Geochem. Geophy. Geosy. 12, Q07Z27.

Coey, J., 2012. Magnetism and magnetic materials - 3rd print. Cambridge Univ. Press.

Cornell, R., Schwertmann, U., 2003. The Iron Oxides, 2nd Edition. Wiley-Vch.

Cox, A., Doell, R., Dalrymple, G., 1963. Geomagnetic polarity epochs and Pleistocene geochronometry. Nature 198, 1049–1051.

Day, R., Fuller, M., Schmidt, V., 1977. Hysteresis properties of titanomagnetites: Grain-size and compositional dependence. Phys. Earth Planet. In. 13, 260–267.

Diehl, R., Halloin, H., Kretschmer, K., Lichti, G., Schoenfelder, V., Strong, A., von Kienlin, A., Wang, W., Jean, P., Knoedlseder, J., Roques, J.P., Weidenspointner, G., Schanne, S., Hartmann, D., Winkler, C., Wunderer, C., 2006a. Radioactive 26Al and massive stars in the Galaxy. Nature 439, 45–47.

Diehl, R., Halloin, H., Kretschmer, K., Strong, A., Wang, W., Jean, P., Lighti, G., Knödlseder, J., Roques, J.P., Schanne, S., Schönfelder, V., von Kienlin, A., Weidenspointner, G., Winkler, C., Wunderer, C., 2006b. ^{26}Al in the inner Galaxy. Astron. Astrophys. 449, 1025–1031.

Dobeneck, T.V., Petersen, N., Vali, H., 1987. Bakterielle Magnetofossilien. Geowiss. in unserer Zeit 5, 27–35.

Dunlop, D., 2002a. Theory and application of the Day plot ($M_{\rm rs}/M_{\rm s}$ versus $H_{\rm cr}/H_{\rm c}$) 1. Theoretical curves and tests using titanomagnetite data. J. Geophys. Res. 107, 2056.

Dunlop, D., 2002b. Theory and application of the Day plot ($M_{\rm rs}/M_{\rm s}$ versus $H_{\rm cr}/H_{\rm c}$) 2. Applications to data for rocks, sediments, and soils. J. Geophys. Res. 107, 2057.

Egli, R., 2003. Analysis of the field dependence of remanent magnetization curves. J. Geophys. Res. 108, 2081.

Egli, R., 2004a. Characterization of individual rock magnetic components by analysis of remanence curves, 1. Unmixing natural sediments. Studia Geophys. Geod. 48, 391–446.

Egli, R., 2004b. Characterization of individual rock magnetic components by analysis of remanence curves, 3. Bacterial Magnetite and natural processes in lakes. Phys. Chem. Earth 29, 869–884.

Egli, R., 2006. Theoretical considerations on the anhysteretic remanent magnetization of interacting particles with uniaxial anisotropy. J. Geophys. Res. 111, B12S18.

Egli, R., 2013. VARIFORC: an optimized protocol for the calculation of non-regular first-order reversal curves (FORC) diagrams. Global Planet. Change 110, 302–320.

Egli, R., Chen, A., Winkelhofer, M., Kodama, K., Horng, C., 2010. Detection of noninteracting single domain particles using first-order reveral curve diagrams. Geochem. Geophy. Geosyst. 11, Q01Z11.

Egli, R., Lowrie, W., 2002. Anhysteretic remanent magnetization of fine magnetic particles. J. Geophys. Res. 107, 1–21.

Ellis, J., Fields, B., Schramm, D., 1996. Geological isotope anomalies as signatures of nearby supernovae. Astrophys J 470, 1227–1236.

Ellis, J., Schramm, D., 1995. Could a nearby supernova explosion have caused a mass extinction? Proc. Natl. Acad. Sci., USA. 92, 235–238.

Fabian, K., 2006. Approach to saturation analysis of hysteresis measurements in rock magnetism and evidence for stress dominated magnetic anisotropy in young mid-ocean ridge basalt. Phys. Earth Planet. In. 154, 299–307.

Fabian, K., Dobeneck, T., 1997. Isothermal magnetization of samples with stable Preisach function: A survey of hysteresis, remanence, and rock magnetic parameters. J. Geophys. Res. 102, 17659–17667.

Fairve, D., Agrinier, P., Menguy, N., Ziddas, P., Pachana, K., Gloter, A., Laval, J., Guyot, F., 2004. Mineralogical and isotopic properties of inorganic nanocrystalline magnetites. Geochim. Cosmochim. Ac. 68, 4395–4403.

Faivre, D., Schüler, D., 2008. Magnetotactic bacteria and magnetosomes. Chem. Rev. 108, 4875–4898.

Famulok, N., Faestermann, T., Fimiani, L., Gómez-Guzmán, J., Hain, K., Korschinek, G., Ludwig, P., Schönert, S., 2015. Ultrasensitive detection method for primordial nuclides in copper with Accelerator Mass Spectrometry. Nucl. Instrum. Methods Phys. Res., Sect. B in press, doi:10.1016/j.nimb.2015.03.042.

Feige, J., 2014. Supernova-Produced Radionuclides in Deep-Sea Sediments Measured with AMS. Ph.D. thesis. University of Vienna.

Feige, J., Wallner, A., Fitfield, L., Korschinek, G., Merchel, S., Rugel, G., Steier, P., Winkler, S., Golser, R., 2013. AMS measurements of cosmogenic and supernova-ejected radionuclides in deep-sea sediment cores. arXiv e-Prints 1311.3481 [astro-ph.EP].

Feldmann, G., Cousins, R., 1998. A Unified Approach to the Classical Statistical Analysis of Small Signals. Phys. Rev. D 57, 3873–3889.

Fields, B., Athanassiadou, T., Johnson, S., 2008. Supernova collisions with the heliosphere. Astrophys. J. 678, 549–562.

Fimiani, L., 2014. Interstellar radionuclides in Lunar samples. Ph.D. thesis. Technische Universität München.

Fimiani, L., Cook, D., Faestermann, T., Gomez-Guzman, J., Hain, K., Herzog, G., Knie, K., Korschinek, G., Ligon, B., Ludwig, P., Park, J., Reedy, R., Rugel, G., 2014. Evidence for deposition of interstellar material on the lunar surface. 45th Lunar and Planetary Science Conference .

Firestone, R., 1996. Table of Isotopes, 8th Edition. John Wiley and Sons Inc.

Fitoussi, C., Raisbeck, G., 2007. Chemical procedure for extracting ^{129}I, ^{60}Fe and ^{26}Al from marine sediments: Prospects for detection of a ∼2.8 My old supernova. Nucl. Instrum. Methods Phys. Res., Sect. B 259, 351–358.

Fitoussi, C., Raisbeck, G., Knie, K., Korschinek, G., Faestermann, T., Goriely, S., Lunney, D., Poutivtsev, M., Rugel, G., Waelbroeck, C., Wallner, A., 2008. Search for Supernova-Produced ^{60}Fe in a Marine Sediment. Phys. Rev. Lett. 101, 121101.

Fortin, D., Langley, S., 2005. Formation and occurrence of biogenic iron-rich minerals. Earth-Sci. Rev. 72, 1–19.

Franke, C., Dobeneck, T.V., Drury, M., Meeldijk, J., 2007. Magnetic petrology of equatorial Atlantic sediments: Electron microscopy results and their implications for environmental magnetic interpretation. Paleoceanography 22, PA4207.

Frankel, R., Blakemore, R., Wolfe, R., 1979. Magnetite in freshwater magnetotactic bacteria. Science 203, 1355–1356.

Freiburghaus, C., Rosswog, S., Thielemann, F.K., 1999. r-Process in Neutron Star Mergers. Astrophys. J. 525, L121–L124.

Fry, B., Fields, B., 2014. Discriminating Among Extra-solar Sources of Live Radioactive Isotopes. arXiv [astro-ph.SR] 1405.4310v.

Fu, Y., Von Dobeneck, T., Franke, C., Heslop, D., Kasten, S., 2008. Rock magnetic identification and geochemical process models of greigite formation in Quaternary marine sediments from the Gulf of Mexico, (IODP Hole U1319A). Earth Planet. Sci. Lett. 275, 233–245.

Fuchs, B., Breitschwerdt, D., de Avillez, M., Dettbarn, C., Flynn, C., 2006. The search for the origin of the Local Bubble redivivus. Mon. Not. R. Astron. Soc. 373, 993–1003.

Galindo-González, C., de Vicente, J., Ramos-Tejada, M., López-López, M., González-Caballero, F., Durán, J., 2005. Preparation and sedimentation behaviour in magnetic fields of magnetite-covered clay particles. Langmuir 21, 4410–4419.

Gall, C., Hjorth, J., Watson, D., Dwek, E., Maund, J., Fox, O., Leloudas, G., Malesani, D., Day-Jones, A., 2014. Rapid formation of large dust grains in the luminous supernova SN 2010jl. Nature 511, 326–329.

Gehrels, N., Laird, C., Jackman, C., Cannizzo, J., Mattson, B., Chen, W., 2003. Ozone depletion from nerby supernovae. Astrophys. J. 585, 1169–1176.

Gehring, A., Kind, J., Charialou, M., García-Rubio, I., 2011. The detection of magnetotactic bacteria and magnetofossils by means of magnetic anisotropy. Earth Planet. Sc. Lett. 309, 113–117.

Gomez, H., 2013. Dust in supernova remnants. Proc. of the life cycle of dust in the universe (LCDU2013) .

Gomez, H., 2014. Astrophysics: Survival of the largest. Nature 511, 296–297.

Hanzlik, M., Winkelhofer, M., Petersen, N., 2002. Pulsed-field-remanence measurements on individual magnetotactic bacteria. J. Magn. Magnet. Mater. 248, 259–267.

Harrison, R., Feinberg, J., 2008. FORCinel: An improved algorithm for calculating first-order reversal curve distributions using locally weighted regression smoothing. Geochem. Geophy. Geosy. 9, Q05016.

Herwig, F., 2005. Evolution of asymptotic giant branch stars. Annu. Rev. Astron. Astrophys. 43, 435–479.

Heslop, D., Dillon, M., 2007. Unmixing magnetic remanence curves without a priori knowledge. Geophys. J. Int. 170, 556–566.

Heslop, D., Roberts, A., Chang, L., 2014. Characterizing magnetofossils from first-order reversal curve (FORC) central ridge signatures. Geochem. Geophy. Geosy. 15, 2170–2179.

Heywood, B., Bazylinski, D., Garrett-Reed, A., Mann, S., Frankel, R., 1990. Controlled biosynthesis of greigite (Fe_3S_4) in magnetotactic bacteria. Naturwissenschaften 776, 536–538.

Hillebrandt, W., Niemeyer, J., 2000. Type Ia Supernova Explosion Models. Ann. Rev. Astron. Astrophys. 38, 191–230.

Honda, M., Imamura, M., 1971. Half-life of ^{53}Mn. Phys. Rev. C 4, 1182–1188.

Hoyle, F., Wickramasinghe, N., 1970. Dust in supernova explosions. Nature 226, 62.

Hunt, C., Singer, M., Kletetschka, G., TenPas, J., Verosub, K., 1995. Effect of citrate-bicarbonate-dithionite treatment on fine-grained magnetite and maghemite. Earth Planet. Sc. Lett. 130, 87–94.

Huss, G., Beyer, B., Srinivasan, G., Goswami, J., Sahijpal, S., 2009. Stellar sources of the short-lived radionuclides in the early solar system. Geochim. Cosmochim. Ac. 73, 4922–4945.

Iben, I., Renzini, A., 1983. Asymptotic giant branch evolution and beyond. Annu. Rev. Astron. Astrophys. 21, 271–342.

Illiadis, C., 2007. Nuclear Physics of Stars. Wiley-VCH Verlag GmbH & Co . KGaG, Weinheim.

Itambi, A., Dobeneck, T., Dekkers, M., Frederichs, T., 2010. Magnetic mineral inventory of equatorial Atlantic Ocean marine sediments off Senegal – glacial and interglacial contrast. Geophys. J. Int. 183, 163–177.

Jackson, M., Carter-Stiglitz, B., Egli, R., Solheid, P., 2006. Characterizing the superparamagnetic grain size distribution f(V,Hk) by thermal fluctuation tomography. J. Geophys. Res. 111, B12S07.

Jacobs, I., Bean, C., 1955. An approach to elongated fine-particle magnets. Phys. Rev. 100, 1060–1067.

Janka, H.T., 2012. Explosion Mechanisms of Core-Collapse Supernovae. Annu. Rev. Nucl. Part. Sci. 62, 407–451.

Jickells, T., An, Z., Andersen, K., Baker, A., Bergametti, G., Brooks, N., Cao, J., Boyd, P., Duce, R., Hunter, K., Kawahata, K., Kubilay, N., laRoche, J., Liss, P., Mahowald, N., Prospero, J., Ridgwell, A., Tegen, I., Torres, R., 2005. Global iron connections between desert dust, ocean biogeochemistry, and climate. Science 308, 67–71.

Johnson, D., Schneider, D., Nigrini, C., Caulet, J., Kent, D., 1989. Pliocene-Pleistocene radiolarian events and magnetostratigraphic calibrations for the tropical Indian Ocean. Mar. Micropaleontol. 142, 33–66.

Kachelriess, M., Neronov, A., Semikoz, D., 2015. Signatures of a two million year old supernova in the spectra of cosmic ray protons, antiprotons and positrons. arXiv e-Prints arXiv:1504.06472, astro–ph.HE.

Karakas, A., 2010. Updated stellar yields from asymptotic giant branch stars. Mon. Not. R. Astron. Soc. 403, 1413–1425.

Karakas, A., Lattanzio, J., 2007. Stellar models and yields of asymptotic giant branch stars. Publ. Astron. Soc. Aust. 245, 103–117.

Kind, J., Gehring, A., Winkelhofer, M., Hirt, A., 2011. Combined use of magnetometry and spectroscopy for identifying magnetofossils in sediments. Geochem. Geophy. Geosy. 12, Q08008.

Knie, K., 1997. Beschleunigermassenspektrometrie mit Isobarenseparation in einem dedizierten gasgefüllten Magneten .

Knie, K., Faestermann, T., Korschinek, G., 1997. AMS at the Munich gas-filled analyzing magnet system GAMS. Nucl. Instrum. Methods Phys. Res., Sect. B 123, 128–131.

Knie, K., Faestermann, T., Korschinek, G., Rugel, G., Rühm, W., Wallner, C., 2000. High-sensitivity AMS for heavy nuclides at the Munich Tandem Accelerator. Nucl. Instrum. Methods Phys. Res., Sect. B 172, 717–720.

Knie, K., Korschinek, G., Faestermann, T., Dorfi, E., Rugel, G., Wallner, A., 2004. ^{60}Fe Anomaly in a Deep-Sea Manganese Crust and Implications for a Nearby Supernova Source. Phys. Rev. Lett. 93, 171103.

Knie, K., Korschinek, G., Faestermann, T., Wallner, C., Scholten, J., Hillebrandt, W., 1999. Indication for supernova produced ^{60}Fe activity on Earth. Phys. Rev. Lett. 83, 18–21.

Kobayashi, A., Kirschvink, J., Nash, C., Kopp, R., Sauer, D., Bertani, L., Voorhout, W., Taguchi, T., 2006. Experimental observation of magnetosome chain collapse in magnetotactic bacteria: Sedimentological, paleomagnetic, and evolutionary implications. Earth Planet. Sc. Lett. 245, 538–550.

Konhauser, K., 2007. Introduction to Geomicrobiology. Blackwell Publishing.

Kopp, R., Kirschvink, J., 2008. The identification and biochemical interpretation of fossil magnetotactic bacteria. Earth-Sci. Rev. 86, 42–61.

Korschinek, G., Bergmaier, A., Faestermann, T., Gerstmann, U., Knie, K., Rugel, G., Wallner, A., Dillmann, I., Dollinger, G., von Gotomski, C.L., Kossert, K., Maiti, M., Poutivtsev, M., Remmert, A., 2010. A new value for the half-life of ^{10}Be by Heavy-Ion Elestic Recoil Detection and liquid scintillation counting. Nucl. Instrum. Methods Phys. Res., Sect. B 268, 187–191.

Korschinek, G., Faestermann, T., Knie, K., Schmidt, C., 1996. Abstracts of the 7th International Conference on Accelerator Mass Spectrometry, Tucson, Arizona, 20-24 May 1996 - ^{60}Fe, a promising AMS isotope for many applications. Radiocarbon 38, 68–69.

Kortenkamp, S., Dermott, S., 1998. Accretion of interplanetary dust particles by the Earth. Icarus 135, 469–495.

Kruiver, P., Dekkers, M., Heslop, D., 2001. Quantification of magnetic coercivity components by the analysis of acquisition curves of isothermal remanent magnetization. Earth Planet. Sc. Lett. 189, 269–276.

Lachner, J., Dillmann, I., Faestermann, T., Korschinek, G., Poutivtsev, M., Rugel, G., Lierse von Gostomski, C., Türler, A., Gerstmann, U., 2012. Attempt to detect primordial ^{244}Pu on Earth. Phys. Rev. C 85, 015801.

Landgraf, M., Baggaley, W., Grün, E., Krüger, H., Linkert, G., 1999. Aspects of the mass distribution of interstellar dust grains in the solar system from in-situ measurements. arXiv e-Prints astro-ph/9908117v1.

Lattimer, J., 2012. The Nuclear Equation of State and Neutron Star Masses. Annu. Rev. Nucl. Part. Sci. 62, 485–515.

Lefevre, C., Frankel, R., Bazylinski, D., 2011. Magnetotaxis in Prokaryotes. In: eLS. John Wiley & Sons Ltd, Chichester. http://www.els.net [doi: 10.1002/9780470015902.a0000397.pub2] .

Leslie, B., Hammond, D., Berelson, W., Lund, S., 1990. Diagenesis in anoxic sediments from the California continental borderland and its influence on iron, sulphur, and magnetite behavior. J. Geophys. Res. 95, 4453–4470.

Limongi, M., Chieffi, A., 2006a. Nucleosynthesis of 60Fe in massive stars. New Astron. Rev. 50, 474–476.

Limongi, M., Chieffi, A., 2006b. The Nucleosynthesis of 26Al and 60Fe in Solar Metallicity Stars Extending in Mass from 11 to 120 $M_{\odot}$: The Hydrostatic and Explosive Contributions. Astr. J. 647, 483–500.

Lovley, D., Stolz, J., Jr., G.N., Phillips, E., 1987. Anaerobic production of magnetite by a dissimilatory iron-reducing microorganism. Nature 330, 252–254.

Ludwig, P., Egli, R., Bishop, S., Chernenko, V., Frederichs, T., Rugel, G., Merchel, S., 2013. Characterization of primary and secondary magnetite in marine sediment by combining chemical and magnetic unmixing techniques. Global Planet. Change 110, 321–339.

Ludwig, P., Faestermann, T., Korschinek, G., Rugel, G., Dillmann, I., Fimiani, L., Bishop, S., Kumar, P., 2012. Search for superheavy elements with $292 \leq A \leq 310$ in nature with accelerator mass spectrometry. Phys. Rev. C 85, 024315.

Lugaro, M., Herwig, F., Lattanzio, J., Gallino, R., Straniero, O., 2003. S-Process Nucleosynthesis in Asymptotic Giant Branch Stars: A Test for Stellar Evolution. Astrophys. J. 586, 1305–1319.

Lugaro, M., Karakas, A., 2008. ^{26}Al and ^{60}Fe yields from AGB stars. New Astron. Rev. 52, 416–418.

Maher, B., 1988. Magnetic properties of some synthetic sub-micron magnetites. Geophysical Journal 94, 83–96.

Mao, X., Egli, R., Petersen, N., Hanzlik, M., Liu, X., 2014a. Magneto-Chemotaxis in Sediment: First Insights. PloS ONE 9, e102810.

Mao, X., Egli, R., Petersen, N., Hanzlik, M., Zhao, X., 2014b. Magnetotaxis and acquisition of detrital remanent magnetization by magnetotactic bacteria in natural sediment: First experimental results and theory. Geochem. Geophys. Geosyst. 15, 255–283.

Martini, E., 1971. Standard Tertiary and Quaternary calcareous nannoplankton zonation. Proc. 2nd Planktonic Conf. Roma 739-785.

Mayer, L., Pisias, N., Janecek, T., et al., 1992. Shipboard Scientific Party. Site 848. Proc. ODP, Init. Repts., College Station, TX, 138, 677–734.

Mayergoyz, I., 1986. Mathematical Models of Hysteresis. Phys. Rev. Lett. 56, 1518–1521.

McNeill, D., Kirschvink, J., 1993. Early dolomitization of platform carbonates and the preservation of magnetic polarity. J. Geophys. Res. 98, 7977–7986.

Mehra, O., Jackson, M., 1958. Iron oxide removal from soils and clays by a dithionite-citrate system buffered with sodium bicarbonate. Clay. Clay Miner. 7, 317–327.

Merchel, S., 1998. Über die Wechselwirkung der kosmischen Strahlung mit extraterrestrischer Materie: Radiochemische Bestimmung der Produktionsrate von kosmogenen langlebigen Radionukliden in Meteoriten. Ph.D. thesis. Universität Köln.

Merchel, S., 2015. Private communication.

Merchel, S., Faestermann, T., Herpers, U., Knie, K., Korschinek, G., Leya, I., Michel, R., Rugel, G., Wallner, C., 2000. Thin- and thick-target cross sections for the production of ^{53}Mn and ^{60}Fe. Nucl. Instrum. Methods Phys. Res., Sect. B 172, 806–811.

Merrill, R., McElhinny, M., McFadden, P., 2012. The magnetic field of the Earth. Academic Press, San Diego, California.

Meyer, B., 2005. Synthesis of Short-lived Radioactivities in a Massive Star, in: Krot, A., Scott, E., Reipurth, B. (Eds.), Chondrites and the Protoplanetary Disk, ASP Conference Series. pp. 515–526.

Middleton, R., 1983. A versatile high intensity negative ion source. Nucl. Instrum. Methods Phys. Res. 214, 139–150.

Moskowitz, B., Frankel, R., Bazylinski, D., Jannasch, H., Lovley, D., 1989. A comparison of magnetite particles produced anaerobically by magnetotactic and dissimilatory iron-reducing bacteria. Geophys. Res. Lett. 16, 665–668.

Muller, R., 1977. Radioisotope dating with a cyclotron. Science 196, 489.

Murad, E., Williams, I. (Eds.), 2002. Extraterrestrial dust in the near-Earth environment, Cambridge Univ. Press, Cambridge (2002).

Muxworthy, A., Dunlop, D., 2002. First-order reversal curve (FORC) diagrams for pseudo-single-domain magnetites at high temperature. Earth Planet. Sc. Lett. 203, 369–382.

Néel, L., 1958. Sur les effets d'un couplage entre grains ferromagnétiques doués d'hystérésis. Academie des sciences Seance du 24.4., 2313–2319.

Nelson, D., Korteling, R., Scott, W., 1977. Carbon-14: direct detection at natural concentrations. Science 198, 507.

Neuhäuser, R., Tetzlaff, N., Eisenbeiss, T., Hohle, M., 2011. On identifying the neutron star that was born in the supernova that placed ^{60}Fe on Earth. arXiv e-Prints 1111.0453v1, [astro–ph.SR].

Newell, A., 2005. A high-precision model of first-order reversal curve (FORC) functions for single-domain ferromagnets with uniaxial anisotropy. Geochem. Geophys. Geosys. 6, Q05010.

Newell, A., 2009. Transition to superparamagnetism in chains of magnetosome crystals. Geochem. Geophys. Geosys. 10, Q11Z08.

Niitsuma, S., Ford, K., Iwai, M., Chiyonobu, S., Sato, T., 2006. Data Report: Magnetostratigraphy and biostratigraphy correlation in pelagic sediments, ODP Site 1225, eastern equatorial Pacific, pp. 1–19.

Nishiizumi, K., Murrell, M., Davis, P., Arnold, J., 1980. Cosmic ray produced ^{53}Mn in deep sea spherules. Meteoritics 15, 342.

Nozawa, T., Kozasa, T., Habe, A., Dwek, E., Umeda, H., Tominaga, N., Maeda, K., Nomoto, K., 2007. Evolution of dust in primordial supernova remnants: can dust grains formed in the ejecta survive and be injected into the early interstellar medium? Astrophys. J. 666, 955–966.

Nucleonica, 2014. Nucleonica Nuclear Science Portal (www.nucleonica.com), Version 3.0.49. Karlsruhe .

Okada, H., Bukry, D., 1980. Supplementary modification and introduction of code numbers to the low-latitude coccolith biostratigraphic zonation. Mar. Micropaleontol. 5, 321–325.

Pan, Y., Petersen, N., Davila, A., Zhang, L., Winkelhofer, M., Liu, Q., Hanzlik, M., Zhu, R., 2005. The detection of bacterial magnetite in recent sediments of Lake Chiemsee (southern Germany). Earth Planet. Sc. Lett. 232, 109–123.

Penninga, I., de Waard, H., Moskowitz, B., Bazylinski, D., Frankel, R., 1995. Remanence measurements on individual magnetotactic bacteria using a pulsed magnetic field. J. Mag. Magn. Mater. 149, 279–286.

Petermann, H., Bleil, U., 1993. Detection of live magnetotactic bacteria in South Atlantic deepsea sediments. Earth Planet. Sc. Lett. 117, 223–228.

Pike, C., Fernandez, A., 1999. An investigation of magnetic reversal in submicron-scale Co dots using first order reversal curve diagrams. J. Appl. Phys. 85, 6668–6676.

Pike, C., Roberts, A., Dekkers, M., Verosub, K., 2001a. An investigation of multi-domain hysteresis mechanisms using FORC diagrams. Physics of the Earth and Planetary Interiors 126, 11–25.

Pike, C., Roberts, A., Verosub, K., 2001b. First-order reversal curve diagrams and thermal relaxation effects in magnetic particles. Geophys. J. Int. 145, 721–730.

Plane, J., 2012. Cosmic dust in the Earth's atmosphere. Chem. Soc. Rev. 414, 6507–6518.

Plane, J., Sánchez, J.C., 2015. Private communication.

Poutivtsev, M., 2007. Extraterrestrisches ^{53}Mn in hydrogenetischen Mangankrusten. Ph.D. thesis. Technische Universität München.

Poutivtsev, M., Dillmann, I., Faestermann, T., Knie, K., Korschinek, G., Lachner, J., Meier, A., Rugel, G., Wallner, A., 2010. Highly sensitive AMS measurements of ^{53}Mn. Nucl. Instrum. Methods Phys. Res., Sect. B 268, 756–758.

Preisach, F., 1935. Über die magnetische Nachwirkung. Z. Phys. 94, 277–302.

Rauscher, T., Heger, A., Hoffman, R., Woosley, S., 2005. Nucleosynthesis in massive stars with improved nuclear and stellar physics. Astrophys. J. 576, 323.

Rho, J., Kozasa, T., Reach, W., Smith, J., Rudnick, L., DeLaney, T., Ennis, J., Gomez, H., Tappe, A., 2008. Freshly Formed Dust in the Cassiopeia A Supernova Remnant as Revealed by the Spitzer Space Telescope. Astrophys. J. 673, 271.

Roberts, A., Chang, L., Heslop, D., Florindo, F., Larrasoaña, J., 2012. Searching for single domain magnetite in the 'pseudo-single-domain' sedimentary haystack: Implications of biogenic magnetite preservation for sediment magnetism and relative paleointensity determinations. J. Geophys. Res. 117, B08104.

Roberts, A., Florindo, F., Villa, G., Chang, L., Jovane, L., Bohaty, S., Larrasoaña, J., 2011. Magnetotactic bacterial abundance in pelagic marine environments is limited by organic carbon flux and availability of dissolved iron. Earth Planet. Sc. Lett. 310, 441–452.

Roberts, A., Pike, C., Verosub, K., 2000. First-order reversal curve diagrams: A new tool for characterizing the magnetic properties of natural samples. J. Geophys. Res. 105, 28461–28475.

Roberts, A., Tauye, L., Heslop, D., 2013. Magnetic paleointensity stratigraphy and high-resolution Quaternary geochronology: successes and future challenges. Quaternary Sci. Rev. 61, 1–16.

Robertson, D., France, D., 1994. Discrimination of remanence-carrying minerals in mixtures, using isothermal remanent magnetization acquisition curves. Phys. Earth Planet. In. 82, 223–234.

Rogers, L., Hill, K., Hawkes, R., 2005. Mass loss due to sputtering and thermal processes in meteoroid ablation. Planet. Space Sci. 53, 1341–1354.

Rolfs, C., Rodney, W., 1988. Cauldrons in the Cosmos. The University of Chicago Press, Ltd., London.

Rowan, C., Roberts, A., Broadbent, T., 2009. Reductive diagenesis, magnetite dissolution, greigite growth and paleomagnetic smoothing in marine sediments: A new review. Earth Planet. Sci. Lett. 277, 223–235.

Ruderman, M., 1974. Possible consequences of nearby supernova explosions for atmospheric ozone and terrestrial life. Science 184, 1079–1081.

Rugel, G., Faestermann, T., Knie, K., Korschinek, G., Poutivtsev, M., Schumann, D., Kivel, N., Günther-Leopold, I., Weinreich, R., Wohlmuther, M., 2009. New Measurement of the ^{60}Fe Half-Life. Phys. Rev. Lett. 103, 072502.

Sanfilippo, A., Westberg-Smith, M., Riedel, W., 1985. Plankton Stratigraphy. Cambridge Univ. Press.

Sarmineto, J., Gruber, N., 2006. Ocean Biogeochemical Dynamics. Princeton University Press.

Schaefer, J., Faestermann, T., Herzog, G., Knie, K., Korschinek, G., Masarik, J., Meier, A., Poutivtsev, M., Rugel, G., Schlüchter, C., Serefiddin, F., Winckler, G., 2006. Terrestrial ^{53}Mn - a new monitor of Earth surface processes. Earth Planet. Sc. Lett. 251, 334–345.

Schumann, D., Raub, T., Kopp, R., Guerquin-Kern, J.L., Wu, T.D., Rouiller, I., Smirnov, A., Sears, S., Lücken, U., Tikoo, S., Hesse, R., Kirschvink, J., Vali, H., 2008. Gigantism in unique biogenic magnetite at the Paleocene-Eocene Thermal Maximum. Proc. Natl. Acad. Sci., USA. 105, 17648–17653.

Shackleton, N., Baldauf, J., Flores, J.A., Iwai, M., Moore, T.J., Raffi, I., Vincent, E., 1995a. Biostratigraphic summary for Leg 138, in: Pisias, N., Mayer, L., Janecek, T., Palmer-Julson, A., van Andel, T. (Eds.), Proc. ODP, Sci. Results, 138, College Station, TX (Ocean Drilling Program). pp. 517–536.

Shackleton, N., Crowhurst, S., Hagelberg, T., Pisias, N., Schneider, D., 1995b. A new late neogene time scale: Application to leg 138 sites, in: Pisias, N., Mayer, L., Janecek, T., Palmer-Julson, A., van Andel, T. (Eds.), Proc. ODP, Sci. Results, 138, College Station, TX (Ocean Drilling Program). pp. 73–101.

Shcherbakov, V., Fabian, K., 2012. The geodynamo as a random walker: A view on reversal statistics. J. Geophys. Res. 117, B03101.

Shipboard Scientific Party, 1992a. Site 848, in: Mayer, L., Pisias, N., Janecek, T., et al. (Eds.), Proc. ODP, Init. Repts., 138, College Station, TX (Ocean Drilling Program). pp. 677–734.

Shipboard Scientific Party, 1992b. Site 851, in: Mayer, L., Pisias, N., Janecek, T., et al. (Eds.), Proc. ODP, Init. Repts., 138, College Station, TX (Ocean Drilling Program). pp. 891–965.

Simpson, E., Kasama, T., Pósfai, M., Buseck, P., Harrison, R., Dunin-Borkowski, R., 2005. Magnetic induction mapping of magnetite chains in magnetotactic bacteria at room temperature and close to the Verwey transition using electron holography. J. Physics: Conf. Series 170, 108–121.

Smith, R., Cox, D., 2001. Multiple supernova remnant models of the Local Bubble and the soft X-ray background. Astron. J. Suppl. 134, 283–309.

Sparks, N., Mann, S., Bazylinski, D., Jannash, H., Frankel, R., 1990. Structure and morphology of magnetite anaerobically produced by a marine magnetotactic bacterium and a dissimilatory iron-reducing bacterium. Earth Planet. Sci. Lett. 98, 14–22.

Spring, S., Bazylinski, D., 2006. Magnetotactic Bacteria. Springer New York.

Stoner, E., Wolfarth, E., 1948. A mechanism of magnetic hysteresis in heterogeneous alloys. Philos. Trans. R. Soc., London 240, 599.

Straub, S., Schmincke, H., 1998. Evaluating the tephra input into Pacific Ocean sediments: Distribution in space and time. Geol. Rundsch. 87, 461–476.

Stuart, F., Lee, M., 2012. Micrometeorites and extraterrestrial He in a ferromanganese crust from the Parific Ocean. Chem. Geol. 322-323, 209–214.

Takahashi, K., Yoshida, T., Umeda, H., 2013. Evolution of progenitors for electron capture supernovae. Arxiv e-prints arXiv:1302.6402, [astro–ph.SR].

Tanaka, M., Okamura, Y., Arakaki, A., Tanaka, T., Takeyama, H., Matsunaga, T., 2006. Origin of magnetosome membrane: proteomic analysis of magnetosome membrane and comparison with cytoplasmic membrane. Proteomics 6, 5234–5247.

Tauxe, L., 1993. Sedimentary records of relative paleointensity of the geomagnetic field: theory and practice. Rev. Geophys. 31, 319–354.

Tauxe, L., Banerjee, S., Butler, R., van der Voo, R., 2014. Essentials of Paleomagnetism. 3rd Web Edition, 2014.

Taylor, K., Macquaker, J., 2011. Iron minerals in marine sediments record chemical environments. Elements 7, 113–118.

Taylor, S., Brownlee, D., 1991. Cosmic spherules in the geologic record. Meteoritics 26, 203–211.

Tenaby, N., Gubbins, D., 2000. The effects of aliasing and lock-in processes on paleosecular variation records from sediments. Geophys. J. Int. 142, 563–570.

Tuniz, C., Bird, J., Fink, D., Herzog, G., 1998. Accelerator Mass Spectrometry - Ultrasensitive Analysis for Global Science. CRC Press LLC.

Vali, H., Förster, O., Amarantidis, G., Petersen, N., 1987. Magnetotactic bacteria and their magnetofossils in sediments. Earth Planet. Sc. Lett. 86, 389–400.

Vockenhuber, C., Bergmaier, A., Faestermann, T., Knie, K., Korschinek, G., Kutschera, W., Rugel, G., Steier, P., Vorderwinkler, K., Wallner, A., 2007. Development of isobar separation for ^{182}Hf AMS measurements of astrophysical interest. Nucl. Instrum. Methods Phys. Res., Sect. B 259, 250–255.

Vondrak, T., Plane, J., Broadley, S., Janches, D., 2008. A chemical model of meteoric ablation. Atmos. Chem. Phys. 8, 7015–7031.

Wallner, A., Bichler, M., Buczak, K., Dressler, R., Fitfield, L., Schumann, D., Sterba, J., Tims, S., Wallner, G., Kutschera, W., 2015a. Settling the Half-Life of ^{60}Fe: Fundamental for a Versatile Astrophysical Chronometer. Phys. Rev. Lett. 114, 041101.

Wallner, A., Faestermann, T., Feige, J., Feldstein, C., Knie, K., Korschinek, G., Kutschera, W., Ofan, A., Paul, M., Quinto, F., Rugel, G., Steier, P., 2015b. Abundance of live ^{244}Pu in deep-sea reservoirs on Earth points to rarity of actinide nucleosynthesis. Nature Communications 6, 5956.

Wanajo, S., Nomoto, K., Janka, H.T., Kitaura, F., Müller, B., 2009. Nucleosynthesis in electron capture supernovae of asymptotic giant branch stars. Astrophys. J. 695, 208–220.

Wang, W., Harris, M., Diehl, R., Halloin, H., Cordier, B., Strong, A., Kretschmer, K., Knödlseder, J., Jean, P., Lichti, G., Roques, J., Schanne, S., von Kienlin, A., Weidenspointner, G., Wunderer, C., 2007. SPI observations of the diffuse ^{60}Fe emission in the Galaxy. Astron. Astrophys. 469, 1005–1012.

Woodcock, K., Vondrak, T., Meech, S., Plane, J., 2006. A kinetic study of the reactions FeO^+ + O, $Fe^+\cdot N_2$ + O, $Fe^+\cdot O_2$ + O and FeO^+ + CO: implications for sporadic E layer in the upper atmosphere. Phys. Chem. Chem. Phys. 8, 1812–1821.

Woolridge, M., 1998. Gas-phase combustion synthesis of particles. Prog. Energy Combust. Sci. 245, 63–87.

Woosley, S., Janka, T., 2005. The physics of core-collapse supernovae. Nat. Phy. 1, 147–154.

Yamazaki, T., 2012. Paleoposition of the intertropical convergence zone in the eastern Pacific inferred from glacial-interglacial changes in terrigenous and biogenic magnetic mineral fractions. Geology 40, 151–154.

Yamazaki, T., Ikehara, M., 2012. Origin of magnetic mineral concentration variation in the Southern Ocean. Paleoceanography 27, PA2206.

Yan, L., Zhang, S., Chen, P., Liu, H., Yin, H., Li, H., 2012. Magnetotactic bacteria, magnetosomes and their application. Microbiol. Res. 167, 507–519.

Zachara, J., Fredrichson, J., Li, S., Kennedy, D., Smith, S., Gassman, P., 1998. Bacterial reduction of crystalline Fe(III) oxides in single phase suspensions and subsurface materials. Am. Mineral. 83, 1426–1443.

Zachara, J., Kukkadapu, R., Fredrichson, J., Groby, Y., Smith, S., 2002. Biomineralization of poorly crystalline Fe(III) oxides by dissimilatory metal reducing bacteria (DMRB). Geomicrobiol. J. 19, 179–207.

Acknowledgments

At the end, I would like to thank a number of people, who have made this work possible:

- Shawn Bishop for providing me with the opportunity to work on such an interesting topic, and for always having an open ear in all challenging situations.
- Ramon Egli, for taking time to introduce me to the field of magnetism and all the help with the magnetic measurements and analyses.
- Gunther Korschinek and Thomas Faestermann, for all the help and guidance with my work and for teaching me a great deal about experimental physics.
- Valentyna Chernenko, for preparing literally hundreds of ^{60}Fe samples with me.
- Karin Hain, Leticia Fimiani, Boyana Deneva, Nicolai Famulok, and José Manuel Gómez-Guzmán for all the help during the beamtimes and a great working atmosphere.
- Silke Merchel, for teaching me a great deal about AMS chemistry, for help in the development of the chemical extraction method for CBD samples, and for performing the preparation of the multi-isotope analysis samples.
- Georg Rugel, for teaching me a great deal about AMS and helping with beamtimes during our time in Garching, and afterward for performing the Be and Al measurements at Dresden.
- The MLL operator team for providing support during beamtimes and help with any technical challenges.
- The MLL workshop team, for all their quick solutions to any mechanical, electronics, and safety issues.
- Our secretaries, Christine Singer, Petra Zweckinger, and Sigrid Weichs, for lots of help with paperwork and organizational issues.
- Thomas Frederichs for providing me with the opportunity to perform AGFM measurements and magnetic extractions at Bremen University, and for several productive discussions.
- Marianne Hanzlik, for performing the electron microscopy.
- The rest of the DREAMS team, for helping with the ^{10}Be and ^{26}Al measurements in Dresden.
- Rudi Lutter and Klaus Steinberger for IT support.
- Xiangyu Zhao, for performing part of the ARM/IRM measurements at LMU Munich.
- Clemens Herlitzius, for programming advice over the years.
- Manuela Franks, for help with sample dating and labeling.
- Prof. John Plane and Juan Carrillo Sánchez, for discussions about micrometeorites and performing the atmospheric entry calculations.
- José Manuel Gómez-Guzmán, Antonio Delgado García and the rest of the ICPMS team of the Centro de Investigación, Sevilla, for the determination for the ICPMS measurements on blank samples.
- My mother Bärbel and my uncle Klaus, for endless support all my life.
- And most importantly: Leticia, for always being there for me in loving support.